

Commissioning of the ATLAS Calorimeters at the Large Hadron Collider and Prospects towards New Physics Search



Hideki Okawa

A thesis submitted to the Department of Physics
for the degree of Doctor of Philosophy

The University of Tokyo

February 2010

Abstract

The Large Hadron Collider (LHC) is the first collider to probe the physics at the TeV-energy scale. At the TeV-energy scale, many models of new physics are expected, of which the Supersymmetry (SUSY) and the Extra Dimensions are prospective examples. In such models, model-independent searches with jets and large missing transverse energy (Missing E_T ; E_T^{miss}) signatures are considered as effective ways to probe the new physics which may manifest itself at the TeV-energy scale. Jets and E_T^{miss} are reconstructed mainly from the calorimeter information, and thus it is of vast importance to understand the performance of the ATLAS calorimeters with the real data even before the collisions.

The ATLAS liquid argon (LAr) and hadronic tile calorimeter (TileCal) systems have been undergoing an extensive period of in-situ commissioning, including a series of cosmic ray runs which began in 2005 and continued in 2006-2008, and single beam runs that were taken in September 2008. The data from these runs improve our understanding of the detectors and also form a useful training ground for studying reconstruction algorithms such as clusters, jets, and E_T^{miss} in the calorimeter systems. In this thesis, commissioning studies of the ATLAS calorimeter system are shown. The in-situ measurement of electronic noise in the calorimeters was performed for the first time with the commissioning data. The Topological Clustering (Topocluster) algorithm, which is one of the standard calorimeter clustering algorithms used in ATLAS, was validated with the real data. The updates on the algorithm were proposed and made in order to achieve the expected performance, considering the non-Gaussian feature of the electronic noise observed in the TileCal. Jet and E_T^{miss} reconstruction algorithms were validated with the data as well. High energy deposits in the calorimeters were observed with the cosmic and the single beam data. Those high energy phenomena were well reproduced and described by Monte Carlo simulations. Such events become background to physics measurements during the collision data taking, so should be considered and treated.

The quality of jet and E_T^{miss} was investigated in detail, and the strategies to cope with the non-collision background (i.e. hot and dead channels, cosmic muons, and beam halo particles) were proposed. Here, so called the “cleaning” approach was adopted, which is to reject the clusters, jets or even the events which contain large contamination of the non-collision sources. The rejection power of the cleaning cuts were measured with the real data, and the selection efficiency of the physics signals were investigated with Monte Carlo simulation samples. Further investigations were performed with the “event overlay” technique, which allows to overlap real data on Monte Carlo samples in order to validate the cleaning cuts under more realistic conditions.

Finally, prospects towards new physics searches using “jet(s) + E_T^{miss} ” event topologies were discussed. Strategies to search for the Large Extra Dimensions (LED) with a monojet signature, and R-parity conserving Supersymmetric Models with a “multi-jet + E_T^{miss} ” event topology were investigated. Under the assumption of the integrated luminosity of 200 pb^{-1} at the center-of-mass energy of 10 TeV, the strategies were evaluated with realistic conditions.

To my mother, father, Anne,
and my mentor in life, Dr. Daisaku Ikeda

Acknowledgments

I would like to thank my supervisor, Prof. Sachio Komamiya for many discussions and suggestions that he has given me throughout these six years, and also letting me participate in this great experiment, ATLAS. I appreciate Prof. Tomio Kobayashi for accepting me in the ATLAS group at the International Center for Elementary Particle Physics (ICEPP) at the University of Tokyo.

I appreciate Prof. Richard Teuscher for the discussions and feedback on the calorimeter commissioning and cosmic analyses. Dr. Robert Stanek, who was the former project leader of the Tile Calorimeter group, accepted me as a member of the Tile Calorimeter project. I would like to express my sincere gratitude for his kindness. I appreciate Dr. Ana Henriques, who is the current Tile Calorimeter project leader, for letting me continue my participation in the group. I thank Dr. Tancredi Carli for many fruitful discussions related to jet and Missing E_T studies using the commissioning data. I would like to thank Dr. Michael Hauschild for becoming my supervisor at CERN. I enjoyed participating in the Data Quality works and shifts at the ATLAS Control Room.

I would like to thank the professors, staffs, and students at ICEPP. I thank Prof. Shoji Asai for the discussions on the studies related to the Supersymmetric Particle search and Missing E_T studies. I thank Prof. Naoko Kanaya for the discussions on the studies of Missing E_T validation using the Minimum Bias and W events. I appreciate Prof. Ikuo Ueda, Prof. Junichi Kanzaki, and Prof. Tatsuo Kawamoto for supporting me with my life at CERN. I thank Prof. Masaya Ishino for the discussions and feedback on the trigger configurations during the cosmic data takings. I would like to thank people in the Japanese analysis team, Prof. Junichi Tanaka, Prof. Osamu Jinnouchi, Prof. Junichi Kanzaki, Prof. Soshi Tsuno, Dr. Shimpei Yamamoto, Dr. Yousuke Kataoka, Dr. Koji Terashi, Dr. Taiki Yamamura, Dr. Tatsuya Masubuchi, and Michiru Kaneda. I would also like to thank Takayuki Sasaki and Kenta Oe for the discussions when I was new to this experiment.

I appreciate the collaborators in the calorimeter commissioning. I would like to thank Dr. Adam Gibson, Bin Guo, Gabe Rosenbaum, Dr. Bernhard Meirose, Dr. Adam Yurkewitz, Dr. Andre Nepomuceno, Travis Bain, Luciano Filho, Louise Heelan and the experts of the Tile and Liquid Argon Calorimeters for many discussions related to the commissioning studies. It was a great pleasure to work with them.

I would like to thank all the ATLAS collaborators and the experts of the LHC, whom I could not mention above, for making this tremendous experiment possible.

I also would like to express my thanks to the members of the Komamiya Laboratory. I appreciate Prof. Yoshio Kamiya, Dr. Masakazu Kurata, Dr. Taiki Yamamura, Dr. Taikan Suehara, Shinsuke Kawasaki, Shinya Sonoda, Tomoya Nakamura, Hakutaro Yoda, Takashi Yamanaka, Masahiro Oroku, Go Ichikawa, Yohei Yamaguchi, and Yutaro Iiyama. It was nice to have discussions and chatting with them.

I thank the secretaries at the Department of Physics and ICEPP, Ms. Kuniko Kono, Ms. Masako Shiota, Ms. Ritsuko Anbiru, Ms. Naoko Kataoka, and Ms. Chieko Kurita for their support.

I deeply appreciate my mother Toshiko, my father Takeshi, and Anne, for their eternal love and support. None of my accomplishments were possible without them. I would like to thank my friends of the Soka Gakkai International (SGI) for the friendship and encouragement. Finally, I would like to express my sincere gratitude to my mentor in life, Dr. Daisaku Ikeda, the president of the SGI for countless encouragement and guidance. He has always been my role model, and I learned from him the importance of courage, sincerity, patience, and endeavor without compromise.

I humbly would like to dedicate this thesis to my mother, father, Anne, and my mentor. Thank you so much.

Contributions of the Author to the ATLAS Collaboration

This thesis is based on the research of the author in collaboration with the members of the ATLAS Collaboration at the LHC.

The author has worked on developing methods for the data-driven estimation of the Standard Model background to Supersymmetric events, using all-hadronic “Multi-jet + E_T^{miss} ” event topology (so called “No-lepton Search Mode” in ATLAS). This has been the first work done in ATLAS in regards to data-driven methods for the estimation of background in Supersymmetric events. The author has also contributed to the development of the validation method of Missing Transverse Energy (Missing E_T ; E_T^{miss}) at the early stage of the experiment using the Minimum Bias and W events, and worked on updating the Missing E_T offline monitor. The largest contribution of the author goes to the commissioning of the ATLAS calorimeters with the cosmic ray and single beam data. The author was the first member from the Japanese institutes to be involved in the commissioning of the ATLAS calorimeters. The author has made a great contribution to the international academic exchange. The author’s work was one of the first works that linked the gap between the detector performance and physics analysis studies with the real data, such as the first in-situ noise measurement of the calorimeter cells, the first validation of “Topological Clustering” algorithm (one of the major clustering algorithms in ATLAS) with the cosmic ray data, and the first validation of jet algorithm with cosmic and single beam data. The first studies of jet and E_T^{miss} quality with the real data were done as well. Not only calorimeter information but also information from the Inner Detector tracks and the muon spectrometer was investigated to tag and reject non-collision effects. The impact of such non-collision background was investigated for various event topology searches using jets and E_T^{miss} , with a strong emphasis on the monojet signature expected from the Large Extra Dimensions and some SUSY models.

These works were presented at International Conferences, International Workshops, the JPS (Japan Physics Society) conferences, the 21 COE (Center-of-Excellence) Symposium at the University of Tokyo, and 46 times at the ATLAS internal meetings (see Appendix A for details).

The author contributed to shifts in the ATLAS Control Room for the Data Quality Working Group (since the M5 Week, the 5th combined cosmic run in October 2007), Tile Calorimeter Group, and Liquid Argon Calorimeter Group (since the M7 Week, the 7th combined cosmic run in May 2008). The author has experienced a referee for the ATLAS public note related to the Tile Calorimeter studies. This vast contribution to the collaboration is one of the characteristics of the author.

Contents

| | | |
|----------|--|-----------|
| I | Introduction | 23 |
| 1 | Introduction | 24 |
| 1.1 | Outline of the Thesis | 25 |
| 2 | The Standard Model and Physics at the LHC | 27 |
| 2.1 | Construction of the Standard Model | 27 |
| 2.2 | Physics at the LHC | 30 |
| 2.2.1 | Higgs Particle Searches | 32 |
| 2.2.2 | Supersymmetry | 35 |
| 2.2.3 | Extra Dimensions | 36 |
| 3 | The Large Hadron Collider | 40 |
| 3.1 | Why the LHC? | 40 |
| 3.2 | LHC Injector Complex | 42 |
| 3.3 | LHC Layout and Technology | 43 |
| 3.4 | Experiments at the LHC | 44 |
| 4 | The ATLAS Detector | 47 |
| 4.1 | Inner Detector | 48 |
| 4.1.1 | Beam Conditions Monitor | 50 |
| 4.1.2 | Pixel Detector | 50 |
| 4.1.3 | Semiconductor Tracker | 50 |
| 4.1.4 | Transition Radiation Tracker | 52 |
| 4.2 | Calorimeters | 52 |
| 4.2.1 | Electromagnetic Calorimeter | 52 |
| 4.2.2 | Hadronic Calorimeter | 54 |
| 4.3 | Muon Spectrometer | 59 |
| 4.3.1 | Muon Drift Tubes | 60 |
| 4.3.2 | Cathode Strip Chamber | 61 |
| 4.3.3 | Resistive Plate Chamber | 61 |
| 4.3.4 | Thin-Gap Chambers | 63 |
| 4.4 | Magnets | 63 |
| 4.5 | Forward Detectors | 66 |
| 4.5.1 | LUCID (LUminosity measurement using Cerenkov Integrating Detector) | 67 |

| | | |
|-----------|--|------------|
| 4.5.2 | ALFA (Absolute Luminosity For ATLAS) Detector | 67 |
| 4.5.3 | Zero-Degree Calorimeter | 67 |
| 4.6 | Trigger System | 70 |
| 5 | Energy Reconstruction in the ATLAS Calorimeters | 75 |
| 5.1 | Introduction: Physics of Calorimetry | 75 |
| 5.1.1 | Energy Loss of Charged Particles Through Matter | 75 |
| 5.1.2 | Interactions of Electrons and Photons in Matter | 77 |
| 5.1.3 | Electromagnetic Cascade | 77 |
| 5.1.4 | Hadronic Cascade | 79 |
| 5.2 | Energy Reconstruction in LAr Calorimeters | 80 |
| 5.2.1 | Optimal Filtering Method and Coefficients | 82 |
| 5.2.2 | Ramp Factor: ADC \rightarrow DAC | 83 |
| 5.2.3 | The M_{phys}/M_{cali} Factor | 83 |
| 5.2.4 | The $F_{DAC \rightarrow \mu A}$ Factor | 83 |
| 5.2.5 | The $F_{\mu A \rightarrow \text{MeV}}$ Factor | 83 |
| 5.3 | Energy Reconstruction in Tile Calorimeter | 85 |
| 5.3.1 | Energy Calibration in Tile Calorimeter | 86 |
| 5.4 | Hadronic Calibration in ATLAS Calorimeters | 88 |
| 5.4.1 | H1-style Calibration | 89 |
| 5.4.2 | Local Hadronic Calibration | 90 |
| II | Commissioning of the ATLAS Calorimeters | 91 |
| 6 | Cosmic and Single Beam Runs | 92 |
| 6.1 | Cosmic Runs | 92 |
| 6.2 | Single Beam Runs | 94 |
| 6.3 | LHC Accident | 94 |
| 6.4 | Data Streams | 95 |
| 6.4.1 | Physics Streams during Cosmic Runs | 96 |
| 6.4.2 | Physics Streams during Single Beam Runs | 98 |
| 6.5 | Runs Used in the Analyses | 99 |
| 7 | Calorimeter Measurement with Random Stream Data | 100 |
| 7.1 | Noise in the Calorimeters | 101 |
| 7.1.1 | Electronic Noise in TileCal | 101 |
| 7.1.2 | Electronic Noise in LAr | 112 |
| 7.2 | Problematic Channels in the ATLAS Calorimeters | 115 |
| 7.2.1 | TileCal Bad Channel Search | 120 |
| 7.3 | Performance of Calorimeter Clusters | 123 |
| 7.3.1 | Sliding Window Algorithm | 123 |
| 7.3.2 | Topological Clustering | 124 |
| 7.3.3 | Performance of Topoclusters in Random Stream Data | 125 |
| 7.4 | Performance of Missing E_T in Random Stream Data | 130 |

| | | |
|------------|---|------------|
| 7.4.1 | Missing E_T Algorithm in ATLAS | 130 |
| 7.4.2 | Performance of E_T^{miss} in Data and Its Improvement | 131 |
| 8 | Calorimeter Measurement with Cosmic Ray Data | 136 |
| 8.1 | Cosmic Rays | 136 |
| 8.2 | Cosmic Monte Carlo Simulation in ATLAS | 138 |
| 8.3 | High Energy Events from Cosmics | 140 |
| 8.4 | Test of Object Reconstruction in the Calorimeters | 144 |
| 8.4.1 | Topological Clusters in Cosmic Ray Data | 144 |
| 8.4.2 | Jet Reconstruction With Cosmic Ray Data | 148 |
| 8.4.3 | Missing Transverse Energy Reconstruction Using Cosmic Ray Data | 155 |
| 9 | Quality of Calorimeter Objects | 159 |
| 9.1 | Quality Variables and Cleaning Cuts | 160 |
| 9.1.1 | Jet-level quality | 160 |
| 9.1.2 | Event-level Quality | 175 |
| 9.1.3 | Cleaning for Pure Cosmic Events | 175 |
| 9.2 | Event Overlay Studies | 176 |
| 9.2.1 | Event Overlay Algorithm | 176 |
| 9.2.2 | Investigations on Event Overlap of Cosmic Rays on Collision Events | 177 |
| III | Prospects towards New Physics Search | 182 |
| 10 | Searches for New Physics with Jets and E_T^{miss} Event Topologies | 183 |
| 10.1 | Jets & E_T^{miss} Signatures from New Physics | 184 |
| 10.1.1 | SUSY Search Modes in ATLAS | 184 |
| 10.2 | Physics Objects and Algorithms | 184 |
| 10.2.1 | Electrons | 185 |
| 10.2.2 | Muons | 185 |
| 10.2.3 | Jets | 185 |
| 10.2.4 | Missing E_T | 185 |
| 10.2.5 | b-Tagging | 186 |
| 11 | Monojet Search for the Large Extra Dimensions | 188 |
| 11.1 | Monojet Signature from the Large Extra Dimensions | 188 |
| 11.1.1 | Real KK-Graviton Emission in Large Extra Dimensions Model . . | 189 |
| 11.2 | Monte Carlo Simulation Samples and Data | 190 |
| 11.3 | Event Selection | 191 |
| 11.3.1 | Trigger Menus for the Monojet Search | 192 |
| 11.3.2 | Absence of Reconstructed Leptons | 192 |
| 11.3.3 | Selection Cuts on Jets | 196 |
| 11.3.4 | Non-collision Background Rejection | 196 |
| 11.3.5 | Event Selection | 203 |

| | |
|--|------------|
| 12 Multi-jet plus E_T^{miss} Search for R-parity Conserving SUSY Models | 208 |
| 12.1 Data-Driven Methods for Background Estimation | 208 |
| 12.2 Monte Carlo Simulation Samples and Data | 209 |
| 12.3 Trigger Menus for the Multi-jet Search | 209 |
| 12.4 Event Selection for No-lepton Search Mode | 211 |
| 12.5 Estimation of Background | 215 |
| 12.5.1 $Z(\rightarrow \nu\bar{\nu})$ +jets Background | 215 |
| 12.5.2 W +jets Background | 219 |
| 12.5.3 $t\bar{t}$ +jets Background | 225 |
| 12.5.4 QCD Multi-jet Background | 228 |
| 12.5.5 Non-collision Background | 228 |
| 12.6 Systematic Uncertainties | 230 |
| 12.6.1 Systematics in Data-driven Methods | 231 |
| 12.6.2 Systematics from Jet and E_T^{miss} Performance | 233 |
| 12.7 Background Subtraction and Signal Significance | 237 |
| 12.7.1 Effective Mass Distributions | 238 |
| 12.7.2 Number Counting Approach | 238 |
| 13 Conclusions | 245 |
| A Contributions in ATLAS Publications and Presentations | 247 |
| A.1 Publications | 247 |
| A.1.1 Articles | 247 |
| A.1.2 ATLAS Note | 247 |
| A.1.3 Proceedings | 247 |
| A.2 Public Plots | 248 |
| A.3 Presentations | 248 |
| A.3.1 International Conference Presentations | 248 |
| A.3.2 ATLAS Workshop Presentations | 248 |
| A.3.3 National Meetings and Symposia | 249 |
| A.3.4 ATLAS Internal Presentations | 249 |
| B Optimal Filtering Method | 253 |
| C Missing E_T Algorithm in ATLAS | 257 |
| D Functions in KK-Graviton Processes | 260 |
| E Monte Carlo Simulation Samples Used | 261 |
| E.1 Samples for Monojet Studies | 261 |
| E.2 Samples for Multi-jet Studies | 262 |
| F Monte Carlo-based Estimation of $Z(\rightarrow \nu\bar{\nu})$ BG for SUSY Searches | 264 |

List of Figures

| | | |
|------|--|----|
| 2.1 | Cross section and branching ratio of the Standard Model Higgs bosons . . . | 33 |
| 2.2 | Feynman diagrams of the Higgs productions | 33 |
| 2.3 | Sensitivity of ATLAS to the discovery of the Standard Model Higgs bosons | 34 |
| 2.4 | Expected Missing E_T distributions of a benchmark Supersymmetric events and the Standard Model background | 35 |
| 2.5 | Experimental limits on the parameters of the modified Newtonian gravi- tational force | 37 |
| 2.6 | Lower limits of M_D in the Large Extra Dimension model | 37 |
| 2.7 | Side-view of a simulated black hole event in ATLAS | 39 |
| | | |
| 3.1 | CERN and the LHC | 41 |
| 3.2 | The LHC Layout | 43 |
| 3.3 | LHC cryodipole in the arc section | 45 |
| 3.4 | LHC Cell | 46 |
| | | |
| 4.1 | ATLAS Detector | 48 |
| 4.2 | Cross section of the ATLAS Detector | 49 |
| 4.3 | Inner Detector | 51 |
| 4.4 | Position of the Beam Conditions Monitor inside the inner detector | 51 |
| 4.5 | Semiconductor Tracker (SCT) module | 52 |
| 4.6 | ATLAS Calorimeter System | 53 |
| 4.7 | EM Accordion Structure | 55 |
| 4.8 | Amount of dead material in front of the EM calorimeter | 56 |
| 4.9 | Thickness of each accordion sampling layer in the EM calorimeter | 56 |
| 4.10 | TileCal Module | 58 |
| 4.11 | TileCal Segmentation | 58 |
| 4.12 | Typical fiber bundles in TileCal | 59 |
| 4.13 | HEC Module | 60 |
| 4.14 | FCAL Module | 60 |
| 4.15 | Muon Spectrometer | 61 |
| 4.16 | Momentum resolution of the muon spectrometer | 62 |
| 4.17 | Muon Trigger System | 62 |
| 4.18 | Sideview of the muon spectrometer | 63 |
| 4.19 | MDT Chamber | 64 |
| 4.20 | CSC | 64 |
| 4.21 | RPC | 65 |

| | | |
|------|--|-----|
| 4.22 | TGC | 65 |
| 4.23 | Schematic view of magnets | 66 |
| 4.24 | Forward Detectors | 68 |
| 4.25 | LUCID Detector | 68 |
| 4.26 | The layout of the ALFA Detector | 69 |
| 4.27 | Schematic view of the ZDC in the TAN | 69 |
| 4.28 | The overview of the ATLAS trigger system | 71 |
| 4.29 | Level-1 Trigger | 71 |
| | | |
| 5.1 | Stopping power for positive muons in copper | 76 |
| 5.2 | Fractional energy loss per radiation length in lead as a function of electron or positron energy | 78 |
| 5.3 | Photon total cross sections as a function of energy in carbon and lead | 78 |
| 5.4 | Cell energy reconstruction formula in LAr | 80 |
| 5.5 | Diagram of the Liquid Argon Calorimeter read-out electronics | 81 |
| 5.6 | Form of the ionization signal and the shaped ionization signal | 82 |
| 5.7 | ADC peaks and input DAC values | 84 |
| 5.8 | Pulse shape from calibration runs and physics runs | 84 |
| 5.9 | Diagram of the TileCal read-out electronics | 86 |
| 5.10 | Calibration in TileCal | 87 |
| 5.11 | Response to a CIS pulse of 2 pC and 560 pC | 87 |
| 5.12 | The cell response of electrons at 20° | 89 |
| | | |
| 6.1 | First Cosmic Data | 92 |
| 6.2 | Cosmic Data in Fall 2008 | 94 |
| 6.3 | First Single Beam Data | 95 |
| | | |
| 7.1 | Contribution of electronic, pile-up and total noise | 102 |
| 7.2 | Electronic and total noise of the calorimeters at the cell-level | 102 |
| 7.3 | Definition of cells in the Tile calorimeter | 103 |
| 7.4 | Electronic noise in the TileCal Barrel at the cell-level in M5 run 29576 | 105 |
| 7.5 | Energy distribution of TileCal cells | 105 |
| 7.6 | Tile Calorimeter power distributions | 106 |
| 7.7 | Non Gaussian distribution of TileCal pedestal | 106 |
| 7.8 | Correlation of electronic noise in TileCal LBA 16 | 108 |
| 7.9 | Correlation of electronic noise among the drawers in TileCal PMT1 in LBA108 | 108 |
| 7.10 | η -dependence of the electronic noise of the TileCal cells in Fall 2008 cosmic data | 109 |
| 7.11 | ϕ -dependence of the electronic noise of the TileCal cells in Fall 2008 cosmic data | 109 |
| 7.12 | Stability of the pedestals of the TileCal in Fall 2008 runs | 110 |
| 7.13 | Stability of the Electronic noise of the TileCal in Fall 2008 runs | 111 |
| 7.14 | Electronic noise of the LAr Calorimeter at the cell-level | 112 |
| 7.15 | Electronic noise and volume of calorimeter cells in LAr as a function of η | 112 |
| 7.16 | Stability of the pedestals of the Liquid Argon Calorimeter in Fall 2008 runs | 113 |

| | | |
|------|---|-----|
| 7.17 | Stability of the electronic noise of the Liquid Argon Calorimeter in Fall 2008 runs | 114 |
| 7.18 | η - ϕ map of LAr and TileCal masked problematic channels | 116 |
| 7.19 | The distributions of EMTopoclusters in M5 run 29576 NIM0 stream | 117 |
| 7.20 | Noise values of LBA PMT 6 for each drawer in M7 run 69373 from the RNDM0 stream | 121 |
| 7.21 | Mean energy of EBA PMT 29 in M7 run 69373 from the RNDM0 stream | 121 |
| 7.22 | Energy difference of PMT's in the same cell (PMT 3 & 4 in LBA) in M7 run from the 69373 RNDM0 stream | 122 |
| 7.23 | Energy distribution of PMT's | 122 |
| 7.24 | Contributions of calorimeter cells to combined towers shown in schematic $\eta - \phi$ grid | 124 |
| 7.25 | Schematic view of Topological Clustering algorithm | 125 |
| 7.26 | Sensitivity of Topoclusters to noise database | 126 |
| 7.27 | Ratio of the RMS and the Gaussian σ | 127 |
| 7.28 | Ratio between the confidence level and the Gaussian sigma | 127 |
| 7.29 | Number of reconstructed Topoclusters | 128 |
| 7.30 | η distributions of reconstructed Topoclusters | 128 |
| 7.31 | $\eta - \phi$ distributions in December 08 reprocessing data and new reconstruction | 129 |
| 7.32 | "MET_Base" Missing E_X and E_Y from random stream data and toy Monte Carlo samples from a Gaussian noise model | 132 |
| 7.33 | "MET_Base" E_T^{miss} from random stream data and toy Monte Carlo samples from a Gaussian noise model | 132 |
| 7.34 | "MET_Topo" Missing E_X and E_Y from random stream data and toy Monte Carlo samples from a Gaussian noise model | 134 |
| 7.35 | "MET_Topo" E_T^{miss} from random stream data and toy Monte Carlo samples from a Gaussian noise model | 134 |
| 7.36 | "MET_Topo" Missing E_X and E_Y from random stream data with and without updated Topocluster algorithm and toy Monte Carlo samples from a Gaussian noise model | 135 |
| 7.37 | "MET_Topo" E_T^{miss} from random stream data with and without updated Topocluster algorithm and toy Monte Carlo samples from a Gaussian noise model | 135 |
| 8.1 | Schematic view of air shower development | 137 |
| 8.2 | Vertical fluxes of cosmic rays in the atmosphere | 137 |
| 8.3 | Schematic view of cosmic Monte Carlo simulation | 139 |
| 8.4 | Layout of ATLAS cavern at Point 1 | 139 |
| 8.5 | Origin of cosmic muons at the surface in the Monte Carlo simulation | 141 |
| 8.6 | Impact point of cosmic muons on surface in cosmic ray data | 142 |
| 8.7 | Momentum of generated muons that reached the ATLAS detector | 142 |
| 8.8 | Momentum distribution of stand-alone muon spectrometer tracks in cosmic data and Monte Carlo | 143 |
| 8.9 | Sum E_T distribution from cosmic ray data and Monte Carlo simulation | 144 |

| | | |
|------|--|-----|
| 8.10 | Sum E_T distribution in each calorimeter partition in run 90272 L1Calo stream | 145 |
| 8.11 | A TeV event in run 90272 L1Calo stream | 146 |
| 8.12 | An air shower event in run 90272 L1Calo stream | 146 |
| 8.13 | The number of EMTopoclusters in M5 run 29576 NIM0 stream | 147 |
| 8.14 | Energy of Tile Topoclusters for M5 run 29576 | 148 |
| 8.15 | Schematic overview of jet reconstruction in ATLAS | 150 |
| 8.16 | Number of reconstructed cone-algorithm jets ($E_T > 7$ GeV) in cosmic data | 151 |
| 8.17 | Number of reconstructed cone-algorithm jets ($E_T > 20$ GeV) in cosmic data | 151 |
| 8.18 | Transverse energy of reconstructed jets in run 90272 | 152 |
| 8.19 | Reconstructed jets' η - ϕ distribution for run 90272 CosmicMuons stream . | 152 |
| 8.20 | Reconstructed jets' η - ϕ distribution for run 90272 L1Calo stream | 153 |
| 8.21 | Comparison of Jet distributions in run 90272 L1Calo stream with cosmic Monte Carlo samples | 154 |
| 8.22 | Comparison of energy distributions of bremsstrahlung photons from cosmic muons and reconstructed "fake" jets in cosmic Monte Carlo samples . . . | 155 |
| 8.23 | E_T^{miss} from MET_Base and MET_Topo algorithm in run 90272 L1Calo stream | 157 |
| 8.24 | Sum E_T vs E_T^{miss} as measured in M8 run 77585. | 158 |
| | | |
| 9.1 | Jet EM fraction in cosmic data and QCD Monte Carlo | 162 |
| 9.2 | Jet EM fraction from Cone4H1TowerJets and Cone4H1TopoJets | 164 |
| 9.3 | Correlation plots of transverse energy of jets and jet EM fraction | 165 |
| 9.4 | Examples of events with mid-EM fraction | 166 |
| 9.5 | Inner Detector event display from cosmic run 90270 | 168 |
| 9.6 | Number of Tracks in cosmic data and QCD dijet Monte Carlo | 169 |
| 9.7 | Numbers of tracks associated with jets | 170 |
| 9.8 | Number of clusters in jets | 172 |
| 9.9 | Number of clusters in Cone4H1TopoJets | 173 |
| 9.10 | Number of cells in Cone4H1TopoJets from run 90272 L1Calo stream and QCD di-jet Monte Carlo samples | 173 |
| 9.11 | Correlation of jet quality variables | 174 |
| 9.12 | Event quality from jet information | 176 |
| 9.13 | Preliminary cleaning on Cone4H1TowerJets and Cone4H1TopoJets . . . | 177 |
| 9.14 | Jet EM fraction in overlaid samples | 178 |
| 9.15 | Number of Topolusters in Jets in overlaid samples | 179 |
| 9.16 | Number of associated tracks in jets in overlaid samples | 179 |
| 9.17 | Jet charge fraction in overlaid samples | 180 |
| | | |
| 10.1 | Distribution of jet b-tagging weight | 187 |
| | | |
| 11.1 | Leading order Feynman diagrams of KK-graviton emission with monojet signature | 190 |
| 11.2 | Cross section of LED monojet processes in SHERPA as a function of the number of extra dimensions | 191 |
| 11.3 | Efficiency of jet triggers at the Event Filter level | 193 |

| | | |
|-------|---|-----|
| 11.4 | Efficiency of E_T^{miss} triggers at the Event Filter level | 193 |
| 11.5 | Number of reconstructed electrons from LED KK-graviton signals and background | 194 |
| 11.6 | Number of reconstructed combined and MS-standalone muons from LED KK-graviton signals and background | 195 |
| 11.7 | Leading jet distributions of LED KK-graviton signals and background | 198 |
| 11.8 | Second leading jet distributions of LED KK-graviton signals and background | 199 |
| 11.9 | Number of jets for events with the leading jet $p_T > 100$ GeV | 200 |
| 11.10 | EM fraction of the leading jet from LED KK-graviton signals and background | 202 |
| 11.11 | Charge fraction of the leading jet from LED KK-graviton signals and background | 202 |
| 11.12 | Expected E_T^{miss} distributions in monojet signature with LED KK-Graviton signals | 205 |
| 12.1 | E_T^{miss} distributions of SUSY signals and Standard Model background after selection cuts | 212 |
| 12.2 | E_T^{miss} and effective mass distributions after No Lepton Mode selection cuts | 213 |
| 12.3 | Invariant mass of dimuons | 215 |
| 12.4 | Trigger efficiency of reconstructed muons | 217 |
| 12.5 | Identification efficiency of muons | 218 |
| 12.6 | Efficiency of Z reconstruction using dimuons as a function of p_T | 219 |
| 12.7 | Estimation of $Z(\rightarrow \nu\bar{\nu})$ background using $Z(\rightarrow \mu^+\mu^-)$ events | 220 |
| 12.8 | Estimation of $W(\rightarrow \tau\nu_\tau)$ background using one-lepton control samples | 223 |
| 12.9 | Estimation of $W(\rightarrow \mu\nu_\mu)$ no-lepton background using $W(\rightarrow \mu\nu_\mu)$ one-lepton control samples | 224 |
| 12.10 | Estimation of $t\bar{t}(\rightarrow b\bar{b}\tau\nu_\tau qq)$ background using $t\bar{t}(\rightarrow b\bar{b}\mu\nu_\mu qq)$ one-lepton control samples | 227 |
| 12.11 | E_T^{miss} distributions of SUSY signals and Standard Model background after selection cuts | 229 |
| 12.12 | Effects of jet and E_T^{miss} systematics on E_T^{miss} distribution of SU3 | 237 |
| 12.13 | E_T^{miss} and effective mass distribution of SU3 signals and Standard Model background | 239 |
| 12.14 | E_T^{miss} and effective mass distribution of SU4 signals and Standard Model background | 240 |
| 12.15 | Effective mass distribution of SU4 signals | 241 |
| 12.16 | Significance of the SUSY signal SU3 scanned over various E_T^{miss} and M_{eff} thresholds | 242 |
| 12.17 | Significance of the SUSY signal SU4 scanned over various E_T^{miss} and M_{eff} thresholds | 243 |
| F.1 | Overview of quasi-data-driven estimation scheme for $Z(\rightarrow \nu\bar{\nu})$ background | 265 |
| F.2 | Normalization factor determined by comparing $Z(\rightarrow l^+l^-)$ Monte Carlo and pseudo-data | 266 |
| F.3 | Estimation of $Z(\rightarrow \nu\bar{\nu})$ background using quasi-data-driven method | 266 |

List of Tables

| | | |
|-----|--|-----|
| 2.1 | Elementary Particles in the Standard Model | 31 |
| 3.1 | LHC Parameters for proton-proton collisions | 45 |
| 4.1 | Primary trigger menus proposed for the luminosity $10^{31}\text{cm}^{-2}\text{s}^{-1}$ at the center-of-mass energy 10 TeV | 73 |
| 4.2 | Primary trigger menus proposed for the luminosity $10^{31}\text{cm}^{-2}\text{s}^{-1}$ at the center-of-mass energy 10 TeV | 74 |
| 6.1 | ATLAS Cosmic Ray Milestone Weeks and Beyond. | 93 |
| 6.2 | Level-1 Calorimeter menus used in the cosmic run 90272 L1Calo stream | 97 |
| 7.1 | Numbers and percentages of masked problematic cells for each partition . | 116 |
| 7.2 | Categories of the problematic LAr channels | 118 |
| 7.3 | Categories of the problematic TileCal channels | 119 |
| 7.4 | Mean of reconstructed number of Topoclusters in each calorimeter region | 127 |
| 8.1 | Profile of generated cosmic Monte Carlo simulation samples | 138 |
| 8.2 | Triggered event rate of high energy events in run 90272 L1Calo stream . | 147 |
| 8.3 | Triggered event rate for numbers of TopoJets per event | 151 |
| 9.1 | Definition of QCD dijet Monte Carlo samples | 161 |
| 9.2 | The breakdown of the ratio of jets remaining after different cut values on the EM fraction for Cone4H1TowerJets | 163 |
| 9.3 | The breakdown of the ratio of jets remaining after different cut values on the EM fraction for Cone4H1TopoJets | 163 |
| 9.4 | The breakdown of the ratio of jets remaining after different cut values on the number of associated tracks in jets | 169 |
| 9.5 | The ratio of jets remaining after different cut values on the jet size | 171 |
| 9.6 | Mean number of cells in jets | 171 |
| 9.7 | The breakdown of the ratio of jets remaining after different cut values on the number of cells | 171 |
| 9.8 | The breakdown of the ratio of jets remaining after different cut values on the EM fraction for Cone4H1TopoJets in overlaid samples | 178 |
| 9.9 | The breakdown of the ratio of jets remaining after different cut values on the number of clusters in Cone4H1TopoJets in overlaid samples | 178 |

| | | |
|-------|--|-----|
| 9.10 | The breakdown of the ratio of jets remaining after different cut values on the number of associated tracks for Cone4H1TopoJets in overlaid samples | 179 |
| 9.11 | The breakdown of the ratio of jets remaining after different cut values on the charge fraction for Cone4H1TopoJets in overlaid samples | 181 |
| 11.1 | Cross section of LED processes in SHERPA | 191 |
| 11.2 | Number of events with no reconstructed electrons | 197 |
| 11.3 | Number of events with no reconstructed muons | 197 |
| 11.4 | Number of events with second leading jet veto | 201 |
| 11.5 | Number of events after EM fraction and charge fraction cuts | 206 |
| 11.6 | Number of events remaining after each selection cut for background processes | 207 |
| 11.7 | Number of events remaining after each selection cut for the LED signals . | 207 |
| 12.1 | Cross section and profile of the benchmark SUSY mSUGRA samples . . | 210 |
| 12.2 | Particle mass spectrum for the benchmark mSUGRA points | 210 |
| 12.3 | Breakdown of events after event selection of no-lepton search mode . . . | 214 |
| 12.4 | Breakdown of events after event selection of no-lepton search mode . . . | 214 |
| 12.5 | Number of events of $Z(\rightarrow \nu\bar{\nu})$ background and estimation | 221 |
| 12.6 | Origin of W background to no-lepton search mode | 221 |
| 12.7 | Number of events of $W(\rightarrow \tau\nu_\tau)$ background and estimation | 222 |
| 12.8 | Number of events of $W(\rightarrow \mu\nu_\tau)$ no-lepton background and estimation . . | 225 |
| 12.9 | Origin of semileptonic $t\bar{t}$ background to no-lepton search mode | 226 |
| 12.10 | Number of events of $t\bar{t}$ no-lepton background with τ inside the acceptance and estimation | 226 |
| 12.11 | Breakdown of the Standard Model background and cosmic-QCD overlay events after event selection of no-lepton search mode | 230 |
| 12.12 | Systematic uncertainties assumed for data-driven estimation of $Z(\rightarrow \nu\bar{\nu})$ background | 231 |
| 12.13 | Systematic uncertainties assumed for data-driven estimation of $W(\rightarrow \tau\nu_\tau)$ background | 232 |
| 12.14 | Systematic uncertainties assumed for data-driven estimation of $W(\rightarrow \mu\nu_\mu)$ background | 232 |
| 12.15 | Systematic uncertainties assumed for data-driven estimation of $t\bar{t}(\rightarrow b\bar{b}\tau\nu_\tau qq)$ background | 233 |
| 12.16 | Breakdown of events after event selection of no-lepton search mode with considerations on jet & E_T^{miss} systematics | 235 |
| 12.17 | Uncertainty of selection efficiency from jet and E_T^{miss} systematics for the Standard Model background | 235 |
| 12.18 | Breakdown of SUSY signal events after event selection of no-lepton search mode with jet & E_T^{miss} systematics | 236 |
| 12.19 | Uncertainty of selection efficiency from jet and E_T^{miss} systematics for the SUSY signals | 236 |
| 12.20 | Significance of mSUGRA benchmark signals | 244 |
| C.1 | E_T^{miss} quantities in ATLAS | 259 |

| | | |
|-----|---|-----|
| E.1 | Cross section and profile of Standard Model samples | 261 |
| E.2 | Cross section and profile of Monte Carlo samples for Z events | 262 |
| E.3 | Cross section and profile of Monte Carlo samples for Z events | 263 |
| E.4 | Cross section and profile of Monte Carlo samples for Top and QCD events | 263 |

Acronyms and Terms

- **ADC:** Analog to Digital Converter.
- **ADD:** The Large Extra Dimension model by Arkani-Hamed, Dimopoulos, and Dvali.
- **AOD:** Analysis Object Data. These are the data files that contain information of reconstructed physics quantities and are used for physics analyses in ATLAS.
- **Athena:** Software framework used in ATLAS.
- **ATLAS:** A Toroidal LHC Apparatus. One of the two general purpose detectors at the LHC.
- **BCID:** Bunch Crossing Identifier. It is the number that defines which bunch crossing an event belongs to.
- **BCM:** Beam Conditions Monitor.
- **BH:** Black Hole. In this thesis, the acronym indicates the extradimensional mini-black holes expected to be produced at the LHC in some extra dimensional models.
- **BSM:** Physics beyond the Standard Model.
- **CIS:** Charge Injection System of the Tile Calorimeter. It is the calibration system to derive the calibration constants which convert the ADC counts to pC.
- **Cone4H1TopoJets:** Jets reconstructed by the cone algorithm with the cone size of 0.4 and the Topoclusters as the inputs for the reconstruction. H1-style hadronic calibration was adopted for the energy reconstruction.
- **Cone4H1TowerJets:** Jets reconstructed by the cone algorithm with the cone size of 0.4 and the combined towers as the inputs for the reconstruction. H1-style hadronic calibration was adopted for the energy reconstruction.
- **CRC:** Cyclic Redundancy Check.
- **CTP:** Central Trigger Processor.
- **DAC:** Digital to Analog Converter.
- **DAQ:** Data Acquisition System.
- **DCS:** Detector Control System. It is the TDAQ system that controls the ATLAS sub-detectors, their common interfaces, and communication with CERN services (cooling, ventilation, electricity distribution, safety, etc.) and LHC accelerator.

- **DMU**: Data Management Unit.
- **DSP**: Digital Signal Processor.
- **EBA**: A-side (positive η) of the Extended-Barrel of the Tile Calorimeter.
- **EBC**: C-side (negative η) of the Extended-Barrel of the Tile Calorimeter.
- **EF**: Event Filter. It is the highest-level trigger in ATLAS.
- **EMB**: Barrel electromagnetic calorimeter.
- **EMEC**: End-cap electromagnetic calorimeter.
- **ESD**: Event Summary Data. These are data files used in ATLAS with more information stored than the AOD's. They contain sufficient information to re-run the reconstruction, and are also used for detailed detector commissioning analyses.
- **FCAL**: The forward calorimeter.
- **H1 calibration**: Cell energy calibration based on the energy density to account for the non-linear energy response of calorimeters to hadrons. H1 is one of the HERA (e-p collider) experiments at DESY.
- **HEC**: The hadronic end-cap calorimeter.
- **HLT**: High-Level Trigger; an inclusive name for the Level-2 trigger and Event Filter.
- **HV**: High voltage.
- **J0-J8**: Monte Carlo simulation samples for QCD dijets. The samples are sliced by the transverse momentum of the leading parton. Nine simulation samples exist from J0 to J8, where the numbers indicate the “n'th” slice. See Chapter 9 and Appendix E for more detail.
- **KK**: Kaluza-Klein. Particles excited due to the boundary conditions of the extra dimensions.
- **L1Calo**: The Level-1 Calorimeter Trigger.
- **LAr**: The Liquid Argon Calorimeters in ATLAS. Inclusive term for the electromagnetic, the end-cap hadronic and the forward calorimeter using the Liquid Argon technique.
- **LED**: The Large Extra Dimensions model proposed by N. Arkani-Hamed, S. Dimopoulos, G. Dvali.
- **LBA**: A-side (positive η) of the Long-Barrel of the Tile Calorimeter.
- **LBC**: C-side (negative η) of the Long-Barrel of the Tile Calorimeter.

- **LHC**: The Large Hadron Collider.
- **LSP**: The lightest Supersymmetric particles.
- **LUCID**: LUMinosity measurement using Cerenkov Integrating Detector. It is the detector that measures the relative luminosity.
- **LV**: Low voltage.
- **M1-M8**: Milestone Weeks. A series of cosmic ray runs in ATLAS motivated to combine and operate all the ATLAS detector components available at the time of running. M1 corresponds to the first Milestone Week.
- **MBTS**: Minimum Bias Trigger Scintillator.
- **Missing E_T** (E_T^{miss}): Missing transverse energy. The variable which quantifies the imbalance of the transverse momentum using the calorimeters and the muon spectrometer.
- **MET_Base, MET_Topo, MET_RefFinal**: Reconstruction schemes of Missing E_T . See Section 7.4.1.
- **OFC**: Optimal Filtering Coefficients. The coefficients used for energy reconstruction from the calorimeter signals with the Optimal Filtering Method.
- **Pixel**: Pixel Detector. It is one of the sensors of the inner detector in ATLAS, placed closest to the interaction point.
- **PMT**: Photo-multiplier. A device to detect light with high gain and sensitivity. It is used as the sensor in the ATLAS Tile Calorimeter.
- **Point 1-8**: Eight numerical names assigned to the underground sites along the LHC ring with equal intervals. Point 1 is where ATLAS locates.
- **PS, PSB, PSEC**: Presampler, barrel presampler, and end-cap presampler.
- **QCD**: Quantum Chromodynamics. It is the quantum gauge field theory that describes the strong interaction.
- **QED**: Quantum Electrodynamics. It is the quantum gauge field theory that describes the electromagnetic interaction.
- **RNDM**: Random-triggered event stream.
- **RPC**: Resistive Plate Chamber. It is the barrel muon trigger chamber.
- **RS**: The warped extra dimension model by L. Randall and R. Sundrum.
- **SCT**: Semiconductor Tracker. It is one of the sensors of the inner detector in ATLAS, and provide precision tracking information in addition to the Pixel Detector.

- **SFO**: Sub-Farm Output. The TDAQ system component which receives accepted events from the Event Filter and send them to the permanent offline event storage.
- **SM**: The Standard Model of particle physics.
- **STACO**: One of the standard muon reconstruction algorithms. It combines Inner Detector tracks and Muon Spectrometer tracks by considering their parameter vectors, and calculating the χ^2 of track matching quality.
- **SUSY**: Supersymmetry.
- **TDAQ**: ATLAS Trigger and DAQ (including DCS).
- **Tier-0, Tier-1, Tier-2**: Tier is the hierarchy of the Grid sites. Tier-0 is the initial site located at CERN, responsible for storing the raw data from the experiments, and running the first reconstruction of data. Tier-1 takes care of storing reconstructed data, and also re-running the reconstruction from data. Tier-2 is responsible for generating Monte Carlo simulation samples, and also for storing data.
- **TileCal**: ATLAS Tile Calorimeter. It is the barrel hadronic calorimeter using the plastic scintillator tiles.
- **TGC**: Thin Gap Chamber. It is the end-cap muon trigger chamber.
- **Topoclusters**: Calorimeter clusters using the topological clustering algorithm. It makes use of the significance of the energy deposit in each calorimeter cell (see Chapter 6 for more detail).
- **TRT**: Transition Radiation Tracker. It is one of the sensors in the inner detector in ATLAS, using the straw chamber technique.

Part I

Introduction

Chapter 1

Introduction

The Large Hadron Collider (LHC) is the first collider to probe the physics at the TeV-energy scale. Its primary motivations are to search for the last missing piece of the Standard Model, the Higgs boson, and to search for the physics beyond the Standard Model.

At the TeV-energy scale, many models beyond the Standard Model are expected, of which the existence of the Supersymmetry (SUSY) and the Extra Dimensions are prospective examples. The lightest Supersymmetric particles (LSP's) from SUSY models and Kaluza-Klein particles from Extra Dimensions models are considered as candidates of the dark matter in the Universe. Those particles are very likely to leave large Missing Transverse Energy (Missing E_T , E_T^{miss}), because they only interact weakly with the ordinary matter. In a large part of such cases, jets with high transverse momentum (p_T) are expected to accompany (e.g. through cascade decays of squarks and gluinos down to the LSP in the R-parity conserving SUSY models).

In this thesis, the emphasis is laid on the searches for physics beyond the Standard Model with jet and E_T^{miss} signatures. For the reconstructions of jets and E_T^{miss} , the calorimeters play significantly important roles. Calorimeters are essential tools for almost any kind of physics measurement in collider physics, and we cannot emphasize too much their importance.

In order to achieve successful searches for new physics with the early data, a large part of this thesis is dedicated to the commissioning studies of the calorimeters in the ATLAS (A Toroidal LHC Apparatus) detector. Here, the current understandings on the performance of the ATLAS calorimeters were shown, and the improvements made in order to undertake successful analyses were mentioned. The data from the cosmic ray runs were extensively used in this thesis. They do not only serve as probes to understand the response of the calorimeters, but also allow us to validate the ATLAS software, and to understand and estimate the contribution of the cosmic muons themselves during the collision data taking, because they will be non-negligible background in various physics measurements. Strategies to cope with such non-collision background were established, and their performance in some of the new physics searches were mentioned.

Strategies to search for the physics beyond the Standard Model with jet and E_T^{miss} signatures were proposed at the final part of the thesis. The emphasis was put on the un-

derstanding and solutions to cope with the non-collision sources during the search. The methods to estimate the Standard Model background in data-driven ways were proposed as well. These studies are especially essential for new physics searches with early data.

1.1 Outline of the Thesis

This thesis consists of three parts. The introductory part (this chapter to Chapter 5), the commissioning part (Chapter 6 - 9), and the prospective part (Chapter 10 - 13).

In Chapter 2, a brief review of the Standard Model was given, and some of the candidates of physics beyond the Standard Model were mentioned, which are important physics motivations of the LHC experiments. Chapter 3 briefly describes the LHC and the accelerator complex. Chapter 4 gives an overview of the ATLAS detector and its performance. Since a large fraction of this thesis is dedicated to the calorimeter studies with the commissioning data, the energy and time reconstruction in the calorimeters is described in a separate chapter (Chapter 5).

The profile of the cosmic and single beam runs recorded since 2005 and up to the fall and winter of 2008 is described in Chapter 6. Commissioning studies of calorimeters were performed with random-triggered (random stream) and cosmic data, where the former is presented in Chapter 7, and the latter in Chapter 8. The analyses of random stream data allowed us to understand the detector conditions such as the electronic noise and problematic channels such as so called the “dead” and “hot” channels. Observations of high energy cosmic rays with the calorimeters allowed for the further validation of the detector systems as well as to deepen our understandings towards the rate and effects from the high energy cosmic muons.

Chapter 9 presents our proposals on how to reject the fake energy components coming from non-collision background. The quality of reconstructed calorimeter objects was investigated with the real and Monte Carlo cosmic data. A comparison with collision Monte Carlo samples such as the QCD dijet, lead to the proposals of “cleaning cuts” to be performed to reject non-collision background, still keeping high enough efficiency for the collision events.

Chapter 10 overviews the motivations of the new physics searches with jet and E_T^{miss} event topologies considered in this thesis.

Chapter 11 shows the expected effects of cosmic ray events on monojet event topology. New physics searches with jets and Missing E_T (E_T^{miss}) can be contaminated with non-collision background, but the use of cleaning cuts overcome the situation. Contributions from the cosmic rays are estimated from the real data, and the rejection power of cleaning cuts were shown.

Chapter 12 shows the strategy toward the multi-jet search for R-parity conserving Supersymmetry. Data-driven methods to estimate the Standard Model background are proposed. An estimation of cosmic ray background to the search is done with the “overlay” of the real cosmic data and QCD multi-jet Monte Carlo simulation.

The closing chapter overviews the thesis and presents conclusions.

Chapter 2

The Standard Model and Physics at the LHC

In this chapter, a brief overview of the Standard Model is given, followed by an introduction of some of the prospective physics to be searched at the LHC.

2.1 Construction of the Standard Model

The particle physics has experienced a tremendous success in explaining many parts of the fundamental aspects of nature.

There are four known fundamental interactions; the electromagnetic, strong, weak, and gravitational interactions. All of the interactions except for the gravitational force are described by the gauge theories of quantum fields (the gravitational force can also be regarded as a gauge theory, but its quantization is not yet achieved). Those theories are called the Standard Model as a whole. In the Standard Model, leptons and quarks are considered as the elementary particles that make up the matter around us, and gauge bosons as the mediators of the fundamental interactions (Table 2.1). The 20th century has been a revolutionary era for the construction of the Standard Model. Here, the brief overview of the construction of the Standard Model is given.

The first attempt to describe a particle interaction by a boson exchange was done by Yukawa [1], which he introduced a new particle (meson) to explain the strong interaction between nucleons inside atoms,

$$\left\{ \Delta - \frac{1}{c^2} \frac{\partial^2}{\partial t^2} - \lambda^2 \right\} U(x) = 0 . \quad (2.1)$$

Here, $U(x)$ is the meson field, λ has the dimension of $[\text{length}]^{-1}$ and related to the mass of the meson ($m = \frac{\lambda \hbar}{c}$), and x is the space-time coordinate. The meson, now known as the pion (π) was discovered in cosmic rays after the discovery of the muon (which at first was expected as Yukawa's meson) [2][3], and proved the validity of the theory. Though the theory is now considered as an effective theory and not fundamental, it opened up a way to the subsequent works to describe the fundamental interaction through particle

exchanges, and thus the construction of the Standard Model. Nambu recalls that Yukawa founded the modern formalism of particle physics in a theoretical way, whereas Lawrence played the same role in the experimental realm through the construction of cyclotrons [4].

The first success of renormalizable quantum gauge field theories was accomplished in describing the electromagnetic force, which is called the Quantum Electrodynamics (QED) [5]-[7]. QED has a Lagrangian invariant under U(1) local gauge transform,

$$\psi(x) \rightarrow e^{i\alpha(x)}\psi(x) , \quad (2.2)$$

where $\psi(x)$ is a Dirac field, x is the space-time coordinate, and $\alpha(x)$ is the phase to be chosen arbitrarily. The Lagrangian density consists of the terms from the gauge field A_μ , and the Dirac field ψ and interactions between the Dirac and gauge fields,

$$\mathcal{L} = -\frac{1}{4}F_{\mu\nu}F^{\mu\nu} + \bar{\psi}(i\gamma^\mu D_\mu - m)\psi , \quad (2.3)$$

where $F_{\mu\nu}$ is the field strength,

$$F_{\mu\nu} = \partial_\mu A_\nu - \partial_\nu A_\mu \quad (2.4)$$

and D_μ is the covariant derivative,

$$D_\mu = \partial_\mu - ieA_\mu . \quad (2.5)$$

The mass term of the gauge field $M^2 A_\mu A^\mu$ (M : mass of the gauge boson) is prohibited by the gauge invariance, and assures the massless feature of the photons. The theory allows to describe and predict the electromagnetic interaction among particles. It has been tested throughout a wide energy range, and demonstrated a powerful prediction power.

A rich spectroscopy of hadron states led to the speculations to describe hadrons by more fundamental particles: the quarks (only the three lightest quarks; u , d , and s were proposed at first) in an SU(3) group [8]. The quarks were considered to carry spin 1/2, with fractional charges. The dilemma to explain a baryon state like Δ^{++} with spin 3/2 inspired an additional quantum number called the color, where the quarks are expected to have three different states (the name came from an analogy to the color of light) [9]. The hypothesis of the new quantum number was supported by the observed rate of $\pi^0 \rightarrow \gamma\gamma$ and e^+e^- annihilation into hadrons. In the deep-elastic electron-nucleon [10] and neutrino-nucleon [11] scattering experiment, the existence of point-like particles inside the protons were confirmed, which lead to the parton description [12]. Partons were invented as constituents of the protons, independently from the quark description. The three-jet events from e^+e^- annihilations observed in PETRA experiments showed the evidence of the gluons [13]. Partons are now considered as quarks and gluons, and their interactions are described by a non-commutative gauge theory (Yang-Mills theory [14]) in an SU(3) group. It is called the Quantum Chromodynamics (QCD). The Lagrangian density of QCD consists of terms from gluon gauge fields, Dirac fields of quarks (q_i : quark field; i : index for flavors), and a term to fix the gauge,

$$\mathcal{L} = -\frac{1}{4}F_{\mu\nu}^a F^{a\mu\nu} + \sum_i \bar{q}_i(i\gamma^\mu D_\mu - m_i)q_i + \mathcal{L}_{\text{gauge-fixing}} . \quad (2.6)$$

In equation (2.6), $F_{\mu\nu}^a$ is the field strength of the gluons (A_μ^a : gluon field; $a, b, c = 1 \sim 8$: number of freedom from gluons; g : the strong coupling constant; f^{abc} : the structure constant of SU(3)),

$$F_{\mu\nu} = \partial_\mu A_\nu^a - \partial_\nu A_\mu^a - gf^{abc}A_\mu^b A_\nu^c, \quad (2.7)$$

and D_μ is the covariant derivative,

$$D_\mu = \partial_\mu - igA_\mu^a T^a, \quad (2.8)$$

where T^a is the generator of SU(3), satisfying,

$$[T^a, T^b] = if^{abc}T^c. \quad (2.9)$$

The short range feature of the strong interaction was once an obstacle to adopt the non-Abelian gauge theory, since the gauge bosons must be massless. The problem was overcome by the notion of the asymptotic freedom [15] and confinement, where the former also allowed for the perturbative calculation of the strong interaction at high energy, and made the QCD as a predictive theory. Though quarks and gluons are not detected independently due to the confinement and only hadrons are observed, their existence is now taken for granted due to the success of the theory in explaining numerous experimental results.

Ascertaining the non-conservation of parity in the weak interaction [16] lead to the description of the ‘‘V-A’’ theory [17], where the weak current J^μ consisted of vector and axial-vector component, such as,

$$J^\mu(x) = \bar{u}_\nu \gamma^\mu \frac{1}{2}(1 - \gamma^5)u_e \quad (2.10)$$

for example (u_ν, u_e are the spinors of the electron neutrino and the electron). An effective theory was established to describe the weak force by a four-point Fermi interaction using the V-A current,

$$\mathcal{M} = \frac{4G_F}{\sqrt{2}} J^\mu J_\mu^\dagger \quad (2.11)$$

and allowed to calculate the amplitude \mathcal{M} for known weak interactions such as the β -decay of nucleons and the Michel decay of muons at the leading order. Higher order calculations were not possible due to its non-renormalizability. The adoption of the Yang-Mills theory in weak interaction seemed impossible at first, because the gauge bosons in the theory must be massless as mentioned above.

The breakthrough was achieved by introducing a spontaneous symmetry breaking mechanism, and the unified description of the electromagnetic and weak interactions by an $SU(2)_L \times U(1)_Y$ group, now called the the Glashow-Weinberg-Salam (GWS) model [18]. For the origin of the electroweak symmetry breaking, the Higgs mechanism was considered as the most probable [19][20]. The gauge term of the GWS Lagrangian

density is described as follows,

$$\begin{aligned} \mathcal{L}_{\text{gauge}} = & -\frac{1}{4}(\partial_\mu A_\nu^a - \partial_\nu A_\mu^a + g\epsilon^{abc}A_\mu^b A_\nu^c)^2 \\ & -\frac{1}{4}(\partial_\mu B_\nu - \partial_\nu B_\mu)^2 \\ & +|D_\mu\phi|^2 - \lambda\left(|\phi|^2 - \frac{|\mu^2|}{2\lambda}\right)^2, \end{aligned} \quad (2.12)$$

$$D_\mu = \partial_\mu - igA_\mu^a T^a - i\frac{1}{2}g'B_\mu, \quad (2.13)$$

where A_ν^a and B_ν are respectively SU(2) and U(1) gauge field, g and g' are coupling constants, ϵ^{abc} is the structure function of the SU(2) gauge group, ϕ is the Higgs field described as a doublet of two complex scalar field, and λ , μ are related to the vacuum expectation value ($v = \sqrt{-\mu^2/\lambda}$). The W^\pm and Z bosons acquire mass by the spontaneous symmetry breaking of the vacuum and mixing of the SU(2) and U(1) gauge fields. The gauge fields of W^\pm and Z bosons are described as

$$W_\mu^\pm = \frac{1}{\sqrt{2}}(A_\mu^1 \mp iA_\mu^2), \quad m_W = g\frac{v}{2} \quad (2.14)$$

$$Z_\mu^0 = \frac{1}{\sqrt{g^2 + g'^2}}(gA_\mu^3 - g'B_\mu), \quad m_Z = \sqrt{g^2 + g'^2}\frac{v}{2} \quad (2.15)$$

and the remaining vector field orthogonal to Z_μ^0 is massless, describing the photon field in the QED,

$$A_\mu = \frac{1}{\sqrt{g^2 + g'^2}}(g'A_\mu^3 + gB_\mu), \quad m_A = 0. \quad (2.16)$$

The confirmation of renormalizability in the GWS model by 't Hooft and Veltman [21] revealed the validity of the theory.

Through many experiments, the Standard Model has revealed its outstanding prediction power to describe particle interactions. No experimental result is observed up to now that contradicts with the Standard Model (the neutrino oscillation is an exception, but this does not change the fundamental structure of the theory).

Though the Standard Model has established its status as a promising theory, there is one missing piece that is actually at the core of the theory: the Higgs bosons. As mentioned above, the Higgs bosons are believed to be the origin of the spontaneous symmetry breaking of the electroweak symmetry. The Higgs bosons are also expected to originate the mass of fermions as well. If the Higgs bosons exist, they are very likely to be captured at the LHC experiments (see Section 2.2.1).

2.2 Physics at the LHC

Despite the success of the Standard Model, it is not believed to be the fundamental theory, and rather regarded as a low-energy effective theory. Some of the reasons are as follows:

| | 1st generation | 2nd generation | 3rd generation |
|---------|----------------|----------------|----------------|
| Quarks | u | c | t |
| | d | s | b |
| Leptons | ν_e | ν_μ | ν_τ |
| | e | μ | τ |

| | electromagnetic force | strong interaction | weak interaction | (gravity) |
|--------------|-----------------------|--------------------|------------------|-----------|
| Gauge Bosons | γ | g | W^\pm, Z^0 | (G) |

Table 2.1: Elementary Particles in the Standard Model: quarks, leptons, and gauge bosons.

- There are too many parameters in the Standard Model which cannot be determined fundamentally from the theory (mass of elementary particles, three mixing angle and one phase parameter in the CKM-matrix, similar missing angles for neutrinos, three gauge coupling constants, QCD vacuum angle, and quadratic and self-coupling constants of Higgs bosons).
- The gravity is not included in the theory (and cannot be included by the current framework due to the non-renormalizability).
- Fundamental forces are believed to unify at high energy, but the precise measurements from the LEP (Large Electron Positron Collider) experiments suggests that the three fundamental forces (electromagnetic, weak, and strong forces) are unlikely to do so within the Standard Model prediction.
- The extreme difference in the scales of quantum gravity (Planck scale: $M_{Pl}c^2 \sim 10^{19}$ GeV), Grand Unified Theory (GUT; $M_{GUT} \sim 10^{15}$ GeV), and electroweak theory ($M_W \sim 10^2$ GeV). This is called the (gauge) hierarchy problem.
- The mass of the Higgs particles are unstable against radiative corrections within the Standard Model, and requires fine-tuning.

The Superstring Theory is a good candidate to answer the first two points, where spin-2 particles are naturally included in the theory. This allows for the quantum description of the gravitons. The fundamental particles are believed to be explained as “vibrations” of strings, where no artificial parameters except for the string length are needed. However, the excitation of strings leads to massive particles, which none of the Standard Model particles belong. Thus, the Standard Model particles are considered as the ground states of the strings, and their mass is expected to originate from other mechanisms which are not found yet.

The supersymmetry provides possible solutions to the remaining problems (it is important ingredient in the Superstring Theory as well). It is a symmetry between bosons and fermions. The supersymmetry predicts the presence of supersymmetric particles each corresponding to the Standard Model particles with the same quantum numbers (including the mass) except for the spin. If they exist, they contribute to the radiative

corrections to the mass of the Higgs bosons, and cancel the contributions from the corresponding Standard Model particles, since they have the opposite spin. In such case, there is no need for any unnatural “fine-tunings” due to the cancellation of loop diagram contributions. However, no supersymmetric particles with the same mass as their Standard Model counterparts are observed in the previous experiments. Thus, if the supersymmetry exists, it is expected to be broken at some energy scale (possibly around TeV), which may also allow for the three fundamental interactions to unite at the GUT scale.

The existence of extra dimensions can provide an alternative explanation for the existence of hierarchy. Arkani-Hamed, Dimopoulos, and Dvali proposed what is called the “Large Extra-Dimensions (LED)” model [27] that there is not actually a hierarchy, but all the scales (Planck, GUT, and electroweak scales) are close. The model insists that the “fake” hierarchy shows up when we observe at four dimensions. Randall and Sundrum took another approach that the weak scale is generated from the Planck scale through exponential hierarchy caused by the background metric coming from an extra dimension (warped extra dimensions), and thus providing a mechanism of the hierarchy [28]. There are other models exploiting the existence of extra dimensions, but they will not be mentioned here.

2.2.1 Higgs Particle Searches

The ATLAS detector is designed to cover almost all the possible decay channels of the Higgs boson along its mass range (~ 1 TeV is considered as the upper limit due to unitarity arguments).

The expected cross section of the Standard Model Higgs boson production at the center-of-mass energy of 14 TeV and its branching ratios are shown in Figure 2.1. The production of the Higgs boson is possible through several mechanisms. They are

- Gluon fusion (Figure 2.2 (a); the red line in the left figure of Figure 2.1): A Higgs boson is produced by the loop of top quarks originating from gluon-gluon interaction. This process has the largest cross section at the LHC.
- Vector boson fusion (Figure 2.2 (b); the pink line in the left figure of Figure 2.1): A Higgs boson is produced by the interaction of W/Z bosons radiated from the quarks. These events are accompanied by 2 forward jets originating from those quarks.
- Associated production with W/Z (Figure 2.2 (c); the green and blue lines in the left figure of Figure 2.1): One of the important production processes at the Tevatron, since it collides protons and antiprotons.
- Associated production with t/b (Figure 2.2 (d); the black line in the left figure of Figure 2.1): Two pair-produced top (or bottom) quarks interact to make a Higgs boson.

Examples of channels are shown below that have considerably been investigated at the ATLAS experiment [23].

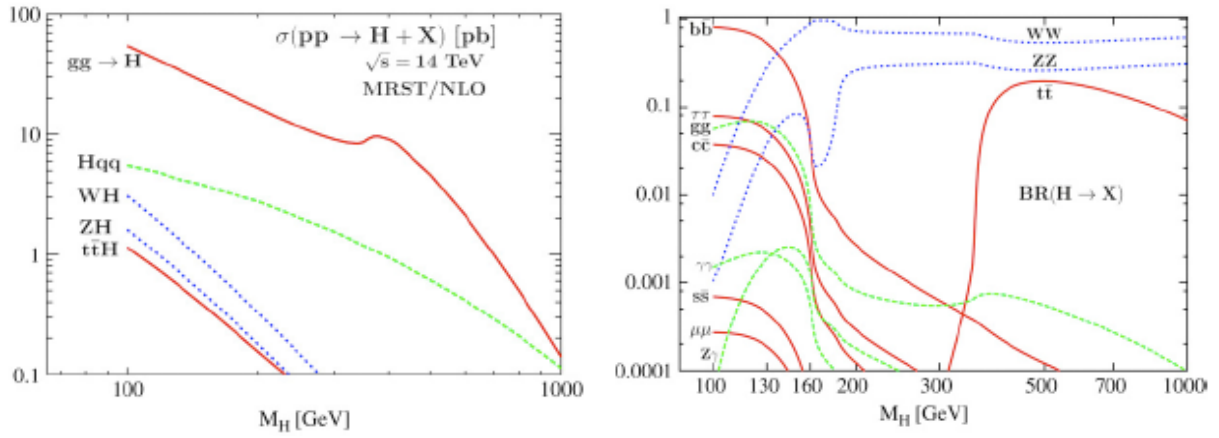


Figure 2.1: Cross section (left) and branching ratio (right) of the Standard Model Higgs bosons at the center-of-mass energy 14 TeV [22].

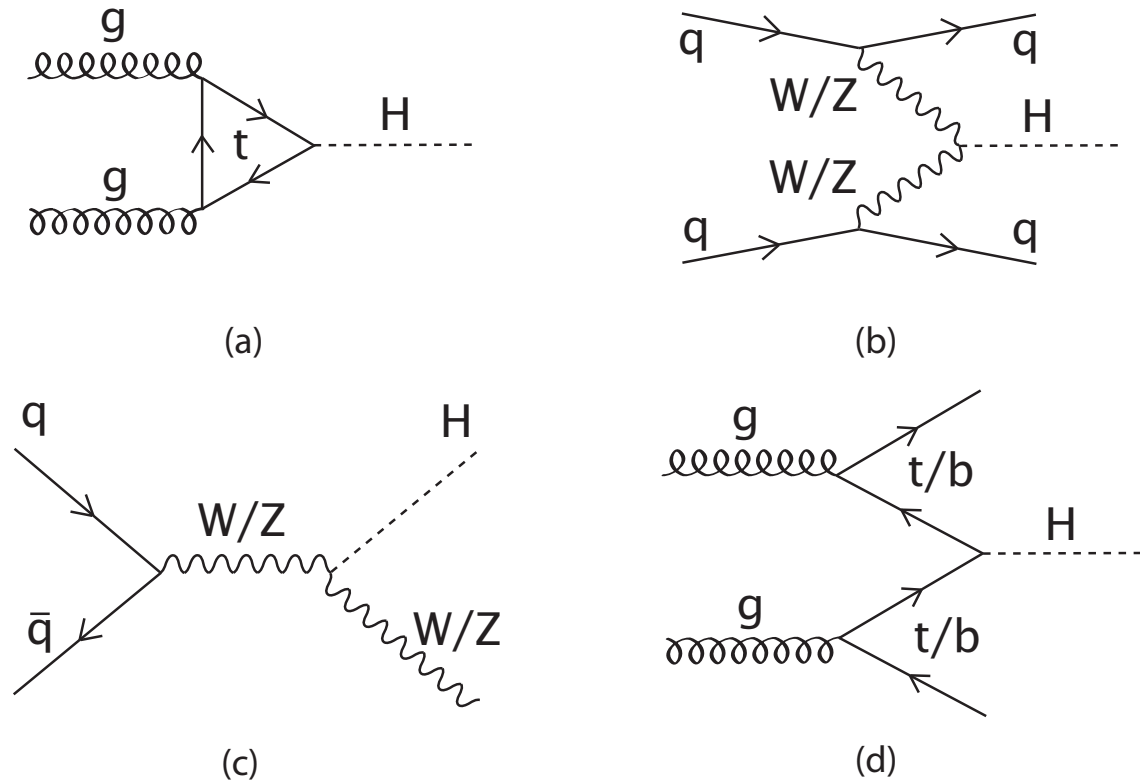


Figure 2.2: Feynman diagrams of the Higgs productions: (a) gluon fusion, (b) vector boson fusion, (c) associated production with W/Z, (d) associated production with top or bottom quarks.

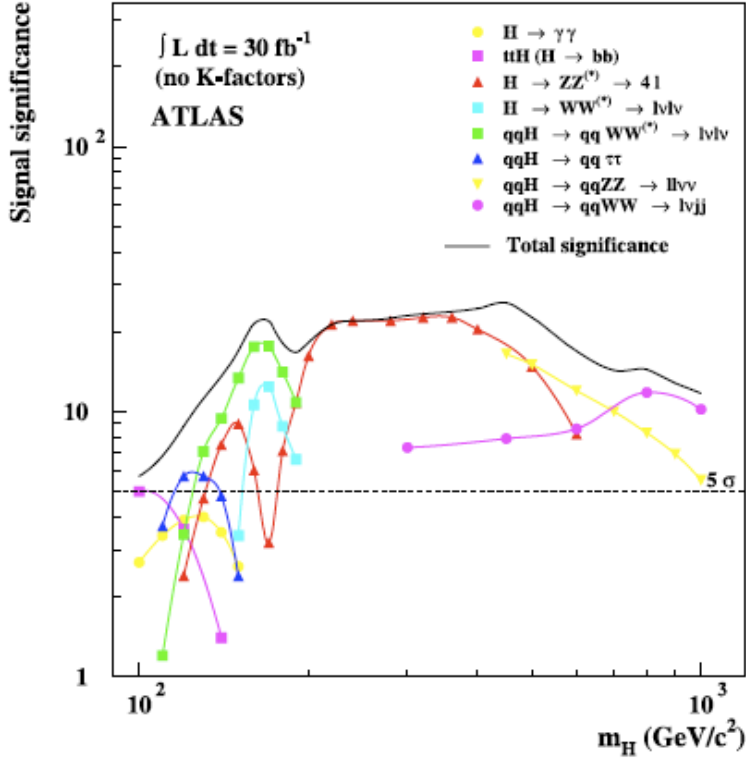


Figure 2.3: Sensitivity of ATLAS for the discovery of the Standard Model Higgs boson [24].

- $pp \rightarrow H \rightarrow ZZ^{(*)} \rightarrow 4l (l = e, \mu)$
- $pp \rightarrow H \rightarrow \gamma\gamma$
- $pp \rightarrow H \rightarrow W^+W^- \rightarrow l^+\nu l^-\nu, lvqq$
- $pp \rightarrow qqH \rightarrow qq\tau^+\tau^-$
- $pp \rightarrow t\bar{t}H \rightarrow t\bar{t}b\bar{b}$
- $pp \rightarrow t\bar{t}H \rightarrow t\bar{t}W^+W^-, pp \rightarrow ZH \rightarrow l^+l^-W^+W^-$

Figure 2.3 shows the sensitivity of the ATLAS detector to the discovery of the Standard Model Higgs boson. From the gluon fusion Higgs productions, the $H \rightarrow ZZ^{(*)} \rightarrow 4l$ channel provides a prominent signature along a large mass range. $H \rightarrow \gamma\gamma$ is an important channel for low mass Higgs ($80 < m_H < 150 \text{ GeV}/c^2$). The degradation of $\gamma\gamma$ invariant mass resolution due to conversions in the material in front of the calorimeter is the major challenge at the ATLAS experiment.

Recently, the Tevatron experiments (CDF and D0) excluded at 95% C.L. the Standard Model Higgs boson with the mass range of 163-166 GeV/c^2 [25]. The exclusion slightly decreased from 160-170 GeV/c^2 (as of March 2009) due to the presence of signal-like

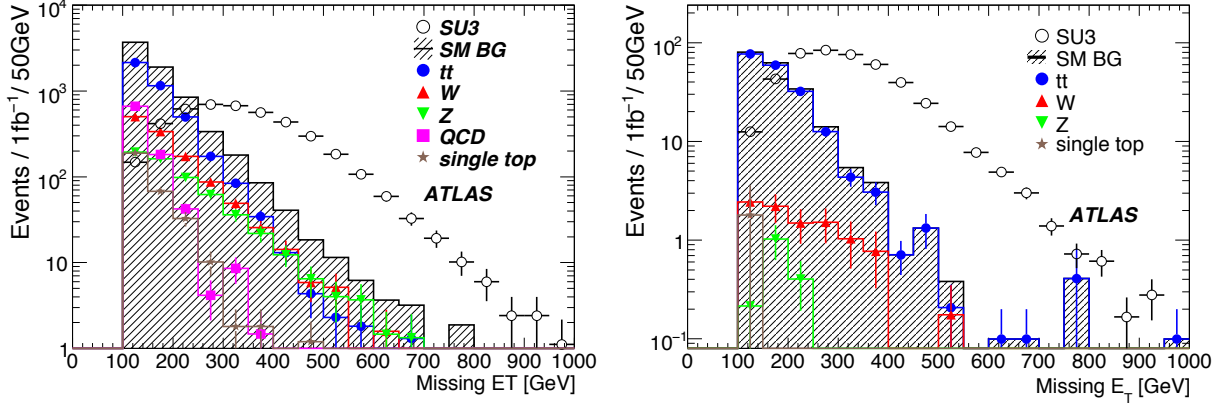


Figure 2.4: Expected Missing E_T distributions of a benchmark Supersymmetric events (named as SU3) and the Standard Model background in No Lepton (left) and One Lepton Mode (right) at the center-of-mass energy of 14 TeV [23].

candidates after the increase in statistics, though the excess was less than one standard deviation in respect to the background.

2.2.2 Supersymmetry

An exact Supersymmetry predicts the existence of at least one set of supersymmetric particles accompanying each Standard Model particle with the same mass and a different spin. Such particles were not detected in the previous experiments, so the exact Supersymmetry is not adopted in nature. The only possibility for the Supersymmetry to exist is that it is softly broken at an energy scale, and giving the supersymmetric particles their mass which were not reachable by the previous high energy colliders.

Several mechanisms were proposed which break the supersymmetry. The gravity-mediated, the Gauge-mediated (GMSB), and the Anomaly-mediated SUSY breakings (AMSB) are well-known mechanisms and have been investigated to quite an extent, phenomenologically and experimentally.

In R-parity conserving Minimal supergravity (mSUGRA) models, where the universality of gaugino masses, scalar masses, and various A-parameters at the GUT (Grand Unification Theory) scale is assumed, the neutralino is normally the lightest-supersymmetric particle (LSP). The LHC tends to have copious productions of squarks and gluinos, and those particles will initiate cascade decays to the LSP's. Since the LSP's are weakly interacting particles, they will create a large Missing E_T (E_T^{miss}) with many jets originating from the cascades. Thus, “multi-jet and large E_T^{miss} ” is one of the standard event topologies that have also been extensively investigated at the Tevatron. ATLAS has a discovery potential for large parameter space of mSUGRA, and such events can obviously show up as an excess in the E_T^{miss} distribution as shown in Figure 2.4 (the left figure shows the E_T^{miss} distribution from all hadronic multi-jet plus E_T^{miss} signature, and the right from 1 lepton, multi-jet plus E_T^{miss} signature).

2.2.3 Extra Dimensions

The prominent features predicted by extra dimensions is the presence of Kaluza-Klein particles and their emissions or decays (will be mentioned below), and productions of mini-black holes.

In the LED model, on top of the normal four dimensional space-time, n extra dimensions are considered to exist, toroidally compactified with a radius, thus with the volume $(2\pi r)^n$. All the Standard Model particles are localized to the four dimensions, and only the gravitons can propagate in the extra dimensions. Considering the action in $4+n$ dimensions, and rewriting and factoring it out the higher dimensional action to match the four dimensional action, we obtain

$$M_{\text{Pl}}^2 = M_{\text{Pl}(4+n)}^{2+n} (2\pi r)^n, \quad (2.17)$$

where M_{Pl} is the standard Planck scale, and $M_{\text{Pl}(4+n)}$ (also often written as M_D) is the actual Planck scale expected in the higher dimensional case. This shows that the strength of the gravitational force is not actually weak, but seems as so, due to the presence of extra dimensions.

There has been a series of experimental tests on the deviation of the Newtonian gravitational force. The potential $V(r')$ of the modified Newtonian force is often simplified and described as,

$$V(r') = -G_N \frac{m_1 m_2}{r'} \left(1 + \alpha e^{-r'/\lambda} \right), \quad (2.18)$$

where G_N is the standard gravitational constant, m_1, m_2 the mass of two objects under consideration, r' the distance between the two objects, α the strength of the unknown short range force, and λ the range of the unknown force related to the mass of the exchanged bosons. The term of the unknown short range force is often called as the ‘‘fifth force.’’ Current limits on the fifth force from various experiments are summarized in Figure 2.5. In the LED model, the number and size of the extra dimensions can be expressed with the non-Newtonian force as [30],

$$\lambda = r \quad (2.19)$$

$$\alpha = \frac{4}{3}(2n) \quad (2.20)$$

Considering that

$$r = \frac{1}{2\pi} \left(\frac{M_{\text{Pl}}^2}{M_{\text{Pl}(4+n)}^{n+2}} \right)^{1/n}, \quad (2.21)$$

in case of $M_{\text{Pl}(4+n)}^{n+2} = 1$ TeV, the size of extra dimensions is 10^{12} m for $n = 1$, 10^{-3} m for $n = 2$, 10^{-8} m for $n = 3$, and etc. It is obvious that $n = 1$ is ruled out in case of $M_{\text{Pl}(4+n)}^{n+2} = 1$ TeV, but the extra dimensions of a millimeter-size ($n = 2$) was not excluded at the time of the proposal of the LED model. Previous collider experiments also imposed further limits on the models, but the lower limits are still around 1 TeV (Figure 2.6). The LHC provides an opportunity to search for the extra dimensions in the range never having to be able to reach before.

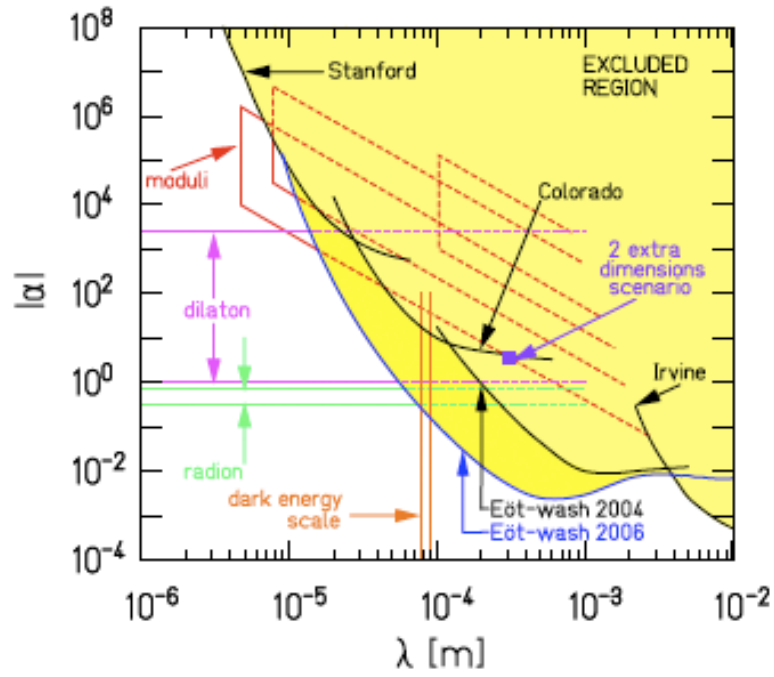


Figure 2.5: Experimental limits on the parameters of the modified Newtonian gravitational force [29].

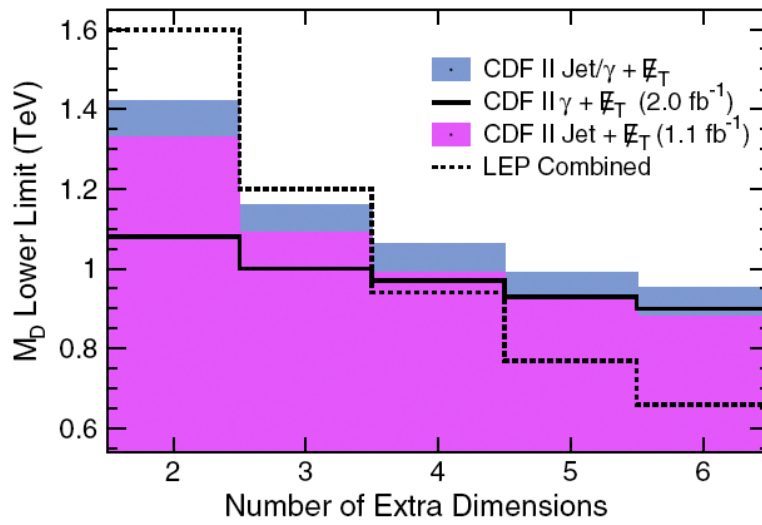


Figure 2.6: Lower limits of M_D in the Large Extra Dimension model from the previous collider experiments [39].

The warped extra dimension is another well-known model (often called the RS model where RS stands for Randall and Sundrum). In the original RS model, only one extra dimension is assumed with non-trivial space-time metric, contrary to the LED model. In the RS model, two 3-brane's exist; one is at the TeV scale, and the other at the Planck scale. The branes are separated by a certain distance along the direction of the fifth dimension. The background space metric is described as,

$$ds^2 = e^{-k|y|} \eta_{\mu\nu} dx^\mu dx^\nu - dy^2, \quad (2.22)$$

where y is the coordinate of the fifth dimension, k is the AdS curvature of the fifth dimension. $e^{-k|y|}$ is called the “warp factor.”

In extra-dimensional models, Kaluza-Klein modes (or particles) occur due to the boundary conditions of the extra dimensions. Only certain eigenvalues of energy is allowed in the direction of the extra dimensions, and those quantized states appear as massive particles from a three dimensional observer. A peculiar difference in KK mode can be seen between the LED and RS model. In LED model, the spacing between the KK modes is $\sim 1/R$ per each extra dimension, whereas in the RS model, the mass spacing is the same as the zero points of the Bessel function. This is due to the warped geometry of the extra dimensions. The detection of several KK particles and their mass spacings will allow us to discriminate the models.

When the extra dimensions are visible at TeV scale, the Schwarzschild radius will be large enough for the impact parameter of the colliding partons to pass it. In such a situation, a mini-black hole can be copiously produced at the LHC [40], and originate striking event features like democratic particle decays. The use of dijet topology is also proposed to investigate the effect from quantum gravity [41].

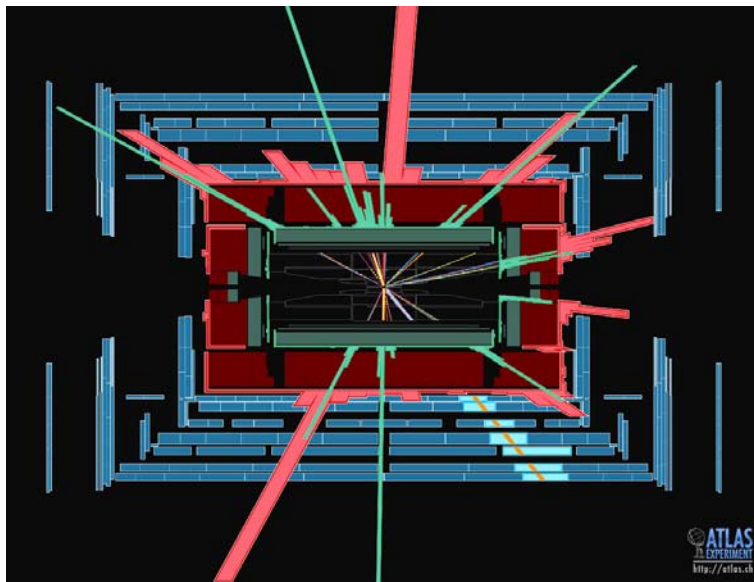


Figure 2.7: Side-view of a simulated black hole event in ATLAS. Inner detectors were magnified in the figure and not depicted to scale.

Chapter 3

The Large Hadron Collider

The Large Hadron Collider (LHC) is a proton-proton collider (and a Pb-Pb collider for heavy ion studies), located at the European Organization for Nuclear Research (CERN) in Geneva, Switzerland [42]-[44]. It was operated at the center-of-mass energy 7 TeV at the end of 2009 and will reach up to 14 TeV which will surpass the current center-of-mass energy from any other colliders around the world (by a significant factor compared to 1.96 TeV of the Tevatron). The design luminosity is $10^{34}\text{cm}^{-2}\text{s}^{-1}$ which is also an unprecedented performance. Beam crossings are 25 ns, and there will be 23 interactions per bunch crossing at the design luminosity. The LHC also has the world's largest circumference of 26.7 km which was succeeded from the Large Electron Positron Collider (LEP).

3.1 Why the LHC?

An accelerator facility that can surpass the current energy frontier and probe the physics at the TeV scale has been aspired for a long time. The LHC is the first collider to meet such requirements.

Although low background and clear experimental environment are essential advantages of experiments at electron-positron colliders, the major obstacle to achieve the acceleration up to such high energy in electron-positron colliders is the synchrotron radiation. The synchrotron radiations can be emitted during the transverse accelerations by deflections, and can significantly contribute to the energy loss. The power emitted by the synchrotron radiation by a deflection is:

$$P = \frac{1}{6\pi\epsilon_0} \frac{e^2 c}{(mc^2)^4} \frac{E^4}{\rho^2} \quad (3.1)$$

where ϵ_0 is the permittivity of vacuum, e the electron charge, c the speed of light, m the mass of the moving particle, E the energy of the moving particle, and ρ the bending radius. As obvious from the equation, energy loss severely depends on the mass of the moving particle and the curvature of the path. In order to achieve high energy acceleration, there are two ways of overcoming the obstacle. One is to use heavy particles for acceleration (large m), and the other is to use a linear accelerator ($\rho \rightarrow \infty$). LHC

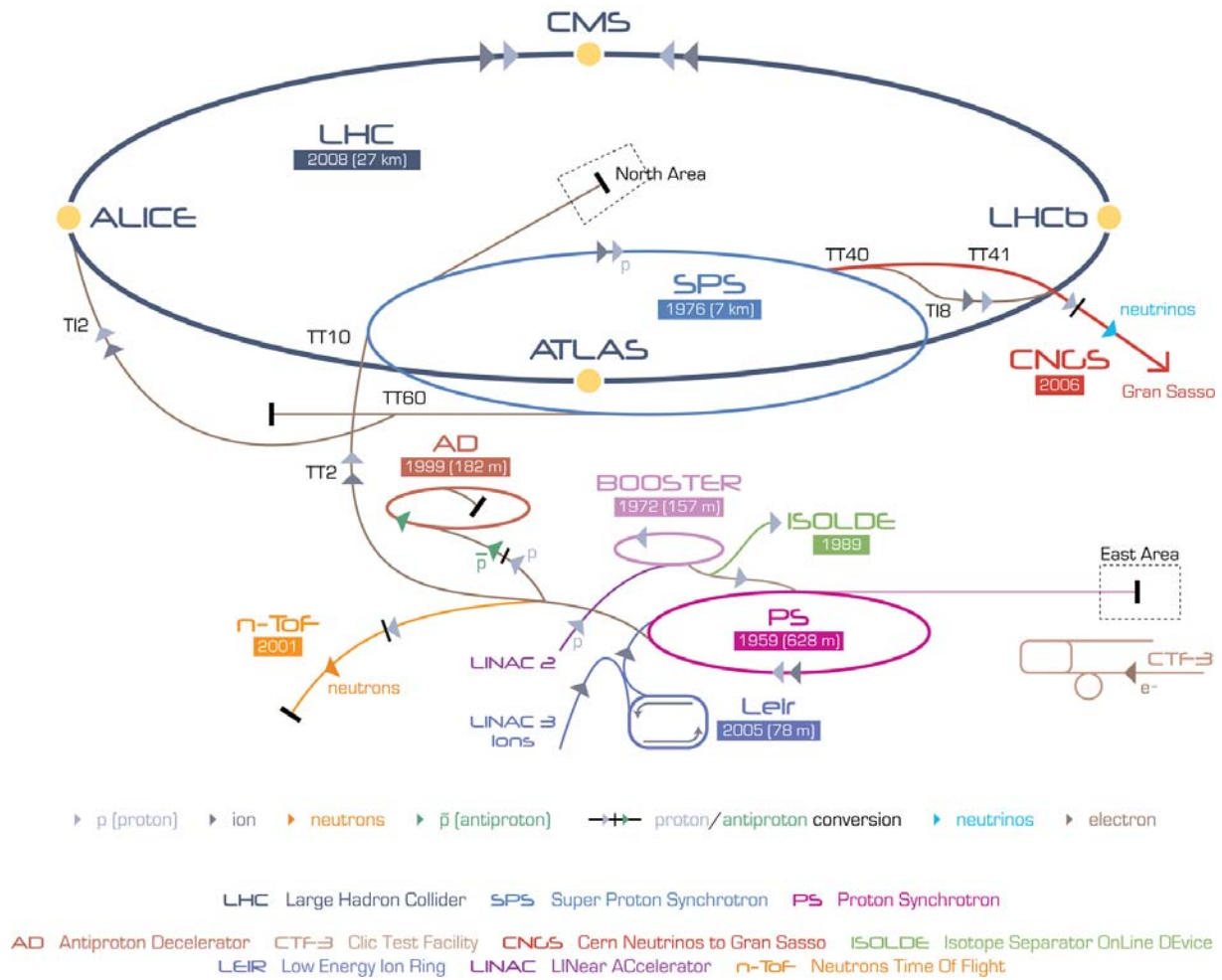


Figure 3.1: CERN and the LHC. The figure is not to scale.

adopted the former solution, to use protons instead of electrons, and use the world-largest LEP tunnel which further suppresses the synchrotron radiation due to its large radius. For such a collider, the synchrotron radiation is rather small, thus the limitation on the acceleration comes from the maximum magnetic field available to bend the protons.

Since the momentum distribution of partons (quarks and gluons) inside the colliding protons is a steeply decreasing function, a high luminosity is also required on top of high center-of-mass energy to search for rare events, in which a parton-parton system of the fundamental processes has large invariant mass. In order to achieve high luminosity, proton-proton collisions were chosen, since it is not possible to reach the required luminosity using protons and anti-protons.

Fulfilling all the requirements mentioned above, LHC will be the first experiment that make it possible to probe the physics at the TeV-energy scale.

3.2 LHC Injector Complex

Many parts of the accelerator complex of the LHC are re-used from previous experiments including the LHC tunnel which used to be called the LEP tunnel, and accelerators used in the injector complex such as Linac, PS, and SPS (Figure 3.1). Those accelerators were upgraded to meet the requirements from the LHC: high intensity proton bunches with small transverse and well-defined longitudinal emittance.

Protons are provided from Linac2 using a duoplasmatron source, and accelerated up to 750 keV with radio-frequency quadrupole (RFQ). An upgrade from the original Cockcroft-Walton injector to RFQ in 1993 made a significant increase in the beam intensity. Due to the installation of the new injector and many improvements in the source, RF, optics, and diagnostics of Linac2, currents of up to 183 mA was achieved.

Those protons are injected into Proton Synchrotron Booster (PSB; Booster in Figure 3.1). PSB was upgraded to increase the output energy from the original 1 GeV to 1.4 GeV. This led to the increase of magnetic field by about 26 % to 0.87 T. A new RF system is tuned to the revolution frequency (RF harmonic $h = 1$), and supplemented with a $h = 2$ system. It contributed to the reduction of space charge effects observed in the previous acceleration scheme by $h = 5$ and more stability of the coupled bunches. This new RF system provides 1 bunch per PSB ring, with 190 ns bunch length.

These 1.4 GeV protons enter Proton Synchrotron (PS), and will reach 25 GeV. Six bunches are delivered from the PSB in two batches, and are captured by harmonic $h = 7$ in the PS. These bunches will be split in three when the second batch is received. This will lead to 18 bunches on $h = 21$, and are accelerated to 25 GeV on this harmonic. By changing the procedure of splitting and using different values of harmonic captures, alternative bunch spacings such as 50 ns or 75 ns can be achieved as well. The bunch spacing at the PS will be preserved up to the LHC.

The Super Proton Synchrotron (SPS) will be the final link in the injector chain to the LHC. Since the SPS is not optimized for the LHC, it can only accelerate about 4×10^{13} protons per cycle, which limits the number of PS bunches per SPS cycle up to four. In order to fit the small aperture of the LHC superconducting magnets and to achieve the high luminosity, the transverse emittance of the beams must be kept small. This is one

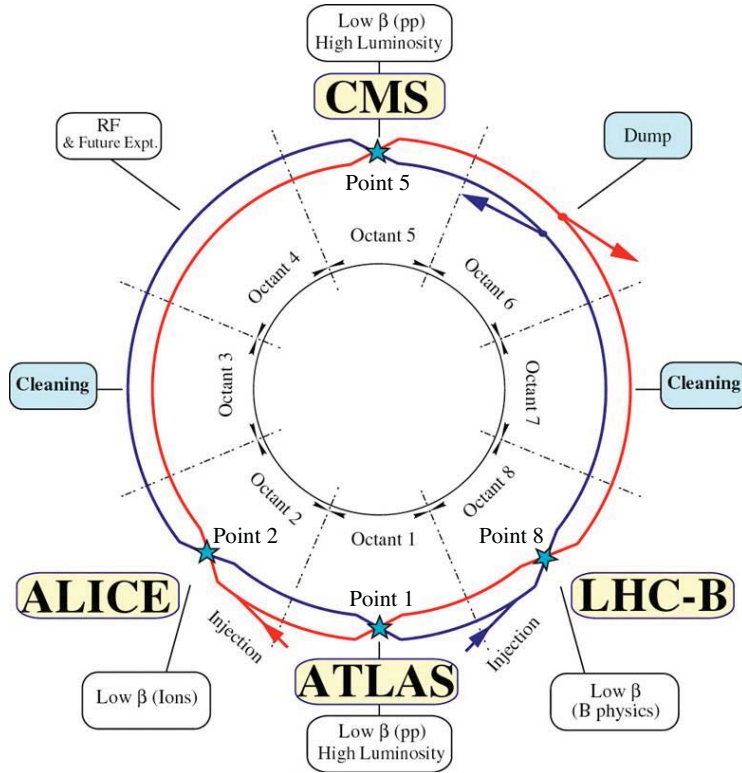


Figure 3.2: The LHC layout. ATLAS locates at Point 1 of the LHC ring.

of the major challenges for the SPS. The acceleration of proton beam up to 450 GeV is performed with a 200 MHz traveling wave RF system. These protons are injected to the LHC by the transfer lines.

3.3 LHC Layout and Technology

The LHC consists of eight arc sections and eight straight sections (Figure 3.2). Protons will counter-rotate in two separate beam pipes and cross at four points, where there are detectors. The four detectors from LHC experiments (will be mentioned in the next section) are installed at the straight sections. Other straight regions are dedicated for the beam cleaning, beam dumping system, RF and beam instrumentation. The RF and beam feedback systems are concentrated at Point 4, and 400 MHz superconducting cavity system will accelerate the protons up to several to 7 TeV.

In the arc sections, protons are deflected by dipole magnets (Figure 3.3). Quadrupole magnets are used for focusing. Each LHC arc consists of 23 cells, where there are six dipole magnets and two quadrupole magnets per cell. One cell is about 106.9 m long (Figure 3.4). Ideally, these magnets would be enough to keep the particle trajectory stable, but sextupole, octupole, and decapole magnets are installed to correct for nonlinear movements due to magnetic field errors.

The main parameters of the LHC for proton-proton collisions are shown in Table 3.1. As mentioned in the previous section, 450 GeV protons are injected into the LHC ring from the SPS, and are accelerated by the RF at Point 4. The designed maximum energy of the protons are 7 TeV.

3.4 Experiments at the LHC

The LHC has two detectors dedicated for high luminosity experiments, ATLAS (A Toroidal LHC Apparatus) [45] and CMS (Compact Muon Solenoid) [46]. These are general purpose detectors designed for various physics motivations such as the discoveries of the Higgs bosons, supersymmetric particles, extra dimensions, and precise measurements of the Standard Model processes. There are two low-luminosity experiments which are LHCb (Large Hadron Collider beauty experiment) [47] for B-physics and TOTEM (TOTal Elastic and diffractive cross section Measurement) [49] for the total cross section measurement. ALICE (A Large Ion Collider Experiment) [48] is dedicated to heavy ion physics studies such as investigations on the quark-gluon plasma with the peak luminosity of $10^{27}\text{cm}^{-2}\text{s}^{-1}$ in lead-lead collisions. LHCf [50] is for the highest-energy cosmic-ray studies, and will validate the models of cosmic hadronic interactions using the LHC data.

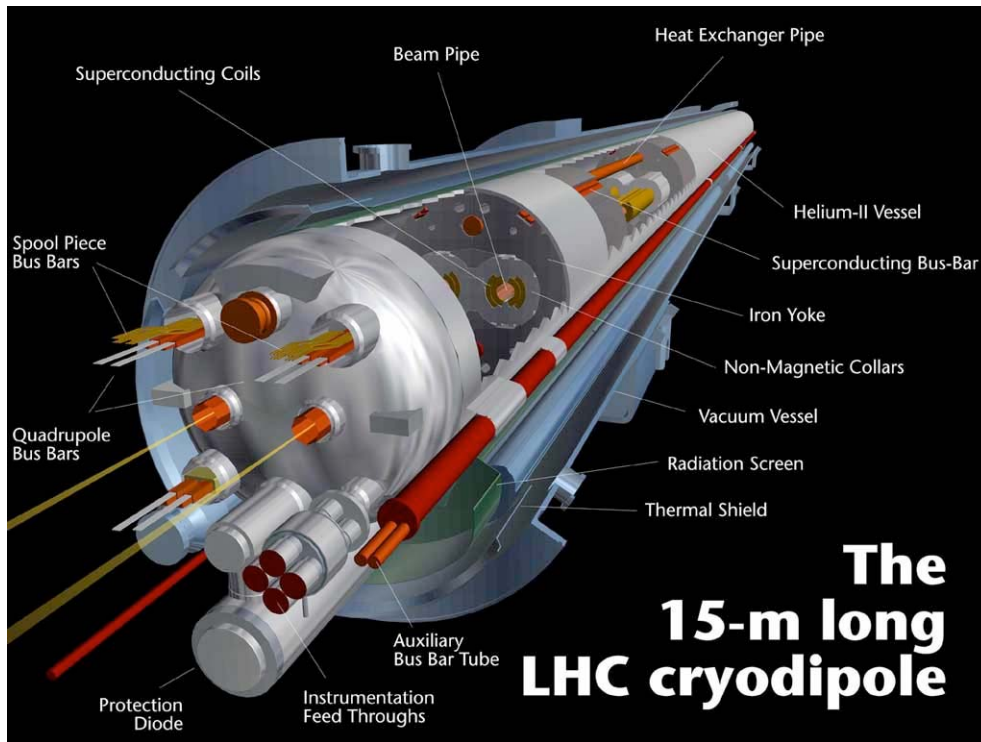
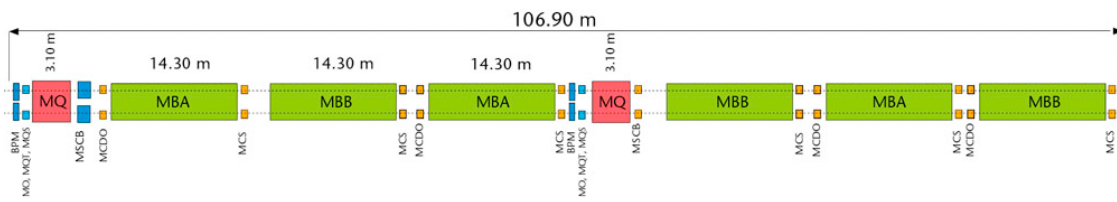


Figure 3.3: LHC cryodipole in the arc section.

| | Design |
|-------------------------------|--|
| Injection Energy | 450 GeV |
| Maximum Energy | 7 TeV |
| Dipole Field | 8.33 T |
| Design Luminosity | $10^{34} \text{cm}^{-2} \text{s}^{-1}$ |
| Number of Particles per Bunch | 1.15×10^{11} |
| Number of Bunches | 2808 |
| Bunches Length | 1.06 ns |
| Bunch spread | 0.22×10^{-3} |
| Bunch Crossing | 24.95 ns |

Table 3.1: LHC Parameters for proton-proton collisions.



- MQ: Lattice Quadrupole
- MO: Landau Octupole
- MQT: Tuning Quadrupole
- MQS: Skew Quadrupole
- MSCB: Combined Lattice Sextupole (MS) or skew sextupole (MSS) and Orbit Corrector (MCB)
- BPM: Beam position monitor
- MBA: Dipole magnet Type A
- MBB: Dipole magnet Type B
- MCS: Local Sextupole corrector
- MCDO: Local combined decapole and octupole corrector

Figure 3.4: LHC Cell. there exist six dipole magnets and two quadrupole magnets per cell.

Chapter 4

The ATLAS Detector

The ATLAS (A Toroidal LHC Apparatus) detector (Figure 4.1) is a general purpose detector designed to meet requirements for a wide range of physics measurements such as searches for Higgs particles, Supersymmetry (SUSY), extra dimensions, and the precise measurement of Top physics and other Standard Model processes. The detection of the Higgs bosons was mainly used as the benchmark for the requirements of the detector performance. The overall requirements for the detector performance can be summarized as follows.

- Very good muon identification and momentum measurement up to 1 TeV with no less than 10% precision. An adequate resolution even with a stand-alone reconstruction with the muon spectrometer to cope with the high luminosity.
- Very good electromagnetic calorimetry with high resolution of photon and electron energy, position and direction measurement with a wide geometric coverage.
- Full coverage of hadron calorimetry for good jet energy and missing transverse energy measurement.
- Inner tracking with very good momentum resolution and tolerance against high radiation doses.
- Triggering and measurement of low p_T particles to cover most of the physics processes of interest.

The details on how each sub-detector fulfilled these requirements will be mentioned in the following sections.

ATLAS is 44 m wide and 25 m tall, and is placed at Point 1 of the LHC tunnel, about 100 meters underground. Its total weight is 7000 tons. New technologies are used in various parts of the detector, such as air-core toroidal magnets, the accordion-structure of the electromagnetic (EM) liquid argon (LAr) calorimeter, the perpendicular configuration of the plastic tiles in the Tile calorimeter, and the hybrid hadron calorimeter system using two different technologies in the barrel (Tile) and the end-cap (Liquid Argon), to name a few.

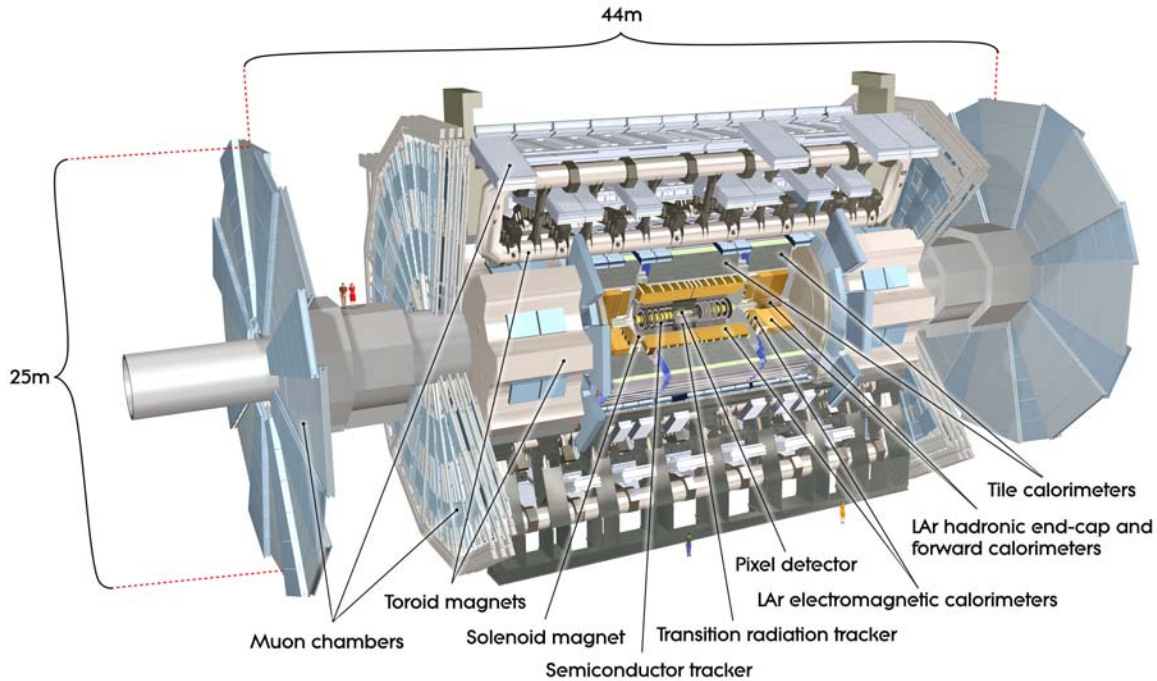


Figure 4.1: ATLAS Detector

The ATLAS detector consists of the inner detector, EM and hadronic calorimeters, muon spectrometer, one solenoidal magnet for momentum measurement of the charged particles at the inner detector, three toroidal magnets for the muon momentum measurement with the muon spectrometer, and forward detectors [45][52][53]. The detector system allows to measure various types of particles, such as electrons and photons by the inner detector and EM calorimeter, hadrons by the hadronic calorimeters, and muons by the outermost muon spectrometer (Figure 4.2). Even the weak-interacting particles such as neutrinos can be measured by exploiting the transverse energy imbalance in the whole detector.

4.1 Inner Detector

There are four sensors so called the inner detector as a whole [54] [55]. From the closest to the beam pipe, they are the Beam Conditions Monitor (BCM) [56], Pixel Detector (Pixel) [57], Semiconductor Tracker (SCT), and Transition Radiation Tracker (TRT). They are contained within a cylinder of 7 m length and a radius of 1.15 m. The inner detector volume is restricted by the dimension of the cryostat containing the LAr EM calorimeter in the radial direction and by the position of the end-cap calorimeters in the beam direction. The inner detector are immersed in 2 T solenoidal magnetic field. The BCM is implemented to detect beam incidents and to measure the luminosity. Pixel and SCT are used for the pattern recognition (charged track reconstruction), momentum and

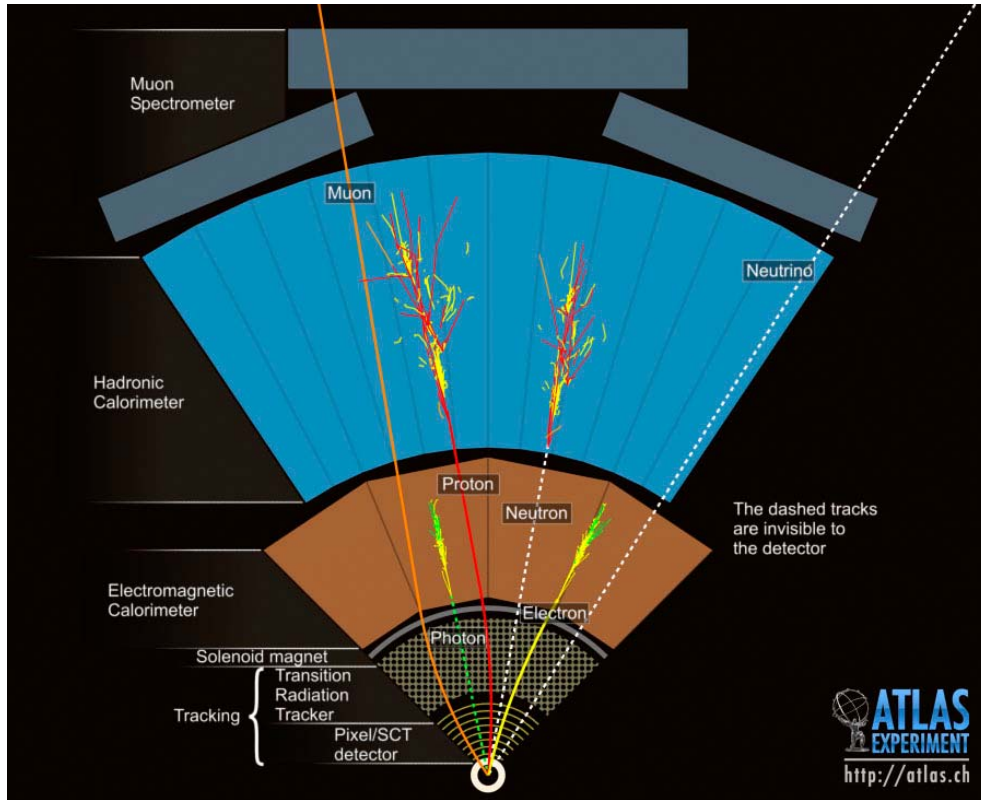


Figure 4.2: Cross section of the ATLAS detector with typical particles traversing through it.

vertex measurement. The TRT uses straw tube technology, and offers additional tracking points to the ones from the Pixel and SCT, which greatly improves the momentum resolution. The TRT can also detect transition radiations in the outer volume of inner detectors which is useful for electron and pion separation.

Each component is briefly reviewed below.

4.1.1 Beam Conditions Monitor

The Beam Conditions Monitor (BCM) is one of the newest detectors stationed at Point 1. It is designed to detect beam incidents such as several bunches hitting the collimators. It also provides measurement of bunch-by-bunch luminosities.

The BCM is based on radiation-hard polycrystalline chemical vapor deposition (pCVD) diamond sensors. It consists of two stations in the forward and backward directions. Eight modules (four on each station) are installed on the pixel detector support frame (Figure 4.4).

4.1.2 Pixel Detector

The Pixel detector allows for a very high-granularity, high-precision measurements with the closest position to the interaction point. It mostly determines the impact parameter resolution.

The Pixel detector is one of the tracking detectors using the semiconductor technology, which covers the region of $|\eta| < 2.5$. In the barrel region, pixels are arranged in three layers around the beam axis in a concentric cylinders, whereas in the end-cap region, they are placed in five layer disks perpendicular to the beam axis. The innermost layer (B-layer) in the barrel suffers greatly from the radiation damage, so the mechanical design allows for the replacement of the B-layer after a few years of running, to maintain the performance of b-tagging. All pixel sensors are identical and the minimum pixel size is $50 \times 400 \mu\text{m}^2$. The pixel layers are segmented in $R - \phi$ and z . Particles typically cross three pixel layers. The position resolution of a single hit is $10 \mu\text{m}$ in $R - \phi$ and $115 \mu\text{m}$ in z . There are approximately 80.4 million channels.

4.1.3 Semiconductor Tracker

The SCT uses the silicon microstrip detector technology, which has successfully been adopted in the previous experiments such as the LEP and the Tevatron. The barrel SCT provides 8 layers of silicon microstrip detectors in the intermediate radial range in order to achieve precision in $R - \phi$ and z coordinates, and contribute to improve the measurement of momentum, impact parameter, and vertex position. Each silicon detector is $6.36 \times 6.40 \text{ cm}^2$ in size with 768 readout strips of $80 \mu\text{m}$ pitch. In the barrel region, the SCT uses 40 mrad stereo strips to measure both coordinates. The active silicon area of the SCT is about 63 m^2 , more than an order of magnitude larger than any other silicon vertex detector used in the previous experiments. The resolution is $17 \mu\text{m}$ in $R - \phi$ and $580 \mu\text{m}$ in z . The total number of readouts is approximately 6.3 million.

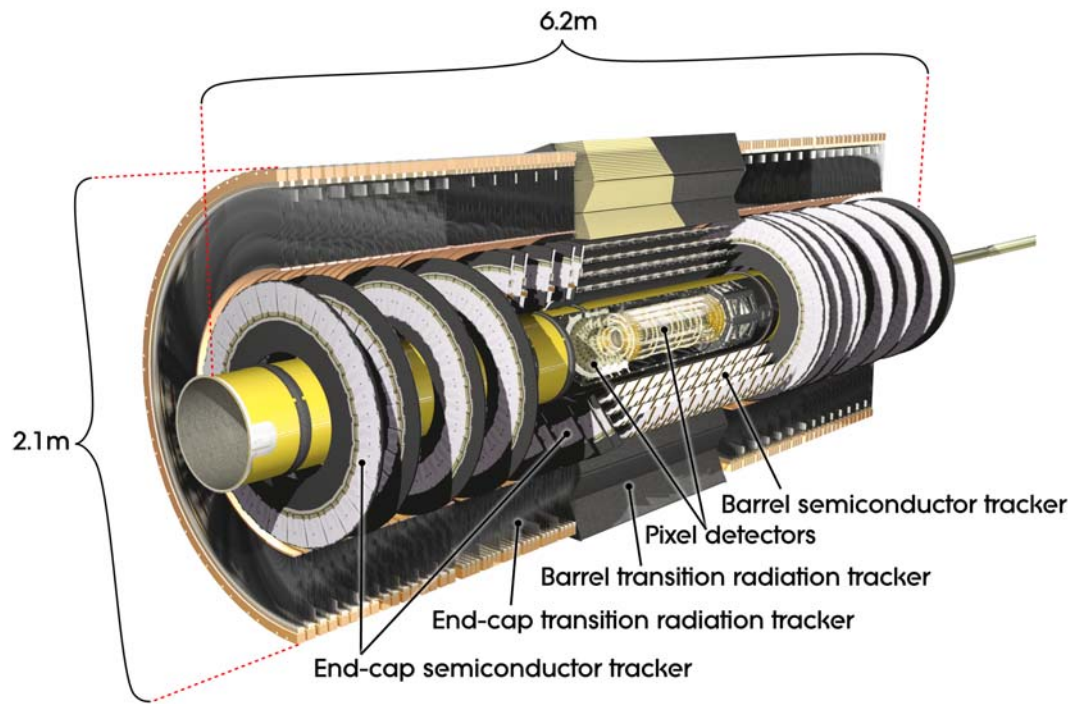


Figure 4.3: Inner Detector.

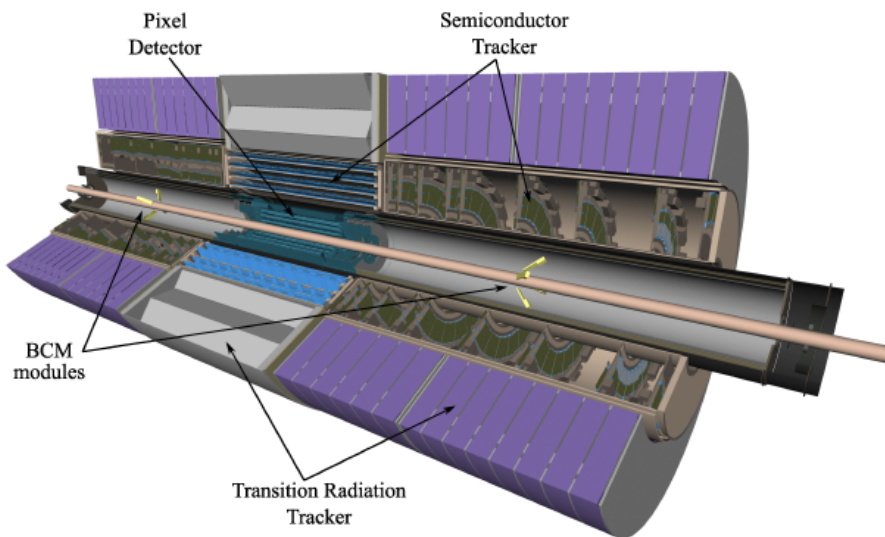


Figure 4.4: Position of the Beam Conditions Monitor inside the inner detector.

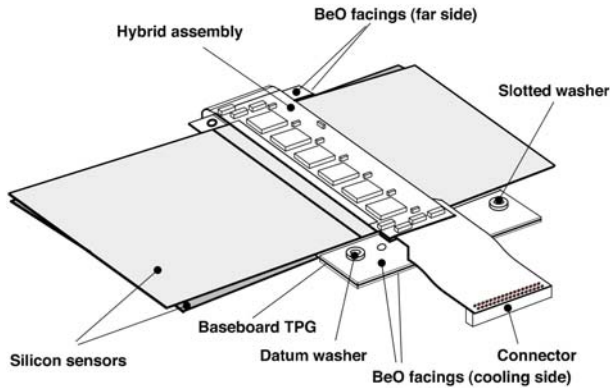


Figure 4.5: Semiconductor Tracker (SCT) module.

4.1.4 Transition Radiation Tracker

TRT uses 4 mm diameter straw tubes equipped with a 31 μm diameter gold-plated W anode wire, which provides typically 36 hits per track. Tracks can be followed up to $|\eta| = 2.0$. TRT only provides $R - \phi$ information. It is operated with Xe-CO₂-O₂ gas mixture (70 %, 27 %, 3 %) under 5 - 10 mbar over-pressure, which allows to detect transition radiation photons created in the radiator (a matrix of polypropylene fibers with a diameter of 19- μm) between the straws. The length of the straw tubes are 144 cm in the barrel, and 37 cm in the end-caps. The barrel contains 52544 straws per module, and 122880 straws for each end-cap. Under the nominal operating conditions, the electron collection time is about 48 ns, and the drift-time accuracy is around 130 μm . The total number of readout channels is approximately 351,000. The continuous tracking by the TRT improves the pattern recognition performance. The straw spacing was optimized for the electron identification. The detection of transition radiation photons provides discrimination between electrons and hadrons.

4.2 Calorimeters

Calorimeters [58] in the ATLAS detector consist of two types of calorimeters, electromagnetic (EM) calorimeter and hadronic calorimeter (Figure 4.6). EM calorimeter uses the LAr technology [59], whereas hadronic calorimeter uses two technologies; Tile technology in the barrel [61], and LAr in the end-cap. Here, overall detector profile of the calorimeters and their performance is described (details of the readout, energy reconstruction and calibration schemes will be mentioned in Chapter 5).

4.2.1 Electromagnetic Calorimeter

The main physics requirements on the EM calorimeter can be summarized as follows:

- **Large acceptance in η .** In order to observe rare physics events such as $H \rightarrow \gamma\gamma$ or $H \rightarrow 4e$ decays with the largest possible acceptance, it is important to cover

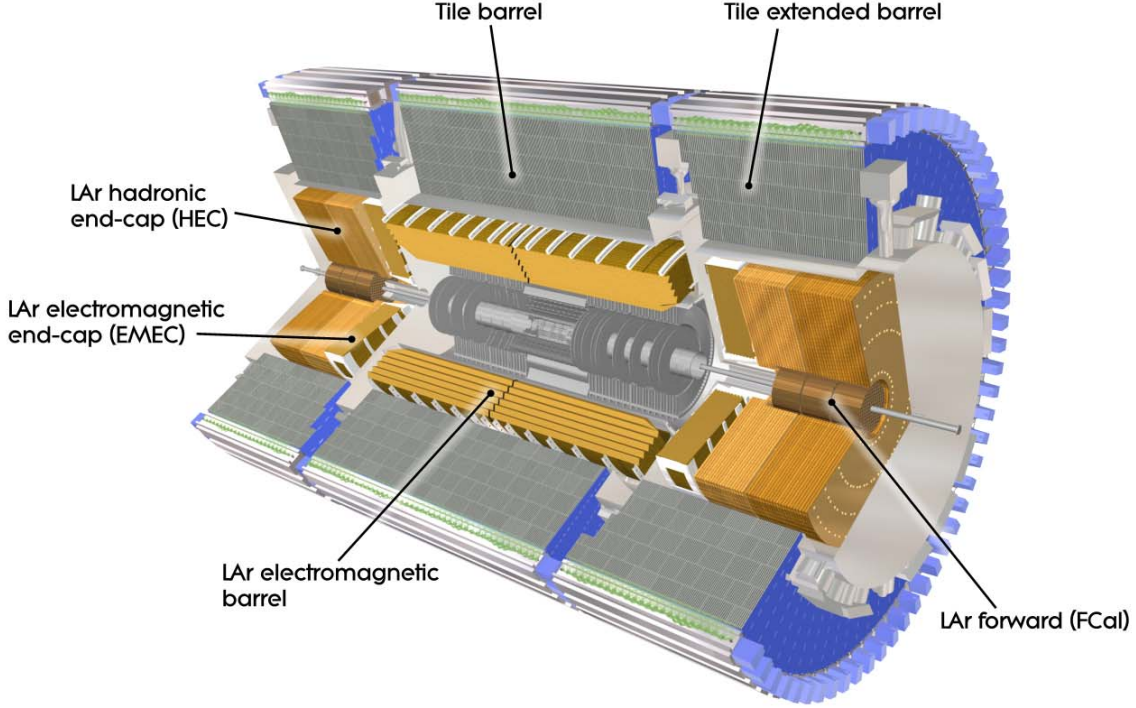


Figure 4.6: ATLAS Liquid Argon and Tile Calorimeters. The calorimeter system has a diameter of 4.25 m and a length of about 13 m.

as much large rapidity as possible. The upper bound comes from the radiation tolerance of the inner detector in the forward region.

- **Very good energy resolution and fine segmentation.** The mass measurement of the Higgs boson from $H \rightarrow \gamma\gamma$ and $H \rightarrow 4e$ impose tight requirements on the performance of the EM calorimeter. Energy resolution of

$$\frac{\sigma_E}{E} = \frac{10\%}{\sqrt{E}} \oplus 0.7\%$$

is required for the energy resolution. Fine segmentation of the EM calorimeter allows for good angular resolution of e, γ and also $e, \gamma/\pi^0$ separation. High granularity also allows for low electronic noise as will be mentioned below.

- **Wide dynamic range (~ 1 GeV to 5 TeV).** ATLAS will measure electrons and photons of wide energy range. The lower bound comes from the need to reconstruct electrons originating from the semileptonic decays of b-quarks to achieve good b-tagging efficiency. TeV-energy electrons may originate from new physics phenomena such as the leptonic decays of Z' and W' bosons.
- **Good time resolution.** Precise time measurement provides a power tool to reject non-collision background such as the cosmic rays, beam gas, and beam halos. It is

also important for identifying non-prompt decays coming from long-lived particles from new physics. Identification of bunch crossing is needed for the trigger purpose. Thus, the time resolution of a few ns is required in the EM calorimeter.

- **Low electronic and pile-up noise.** The aim to achieve very good mass resolution for $H \rightarrow \gamma\gamma$ and $H \rightarrow 4e$ channels requires low noise of various types. High granularity of the calorimeter allows for the low incoherent electronic noise. Fast detector response and electronics are required to suppress the pile-up noise. Due to the large number of channels in the calorimeter, coherent noise can largely spoil the resolution of E_T^{miss} as well, which is important for the mass measurement of the Higgs boson in $H \rightarrow \tau\tau$ channel, for example.

The EM calorimeter is located in two separate regions, the barrel and the end-cap. The barrel EM calorimeter covers up to $|\eta| = 1.475$, and the end-cap EM calorimeter covers $1.375 < |\eta| < 3.2$. Each of them is housed in a separate cryostat. In order to reduce the material before the calorimeter, the central solenoid and the LAr calorimeter share a common vacuum vessel. The barrel calorimeter consists of two identical half-barrels, separated at $z=0$ with a 4 mm gap. Each end-cap EM calorimeter consists of two mechanical coaxial wheels, which the outer wheel covers $1.375 < |\eta| < 2.5$ and the inner wheel covers $2.5 < |\eta| < 3.2$.

For the active material, LAr is used, and lead (Pb) as the absorber.

In the region up to $|\eta| < 1.8$, the presampler is located in front of the EM calorimeter to measure the energy lost in the dead material in front of the EM calorimeter (Figure 4.8). The EM calorimeter consists of three sampling layers (Figure 4.9). Due to the accordion structure [60] (Figure 4.7), the readout from front and back is possible and allows for the complete ϕ symmetry without azimuthal cracks. The accordion waves in the barrel are axial and run in ϕ , and the folding angles vary with radius to achieve constant liquid-argon gap of 2.1 mm. This gap width corresponds to 450 ns of total drift time for operating voltage of 2000 V. In the end-cap, the accordion waves are parallel to the radial direction and run in the axial direction. The LAr gap in the end-cap increases with radius, and the wave amplitude and the folding angle of the absorber and the electrodes vary with radius to achieve uniform performance. The total thickness of the modules is at least 22 radiation lengths (X_0) in the barrel, and greater than 24 X_0 in the end-cap (except for $|\eta| < 1.475$). The fine granularity of the EM calorimeter matched with the inner detector allows for the precise measurement of electrons and photons.

4.2.2 Hadronic Calorimeter

ATLAS hadronic calorimeter uses hybrid technology as mentioned above, the Tile technology in the barrel part, and the LAr technology in the end-cap and forward region. The LAr forward calorimeter expands the coverage up to $\eta = 5.0$ to improve the E_T^{miss} resolution.

The major role of the hadronic calorimeter is to reconstruct jets and contribute to the measurement of E_T^{miss} . The requirements on the performance of the hadronic calorimeter are summarized as follows:

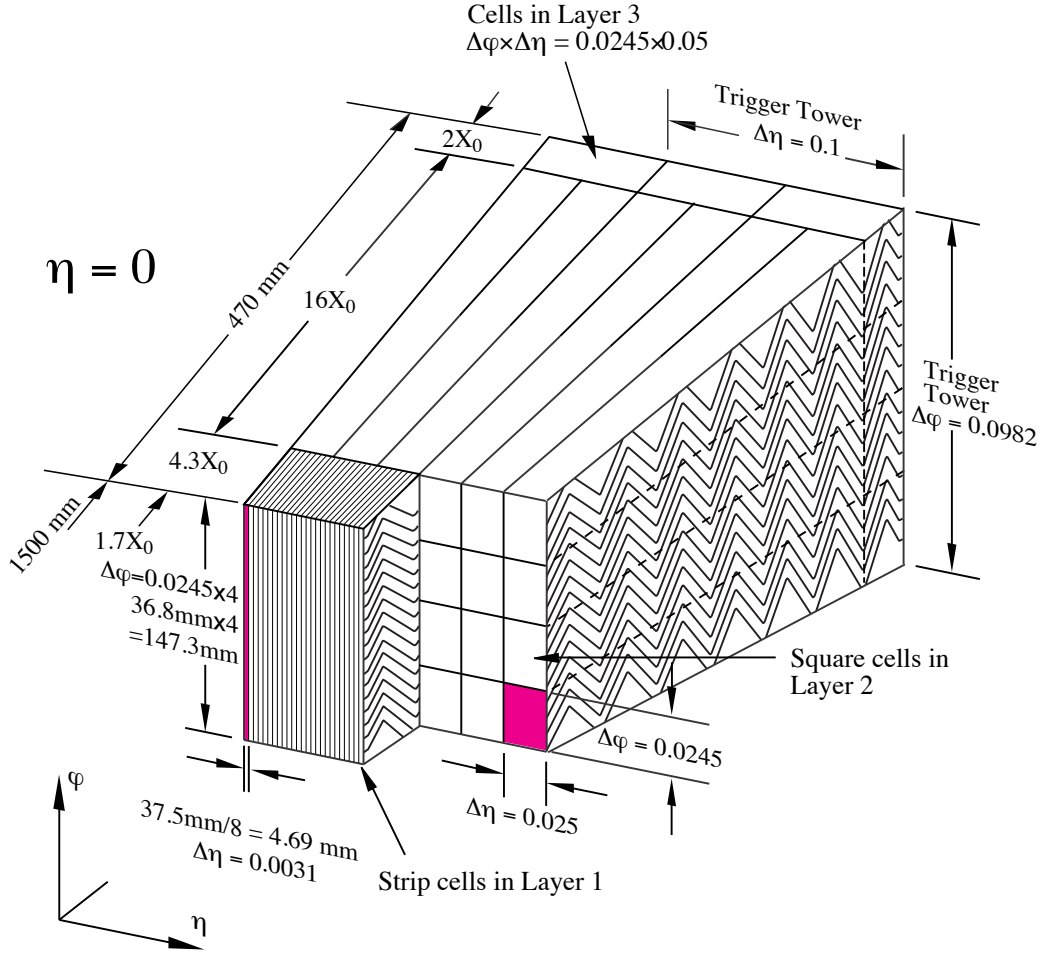


Figure 4.7: Sketch of a barrel module in EM LAr calorimeter

- **Good rapidity coverage.** The extension of the rapidity coverage up to $|\eta| \sim 5$ allows for an efficient tagging of the forward jets expected to associate to the production of heavy Higgs bosons. A large rapidity coverage also improve the resolution of E_T^{miss} .
- **Adequate granularity.** A successful reconstruction of dijets originating from high- p_T W bosons impose the most stringent requirement on the granularity. Granularity of $\Delta\eta \times \Delta\phi = 0.1 \times 0.1$ is needed in the region of $|\eta| < 3$, and $\Delta\eta \times \Delta\phi = 0.2 \times 0.2$ is sufficient at larger η regions.
- **Energy resolution.** The required energy resolution performance in the end-cap and the forward region is as follows:

$$\frac{\sigma_E}{E} = \frac{50\%}{\sqrt{E}} \oplus 3\% \quad (|\eta| < 3)$$

$$\frac{\sigma_E}{E} = \frac{100\%}{\sqrt{E}} \oplus 10\% \quad (3 < |\eta| < 5)$$

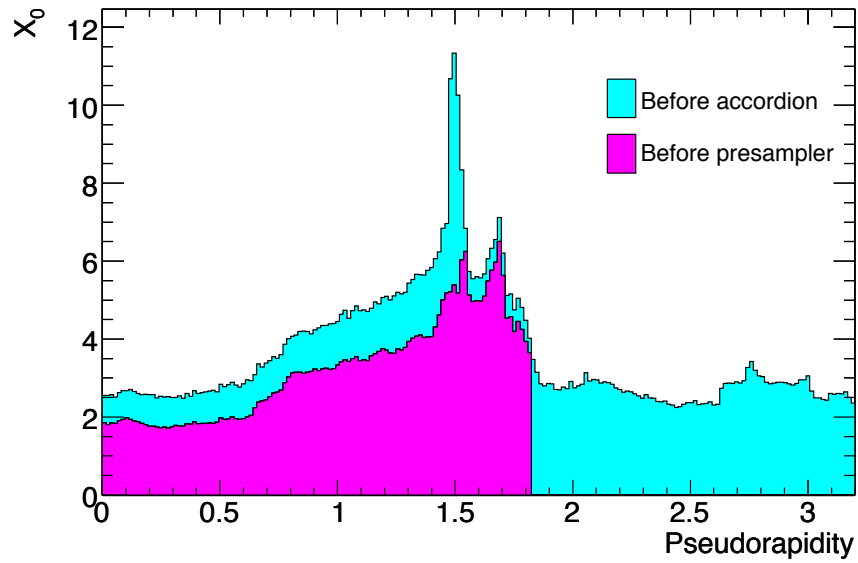


Figure 4.8: Amount of dead material in front of the EM calorimeter.

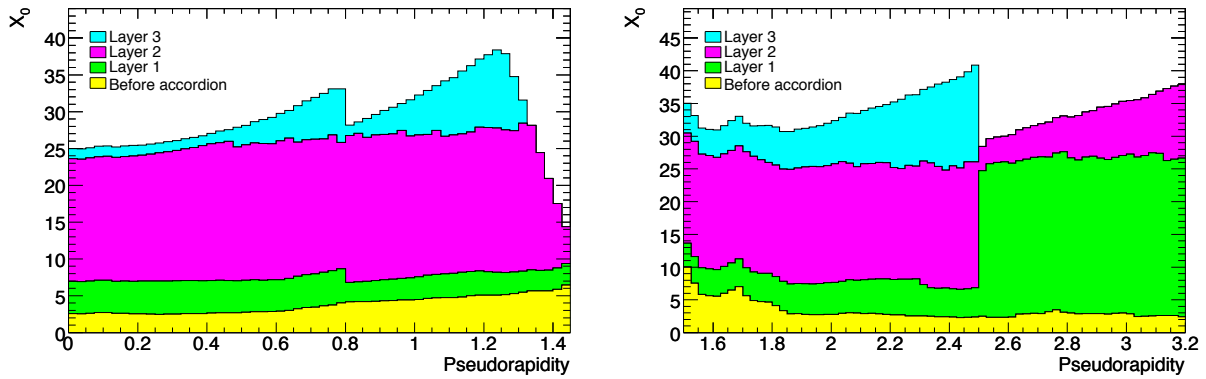


Figure 4.9: Thickness of each accordion sampling layer in the EM calorimeter in the barrel (left) and the end-cap (right).

The resolution is sufficient for the jet and E_T^{miss} measurement.

Tile Hadronic Barrel Calorimeter

Tile Calorimeter (TileCal) consists of three cylindrical sections. The Long-Barrel (LB: $|\eta| < 1.0$), 5.8 m in length, is contained in a single cylinder with separate partitions for positive and negative η . Two partitions of the Extended-Barrel (EB: $0.8 < |\eta| < 1.7$), each of them 2.6 m in length, are respectively contained in a cylinder. The Tilecal has the inner radius of 2.28 m and the outer radius of 4.25 m. The four partitions are named as LBA, LBC, EBA, and EBC, where A corresponds to the positive η (Anti-clockwise direction of the beam-line) and C the negative η (Clockwise direction). The radial depth of TileCal is about 7.4 interaction lengths (λ). TileCal has three sampling layers (sampling A, BC, D; Figure 4.11). Scintillating tiles are used as active material, and steel is used as an absorber. Tiles are placed perpendicular to the beam axis and radially staggered in depth. It allows for a simpler readout and tile configuration in order to combine all the signals from towers [62](Figure 4.10). Signals are read out by photomultipliers (PMT's) with wavelength shifting (WLS) fibers connected to both side of the tiles (Figure 4.12). Hamamatsu R7877 8-stage metal channel dynode PMT's are used. WLS fibers have a diameter of 1mm (Kuraray Y11(200)MSJ double-clad fibers), and their emission peak is at 476 nm with a decay time of ~ 6 ns. The photomultiplier tubes and front-end electronics are mounted in "drawers," which are aluminum structures of 3 meter length placed in a girder frame along the outer edge of each module. TileCal has good time resolution, around 1 ns, and adequate granularity ($\Delta\eta \times \Delta\phi = 0.1 \times 0.1$, and 0.2×0.1 for the last layer) to achieve good enough jet energy and missing transverse energy resolution.

LAr Hadronic End-Cap Calorimeter

For the hadronic end-cap calorimeter (HEC), liquid argon is used as the active material and copper (Cu) as the absorber. It consists of 2 independent wheels per end-cap and covers $1.5 < |\eta| < 3.2$. Each wheel is divided into 2 layers, thus composing 4 layers for each end-cap. The extension of HEC up to $|\eta| = 3.2$ which overlaps with FCAL, was done to avoid material reduction in the transition region of HEC and FCAL. The copper plates are interleaved with LAr gap of 8.5 mm (Figure 4.13). The typical drift time of electrons is 430 ns under the nominal voltage, 1800 V.

LAr Forward Calorimeter

Forward Calorimeter (FCAL) [63] covers the η range of 3.1 to 4.9. It is approximately 4.7 m away from the interaction point, 10 interaction lengths deep, and consists of three modules which the first layer is for electromagnetic measurement whereas the second and the third modules is for hadronic measurement (Figure 4.14). It contributes to the uniformity of the calorimeter coverage. A shielding plug was placed behind the third layer to reduce background in the muon spectrometer. The first module uses copper for absorber, and the second and the third modules use tungsten. Since, FCAL is exposed to high fluxes of particles, the liquid argon gaps were kept very small, with the electrode

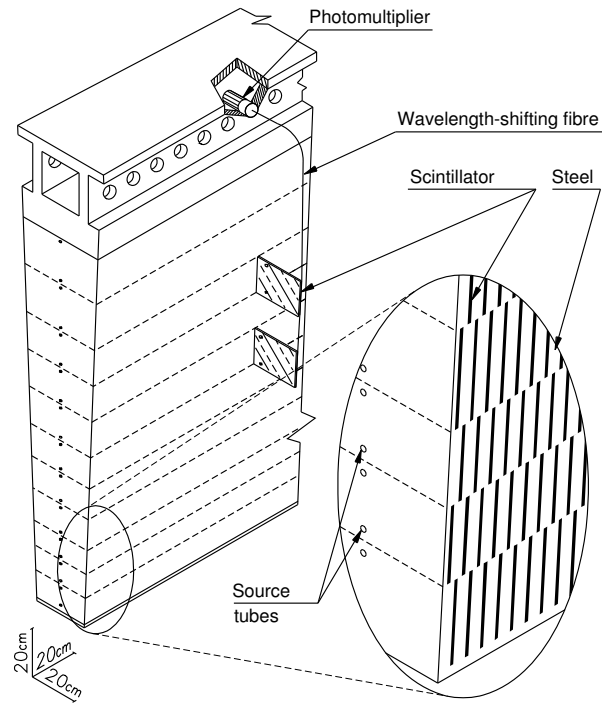


Figure 4.10: TileCal Module

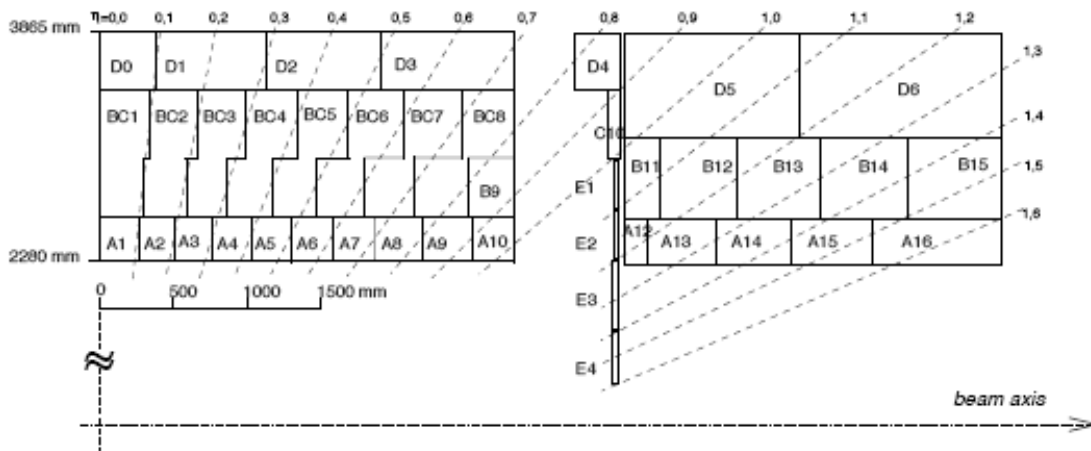


Figure 4.11: Segmentation in depth and η of the tile calorimeter modules in the long-barrel and extended-barrel

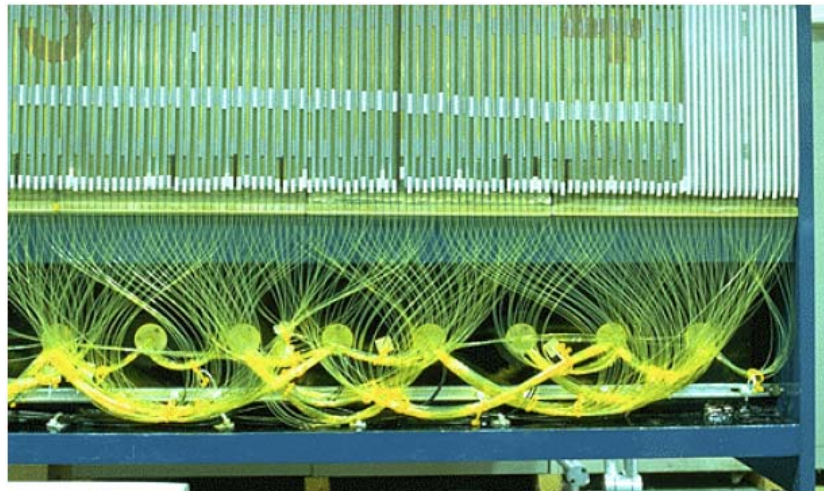


Figure 4.12: Typical fiber bundles in TileCal [61]. Each bundle is read out by a single PMT.

structure of small-diameter rods, centered in tubes. These tubes were placed parallel to the beam direction. In the first FCAL layer, the triangular current pulse at the electrode has a total drift time of 60 ns.

4.3 Muon Spectrometer

Muon spectrometers [64] consist of 4 detectors, 2 dedicated for track reconstruction (Monitored Drift Tubes and Cathode Strip Chambers), and the others for trigger purposes (Resistive-Plate Chambers and Thin-Gap Chambers; Figure 4.15).

The muon momenta are measured with the magnetic deflection of tracks by the large superconducting air-core toroid magnets. They are designed to measure tracks up to $|\eta| < 2.7$, and to trigger on particles in the region of $|\eta| < 2.4$. For the range $|\eta| < 1.4$, tracks are bent with the barrel toroidal magnetic field, whereas in $1.6 < |\eta| < 2.7$, the magnetic bending is provided by the small end-cap toroid magnets placed on the both ends of the barrel toroid. The region of $1.4 < |\eta| < 1.6$ is called the transition region where the magnetic deflection is provided by both the barrel and end-cap toroids. The performance goal is to measure 1 TeV tracks with a resolution of 10% with a stand-alone momentum reconstruction. The stand-alone measurements still provide adequate resolution and charge identification up to a few TeV (~ 3 TeV), and down to a few GeV (~ 3 GeV). Various contributions to the momentum resolution of the Muon Spectrometer tracks are shown in Figure 4.16.

The trigger chambers provide fast information from muon tracks. They are required to discriminate the muon momentum, to identify the bunch-crossing, and to provide fast and coarse tracking information to be used for the high-level triggers (Level-2 and Event Filter; see Section 4.6). They also provide ϕ hits to complement the MDT measurement. The resolution requirement greatly differs in the barrel and the end-cap region, which lead to the separate trigger chamber systems. With RPC and TGC, muon triggers can

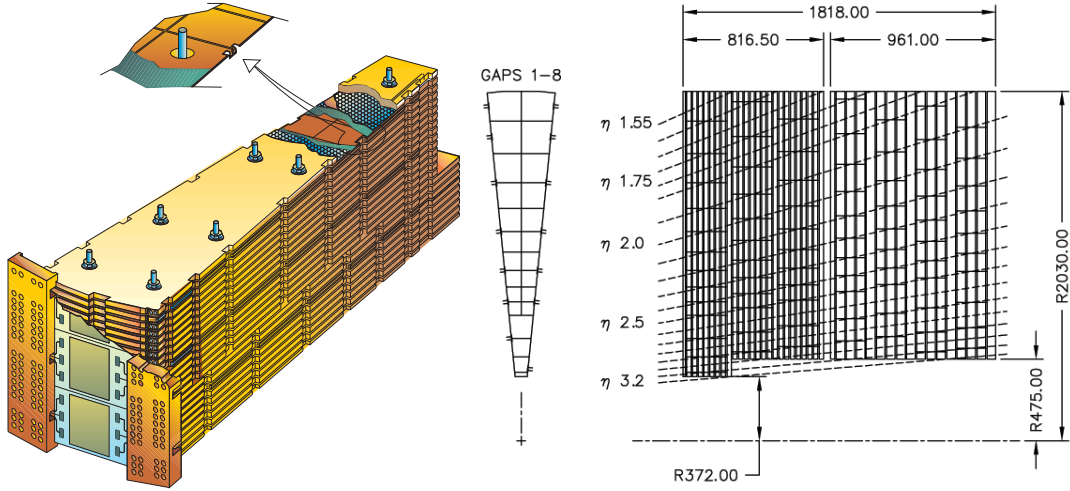


Figure 4.13: Schematic view of HEC module

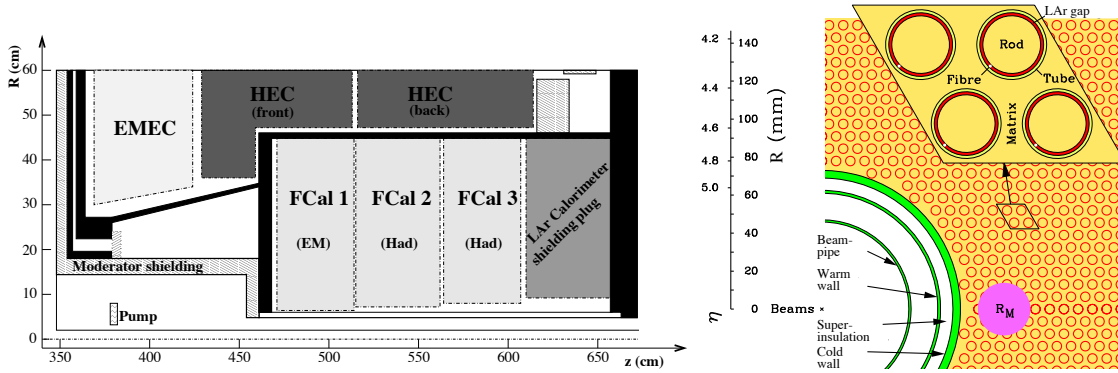


Figure 4.14: Schematic view of FCAL partitions and module

cover the low and high p_T muons in wide η regions (Figure 4.17).

4.3.1 Muon Drift Tubes

Muon Drift Tubes (MDT) are one of the two precision-tracking chambers dedicated for the determination of the coordinate of the track in the bending plane. MDT has a projective geometry, which means that the layer dimension and chamber size increase proportionally to their distance from the interaction point. It is used both in the barrel and the end-cap, and covers the region of $|\eta| < 2.7$, but the innermost layer in $2 < |\eta| < 2.7$ is covered by the CSC (Figure 4.18). It consists of pressurised drift tubes made of aluminum (diameter 29.970 mm), filled with Ar/CO₂ gas (mixed with the ratio of 93% and 7%) at 3 bar (Figure 4.19). The electrons produced from ionization are collected at the tungsten-rhenium wire (diameter 50 μm) with the potential of 3080 V. The gas gain is 2×10^4 . There are several advantages for using individual tubes with single wires. The stiffness of the tubes provides mechanical precision and strength. Also, a high operational performance is expected, since the failure from a single tube will not affect most of the

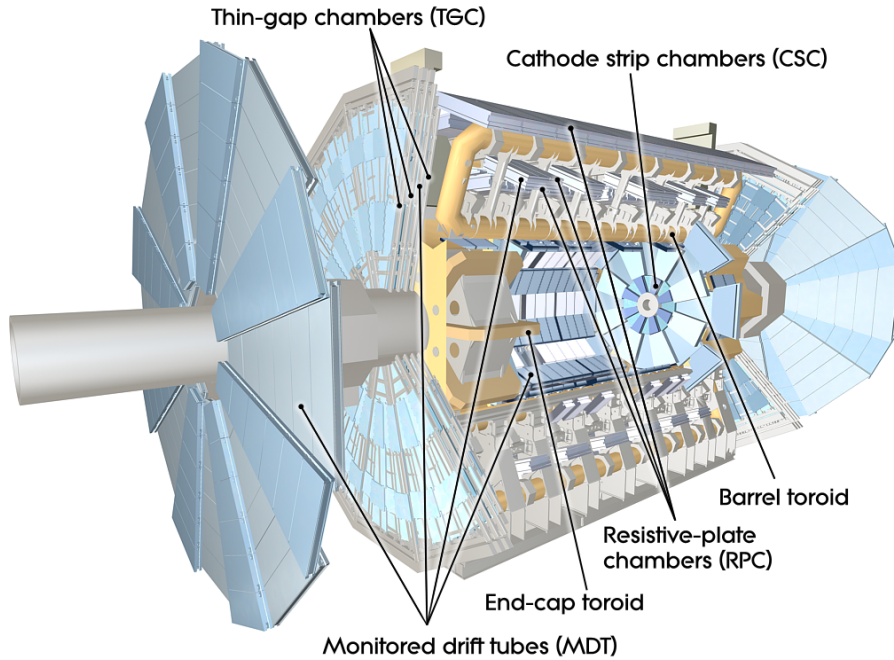


Figure 4.15: Overview of the Muon Spectrometer

other tubes. A disadvantage comes from the long drift time, which the maximum is about 700 ns when furthest from the tangential point. The average resolution per tubes is about $80 \mu\text{m}$.

4.3.2 Cathode Strip Chamber

The Cathode Strip Chamber (CSC) is a multi-proportional chambers with radially-oriented wires. Counting rates are expected to be higher in the end-cap region, and will exceed the safe operation limit of MDT (150 Hz/cm^2) in the first layer at $|\eta| > 2$. In such regions, the MDT is replaced with the CSC (Figure 4.18). Its safe operation limit is up to the counting rate of about 1000 Hz/cm^2 , which is sufficient up to $|\eta| = 2.7$. It is segmented in ϕ with large and small chambers (8 for each). The anode wire diameter is $30 \mu\text{m}$ with 1900 V applied. The CSC is filled with Ar/CO₂ (80/20). The gas gain is 6×10^4 . The position of tracks is obtained by interpolating the charges induced on cathode strips. The signals are not read out from the CSC wires. The CSC is suitable for the high particle density region due to its good two-track resolution, short electron drift time (less than 40 ns), and low neutron sensitivity.

4.3.3 Resistive Plate Chamber

Resistive Plate Chamber (RPC) is the muon trigger system in the barrel region. It consists of three concentric cylindrical layers. It is a gaseous parallel electrode-plate detector without any wires. The resistive plates are made of phenolic- melaminic plastic laminate. The nominal operating voltage is 9.8 kV, and the gas gap is 2 mm. The gas

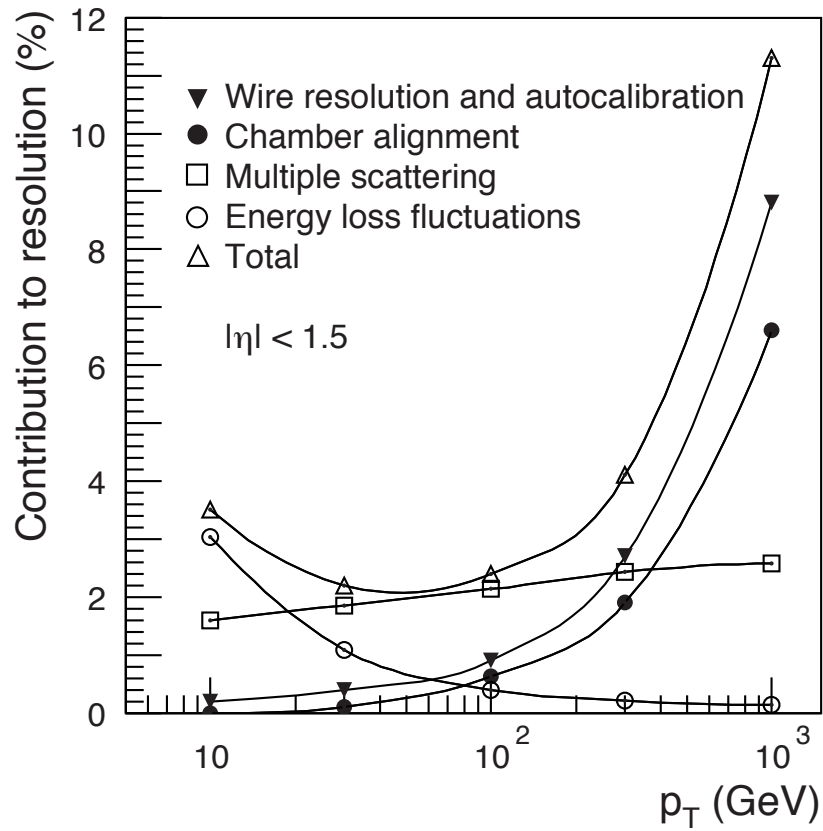


Figure 4.16: Momentum resolution of the muon spectrometer

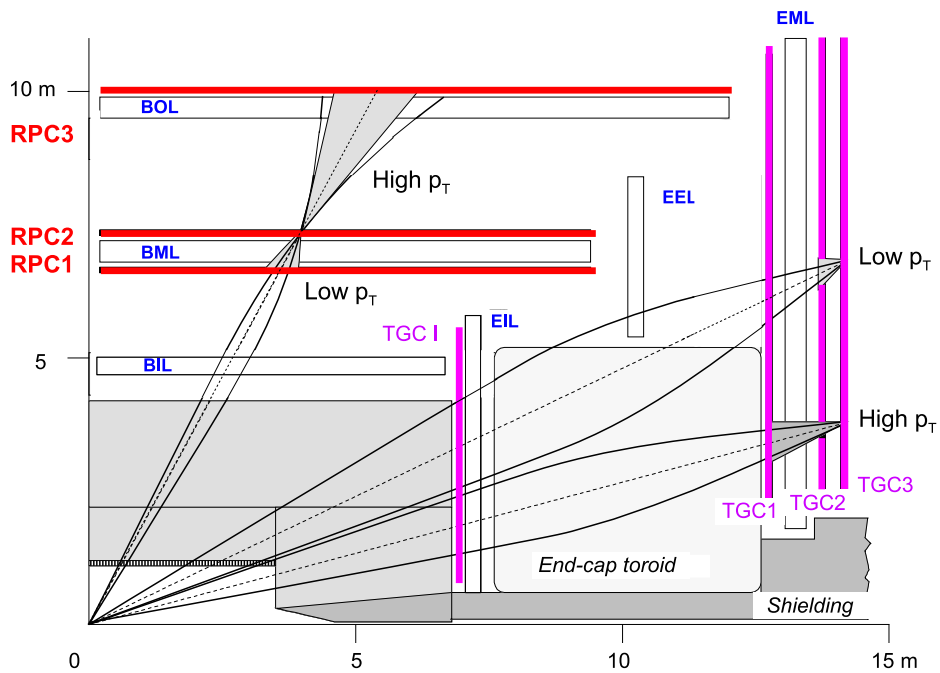


Figure 4.17: Schematic view of the Muon Trigger System

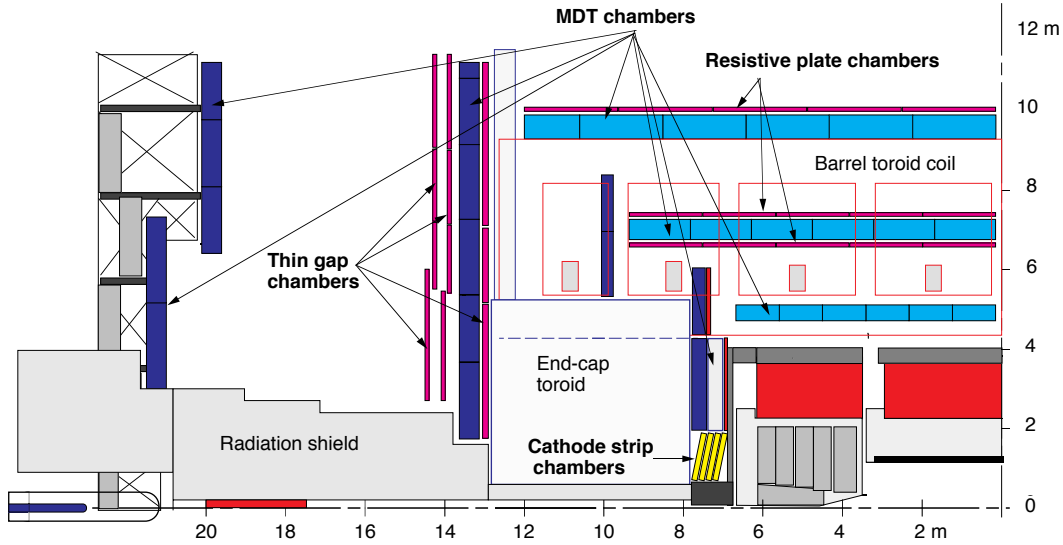


Figure 4.18: Sideview of the muon spectrometer.

filled in the gap is a mixture of $C_2H_2F_4$ /Iso- C_4H_{10} / SF_6 (94.7/5/0.3), which allows for relatively low operating voltage, non-flammability and low cost. The detection efficiency per layer is larger than 98.5 %.

4.3.4 Thin-Gap Chambers

Thin Gap Chambers (TGC) are the trigger systems in the end-cap region. They also provide the second azimuthal coordinate to complement the MDT measurement. The TGC's are multi-wire proportional chambers. The distance of wires to the cathodes is 1.4 mm, and it is smaller than the wire pitch of 1.8 mm. The anode wire diameter is $50 \mu m$ with 2900 V applied. They are operated with the gas mixture of CO_2 /n- C_5H_{12} (n-pentane). The gas gain is 3×10^5 .

4.4 Magnets

As mentioned above, ATLAS exploits of one solenoidal magnet and three toroidal magnets (Figure 4.23). This is a unique hybrid technology of combining four superconducting magnets. The overall size of the magnet system is 22 m in diameter and 26 m in length. It will store energy of 1.6 GJ. The system will provide the magnetic field over about $12,000 m^3$.

The central solenoid is placed before the LAr EM calorimeter as mentioned before. It provides 2 T axial field. The single-layer coil is made of a Al-stabilised NbTi conductor. It is 5.8 m long, and the inner and outer diameters of the solenoid are 2.46 m and 2.56 m. It stores the energy of 40 MJ. The cold mass can absorb the stored energy in case of a quench, with temperature increase up to 120 K at maximum which is a safe value. It takes about 30 minutes to charge or discharge the solenoid. Its re-cooling to 4.5 K can be achieved within a day.

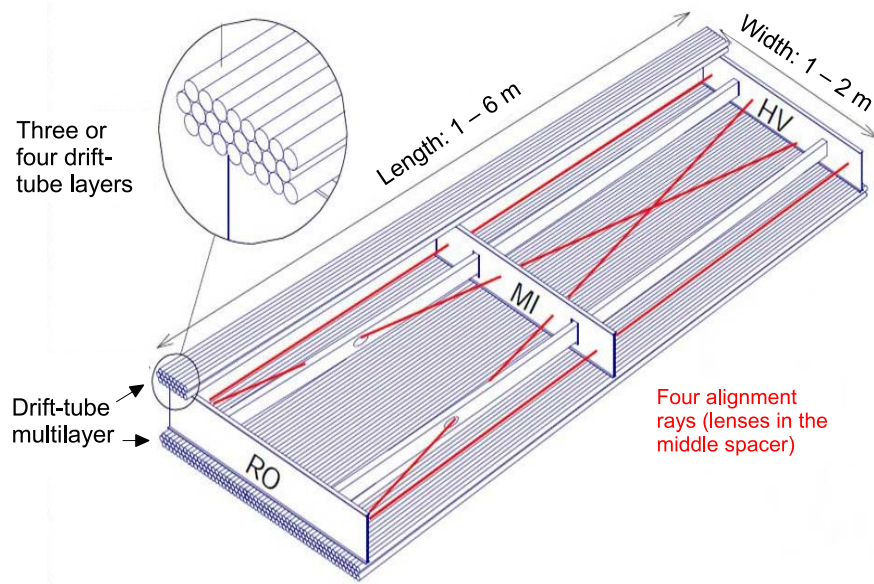


Figure 4.19: Mechanical view of MDT chamber

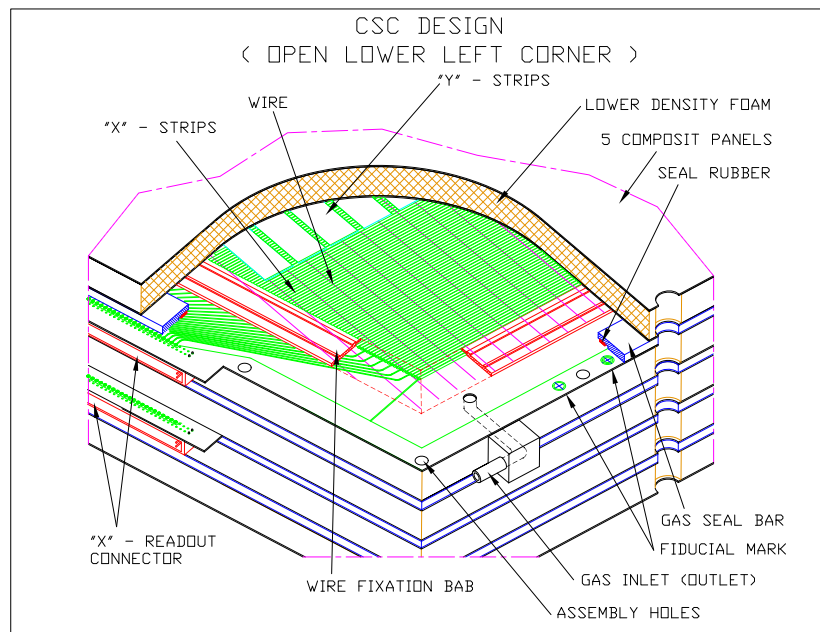


Figure 4.20: Structure of CSC

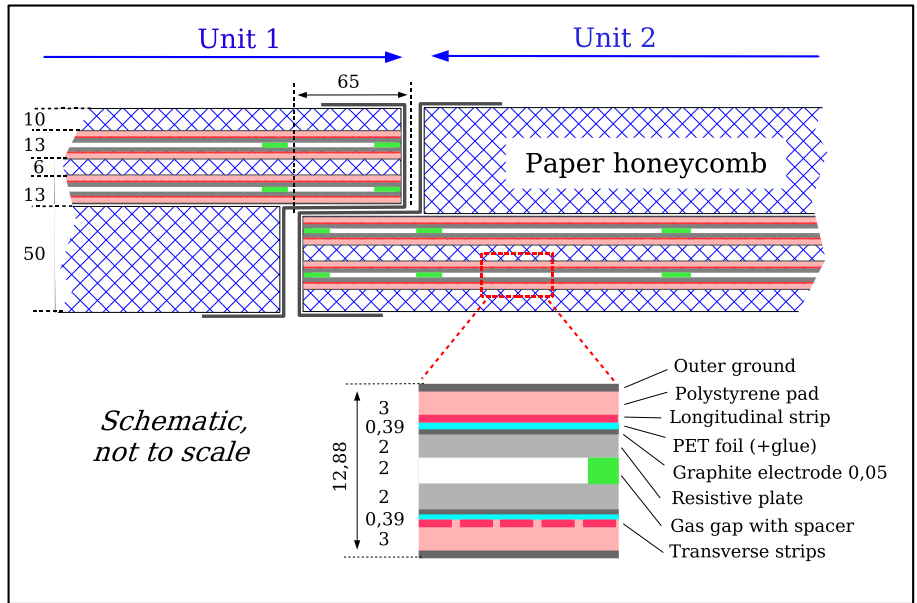


Figure 4.21: Cross section of RPC

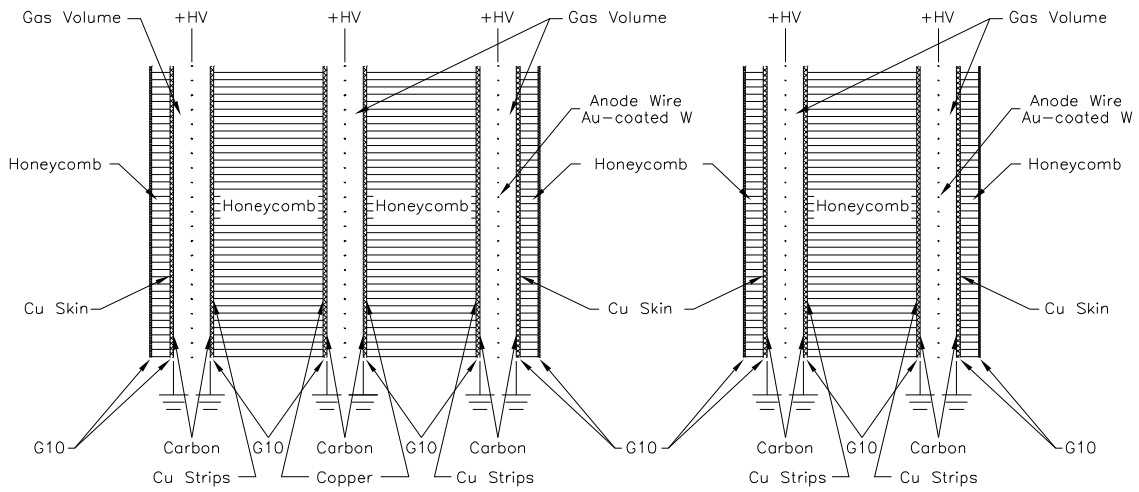


Figure 4.22: Cross section of TGC

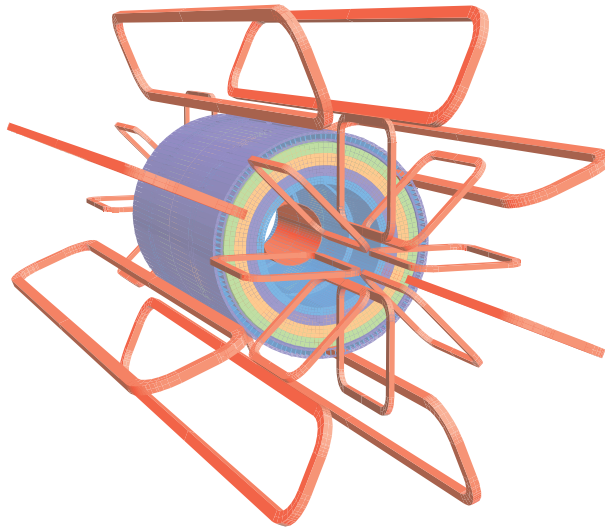


Figure 4.23: Schematic view of magnets. Eight barrel toroidal magnets and two sets of eight end-cap toroidal magnets are depicted as red windings. The cylinder with four layers indicate the Tile Calorimeter and a return yoke. The soleinoidal magnet is drawn as a red cylinder inside the Tile Calorimeter.

The barrel toroid provides the magnetic field in the cylindrical volume surrounding the calorimeters and both of the end-cap toroids. It consists of eight coils individually contained in the stainless-steel vacuum vessels. The overall size of the toroid is 25.3 m in length with inner and outer diameters of 9.4 and 20.1 m. The large size of the toroidal magnets allows for good momentum measurement of high energy muons. Basically, the same conductor and coil-winding technology is used in the barrel and the end-cap toroids. The technology exploits the winding of a pure Al-stabilised Nb/Ti/Cu conductor into pancake-shaped coils. It will provide approximately 0.5 T in the central region. It stores the energy of 1.1 GJ, and in case of a quench, the energy will be absorbed by the cold mass enthalpy followed by the activation of four quench heaters per coil which forces the entire magnet to the normal conducting state within less than two seconds.

The end-cap toroids are placed at both side after the end-cap and forward calorimeters. They provide magnetic field for the end-cap muon momentum measurement. They consist of eight coils each with a single cold mass on each side.

4.5 Forward Detectors

There are three detectors so called the forward detectors [65]. The one closest to the interaction point is the LUCID detector (LUminosity measurement using Cerenkov Integrating Detector), and the Zero-Degree Calorimeter (ZDC) and the ALFA (Absolute Luminosity For ATLAS) detector follow (Figure 4.24).

4.5.1 LUCID (LUMinosity measurement using Cerenkov Integrating Detector)

The LUCID measures the relative luminosity. There are several detectors than can measure the luminosity, but the LUCID is unique in the sense that it is primarily dedicated to the online luminosity monitoring. In order to provide the integrated luminosity and the online monitoring of the instantaneous luminosity and beam conditions, the inelastic p-p scattering is detected. It can also be used for the diffractive studies, to apply a rapidity-gap veto or tag diffractive signals.

The concept of the detector to use the array of Cerenkov tubes was originally developed by the CDF collaboration [66]. The LUCID consists of 20 aluminium tubes set around the beam pipe pointing toward the interaction point (Figure 4.25). The 1.5 m long mechanically polished tubes (diameter of 15 mm) are placed in a light-weight aluminium gas vessel. The tubes are filled with C_4F_{10} at the pressure of 1.2-1.4 bar, which provide a Cerenkov threshold of 2.8 GeV for pions and 10 MeV for electrons. The LUCID detectors are installed about 17 m away from the interaction point, surrounding the beam pipe with 10 cm radial distance ($|\eta| \sim 5.8$). The Cerenkov light emitted by the particles passing the detector will be read out by photomultiplier tubes (PMT's). The signal amplitude of the PMT's provide the numbers of particles per tube, and the fast timing response allows for the identification of the individual bunch crossings.

4.5.2 ALFA (Absolute Luminosity For ATLAS) Detector

ATLAS adopted the traditional technology to measure the absolute luminosity using the elastic scattering at small angles with the ALFA detector. The luminosity can be derived from the total cross section calculated from the elastic scattering amplitude at forward regions by the optical theorem. In order to measure at the very small angles ($3 \mu\text{rad}$), the detector will be located at ± 240 m from the interaction point. The Roman Pot technique [67] is adopted for the measurement. The technique exploits cylindrical vessels (the pots) that are separated from the vacuum of the accelerator, but equipped with bellows that connects them to the beam-pipe (Figure 4.26). The Roman Pots can reach as close as 1 mm to the beam. Scintillating fiber trackers are placed in the Roman Pots to perform position sensitive measurement.

4.5.3 Zero-Degree Calorimeter

The ZDC will measure forward neutrons with $|\eta| > 8.3$ in heavy-ion collisions. Such measurement allows to determine the centrality of the collisions, since it strongly correlates with the number of forward neutrons. During the proton-proton data taking, the ZCD will contribute as the additional acceptance to the other ATLAS detectors for diffractive processes and can also act as an additional minimum bias trigger. The beam gas and beam halo background can largely be rejected by requiring a tight coincidence from the two arms of the ZDC. It is housed in a slot of the Target Absorber Neutral (TAN) located at ± 140 m from the interaction point (Figure 4.27), where the beam pipes are separated

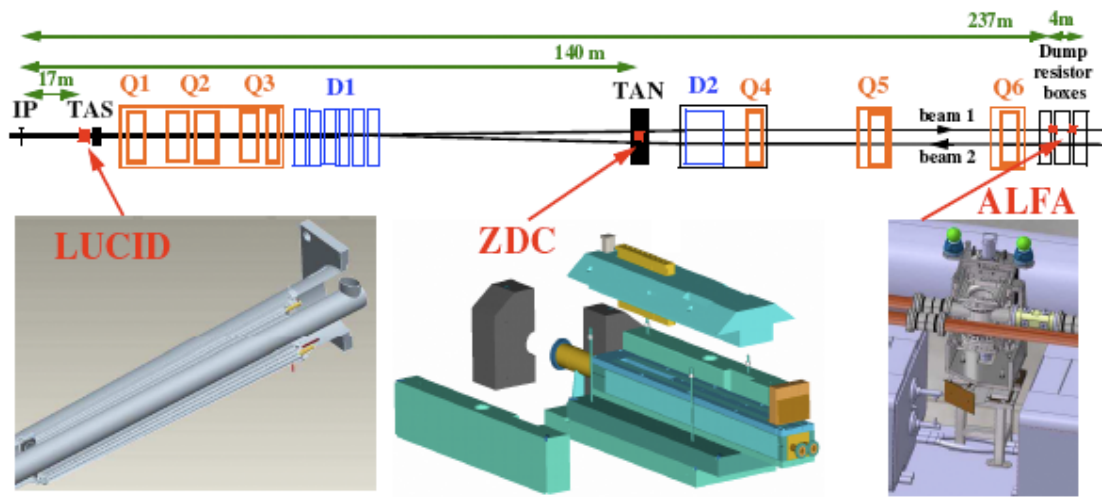


Figure 4.24: Forward detectors

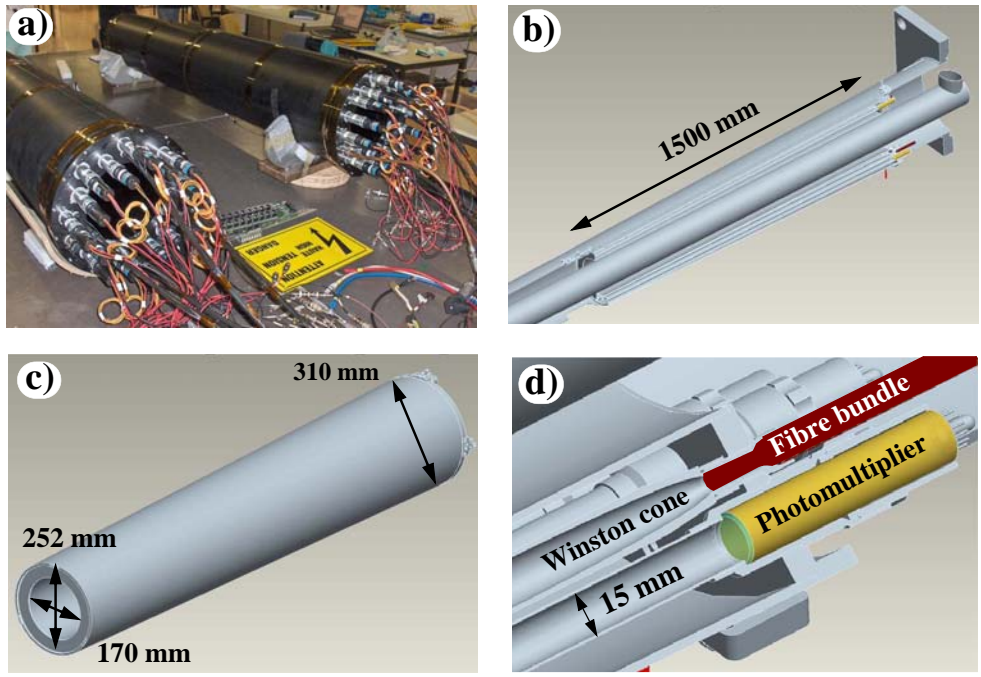


Figure 4.25: LUCID Detector

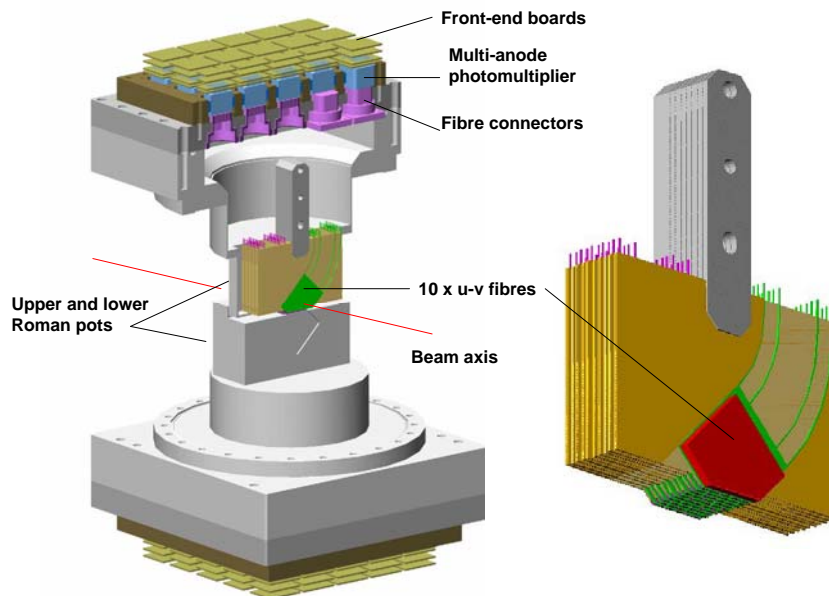


Figure 4.26: The layout of the ALFA Detector. The red line shows the beam axis.

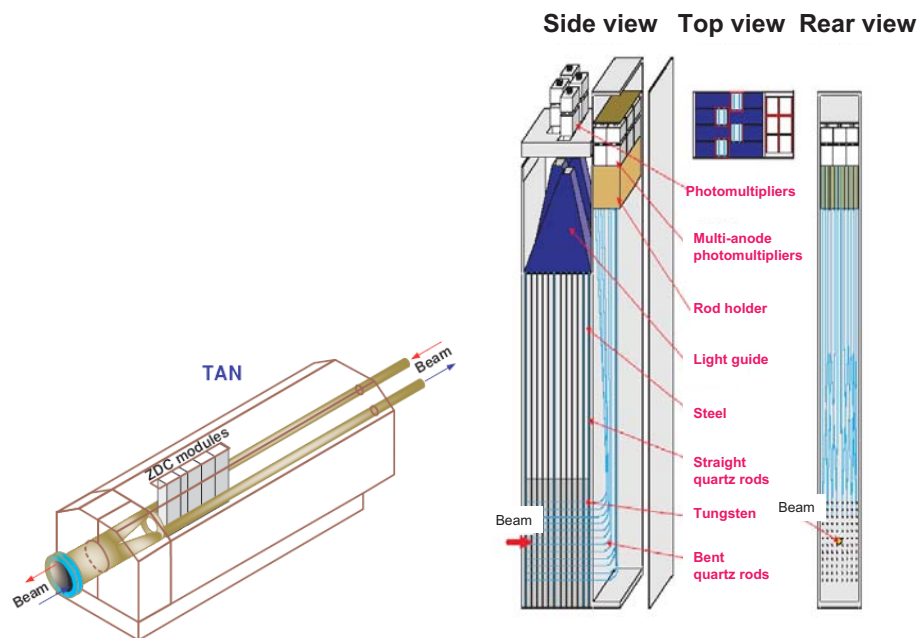


Figure 4.27: (Left) Schematic view of the ZDC in the TAN. (Right) The electromagnetic ZDC module.

into the two independent beam pipes. The ZDC consists of 1 electromagnetic (EM) module with about 29 radiation lengths and 3 hadronic modules with about 1.14 radiation lengths each. The EM modules consist of 11 tungsten plates with 91.4 mm wide, 180 mm high and 10 mm thick. Steel plates are extending above for 290 mm. Quartz rods with 1.0 mm in diameter penetrate the tungsten plates. They are bent vertically by 90° and are read out by multi-anode phototubes (MAPMT), which allows to observe Cerenkov light from shower products from the incident particles. Quartz strips with 1.5 thickness are also placed between the tungsten and steel plates, and are viewed by photomultiplier tubes from above. The strips are placed in order to improve the energy measurement performed by the position-sensitive rods. The hadronic modules have similar setups. The main differences are the way the rods are read out by the MAPMT (4 rods onto 1 pixel instead of one to one in the EM modules), and not all hadronic modules have position sensitive rods.

4.6 Trigger System

The trigger system in ATLAS consists of three levels of event selection, which are Level-1 (L1), Level-2 (L2), and event filter [68][69][70]. The Level-2 and the event filter make up the High-Level Trigger. The L1 trigger operates with custom-made electronics, whereas the HLT runs at the software level with commercially available computers and networking hardware. The overview of the trigger system is shown in Figure 4.28. The L1 trigger reduces the rate to 75 kHz (can be upgraded to handle in 100 kHz) in less than $2.5 \mu\text{s}$, and it is further reduces down to about 200 Hz by the higher level triggers.

The L1 trigger exploits the RPC, TGC, and all the calorimeter sub-systems with reduced granularity information (Figure 4.29) to search for high p_T muons, electrons/photons, jets, τ -leptons decaying into hadrons, large missing transverse energy (E_T^{miss}) and total transverse energy. Results from the L1 trigger are passed to the central trigger processor where trigger selections are performed based on the “trigger menus” implemented there. The L1 trigger also provides the information on the Regions-of-Interest (RoI’s): the $\eta-\phi$ coordinates of the detector regions that the selection process identified as having interesting features. The RoI information is passed to the L2.

The L2 selection is seeded by the RoI information received from the L1. The L2 uses the detector information within the RoI’s with full-granularity and precision. The L2 trigger reduces the event rate below 3.5 kHz within an event processing time of approximately 40 ms in average.

The event filter further reduces the event rate down to about 200 Hz with an average processing time of order of seconds. The event filter is based on the offline analysis procedure to reduce the event rate to be recorded for the offline analysis.

Trigger menus planned for early data with the center-of-mass energy of 10 TeV and the luminosity of $10^{31} \text{cm}^{-2}\text{s}^{-1}$ are shown in Table 4.1 and 4.2. For minimum bias studies, “mbSpTrk” starts from random triggered data, and “mbMbts_2,” uses the Minimum Bias Trigger Scintillator (MBTS). There are various triggers for each physics object such as electrons, photons, muons, tau leptons, jets, E_T^{miss} , and Sum E_T (scalar sum of transverse energy). In Table 4.1 and 4.2, the numbers before the objects shows the

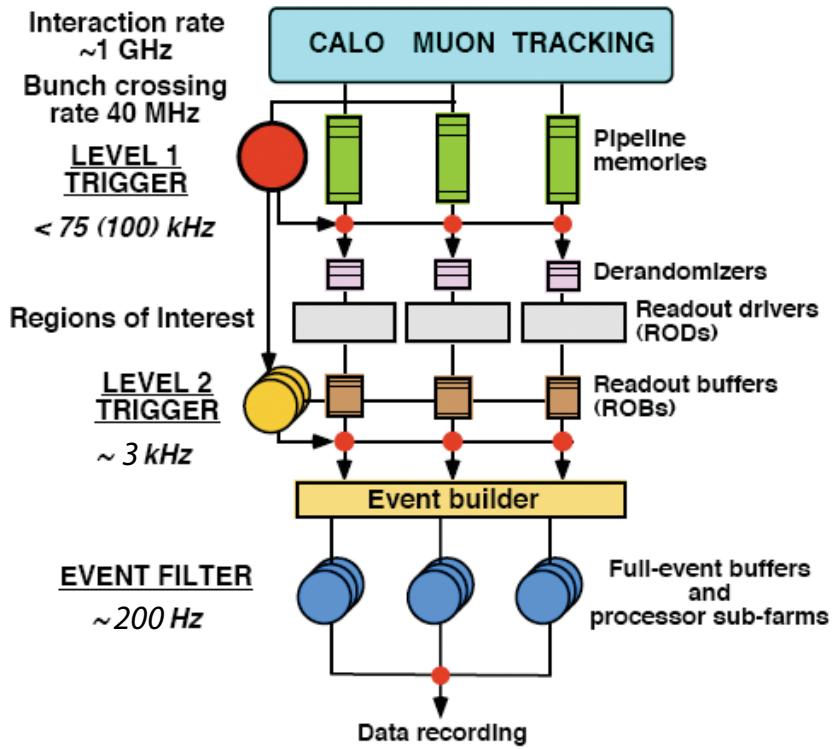


Figure 4.28: The overview of the ATLAS trigger system.

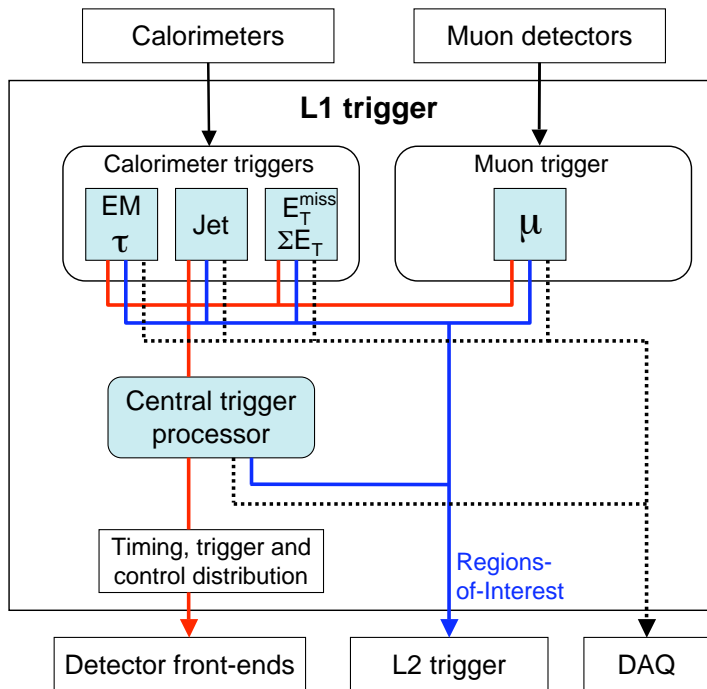


Figure 4.29: The block diagram of the Level-1 trigger.

required multiplicity, and the numbers after the objects corresponds to the transverse energy threshold (e.g. “3j20” means three jets with transverse energy large than 20 GeV).

Table 4.1: Primary trigger menus proposed for the luminosity $10^{31}\text{cm}^{-2}\text{s}^{-1}$ at the center-of-mass energy 10 TeV [71]. Prescales are respectively shown for the Level-1, Level-2, and the Event Filter. For “mbSpTrk,” prescale at the Level-1 is applied on top of the random trigger.

| Type | Name | Rate [Hz] | Prescale | Physics/Motivations |
|----------------|-----------------------|-----------|------------|----------------------------|
| Minbias | mbSpTrk | 3.85 | 5*,9,1 | Minbias |
| Minbias | mbMbts_2 | 4.00 | 184000,1,1 | Minbias |
| e/ γ | e10_medium | 26.6 | 1,1,1 | SM, BSM |
| e/ γ | 2e5_medium | 1.85 | 1,1,1 | SM |
| e/ γ | e20_loose | 6.17 | 1,1,1 | SM |
| e/ γ | em105_passHLT | 1.03 | 1,1,1 | check for problems |
| e/ γ | g20_loose | 8.02 | 1,1,1 | SM, GMSB |
| e/ γ +X | g25_loose_xe30 | 0.1 | 1,1,1 | W, Z γ , LED |
| μ | mu10 | 21.8 | 1,1,1 | B,W,Z,Top |
| μ | 2mu4 | 15.4 | 1,1,1 | B,W,Z |
| μ | mu20_MOnly | — | 1,1,1 | |
| τ | tau50_loose | 2 | 1,1,1 | BSM, Higgs |
| τ | 2tau_20i_loose | 1.3 | 1,1,1 | Higgs |
| τ | 2tau_29_loose | 1 | 1,1,1 | Higgs |
| τ +X | tau12_loose_e10_loose | 1.95 | 1,1,1 | Z,Top,Higgs,SUSY |
| τ +X | tau16_loose_xe25 | ~ 10 | 1,1,1 | W($\rightarrow \tau\nu$) |
| τ +X | tau16i_loose_EFxe30 | 3.6 | 1,1,1 | W,Z,Top,Higgs |
| τ +X | tau16i_loose_mu10 | 1.34 | 1,1,1 | Z,Top,Higgs |
| τ +X | tau16i_loose_3j40 | 2.8 | 1,1,1 | SUSY |
| τ +X | tau16i_loose_j120 | 1.65 | 1,1,1 | SUSY |
| τ +X | tau16i_loose_2b23 | <0.01 | 10000,1,1 | SUSY,Higgs |
| B | MU4_DiMu_FS | 0.62 | 1,1,1 | B ,low-mass Drell Yan |
| B | MU4_Jpsimumu_FS | 0.1 | 1,1,1 | $J/\psi, B$ xsec |
| B | MU4_Upsimumu_FS | 0.51 | 1,1,1 | Υ |
| B | MU4_Bmumu_FS | — | 1,1,1 | B ,low-mass Drell Yan |
| B | 2mu4_DiMu | 0.62 | 1,1,1 | B ,low-mass Drell Yan |
| B | 2mu4_Jpsimumu | ~ 0 | 1,1,1 | $J/\psi, B$ xsec |
| B | 2mu4_Upsimumu | 0.10 | 1,1,1 | Υ xsec |
| B | 2mu4_Bmumu | — | 1,1,1 | $J/\psi, B$ xsec |
| B | MU4_Jpsie5e3_FS | 13.3 | 1,1,1 | $J/\psi(\rightarrow ee)$ |
| B | mu4_DsiPhiPi_FS | 8.54 | 1,1,1 | B with D_S decays |

Table 4.2: Primary trigger menus proposed for the luminosity $10^{31}\text{cm}^{-2}\text{s}^{-1}$ at the center-of-mass energy 10 TeV [71]. Prescales are respectively shown for the Level-1, Level-2, and the Event Filter.

| Type | Name | Rate [Hz] | Prescale | Physics/Motivations |
|---------------------|------------------|-----------|------------|---------------------|
| Jet | j10v3 | 0.79 | 2000,100,1 | QCD |
| Jet | j20v2 | 0.79 | 1000,100,1 | QCD |
| Jet | j40 | 0.99 | 50,100,1 | QCD |
| Jet | j80v2 | 1.37 | 3,100,1 | QCD |
| Jet | j140v2 | 1.37 | 1,50,1 | Monojet, BH |
| Jet | j200v2 | 3.73 | 1,10,1 | Monojet, BH |
| Jet | j260 | 4.04 | 1,1,1 | Monojet, BH |
| Jet | 3j20 | 0.2 | 200,100,1 | QCD, BSM |
| Jet | 3j40 | 0.14 | 1,10,1 | QCD, BSM |
| Jet | 3j60v2 | 0.51 | 1,1,1 | QCD, BSM |
| Jet | 4j20 | 0.28 | 20,100,1 | QCD, BSM |
| Jet | 4j30 | 0.22 | 20,1,1 | QCD, BSM |
| Jet | 4j40 | 0.39 | 1,1,1 | QCD, BSM |
| Jet | 2fj18 | 0.07 | 100,1,1 | Diffraction |
| Jet+X | j80_xe30 | — | 1,1,1 | Top, SUSY |
| Jet+X | 2j40_xe30 | — | 1,1,1 | Top, SUSY |
| b-jet | 2b20_3L1J20 | 1.5 | 100,1,1 | Hadronic Top |
| b-jet | 3b20_4L1J20 | 0.001 | 1,1,1 | Higgs |
| b-jet | 1b40_2b20_3L1J10 | — | 20000,1,1 | Debugging |
| b-jet | 1b40_2b20_3L1J20 | — | 100,1,1 | Debugging |
| b-jet | 2b40_3L1J20 | — | 100,1,1 | Debugging |
| b-jet | 3b20_4L1J10 | — | 4000,1,1 | Debugging |
| E_T^{miss} | xe30 | — | — | SM, SUSY |
| E_T^{miss} | xe35_tight | — | — | SM, SUSY |
| Sum E_T | te360 | 0.3 | 40,1,1 | Black Holes |

Chapter 5

Energy Reconstruction in the ATLAS Calorimeters

In this chapter, the physics of calorimetry is briefly reviewed in Section 5.1. In Section 5.2 and 5.3, the energy reconstruction schemes in the ATLAS Liquid Argon and Tile Calorimeter are mentioned.

5.1 Introduction: Physics of Calorimetry

Calorimetry is one of the major detection methods widely used in particle physics to measure the energy and direction of incoming particles [72][73]. Calorimeters make use of large amounts of materials in which particles traversing them deposit energy by electromagnetic or hadronic showers. Even weakly interacting particles such as neutrinos can be indirectly detected by measuring the energy imbalance in the whole detector (in case of hadron colliders, only the imbalance in the transverse momentum carry information, due to the fact that the energy of interacting partons is unknown).

Calorimeters can be grouped into electromagnetic calorimeters and hadronic calorimeters. Electromagnetic calorimeters mainly measure electrons and photons by capturing their electromagnetic showers. Hadronic calorimeters measure energy of hadrons by detecting the outcome of the strong interactions, though the processes are more complicated than the electromagnetic cascade and makes the detectors more difficult to optimize.

The calorimeters can further be grouped into sampling calorimeters and homogenous calorimeters. Sampling calorimeters consist of consecutive layers of two kinds of materials, the absorber and the active medium. The absorber is made up of a dense material in order to develop electromagnetic or hadronic showers. The active medium provides signals to be detected. Homogenous calorimeters are made up of only one type of material that simultaneously offers shower development and signal generation.

5.1.1 Energy Loss of Charged Particles Through Matter

For moderately relativistic charged particles except for electrons, ionization and atomic excitation are the major physics processes which those particles lose their energy. The

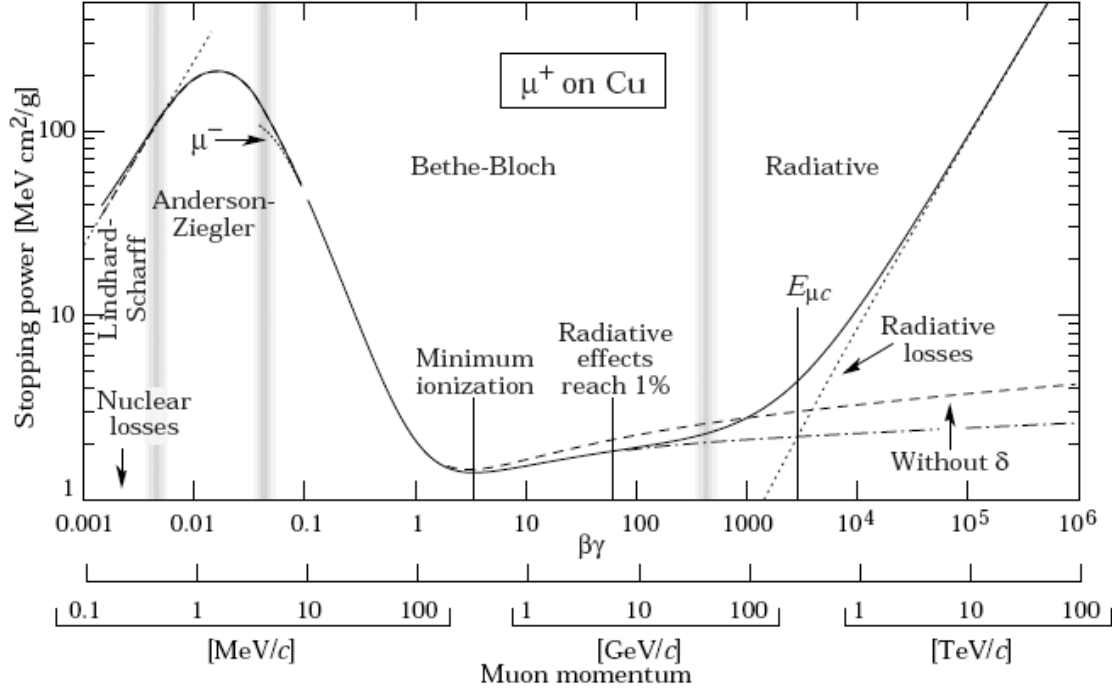


Figure 5.1: Stopping power for positive muons in copper (PDG, 2008)

mean rate of the energy loss is described by the Bethe-Bloch formula [74].

$$-\frac{dE}{dx} = Kz^2 \frac{Z}{A} \frac{1}{\beta^2} \left[\frac{1}{2} \ln \frac{2m_e c^2 \beta^2 \gamma^2 T_{max}}{I^2} - \beta^2 - \frac{\Delta(\beta\gamma)}{2} \right] \quad (5.1)$$

In the equation, K stands for $4\pi N_A r_e^2 m_e c^2$ (N_A : Avogadro's number, r_e : classical electron radius, m_e : electron mass). Z is the atomic number of the absorber material in which the particles are traversing, A is the atomic number of the absorber, β and γ follow the standard meaning in relativity, T_{max} is the maximum energy that can be given to a free electron in a collision, and $\Delta(\beta\gamma)$ is the density effect correction to ionization energy loss as a function of $\beta\gamma$.

At lower energy, various corrections have to be made [74] as is obviously seen in Figure 5.1. At higher energy, the effects of radiative losses become prominent, such as bremsstrahlung, direct pair production, and photo-nuclear interaction.

Muons with a momentum of a few hundred MeV/ c to a few hundred GeV/ c have a mean energy loss very close to the minimum ionization and are called minimum ionizing particles (MIP's). However, MIP's are hypothetical ideal particles, and muons are not MIP's in a strict sense [73], since in the high energy region even muons undergo radiative losses, and also in the low energy region the energy loss is far greater than the minimum ionization energy loss. These subtle differences have to be considered when muons are used for calibration purposes.

5.1.2 Interactions of Electrons and Photons in Matter

The fractional energy loss of electrons and positrons (will be mentioned unitedly as “electrons” in the following description unless explicitly mentioned) in lead is shown in Figure 5.2 [74]. When the incident electrons have small energy, the main physics process that account for the energy loss is the ionization. There are also small contributions from Møller scattering for electrons, and Bhabha scattering for positrons. Positrons can also annihilate with the electrons in the matter. Since electrons have a small mass, the main source of energy loss is bremsstrahlung for incident energy larger than ~ 10 MeV.

Figure 5.3 shows the cross section of photons in matter. At low energy, the largest contribution comes from the photoelectric effect, which an atom in the matter absorbs a photon and emits an electron. The excited atom returns to the ground state and emits X-rays or Auger electrons. Rayleigh scattering also has a large cross section for low energy photons, though the photons are simply deflected by an atomic nucleus and does not lead to an energy loss. Compton scattering is the most probable process in a few hundred keV to ~ 5 MeV energy range. In this process, a photon scatters with an electron in an atom, and enough energy is transferred to the electron so that it becomes unbound. Around a few tens of MeV in Lead, photonuclear interactions contribute to the energy loss. In such processes, the nucleus is broken up. At high energy, electron-positron pair productions by nuclear or atomic electron field become dominant.

5.1.3 Electromagnetic Cascade

As mentioned in the previous section, electrons and photons with sufficiently high energy will create secondary photons by bremsstrahlung, or originate secondary electrons and positrons by pair productions. These secondary particles will initiate the same process and thus form a cascade of particles. Such a phenomenon is called the electromagnetic cascade or the electromagnetic shower. The number of particles increase until the electrons lose enough energy so that the energy can only be degraded through ionizations. Critical energy ϵ indicates the energy when the main cause of the energy loss changes from radiative losses to ionization and excitation. There are two standard definitions of the critical energy; one is defined as the energy when the radiative energy losses equals those from ionization, and the other is the energy when the energy losses from ionization per radiation length (explained below) equals the traversing electron energy (the definition used in [74]).

The longitudinal and lateral size of electromagnetic showers can be described by a parameter so called the radiation length X_0 . It represents the average distance that an electron or positron traverses in matter to reduce the energy down to $1/e$ of the original energy E_0 . Thus, the mean energy of electrons after traveling the distance x is described as

$$\langle E(x) \rangle = E_0 e^{-x/X_0} . \quad (5.2)$$

Its value is material-dependent and can be expressed as

$$X_0 \simeq \frac{716A}{Z(Z+1)\ln(287/\sqrt{Z})} [\text{g/cm}^2] \quad (5.3)$$

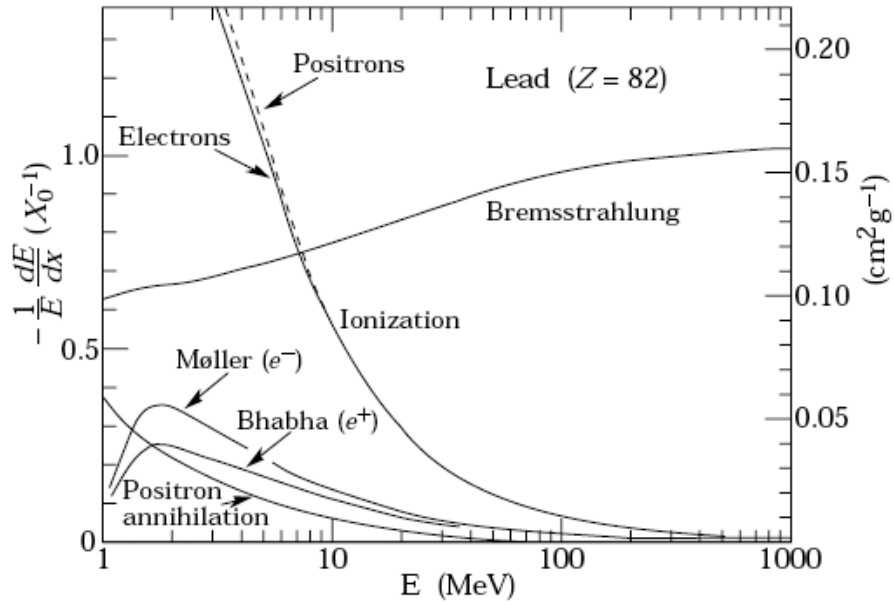


Figure 5.2: Fractional energy loss per radiation length in lead as a function of electron or positron energy [74]

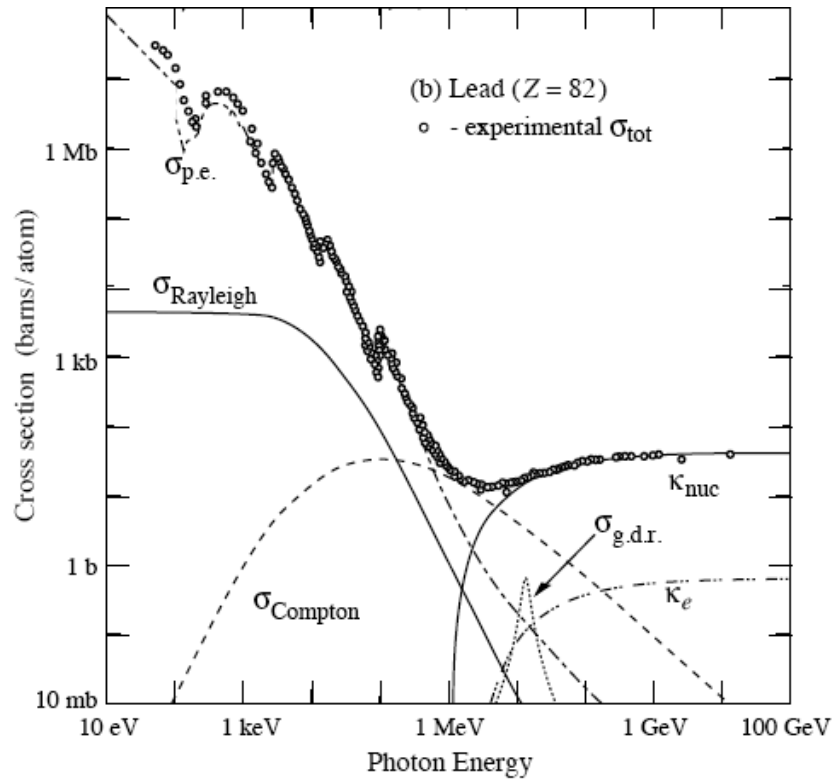


Figure 5.3: Photon total cross sections as a function of energy in carbon and lead [74]

where Z is the atomic number of the material and A is the atomic weight.

Similarly, the average intensity of photons $I(x)$ as a function of the traveling distance is,

$$\langle I(x) \rangle = I_0 e^{-(7/9)(x/X_0)} , \quad (5.4)$$

where I_0 is the original intensity. The factor $7/9$ comes from the difference in the cross sections of electron's bremsstrahlung and photon's pair creation. Intensity was used to describe the attenuation of photons, because unlike the charged particles, a single photon is either absorbed completely or scattered by a large angle by an interaction.

The transverse spread of electromagnetic showers mainly ascribes to the multiple scatterings of electrons and positrons. Bremsstrahlung photons and their secondary particles also contribute to further spread, due to their non-zero angles of the emission. The Molière radius R_M gives a transverse size defined from measurements over the full shower depth, and can approximately described as

$$R_M \simeq 21 \frac{X_0}{\epsilon} [\text{g/cm}^2] \quad (5.5)$$

About 90 % of the energy is contained within a cylinder of Molière radius R_M , and provides an indication of segmentations of calorimeters.

5.1.4 Hadronic Cascade

The energy loss of hadrons occurs through the sequential strong interactions as electromagnetic cascade does through electromagnetic interactions, though the process is far more complicated than the electromagnetic cascade. Characteristic processes in hadronic cascade are production of secondary hadrons by the strong interaction within a mean free path (so called an "interaction length λ "), thus the mean energy of high energy hadrons after traveling the distance x is described as

$$\langle E(x) \rangle = E_0 e^{-x/\lambda} , \quad (5.6)$$

where E_0 is the original energy of incident hadrons.

A large component of secondary hadrons are pions, and about one third of them are neutral pions decaying into two photons and depositing all of their energy in the calorimeter (so called the electromagnetic component). The fraction of electromagnetic component in the hadronic shower is energy-dependent and increases with the incident hadron energy. Thus, neutral pions (and also other neutral mesons such as η) do not contribute to the development of the cascade, but play dominant roles in the measurement of energy by depositing all their energy by the photons. The remaining charged hadrons deposits energy by ionization and may also expand the cascade further by sequential strong interactions. The visible energy deposits from hadrons occur through the neutral meson decays into photons, ionization by charged hadrons, and interaction of neutrons with matter (e.g. elastic and inelastic scattering, neutron capture, (n, α) reactions). The energy deposit from the ionization of charged hadrons, kinetic energy evaporation of neutrons, and invisible energy (will be explained below) is called the non-electromagnetic component of the hadronic cascade.

A peculiar aspect of hadronic cascade is the presence of “invisible energy,” which indicates that a certain fraction of the hadronic cascade is fundamentally undetectable, in contrast to the electromagnetic cascade where all the energy is deposited and detected in the calorimeter. When, incident hadrons strike a nucleus in the absorbing material, the spallation process may occur (and a creation of hadrons may accompany in case of high energy incident, which lead to the development of cascade as mentioned above). In the spallation process, some nucleons inside the nucleus are excited. When the excited nucleus goes through de-excitation, it is broken up and emit some particles, mainly free nucleons, until the excitation energy is less than the binding energy of a nucleon. In this process, some fractions of energy are used to release the nucleons from the nucleus to surmount the binding energy and are lost. This is the source of the “invisible energy.” The fraction of this invisible energy has a large fluctuation, due to the diversity of processes taking place in the hadronic cascade. The contribution of the invisible energy can be zero in the extreme case (e.g. $\pi^+n \rightarrow \pi^0p$), or may use up 60 % of the energy during the spallation process. On average, 30 % - 40 % of the non-electromagnetic component disappear as the invisible component.

5.2 Energy Reconstruction in LAr Calorimeters

An overview of the LAr readout electronics is shown in Figure 5.5 [75]. LAr ionization electrons drifting in the LAr gap with electric field applied by the high voltage are collected by the electrode in each cell. The raw signals are passed through the cryostat feed-throughs and mapped on to the Front End Board (FEB) inputs. Then, the preamplifier amplifies the signals, and passed onto the shaper where the signals are split into four. Three of the signals are shaped in three gains (high, medium, and low) and the remaining signal of the four is used for the Level-1 calorimeter trigger. This multi-gain system is adopted in order to cover the large dynamic range (~ 1 GeV to 5 TeV) required from the physics motivations (mentioned in Section 4.2.1). The three linear gains are in the ratio of 1/10/100. Then, a bipolar $CR - (RC)^2$ analogue filter is applied to optimize the signal-to-noise ratio. The time constant of 15 ns was chosen to minimize the overall noise (the electronic noise and the pile-up noise; see Figure 7.1). When an event is triggered, the signals are subsequently digitized by a 12 bit ADC (Analog to Digital Converter) every 25 ns (Figure 5.6). The pedestal is around 1000 ADC counts to

$$E_{\text{cell}} = F_{\mu\text{A} \rightarrow \text{MeV}} \cdot F_{\text{DAC} \rightarrow \mu\text{A}} \cdot \frac{1}{\frac{M_{\text{phys}}}{M_{\text{call}}}} \sum_{i=1}^{M_{\text{ramps}}} R_i \left[\sum_{j=1}^{N_{\text{samples}}} a_j (s_j - p) \right]^i$$

Figure 5.4: Cell energy reconstruction formula in LAr.

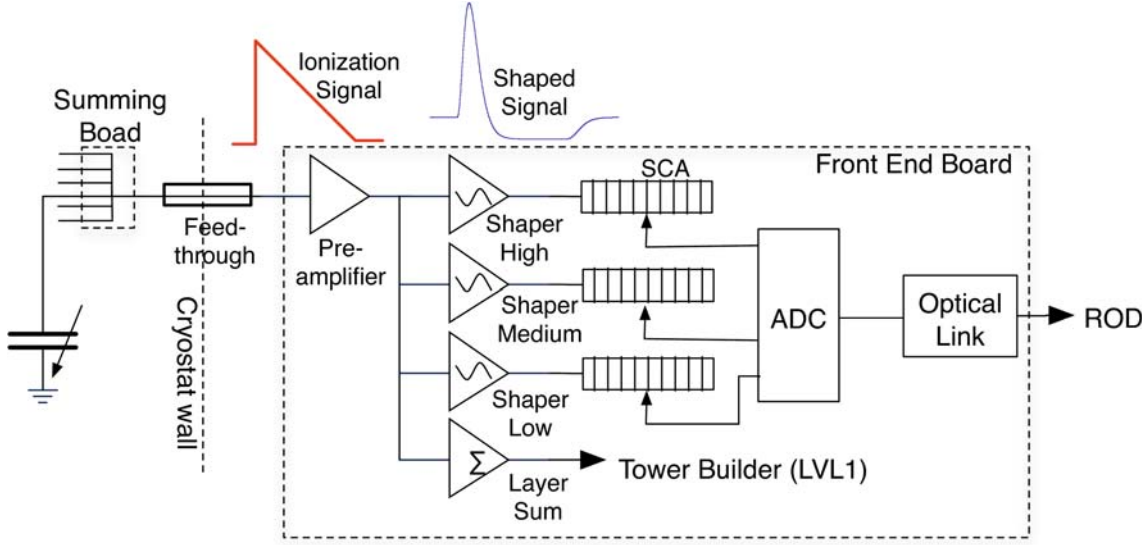


Figure 5.5: Diagram of the Liquid Argon Calorimeter read-out electronics.

accommodate the undershoot of the shaper. During the collision data taking, the pulse will be sampled and digitized in five points every 25 ns, but for the calibration and other commissioning purposes, more than 5 samplings were recorded in order to investigate the pulse shape in detail (32 samplings at most). For the Tier-1 reprocessed cosmic and single beam data (the Tier-0 grid site runs the first reconstruction of data, and Tier-1 takes care of re-running's of the reconstruction with updated database and software setups; see “Acronyms and Terms” and Chapter 6), only the first 5 samplings were used for the energy reconstruction, regardless of the actual recorded number of samples, in order to reconstruct the signals in the same condition as the collision data taking, where only the first five samples are recorded.

The formula in Figure 5.4 describes the electronic calibration chain of the LAr cell energy. Optimal Filtering Method [76] (described in the next section and B) is used for the energy and time reconstruction in LAr [77], and the energy is reconstructed from the pulse height in ADC counts (corresponds to $\sum_{j=1}^{N_{\text{samples}}} a_j (s_j - p)$; a_j is the optimal filtering coefficients (OFC), s_j is the ADC count in each sampling, p is the ADC count of the pedestals, and N_{samples} is the number of samplings). The energy is converted from the ADC counts to DAC (Digital to Analog Converter) values by so called the Ramp factor R_i derived from calibration pulses. The subtle difference in the signal heights in the calibration and physics runs are corrected by $M_{\text{phys}}/M_{\text{cali}}$ factor (~ 1.05) in order to perform precise energy reconstruction. The DAC value is further converted to the current value determined by the characteristics of calibration board. The current value is finally converted to MeV values considering the sampling fraction and various parameters of the electrodes.

The details of each constant are mentioned below.

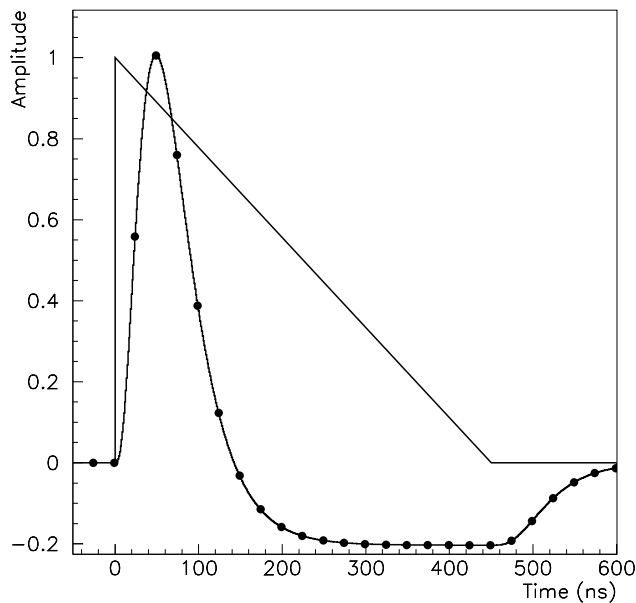


Figure 5.6: Form of the ionization signal and the shaped ionization signal in the LAr EM calorimeter

5.2.1 Optimal Filtering Method and Coefficients

The Optimal Filtering method is a sophisticated method to compute the peak of the shaped signals with reduced sensitivity to channel-to-channel variations, electronic and pile-up noise.

The amplitude of the signal (A) and the time offset from the digitizer output (τ) are what we want to measure. They are derived from the weighted sum of the digital samples as below.

$$A = \sum_{j=1}^{N_{samples}} a_j(s_j - p) \quad (5.7)$$

$$A\tau = \sum_{j=1}^{N_{samples}} b_j(s_j - p) \quad (5.8)$$

Here, the ADC count-values from each sampling s_j are the only inputs from the measurement. The OFC's (a_j, b_j) and the average pedestal value for each channel (p) are determined beforehand by series of calibration runs. $N_{samples}$ is the number of samplings used for the energy reconstruction, and five samplings are used during the collision data taking as mentioned before. The details on the mechanism of the Optimal Filtering Method is described in Appendix B.

5.2.2 Ramp Factor: ADC \rightarrow DAC

The Ramp factor R_i converts ADC counts to DAC values. It is measured regularly by the electronic calibration system.

In the calibration runs, each cell is pulsed around 100 times with a given input currents typically ranging from 0 to 1500 DAC values [77]. Figure 5.7 shows the ADC peak values as a function of input DAC values in the first sampling layer of the electromagnetic calorimeter. The Ramp factors are extracted by fitting the DAC-ADC relation in the non-saturating region with a polynomial function. Currently, the conversion is treated only linearly (thus only the first order polynomial is considered; only R_1 in Figure 5.4), but non-linearity of the electronic chain can be taken into account by including higher polynomial terms ($i \geq 2$).

5.2.3 The M_{phys}/M_{cali} Factor

The M_{phys}/M_{cali} factor corrects the Ramp factor considering the difference of the signal heights between the calibration and the physics runs (Figure 5.8). The difference in the pulse shape arises because in the actual physics runs, the signals initiate inside the capacitors, whereas in the calibration runs, the signals are injected outside the capacitor. This correction factor is needed to achieve the required energy resolution in the electromagnetic and hadronic end-cap calorimeter. However, the Forward Calorimeter does not predict the ionization pulse shape from the calibration runs, since the performance requirement is more relaxed compared to the EM and hadronic end-cap calorimeters. In those calorimeters, M_{phys}/M_{cali} are around 1.05 as mentioned before, but set to 1 and not considered for the Forward Calorimeter.

5.2.4 The $F_{DAC \rightarrow \mu A}$ Factor

The $F_{DAC \rightarrow \mu A}$ factor converts the DAC value to the current (μA). This factor is determined by the characteristics of the calibration board and the injector resistor on the motherboard as shown below.

$$F_{DAC \rightarrow \mu A} = \frac{79.295 \mu V}{R_{inj}} . \quad (5.9)$$

R_{inj} is the injection resistor.

5.2.5 The $F_{\mu A \rightarrow MeV}$ Factor

This factor converts the current value to the energy at the MeV scale. It consists of the energy-to-current conversion factor E/I and the sampling fraction factor f_{samp} .

$$F_{\mu A \rightarrow MeV} = \frac{1}{\frac{I}{E} f_{samp}} . \quad (5.10)$$

The energy to current conversion factor is described as

$$\frac{I}{E} = \frac{e}{W_0} f_{recomb}(\mathcal{E}) V_d(\mathcal{E}) \frac{\mathcal{E}}{U} , \quad (5.11)$$

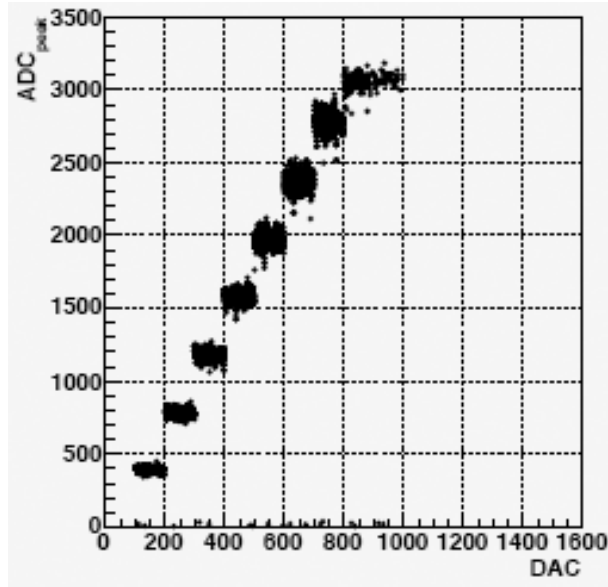


Figure 5.7: ADC peaks and input DAC values in the first sampling layer of the electromagnetic calorimeter [77]

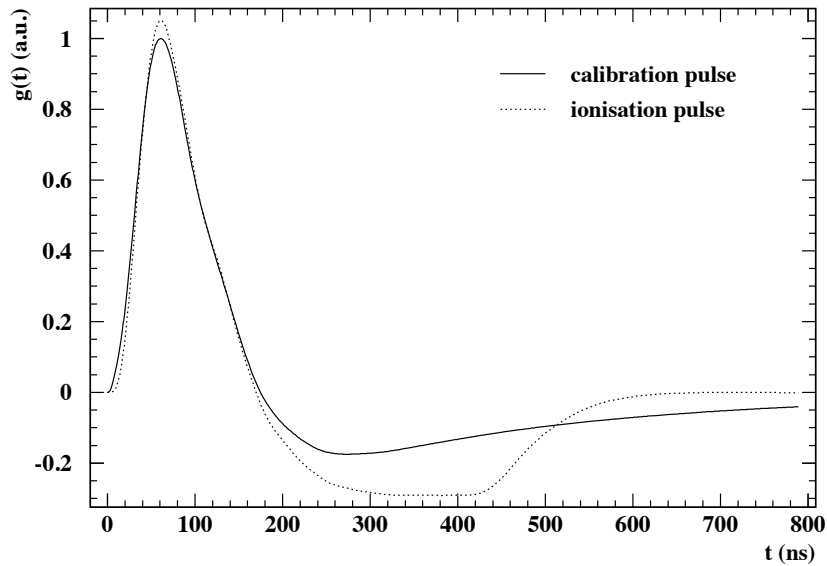


Figure 5.8: Pulse shape from calibration runs and physics runs (black line is the pulse shape from calibration runs, and the red line is from the physics runs) [78]

where e is the unit electric charge ($=1.6\times 10^{-19}$ C), W_0 ($=23.6$ eV) is the ionization potential of Liquid Argon, \mathcal{E} is the electric field in the channel, f_{recomb} is the correction factor for recombination effects (\sim a few %), $V_d(\mathcal{E})$ is the drift velocity, and U is the voltage applied between the electrodes (~ 2000 V).

The sampling fraction is the ratio between the energy deposited in the active layer and the total energy deposit. It can be estimated by considering the energy deposited by a MIP in active material and the absorber, plus a correction factor e/mip to take care of additional energy deposit by electrons' radiation.

$$f_{\text{samp}} = \frac{e}{mip} \times \frac{(dE/dx)_{\text{active}}^{\text{mip}}}{(dE/dx)_{\text{active}}^{\text{mip}} + (dE/dx)_{\text{absorber}}^{\text{mip}}} \quad (5.12)$$

5.3 Energy Reconstruction in Tile Calorimeter

The TileCal is also a sampling calorimeter. The scintillation light in the tile produced by the impinging particles is propagated by the WLS fibers and read out by the PMT's.

The PMT block consists of a light mixer, a photomultiplier tube, a voltage divider, and 3-in-1 card (Figure 5.9). The light mixer is an optical plastic insert and it mixes the light from WLS fibers to allow for uniform illumination of the photo-cathode of the PMT. The 3-in-1 card is used for three purposes as expressed in its name. First of all, a unipolar signal shaping is performed with a time constant of 50 ns, and two outputs with a relative gain of 64 (so called the low and high gain) are given. This bi-gain scheme was adopted to cover the large dynamic range (~ 20 MeV to ~ 1.3 TeV) just as in the case of LAr's tri-gain system mentioned in Section 5.2. Secondly, the charge-averaging amplifiers on the 3-in-1 card are used for used for the cell calibration and monitoring. Thirdly, the 3-in-1 card also provides analogue signals to be used for the Level-1 Calorimeter triggers.

The bi-gain outputs are then passed onto the digitizer and digitized every 25 ns using two 10 bit ADC's. Seven digitized samples are used for the energy reconstruction (nine samples can be recorded and used at most).

The Optimal Filtering method (explained in the previous section) was used since the Tier-1 reprocessing in December 2008, but the "Fit Method" [79] [95] has been used for a long time during the Tier-0 reconstruction in the cosmic and single beam runs of Fall, 2008.

Fit Method uses the knowledge of the pulse shape of the signal from the front-end electronics to extract energy and timing. For each channel, fit is done with the function,

$$f(t) = Ag(t - \tau) + p \quad (5.13)$$

where, $f(t)$ is the function, A is the amplitude of the signal, g is the normalized pulse shape previously determined from calibration runs, τ is the timing, and p is the pedestal. The χ^2 -minimization is used for the fit.

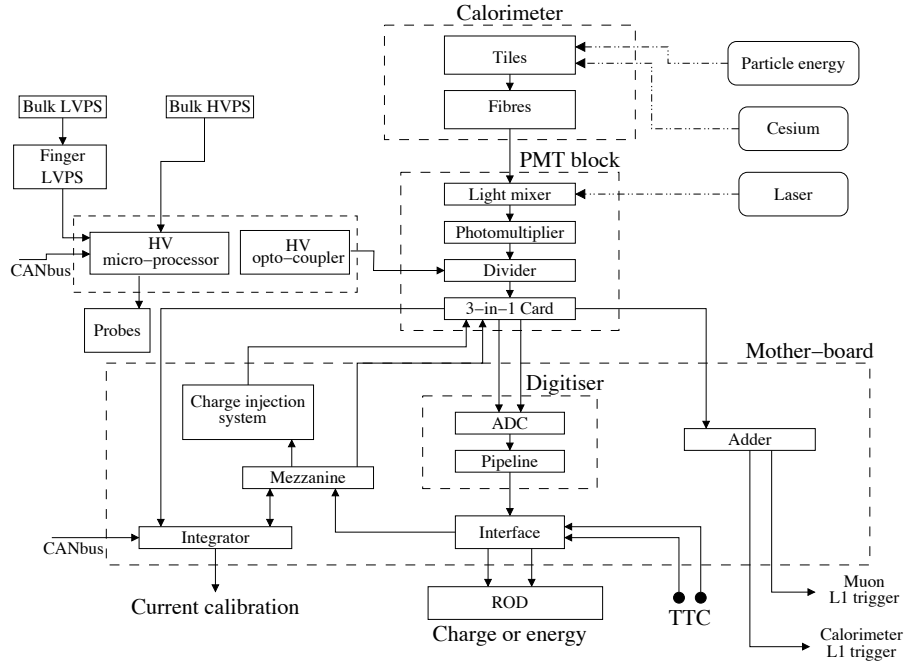


Figure 5.9: Diagram of the TileCal read-out electronics

5.3.1 Energy Calibration in Tile Calorimeter

For the accurate measurement of the energy in each channel, TileCal has sophisticated calibration systems to take care of all the signal paths in the calorimeter (Figure 5.9, 5.10). The systems consist of the electronic Charge Injection System (CIS) [99][100] solely for monitoring the readout, the pulsed laser system for monitoring the PMT and readout response, a movable Cesium (^{137}Cs) radioactive source for monitoring the scintillator and PMT response, and a Minimum Bias (MB) monitoring system which will use Minimum Bias events to monitor the calorimeter response during physics runs. TileCal has an independent readout (monitor system electronics) for the Cs and MB monitoring systems in addition to the fast readout used for the laser, CIS calibration systems, and for events from the physics runs.

The energy reconstruction of TileCal can be summarized as follows [81],

$$E_{\text{cell}} = [F_{\text{GeV} \rightarrow \text{pC}}]^{-1} \times [F_{\text{pC} \rightarrow \text{ADC}}]^{-1} \times F_{\text{LAS}} \times F_{\text{Cs}} \times A^{\text{OFC}}[\text{ADC}] \quad (5.14)$$

where E_{cell} is the reconstructed cell energy at the GeV scale, $F_{\text{GeV} \rightarrow \text{pC}}$ is the EM scale factor determined from the test-beam analyses, $F_{\text{pC} \rightarrow \text{ADC}}$ is the ADC/pC conversion factor determined by the Charge Injection System, F_{LAS} is the correction factor for non-linearity measured by the Laser Calibration system, F_{Cs} is the correction factor from the Cesium Calibration system to apply to achieve better uniformity among the TileCal cells, and $A^{\text{OFC}}[\text{ADC}]$ is the amplitude of the pulse determined by the Fit Method or the Optimal Filtering Method.

The characteristics of each calibration system will be briefly mentioned below.

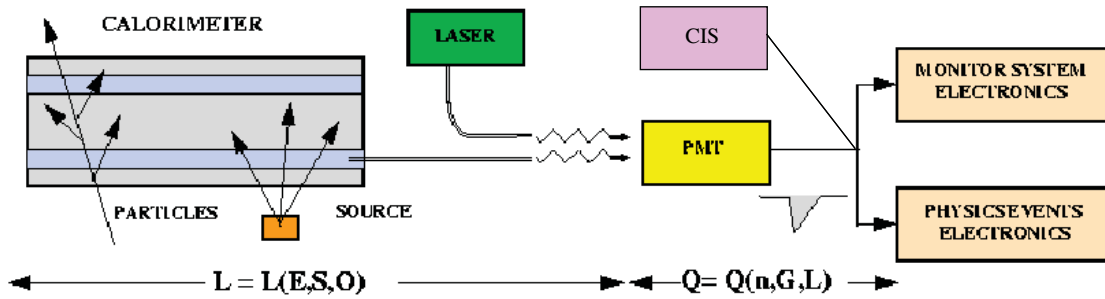


Figure 5.10: Conceptual diagram of calibration in TileCal; $L(E,S,O)$ is light response (E =energy, S =sampling fraction, O : response of optical component (scintillator and WLS fibers)). Light pulse is converted into a charge $Q(n,G,L)$ at PMT's (n =quantum efficiency, G =gain of the PMT). Figure revised from [61].

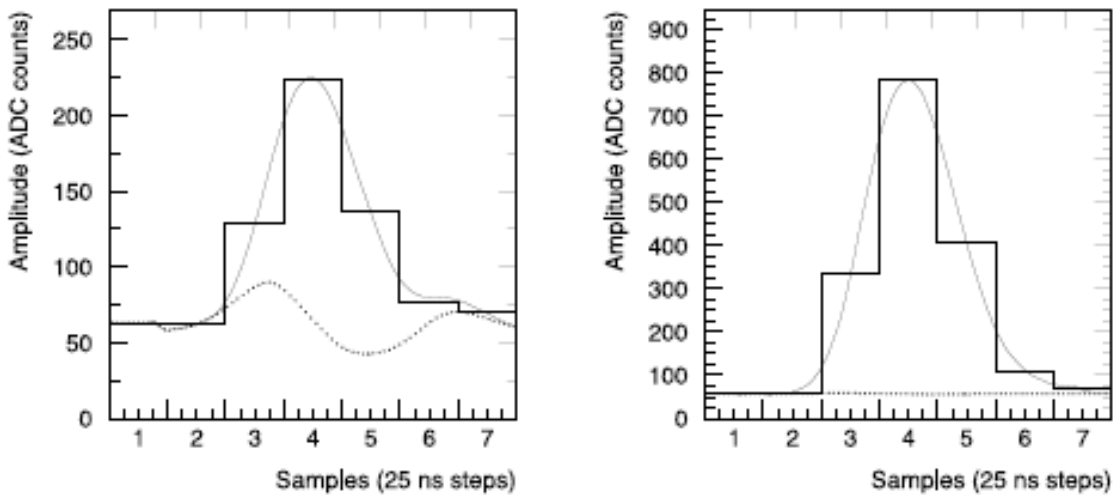


Figure 5.11: Response to a CIS pulse of 2 pC in the high gain (left) and 560 pC in the low gain (right)[95].

Charge Injection System: ADC \rightarrow pC

In between physics runs, pedestal, laser, and CIS runs will be taken. The CIS is a system which injects well defined charge into fast bi-gain electronics. This system provides ADC/pC conversion for both gains. In Figure 5.11, the left figure is for the high gain and the right for the low gain. The histograms show the the ADC samples, the dotted lines show the contributions from the capacitance of the switch, and the solid lines show the overall fit. It also provides an offline correction for nonlinearity in the low-gain.

Laser Calibration: Non-linearity Correction

Laser runs will also be taken in between physics runs to understand PMT response changes in regards to linearity and gains. Laser pulses are sent to a set of photodiodes and their response is monitored. The laser system can measure the absolute gains of each

PMT as well, and is also used for time calibration of the readout digitizers.

Cesium Calibration: Uniformity Correction

The Cs scans are also done outside the beam periods. The ^{137}Cs γ -source ($E_\gamma = 0.662$ MeV, half-life $t_{1/2} = 30.2$ y) is used. The source flows through the holes in scintillating tiles (Figure 4.10) with a uniform speed, and monitors the response for each channel. They allow for the cell intercalibration to equalize the signal response from all the cells, and also to monitor the cell response in time. The EM scale factor (pCb/GeV) is defined from testbeam analyses as mentioned below, and the same factor is applied to all the cells. Online cell intercalibration is done by adjusting the high voltage (HV) of the PMT's based on a fast analysis of the Cs scanned data.

Minimum Bias Monitoring System

The Minimum Bias monitoring system plays complementary roles to the Cs scans, due to the advantage that it can operate during the collision data taking, making use of the soft inelastic proton-proton collisions called the Minimum Bias events. Since the Minimum Bias events are uniform in ϕ with a moderate dependence in η , and occur with very high rate, they induce quasi-DC currents in the PMT's. Such feature of the Minimum Bias events allows to monitor the response of each channel in time.

EM Calibration from the Combined Test Beam Runs

As mentioned in the Cs section, the EM scale factor is determined from the testbeam runs using electrons with the energy from 20 GeV to 180 GeV. The measurement was performed with data from 3 long-barrel and 5 extended-barrel modules. The responses from about 200 cells are shown in Figure 5.12. The mean value for the energy response was 1.050 ± 0.003 pC/GeV. The RMS of the distribution was 2.4 ± 0.1 %.

5.4 Hadronic Calibration in ATLAS Calorimeters

The hadronic energy calibration in ATLAS is applied on top of energy at the EM scale (mentioned in Section 5.2 and 5.3), in order to successfully reconstruct the actual energy of impinging hadrons. Such a procedure is needed due to the fact that the response of the calorimeters to the EM component and the non-EM component of the hadronic cascade differs (this relation is called non-compensation). So, the offline reconstruction software recovers the compensation. Two standard algorithms exist in ATLAS for the purpose [23]; one is the H1-style calibration which was used in the H1 experiment at the electron-proton collider HERA (the Hadron Electron Ring Accelerator) located at DESY (Deutsches Elektronen-Synchrotron) [83][84] and the other is the Local Hadronic Calibration [85][86].

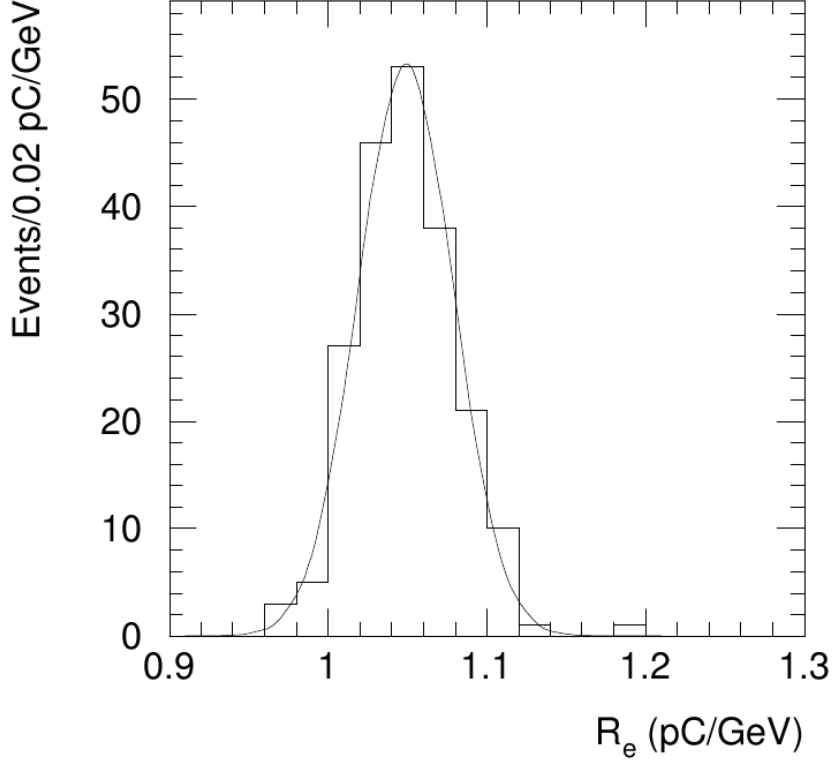


Figure 5.12: The cell response of electrons at 20°

5.4.1 H1-style Calibration

The H1-style calibration is a global hadronic calibration method, which the correction is applied at the cell-level in regards to the energy density of the cells. It makes use of the fact that the EM component of the hadronic cascade makes a highly dense energy deposit, but the non-EM component deposit its energy in more broad and less dense ways. In ATLAS, jets are reconstructed from calorimeter clusters at the EM energy scale, and H1 calibration factors are later applied to cells inside the jets to reconstruct the energy E at the hadronic scale,

$$E = \sum_i^{N_{\text{cell}}} w_i E_i^{\text{EM}} . \quad (5.15)$$

Here, i corresponds to the cells inside the jet, w_i is the H1 calibration factor to be applied to the cell, and E_i^{EM} is the cell energy at the EM scale. These correction factors depend on the calorimeter region and the cell volume. The weights are defined as,

$$w^{k,j} = \sum_{m=0}^{N_p-1} a_m^k \log^m \left(\frac{E}{V} \right)_j \quad (5.16)$$

where, N_p is the number of parameters, $a_m^{(k)}$ is the parameters to be defined from a fit with Monte Carlo expectation, k is the index for the calorimeter region (total of 17 regions),

and j is the categorization of the energy density into 16 ranges defined as,

$$j = \text{int} \left(\frac{\ln \frac{E_i^{\text{EM}}}{V_i^{\text{cell}}}}{\ln 2} + 26 \right) . \quad (5.17)$$

Thus, one of the 17×16 weights are applied to the cells inside jets considering their location in the calorimeter and energy density. The set of parameters a_m^k are extracted from fits using QCD dijet Monte Carlo simulation samples to recover the actual hadronic energy.

5.4.2 Local Hadronic Calibration

The Local Hadronic Calibration takes different strategy compared to the H1 calibration. Here, hadronic calibration is not performed after the jet reconstruction from clusters at the EM energy scale, but at the calorimeter cluster level before the jet reconstruction. So called the Topological Clusters (or Topoclusters; see Section 7.3.2) are used. The Topoclusters are categorized into “electromagnetic-like” or “hadron-like” using various cluster variables, such as lateral and longitudinal spread of the clusters, energy density, energy fraction in the EM calorimeter, the energy fraction of the most energetic cell, etc. and their moments. The hadronic calibration weights to be applied are derived from Geant4 simulations of single charged pions to recover the actual energy.

Part II

**Commissioning of the ATLAS
Calorimeters**

Chapter 6

Cosmic and Single Beam Runs

6.1 Cosmic Runs

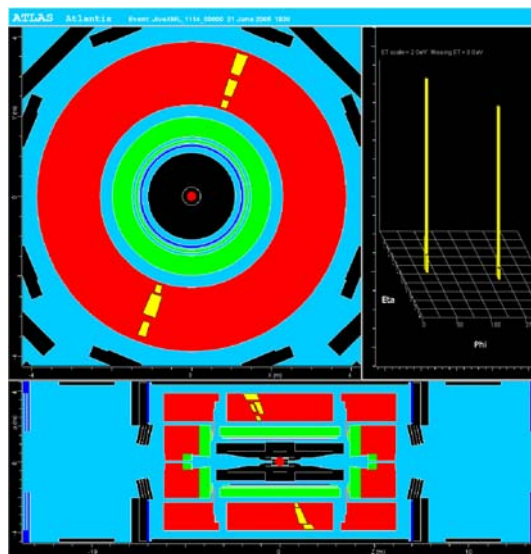


Figure 6.1: First “data” in the LHC recorded by the ATLAS Tile Calorimeter [89].

The ATLAS detector has been undergoing an extensive period of in-situ commissioning, including a series of cosmic ray runs which began in June 21, 2005 [87] [88], and continued in 2006-2008, in preparation for the first LHC beam in September 2008. Tile-Cal was the first sub-detector to be included in ATLAS, and took the “first data” in the LHC [89] (Figure 6.1).

The data from these runs allowed us to understand and to have an overall view of the detector conditions, and also formed a useful training ground to validate the ATLAS offline software algorithms and study reconstructed objects such as calorimeter cells, clusters, jets, E_T^{miss} , and tracks from inner detector and muon spectrometers.

Since December 2006, combined cosmic runs so called “Milestone Weeks” began which ran with various sub-detectors included in the data-taking. The objective of the Milestone

Table 6.1: ATLAS Cosmic Ray Milestone Weeks and Beyond.

| Period | Dates |
|-----------|-------------------------|
| M1 | Dec. 11 - Dec. 19, 2006 |
| M2 | Feb. 28 - Mar. 13, 2007 |
| M3 | Jun. 4 - Jun. 18, 2007 |
| M4 | Aug. 22 - Sep. 2, 2007 |
| M5 | Oct. 22 - Nov. 5, 2007 |
| M6 | Mar. 5 - Mar. 11, 2008 |
| M7 | May 13 - Jun. 3, 2008 |
| M8 | Jul. 11 - Jul. 20, 2008 |
| Fall 2008 | Sep. 13 - Dec. 2, 2008 |

Weeks was to operate the ATLAS detector as a whole, using the sub-detector systems available during the period. Eight Milestone Weeks have undergone since then, and the number of sub-detectors were included during the data-taking has been increasing “week by week”. The last Milestone week (M8 Week) experienced the complete combined operation which all the sub-detectors were included and successfully received data. The period of Milestone Weeks is shown in Table 6.1. Even in between Milestone Week period, the data-taking has been on-going, but emphasis was on the stand-alone data taking of each sub-detector for pedestal measurement, calibration studies, and etc.

After the final Milestone week, the largest set of combined cosmic runs were recorded. Most of the analysis results shown in this thesis are from the selected runs in such “post-M8” data taking period. The integrated statistics of recorded cosmic data since September 13, 2008 is shown in Figure 6.2. In some runs, LAr was taken out, which allowed higher trigger accept rates of about 500 Hz (rises seen in Figure 6.2). More than 500 million events were recorded by ATLAS in 2008, which correspond to raw data of about 1.2 PB and derived data of about 700 TB. Runs with fairly long data taking time (more than 500,000 events) and good detector conditions were selected from September 13 to December 1, 2008, and those 127 selected cosmic runs (from run 88425 to 96982) were reconstructed from the raw data by the ATLAS production team using the Tier-1 computing facility. Of the 127 runs, 39 runs were without solenoidal and toroidal magnetic field (categorized as “data08_cos”), 21 runs were Inner Detector specific commissioning runs (“data08_idcomm”), and remaining 67 runs were combined cosmic runs with magnetic field (“data08_cosmag”). The central reprocessings occurred twice (as of May 2009). One in December 2008 and the other in March 2009. The understandings of the ATLAS detector were improved with the first reprocessed data, and the knowledge was reflected in the reconstruction algorithms, which led to the second reprocessing.

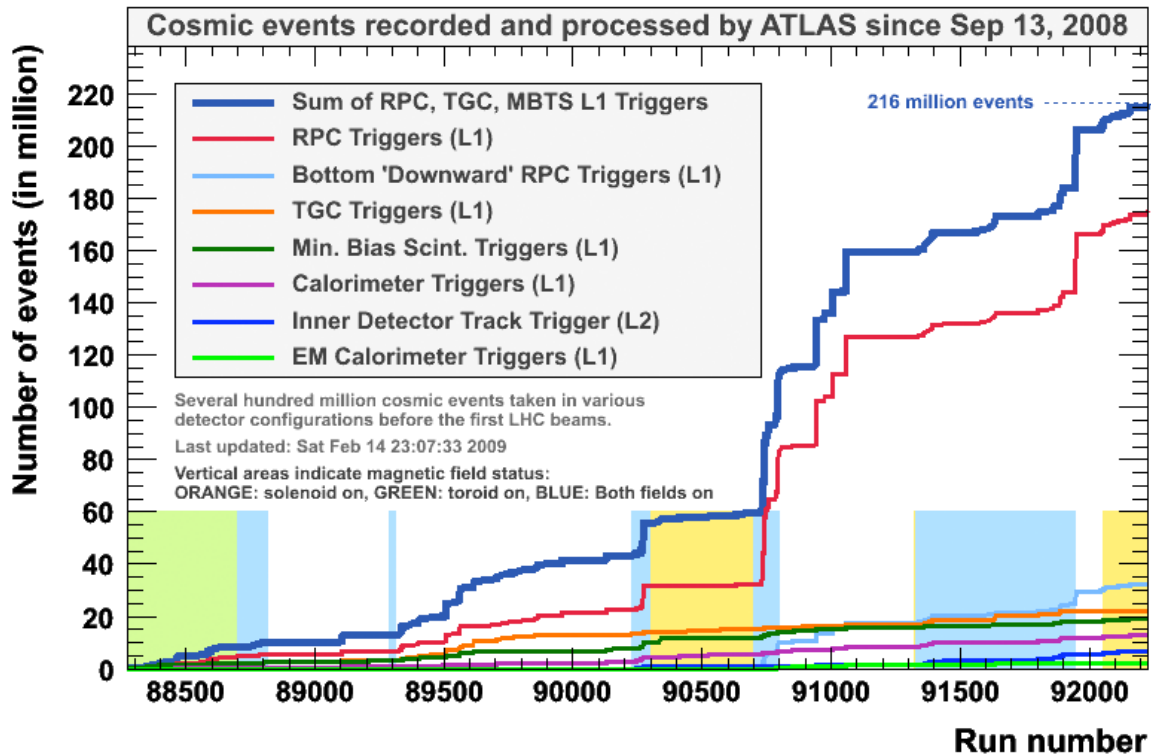


Figure 6.2: Cosmic Data recorded in the Fall of 2008.

6.2 Single Beam Runs

The historical first beam of the LHC has circulated the ring on September 10, 2008. The circulation of beams in both directions has been achieved, and many beam halo particles were recorded by the ATLAS detector. Figure 6.3 shows the first single beam data with a large “beam splash” (the proton bunch hitting the collimator before the ATLAS and originating huge numbers of particles). The single beam data taking took place from September 10 to 13. Ten single beam runs with fairly long data taking time and good detector conditions were selected and have been included in the central reprocessing mentioned in the previous section.

Due to the accident in the LHC on September 19, 2008, no more beam circulation was possible, which is mentioned in the next section. Further single beam data taking will occur in 2009, which will be followed by beam collision data takings possibly at the end of 2009.

6.3 LHC Accident

The malfunction was initially caused by a faulty electrical connection between two of the accelerator’s magnets [90]. It lead to the mechanical damage and released helium from the magnet cold mass into the LHC tunnel. No one was injured during the accident, due to the proper safety procedures.

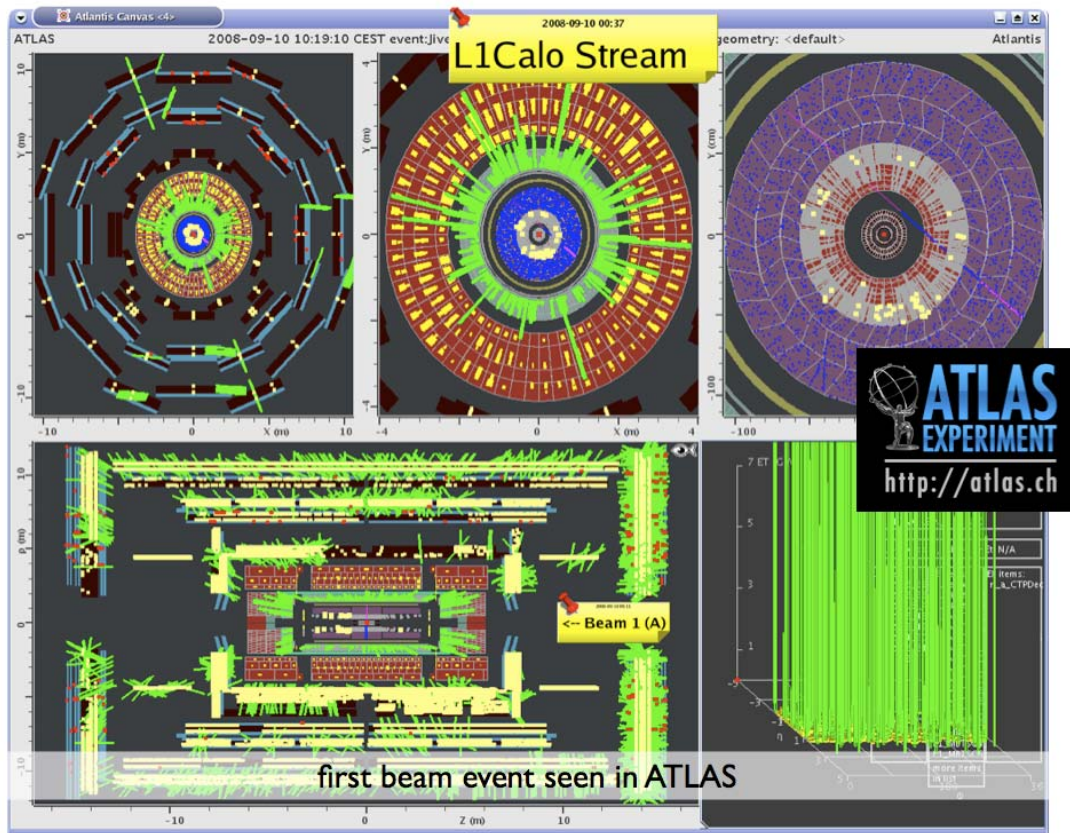


Figure 6.3: First single beam data recorded in ATLAS on September 10, 2008.

6.4 Data Streams

During the collision data takings, data will be collected in 4 event streams based on the trigger decisions. The event streaming determines the final file destination of an event, and the main motivation of the streaming is to decouple the HLT from DAQ. A single event can belong to several streams.

- Physics stream: data used for the physics analyses
- Calibration stream: data specifically used for detector calibration purposes
- Express stream: the full events with the fast reconstruction for monitoring and data quality purposes, only containing partial information
- Debug stream: events which the trigger could not make a decision due to failures in the online system

Calibration and express streams were not operating during the cosmic and single beam data taking in 2008. In this thesis, we will look into the commissioning data belong to the physics streams.

Many trigger menus which will be used during the collision data taking were validated during the cosmic commissioning. On top of the trigger validation, in order to efficiently record the cosmic muons reaching the detector, some trigger settings have changed the threshold or a part of their criteria from the standard collision settings, and there were also specific triggers for tagging cosmic muons.

6.4.1 Physics Streams during Cosmic Runs

There were 11 physics streams that operated during the post-M8 cosmic data taking: L1Calo, L1CaloEM, RPCwBeam, TGCwBeam, CosmicDownwardMuons, CosmicMuons, IDCosmic, TRTCosmic, MBTS_BCM_LUCID, RNDM and LateEvents stream. Each physics stream consists of a set of particular trigger menus (L1Calo stream consists of events triggered by the Level-1 Calorimeter, for example). There are overlaps of the same events among the physics streams.

The same physics stream names were used for the cosmic and single beam runs, but their names do not always describe the precise trigger settings actually used.

L1Calo

The L1Calo stream contains events triggered by the Level-1 Calorimeter (L1Calo; Table 6.2). The events are stored by taking the “OR” of all the L1Calo trigger bits. “L1_EM3” triggers on events with EM trigger towers passing the energy threshold of 3 GeV.

L1CaloEM

The L1CaloEM stream is a complete duplicate of the subset of the L1Calo stream, which the EM trigger towers passed the threshold.

RPCwBeam

The RPCwBeam stream stores events triggered by the RPC in filled bunches. “Beam” was meant for the coincidence with the BPTX, which was originally planned for the collision data taking, but this trigger requirement was not used during the cosmic runs.

TGCwBeam

The TGCwBeam stream contains events triggered by the TGC in-time items. The coincidence with the BPTX was not required during the cosmic runs as the RPCwBeam.

MBTS_BCM_LUCID

Only the Minimum Bias Trigger Scintillator (MBTS) is used for the cosmic runs. Events triggered by the MBTS is stored in the stream.

Table 6.2: Level-1 Calorimeter menus used in the cosmic run 90272 L1Calo stream

| Trigger Menu | Prescale | # of Events |
|--------------|----------|-------------|
| L1_EM3 | 1 | 71832 |
| L1_EM7 | 1 | 10436 |
| L1_EM10 | 1 | 6116 |
| L1_EM13 | 1 | 4150 |
| L1_EM13I | 1 | 3887 |
| L1_EM18 | 1 | 2469 |
| L1_2EM3 | 1 | 179 |
| L1_2EM7 | 1 | 42 |
| L1_2EM10 | 1 | 19 |
| L1_TAU5 | 1 | 195921 |
| L1_TAU6 | 1 | 149898 |
| L1_TAU9 | 1 | 86862 |
| L1_TAU9I | 1 | 86735 |
| L1_TAU11I | 1 | 65378 |
| L1_TAU16 | 1 | 38187 |
| L1_TAU16I | 1 | 38067 |
| L1_TAU40 | 1 | 9808 |
| L1_2TAU6 | 1 | 2000 |
| L1_2TAU9I | 1 | 856 |
| L1_EM3_BPTX | 2000 | 38 |
| L1_TAU5_BPTX | 1 | 195921 |
| L1_EM4 | 1 | 26602 |
| L1_EM7I | 1 | 10114 |

| Trigger Menu | Prescale | # of Events |
|--------------|----------|-------------|
| L1_2EM4 | 1 | 111 |
| L1_2EM7I | 1 | 30 |
| L1_J5 | 1 | 212983 |
| L1_J10 | 1 | 80734 |
| L1_J18 | 1 | 34414 |
| L1_J23 | 1 | 23954 |
| L1_J35 | 1 | 12884 |
| L1_J42 | 1 | 9698 |
| L1_J70 | 1 | 4238 |
| L1_2J5 | 1 | 2215 |
| L1_2J10 | 1 | 535 |
| L1_2J18 | 1 | 142 |
| L1_2TAU5 | 1 | 2945 |
| L1_2TAU9 | 1 | 868 |
| L1_FJ18 | 1 | 3 |
| L1_FJ3 | 1 | 2002 |
| L1_2FJ18 | 1 | 0 |
| L1_2FJ3 | 1 | 0 |
| L1_3J10 | 1 | 14 |
| L1_XE20 | 1 | 29321 |
| L1_JE120 | 1 | 0 |
| L1_JE340 | 1 | 0 |

RNDM

RNDM stream exploits the random trigger which fires in accordance with the Central Trigger Processor (CTP) clock. It was called RNDM0 stream during Milestone Weeks. The CTP clock can be synchronized to the LHC clock, or otherwise to an internal source in ATLAS. The random trigger rate can be parameterized from 40 MHz or less. During the cosmic data taking, the events were randomly triggered in about 1 Hz with a prescale of about 78400.

CosmicMuons

Events triggered by the RPC and TGC Level-1 logic with looser requirements on the coincidence than the configurations used for the collision data taking. No coincidence is required with the beam specific triggers such as BPTX.

CosmicDownwardMuons

This stream has events streamed with level-1 RPC or TGC RoI in the bottom sector of the detector.

IDCosmic

Inner Detector tracking is performed at the Level-2 trigger level on all the physics Level-1 triggered events. Only Level-1 physics triggered events with ID segments are recorded in this stream. The implementation of inner detector HLT allowed for storing cosmic events passing the inner detector with high statistics.

TRTCosmic

This stream exploits the Transition Radiation Tracker (TRT) Level-1 trigger [91] specifically developed for the cosmic data taking. The trigger was used at the end of November 2008 for the first time. It makes use of the TRT high threshold (HT) hits. This trigger operate only during the commissioning, and during the collision data taking, it will be exploited for other purposes.

LateEvents

The LateEvents stream was recorded only for run 89507 among the Tier-1 reprocessed data. This stream stores events which arrived at the SFO's after the luminosity block is closed.

6.4.2 Physics Streams during Single Beam Runs

There were 4 physics trigger streams that operated during the single beam data taking: BPTX, L1Calo, MBTS_BCM_LUCID, and RNDM stream.

BPTX

Events triggered by beam pick-up items.

L1Calo

The same as in the cosmic runs.

MBTS_BCM_LUCID

Events triggered by the MBTS, BCM or LUCID. A huge fraction of the events are coming from the MBTS.

RNDM

The same configuration as the cosmic RNDM stream.

6.5 Runs Used in the Analyses

Out of various physics streams mentioned in the previous section, analyses were mainly concentrated on RNDM and L1Calo stream. The analyses with RNDM stream data allow us to understand the electronic noise and problematic channels, and are mentioned in the next chapter. All the 90 runs from Fall'08 data with the RNDM stream were used in the analyses. Chapter 8 shows results of cosmic measurement with the calorimeters. The L1Calo stream records cosmic events with large energy deposit in the calorimeters, and allow us to validate the detector systems, and also to understand the rate and effects from the high energy cosmic muons.

Chapter 7

Calorimeter Measurement with Random Stream Data

By measuring the energy distributions of calorimeter cells in dedicated pedestal runs and random stream data, and calculating the Root-Mean-Square (RMS) of the energy distribution, we can determine the electronic noise at the cell-level (and also at the PMT channel-level for TileCal). The electronic noise will set the minimum detectable signal and the limitation on the energy and time resolution.

Due to the large dynamic range and the adoption of multi-gain systems in the calorimeters (i.e. each signal is split into three gain scales in the ratio of 1/10/100 for LAr, and two gain scales in the ratio of 1/64 for TileCal; see Section 5.2 and 5.3), the electronic noise must be well understood and kept under control, especially in the LAr EM calorimeter, to meet the high precision requirements from Higgs analyses using electrons ($H \rightarrow ZZ \rightarrow 4e$) and photons ($H \rightarrow \gamma\gamma$). The noise-level in the calorimeters is considered and treated during the reconstruction of calorimeter objects (e.g. clusters, jets, and E_T^{miss}), thus it must be correctly measured and stored in the ATLAS database. Any mis-consideration of the noise-level in the database can deteriorate the noise suppression and performance of the calorimeter objects; especially the energy resolution.

The noise measurement has previously been performed with the testbeam data in 2000-2003 [93]-[95], but here, the first in-situ noise measurement of calorimeter cells using the random stream data is shown [A.3.4.15] [96] ([A.3.4.15] indicates the 15th presentation mentioned in Appendix A.3.4).

On top of the noise measurements, effects of problematic channels in the calorimeters were investigated. A phenomenological approach to search the bad channels were proposed for the TileCal. It is of vast important to identify the bad channels, understand their effects on the performance, and to develop strategies to cope with the effects.

At the final sections, the performance of calorimeter clusters and E_T^{miss} is validated with the data, and proposals on the updates of cluster algorithm to take care of the actual noise feature and the improvements observed after adopting the new algorithm are shown.

Investigations of random-stream data, and validation of offline reconstruction with the data will be an important first step towards the physics analyses with the collision

data to come.

7.1 Noise in the Calorimeters

For the energy reconstruction in the ATLAS calorimeters, several kinds of noise arise.

Electronic noise is due to the fluctuation of the baseline. Basically, two mechanisms contribute to the electronic noise; velocity and number fluctuations of electric currents [102]. The former effect originates from the thermal motion. Each electron has a random velocity fluctuation around the average drift velocity due to thermal excitation. The number fluctuations can occur due to a potential barrier for the emission of carriers, or by the trapping of carriers during the current flow. Due to the large dynamic range (and thus multiple gains used in the energy reconstruction) of the ATLAS calorimeters (from a few tens of MeV to about 3 TeV), the electronic noise should be kept as low as possible.

Other than the noise originating from such detector characteristics, there is another contribution which must be considered during the high luminosity operations. It is the pile-up noise coming from the overlaps of soft proton-proton collision products (Minimum Bias events) during such high-luminosity data takings. At the design luminosity of $10^{34} \text{ cm}^{-2}\text{s}^{-1}$ and the center-of-mass energy of 14 TeV, an average number of 23 Minimum Bias events are expected in a single bunch crossing (every 25 ns).

To suppress electronic noise, longer shaping time of signals are preferred, but on the other hand, shorter shaping time is preferred to decrease the contamination of pile-ups (Figure 7.1). The time constant is chosen to compromise the effects and minimize the overall noise (e.g. 15 ns for the LAr calorimeters and 50 ns for the TileCal). The expected electronic noise and total noise during the design luminosity data taking are shown in Figure 7.2.

With the current commissioning data, only the electronic noise can be measured, since there were no collisions (as of September 2009; the first collision took place on November 23, 2009). Minimum Bias events in the early collision running will provide useful information to estimate the pile-up noise during the collision data-taking.

7.1.1 Electronic Noise in TileCal

The Tile Calorimeter (TileCal) is instrumented with approximately 10,000 PMT's (channels), with two PMT's reading out each cell, giving about 5000 cells. The TileCal is divided into a Long-Barrel (LB) cylinder and two Extended-Barrel (EB) cylinders as mentioned in Chapter 4, and each cylinder consists of 64 modules in ϕ , with three longitudinal sampling depths (A, BC, D). The long barrel is divided into two logical partitions (LBA, LBC), and the front-end electronics in each module are referred to as "drawers". Figure 7.3 shows the geometry and definitions of cells and PMT's in a drawer from each partition. In order to cover a large dynamic range (~ 20 MeV to ~ 1.3 TeV in a single cell), bi-gain system is adopted. Those gains are called the low and high gain, with the relative amplification difference of a factor 64. The transition from the high to low gain is around 20 GeV in a PMT.

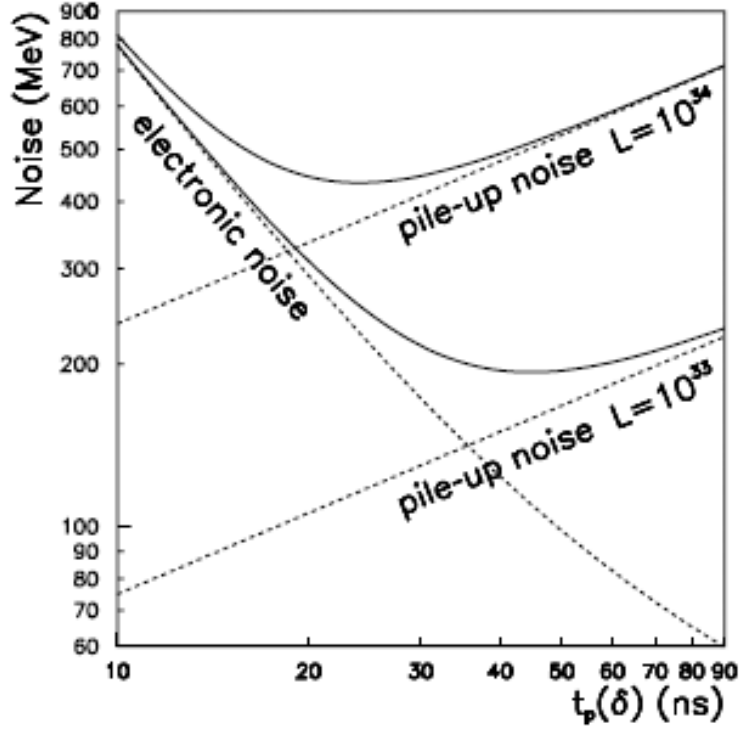


Figure 7.1: Contribution of electronic, pile-up and total noise to an electromagnetic shower at $\eta = 0$ at low and high luminosity [51].

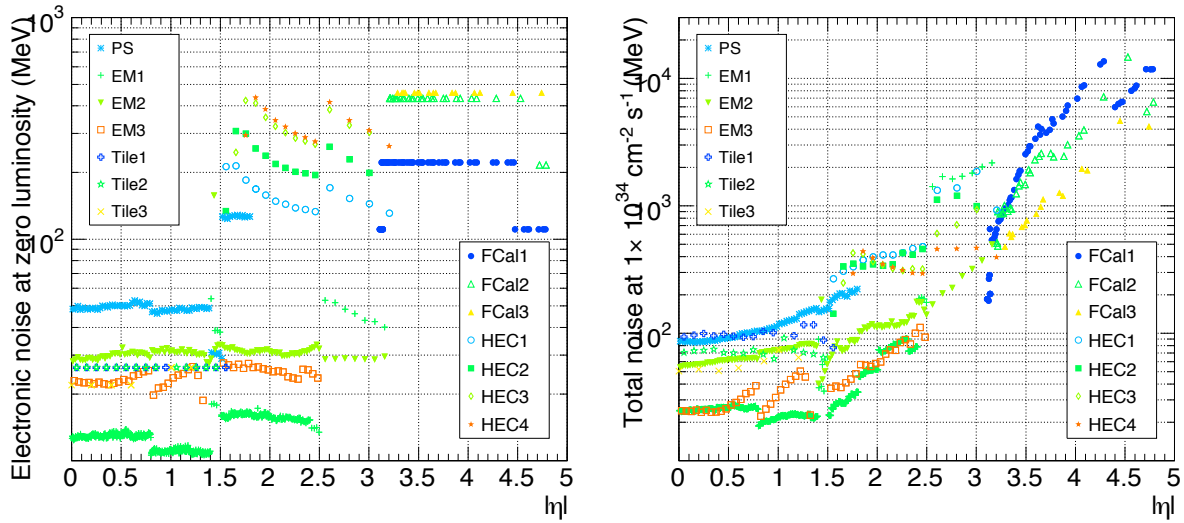


Figure 7.2: Electronic noise of the calorimeters at the cell-level (left) and total noise with pile-up effects at the design luminosity of $10^{34} \text{cm}^{-2} \text{s}^{-1}$ (right) as a function of pseudorapidity (η) [92].

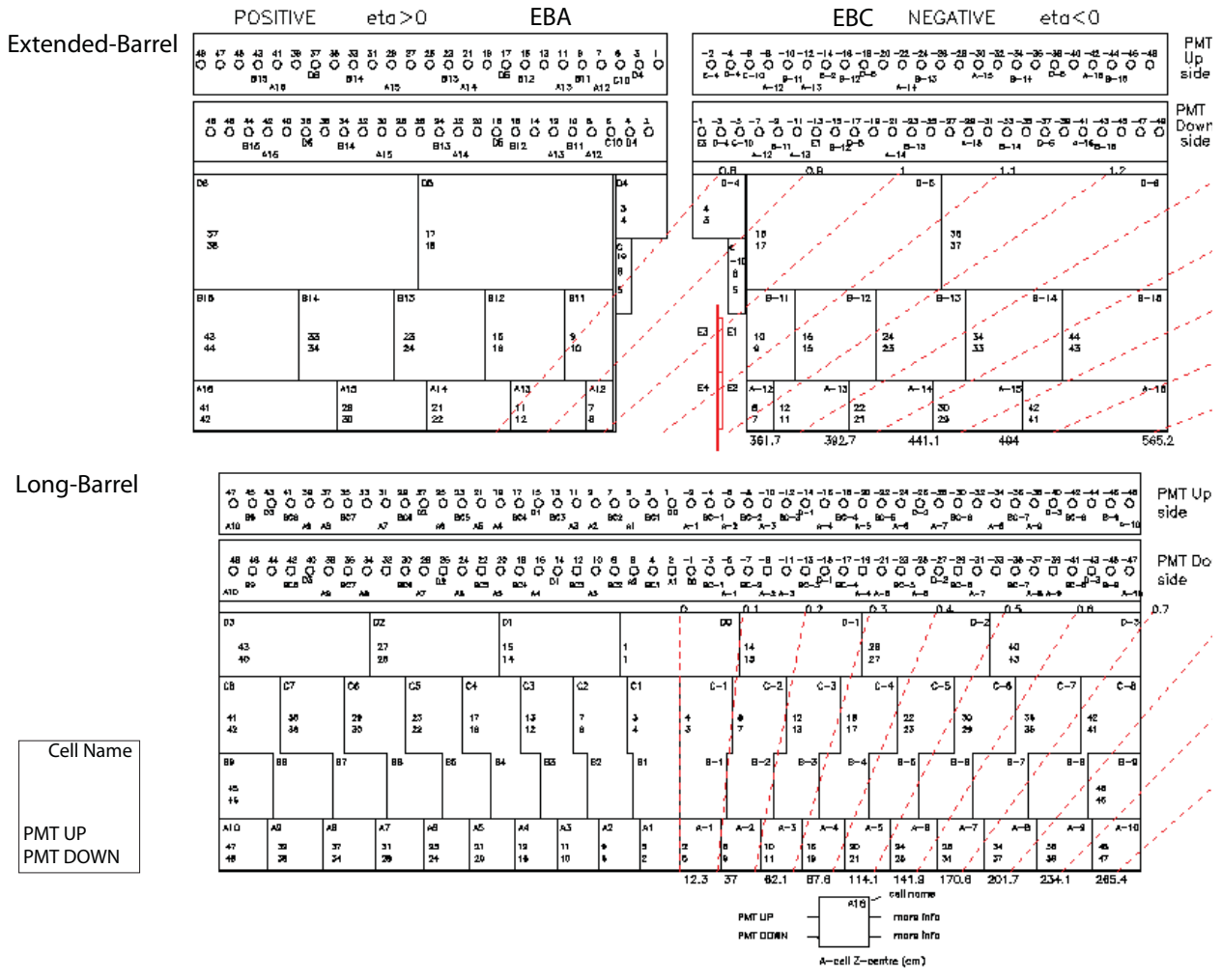


Figure 7.3: Definition of cells in the Tile calorimeter. The rectangles indicate the cells, cell names are shown inside the region (e.g. A-1), and two numbers are the PMT numbers (e.g. 2, 3).

The Milestone Weeks were the transition era of the data format from the TileCal-specific ntuples to the ones from the central reconstruction software (“RecExCommission” package, afterward merged with “RecExCommon” package in the Athena framework). Measurement of the random stream data were preceded by the validation of the reconstruction software and the ATLAS database [A.3.4.18]. The plots shown here are from the condition after the update was made.

The electronic noise in TileCal consists of contributions from the electronics and the power supplies. The intensity of dark current in the PMT’s is low (lower than 100 pA at the nominal gain [61]) and has negligible effects in the energy reconstruction. The main contributions from the electronics are from the front-end electronics. The noise from the low voltage power supplies also has perceptible effects, and will be mentioned again in the following text.

Figure 7.4 shows the electronic noise in the TileCal Long-Barrel ($0 < |\eta| < 1$) at the cell-level as a function of pseudorapidity (η) and sampling depth. This was the first in-situ measurement of the electronic noise of the TileCal[A.3.4.15]-[A.3.4.28]. The left plot indicates the noise levels used in the current Monte Carlo simulation, while the center and right plots give the noise values measured from a cosmic run (run 29576 during the M5 Week in the fall of 2007), averaged over all the TileCal modules in ϕ . The Extended-Barrels ($0.8 < |\eta| < 1.7$) were not operating during the M5 Week. In the center plot, noise values are derived from the width of a Gaussian, fitted iteratively over a 2σ range. The right plot shows the noise values defined as the Root Mean Square (RMS) of the cell energy distributions. Two features were observed, which were not expected and treated in the Monte Carlo simulation. One is the η -dependence of the electronic noise. The other feature is the non-Gaussian structure of the noise, which obviously shows up in the energy distributions of cells especially in larger pseudorapidity regions (Figure 7.5) and also in the difference between the σ from a Gaussian fit and the Root-Mean-Square (RMS) of the cell energy distribution. These features have continuously been observed in-situ since the M5 Week, throughout the following Milestone Weeks and Fall 2008 cosmic data. Although these effects are at the level of only 10 - 30 MeV per cell compared to a flat distribution, and are not problematic as long as the correct noise values are stored in the ATLAS database, we further investigated to nail down the cause of such phenomenon. We will also mention the current status of the TileCal detector.

The main origin of the non-Gaussian tail can be ascribed to the low voltage power supply (Figure 7.6). The low voltage power supply is contained in a small closed volume known as a “finger”. A significant increase of non-Gaussian tails in the pedestals were observed in January 2006 [98] when the low voltage power supply was changed from commercial power supply to the finger power supply (Figure 7.7). The migration of the low voltage power supply was mandate in order to operate the TileCal at Point 1, where very limited space is available.

In order to suppress common mode noise coming from the power supply, chokes were implemented on the DC/DC converter outputs. Sizable chokes will mostly eliminate such common mode, but only limited space is available in the finger power supply. In order to cope with the space limitation, ferrite chokes were adopted and used. The non-Gaussian

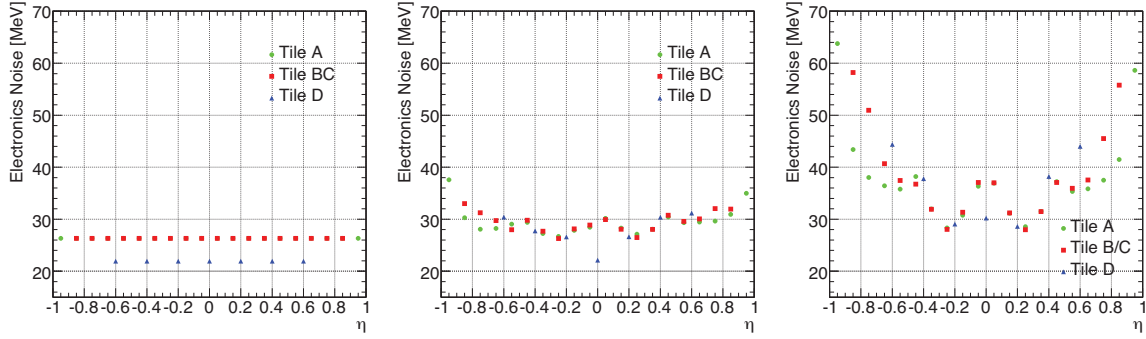


Figure 7.4: Electronic noise in the TileCal Barrel at the cell-level as a function of pseudorapidity (η) and sampling depth (A, BC, D). The left plot gives the noise levels in Monte Carlo simulation, while the center and right plots give the noise values measured from a cosmic ray run in 2008 (M5 run 29576) from a Gaussian fit (center) and the RMS (right).

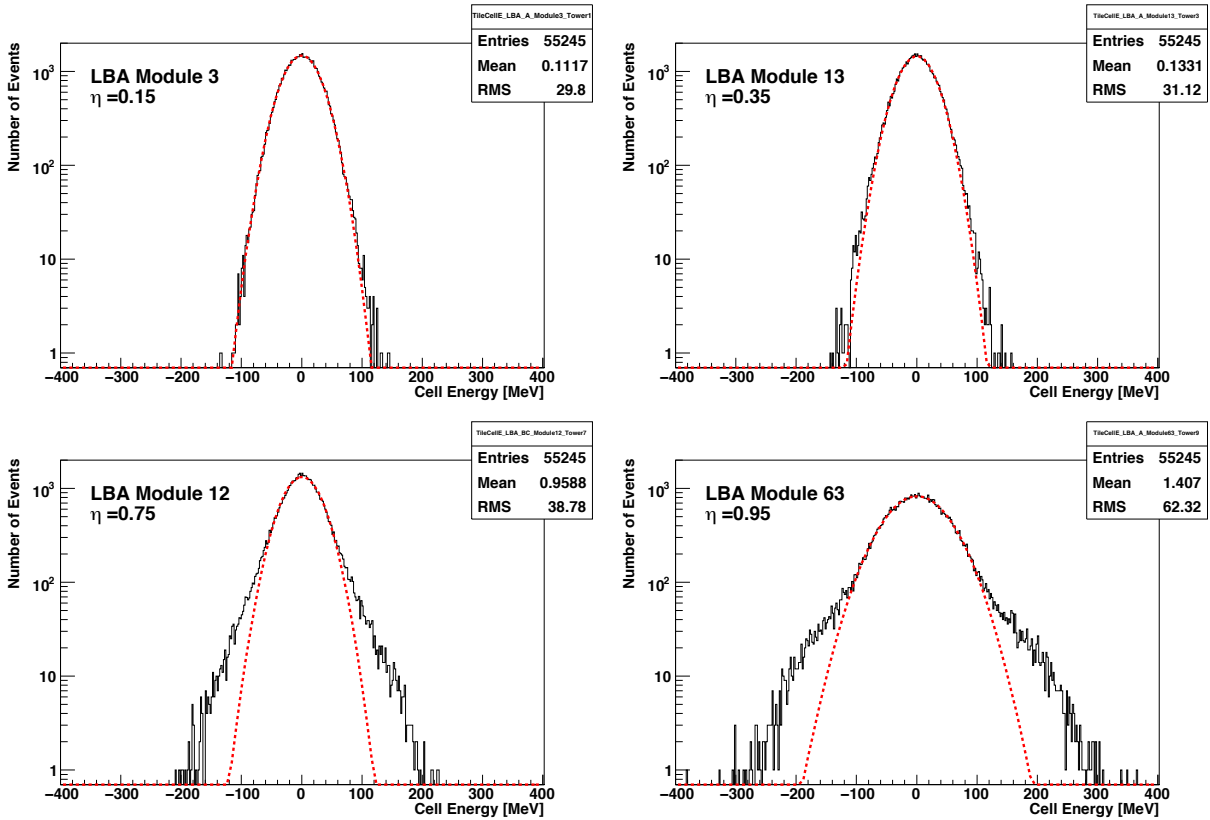


Figure 7.5: Energy distribution of TileCal cells. Non-Gaussian tails are obvious from the cell distribution in high η .

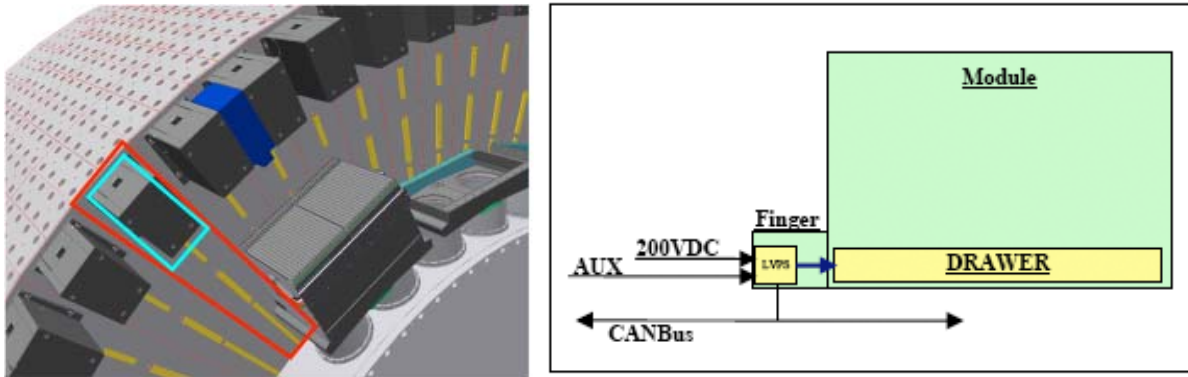


Figure 7.6: Tile Calorimeter power distributions. The left figure shows the location of the finger low voltage power supply (the red box indicates a single TileCal module and the light blue box indicates the finger), and the right figure shows the overall scheme of the power distribution [97].

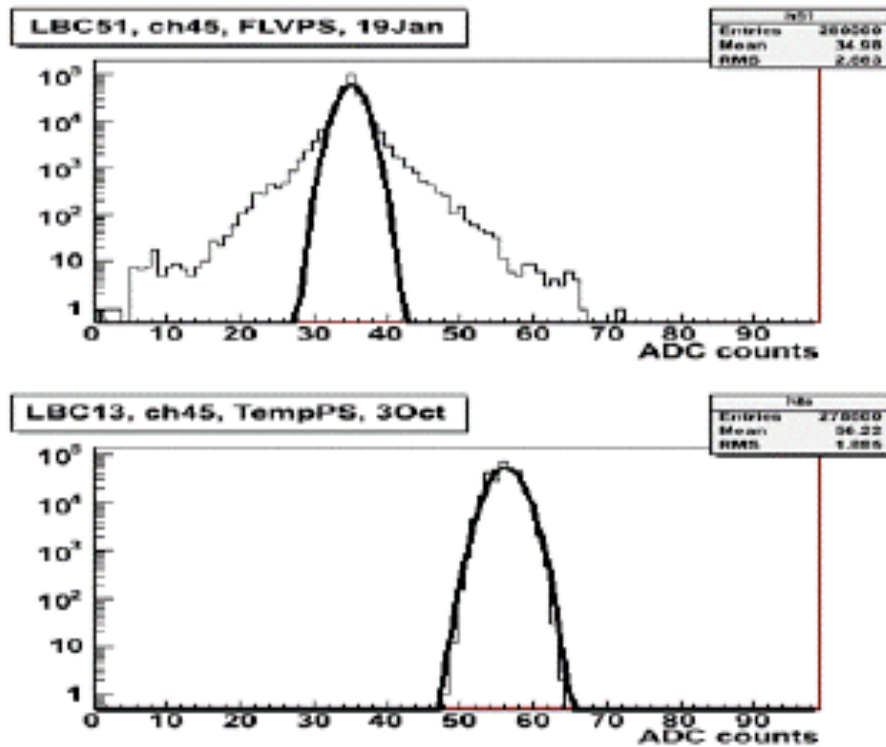


Figure 7.7: Non Gaussian distribution of TileCal pedestal after migrating into finger low voltage power supply (top) and before the migration using commercial power supply (bottom) [97].

tails were fairly reduced [97], but the still-remaining feature was what we observed during the in-situ measurement.

Recently, large component of the non-Gaussian tails were found to be related to the noise correlation among channels in the same drawer [104][105]. Figure 7.8 shows the correlation coefficients of PMT noise in LBA Drawer 16. The correlation coefficients of two PMT's $c_{i,j}(i, j: \text{PMT numbers})$ were calculated from the digitized outputs (seven samplings; digitized every 25 ns) of the PMT's (A_i, A_j) by

$$\begin{aligned} c_{i,j} &= \frac{\text{cov}(A_i, A_j)}{\sigma_{A_i} \sigma_{A_j}} \\ &= \frac{\text{cov}(A_i, A_j)}{\sqrt{\langle (A_i - \langle A_i \rangle)^2 \rangle} \sqrt{\langle (A_j - \langle A_j \rangle)^2 \rangle}}, \end{aligned} \quad (7.1)$$

where $\text{cov}(A_i, A_j)$ is the covariance of the two variables (A_i, A_j),

$$\text{cov}(A_i, A_j) = \langle A_i A_j \rangle - \langle A_i \rangle \langle A_j \rangle, \quad (7.2)$$

and

$$\langle A_i A_j \rangle = \frac{1}{N_{\text{sample}} N_{\text{event}}} \sum_{s=1}^{N_{\text{sample}}} \sum_{n=1}^{N_{\text{event}}} A_i^{(s,n)} A_j^{(s,n)}, \quad (7.3)$$

$$\langle A_i \rangle = \frac{1}{N_{\text{sample}} N_{\text{event}}} \sum_{s=1}^{N_{\text{sample}}} \sum_{n=1}^{N_{\text{event}}} A_i^{(s,n)}. \quad (7.4)$$

where N_{sample} is the number of samplings ($=7$ for TileCal), N_{event} is the number of events in the data, and $A_i^{(s,n)}$ indicates the output of PMT i in the s -th sampling and n -th event.

Local structures were observed in the correlation, which fairly match with the motherboard and digitizer configuration; 12 (6) out of 48 channels in a drawer share the same motherboard (digitizer). The amount of coherence and the feature of local structures slightly vary from drawer to drawer, but basically has the same tendency.

The non-Gaussian tails of the channel energy distribution can be reduced with offline energy correction using linear functions to ravel and reduce the correlation effects [104] or common-mode suppression [105]. However, the non-negligible amount of non-Gaussian tails remain, and can affect the performance of the calorimeter objects (clusters, jets and $E_{\text{T}}^{\text{miss}}$). We will further look into this issue and propose a strategy to cope it in Section 7.3.3 and 7.4.

The correlation of electronic noise among the different drawers were shown in Figure 7.9. The correlation coefficients are calculated as the same way as equation (7.1), except that i and j are now drawer numbers (1~64). The correlation was calculated between the PMT's with the same number (the same η) in two drawers. The correlation of noise between the drawers was very small and almost negligible. However, small inter-drawer correlations were observed for some PMT's (especially in the low gain).

The overall performance from RNDM stream data taken in the fall of 2008 is shown in Figure 7.10 and 7.11.

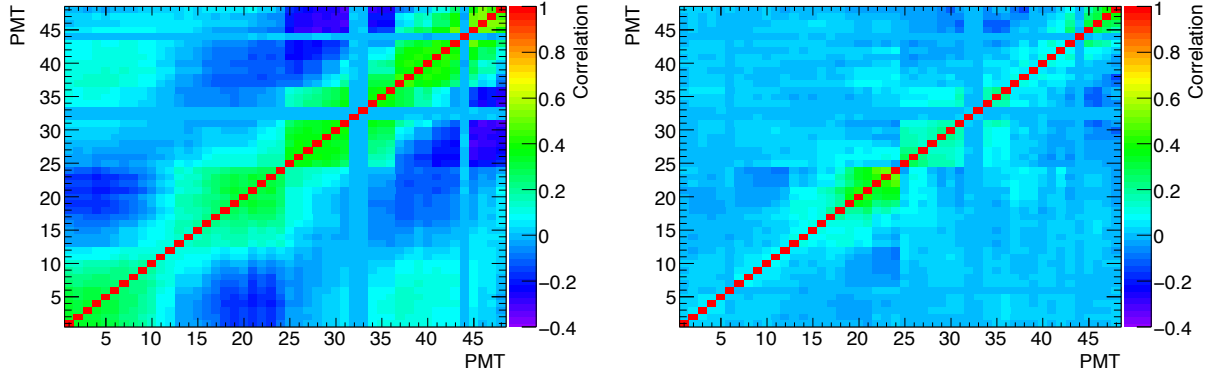


Figure 7.8: Correlation of electronic noise in TileCal LBA Drawer 16 for the high gain (left) and low gain (right).

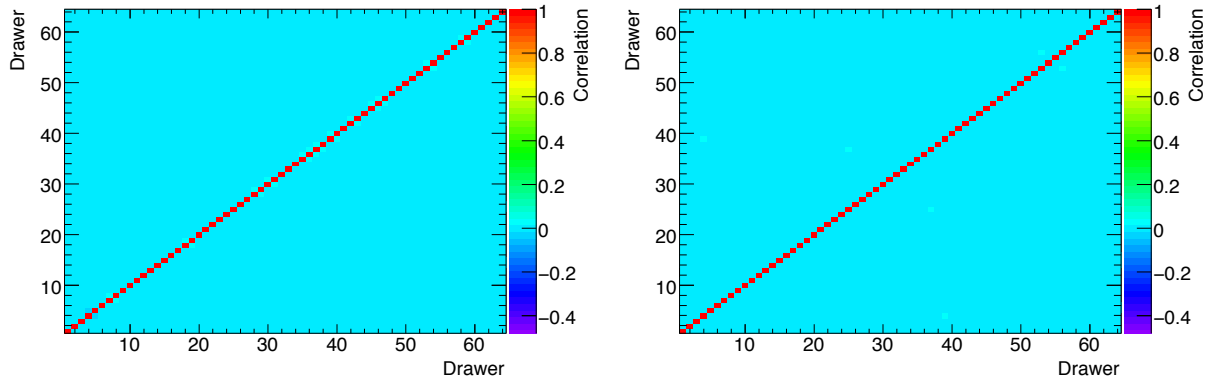


Figure 7.9: Correlation of electronic noise among the drawers in TileCal PMT1 in LBA for the high gain (left) and low gain (right).

The stability of the electronic noise throughout the commissioning runs in the Fall 2008 was also investigated (Figure 7.12 and 7.13). Figure 7.12 shows the mean energy (black circle) and the mean of the Gaussian fitted iteratively between $\pm 2\sigma$ range (black inverted triangle) of the TileCal cell energy distribution for each partition. The discrepancy of the two “means” is due to the asymmetric non-Gaussian tails of the cell energy distribution, and thus the mean of the Gaussian better represent the pedestal values. The pedestal shifts were below 0.2 MeV (about 0.01 ADC counts), and its stability was very good over a few months of cosmic data taking. Figure 7.13 shows the stability of electronic noise of cells for each partition. The stability of the electronic noise was basically within 1 %, which assures the use of fixed noise database throughout some period of time. Of course, the electronic noise level is monitored throughout the whole data taking, and any variation in the performance will be identified and considered in the offline data analyses.

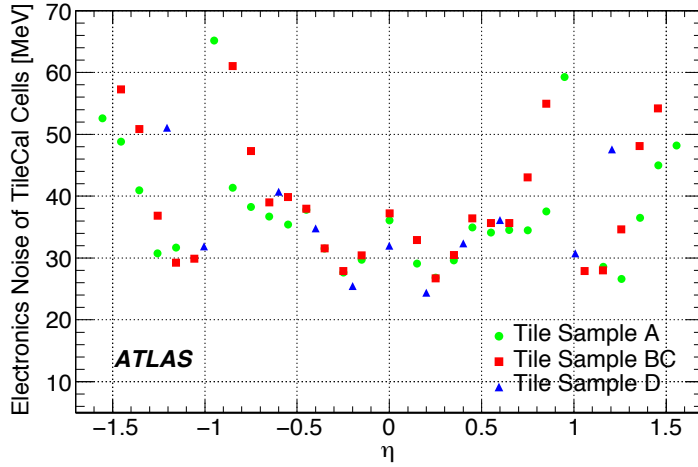


Figure 7.10: Electronic noise of the TileCal cells from Fall 2008 run 90272 RNDM stream data.

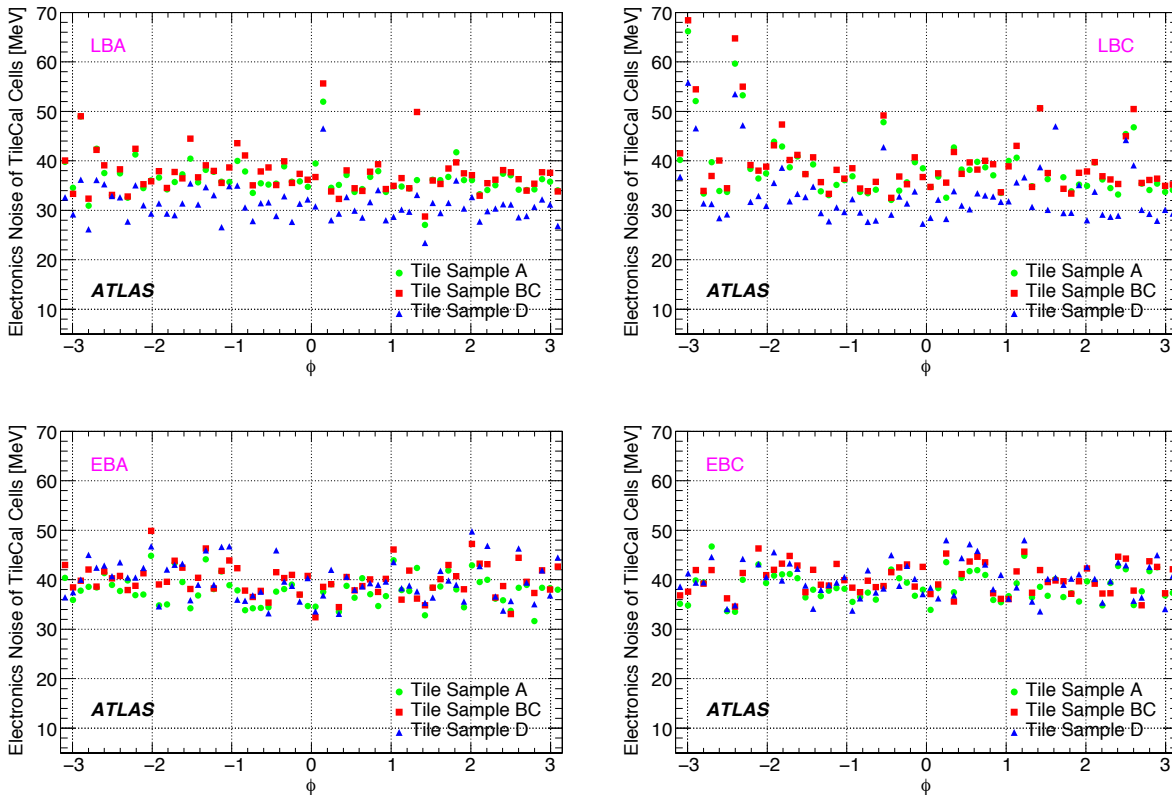


Figure 7.11: Electronic noise of the TileCal cells in each partition from Fall 2008 run 90272 RNDM stream data.

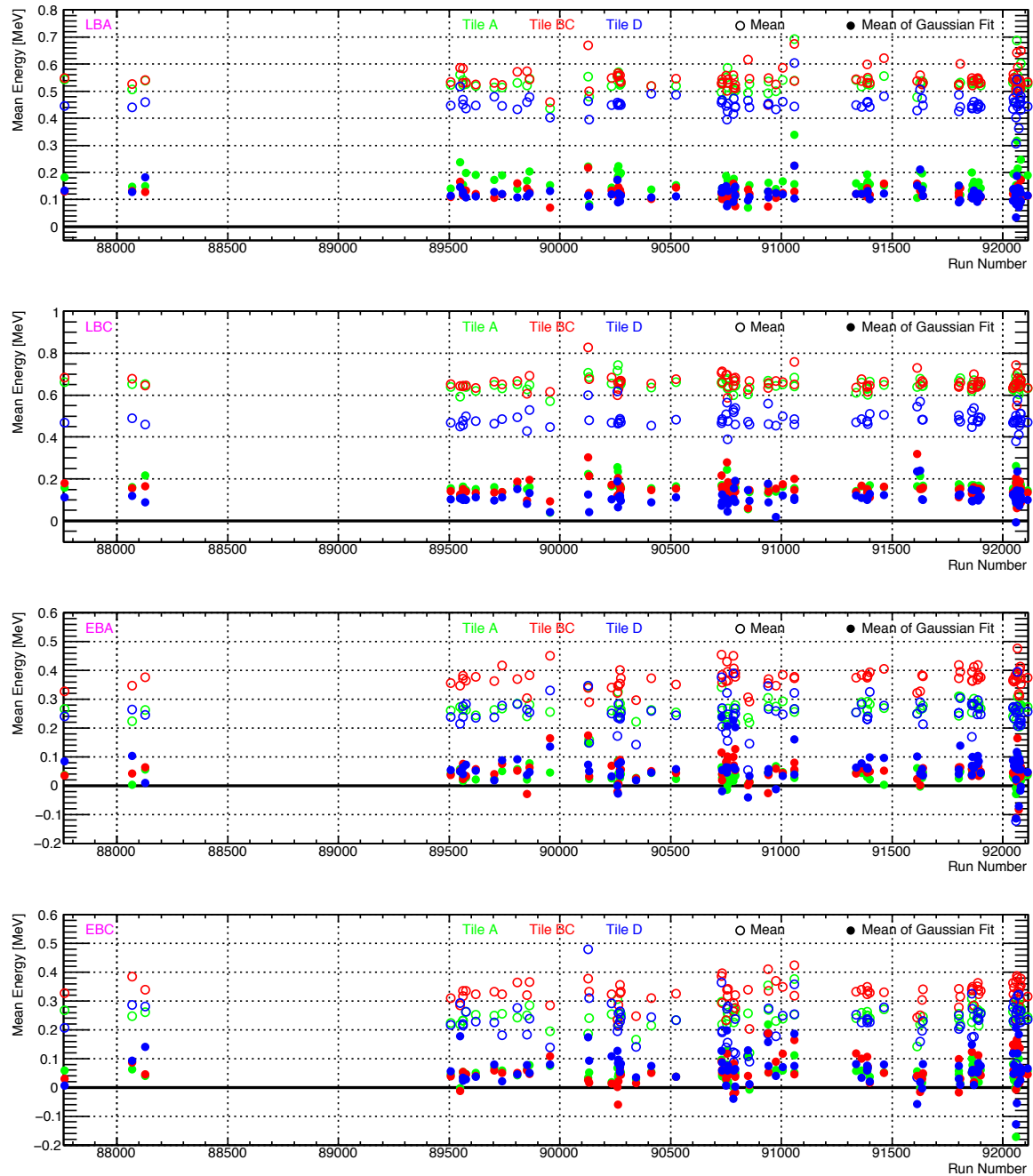


Figure 7.12: Stability of the pedestals of the TileCal in Fall 2008 runs. The pedestal stability is shown for each sampling layer in each partition. Open circular points indicate the mean of the cell energy distributions, and the solid circular points indicate the mean from the Gaussian fits.

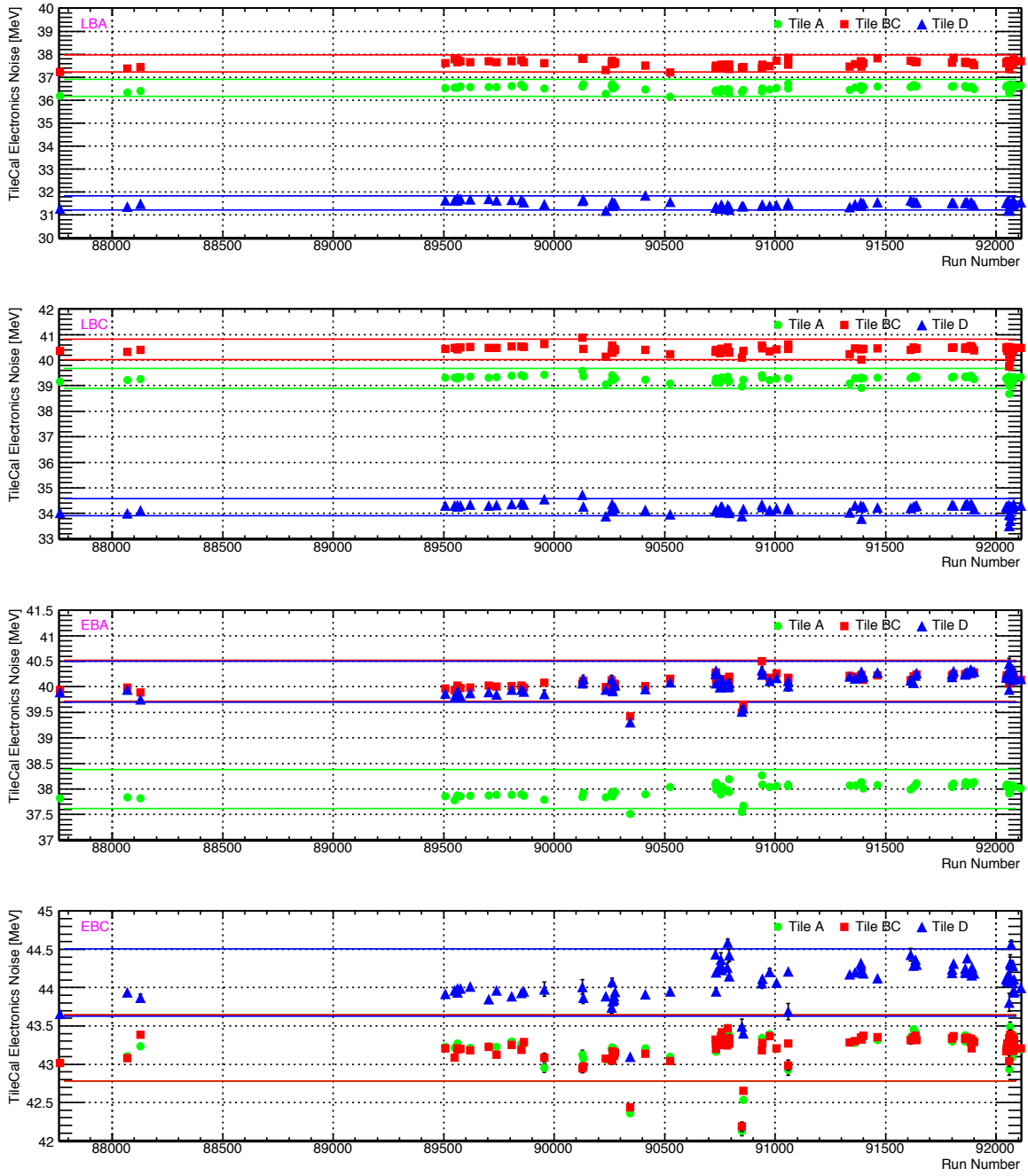


Figure 7.13: Stability of the Electronic noise of the TileCal in Fall 2008 runs. The noise stability is shown for each sampling layer in each partition. Lines indicate $\pm 1\%$ from the mean values.

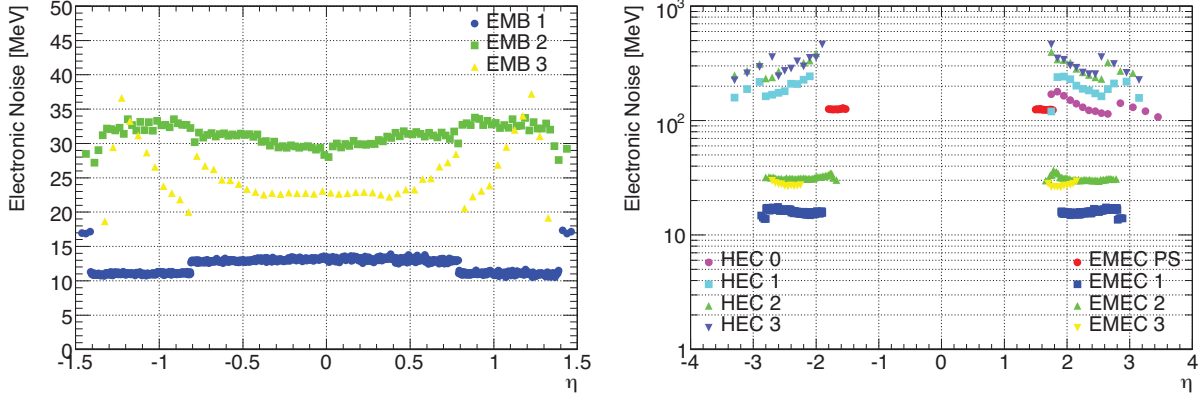


Figure 7.14: Electronic noise of the LAr Calorimeter at the cell-level as a function of η for the LAr barrel (left) and LAr end-cap (right), measured in-situ from M5 run 29576.

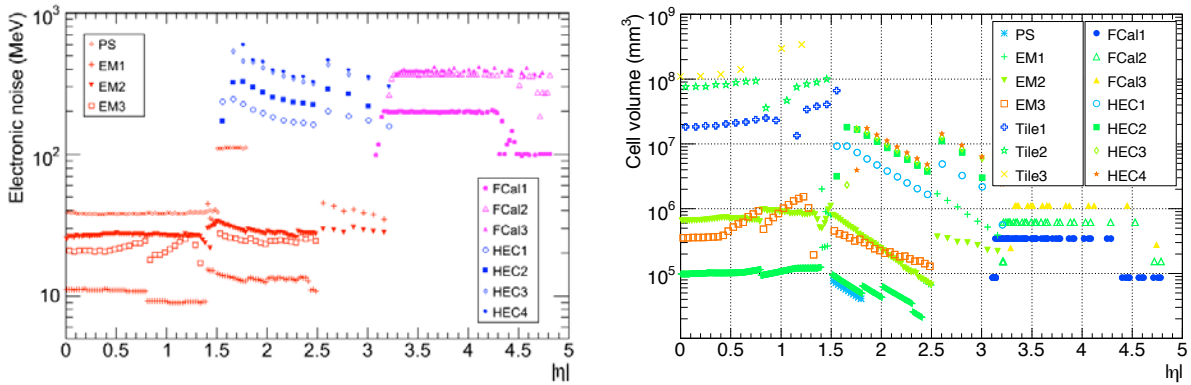


Figure 7.15: Electronic noise in Fall 2008 [106] (left) and volume of calorimeter cells in LAr as a function of η . Volume of calorimeter cells as a function of η [92] (right).

7.1.2 Electronic Noise in LAr

The LAr EM calorimeter has the most stringent requirement on the electronic noise, since the energy resolution of electrons and photons directly affect the reconstruction of the invariant mass of Higgs bosons decaying into electrons ($H \rightarrow ZZ \rightarrow 4e$) or photons ($H \rightarrow \gamma\gamma$). The coherent noise should also be suppressed as much as possible, especially due to the fact that significant number of channels exist in the LAr EM calorimeter (about 180,000 channels). Even a small amount of coherence can severely deteriorate the performance of E_T^{miss} , thus it is required to be less than 3 MeV per channel [58]. This also sets a limit to the tolerable level of pedestal shifts per channel.

Electronic noise in the Liquid Argon calorimeter (LAr) was measured in-situ for the first time with M5 run 29576 [A.3.4.19]. Figure 7.14 gives the values of the electronic noise in LAr at the cell level. The electronic noise in LAr is roughly proportional to the cell volume as previously mentioned, as shown in Figure 7.14 and 7.15 [112]. The electronic noise simulated in Monte Carlo for LAr (Figure 7.15) [111] is basically found

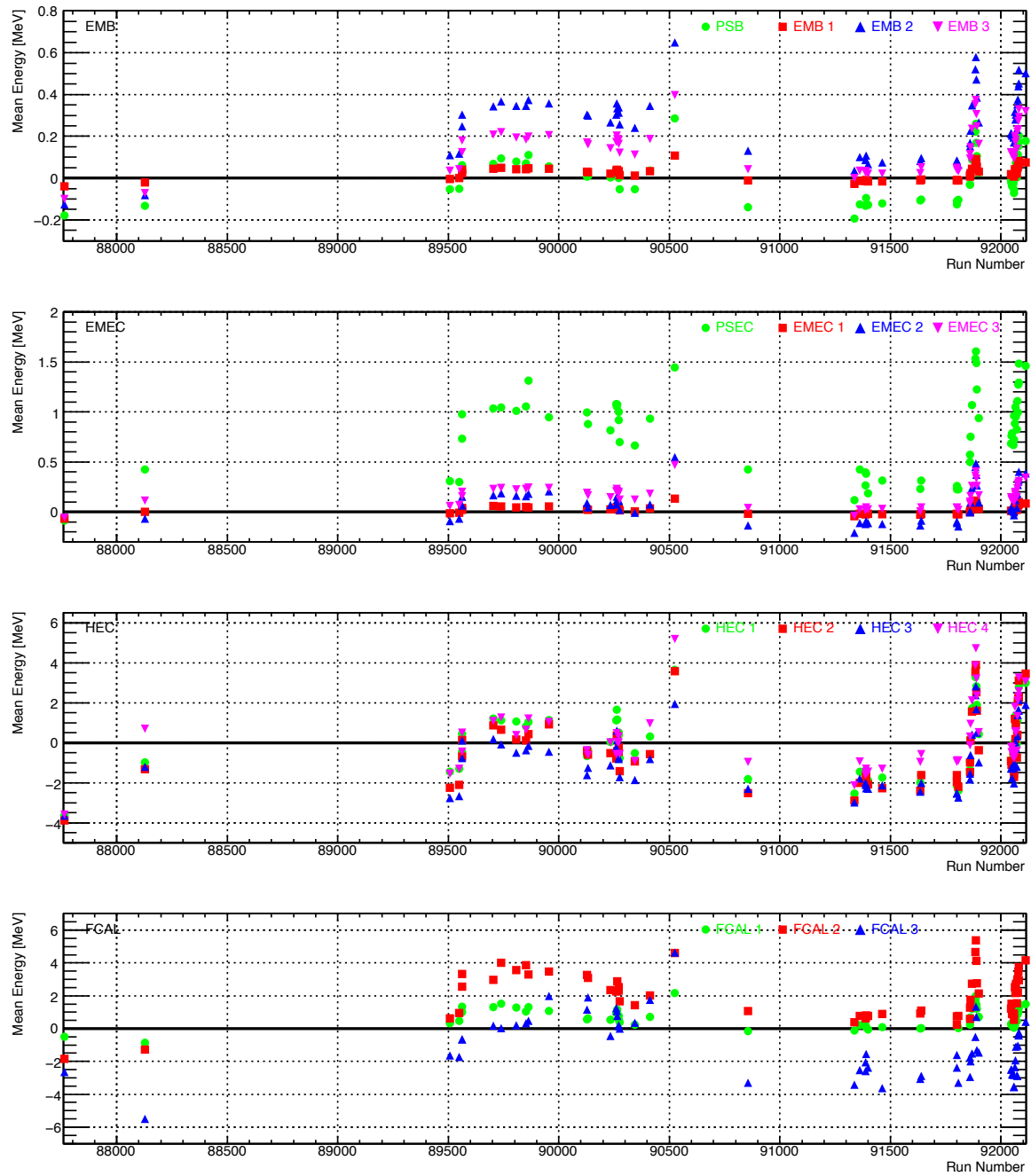


Figure 7.16: Stability of the pedestals of the Liquid Argon Calorimeter in Fall 2008 runs is shown for each sampling layer in each region.

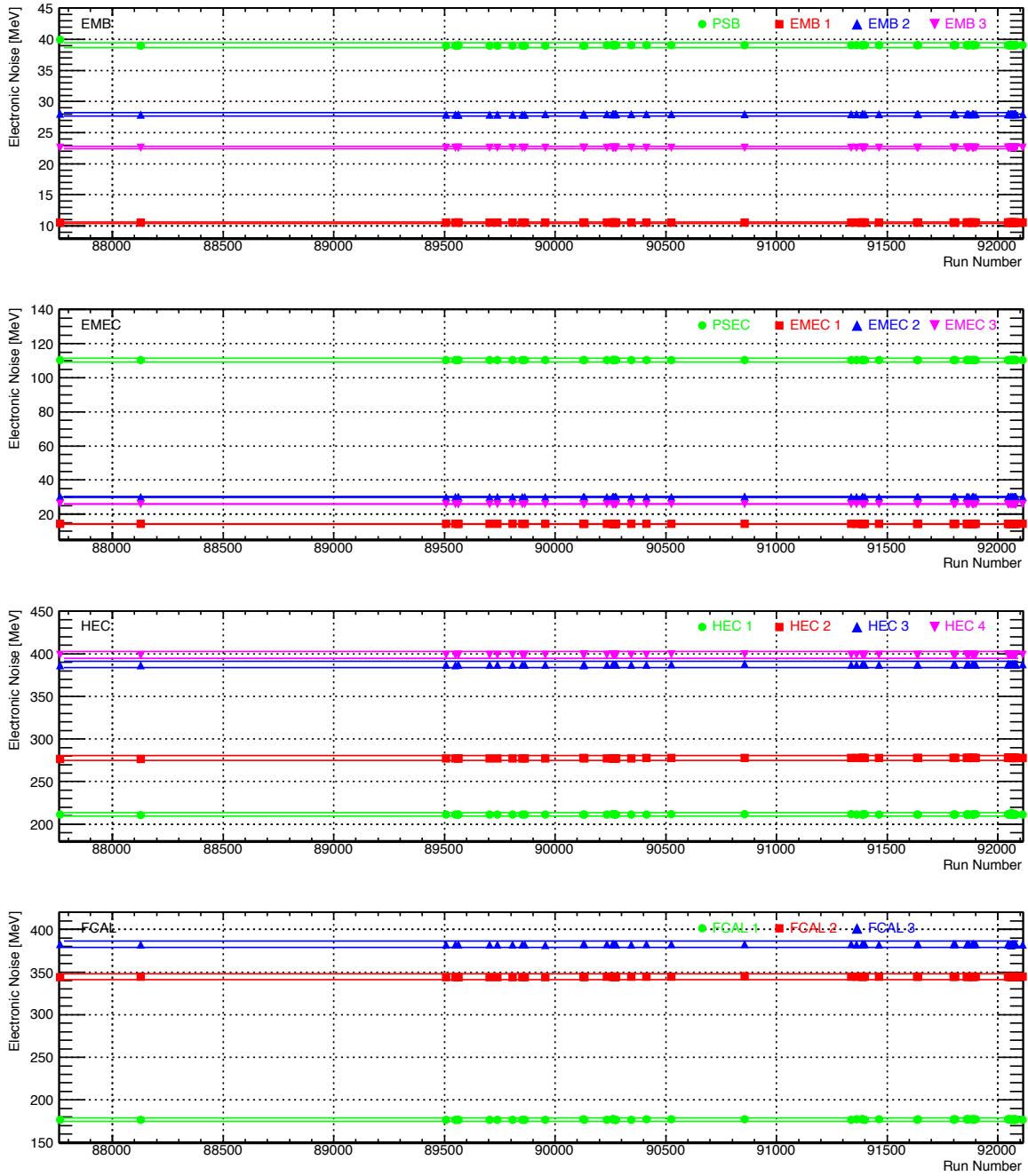


Figure 7.17: Stability of the electronic noise of the Liquid Argon Calorimeter in Fall 2008 runs is shown for each sampling layer in each region. Lines indicate $\pm 1\%$ from the mean values.

to be consistent with that measured in cosmic ray runs.

There have been extensive investigations and measurements on the performance of the LAr calorimeters up to now, fully exploiting the commissioning data. Here, we will briefly mention the current status of the detector.

The adoption of the Liquid Argon technique requires the calorimeters to be housed in cryostats as previously mentioned, and temperature variations directly influences the readout signals through the effects on the drift velocity of ionization electrons and also on the effects of the liquid density. In order to keep the constant term of the energy resolution below 0.2%, the uniformity of the temperature is required to be within 100 mK [107]. The measurement of the temperature stability was performed for ten days around the winter break in 2008, when the detector installation activities in the ATLAS cavern were not ongoing. The temperature dispersion was 1.6 mK in average, and 5 mK in maximum [106], and was well below the physics requirement. The purity of the Liquid Argon was also stable and well below the requirement (less than 300 ppb from July 2007 to July 2009; better purification is need when larger than 1000 ppb).

The stability of the pedestals and electronic noise in Fall 2008 cosmic runs is shown in Figure 7.16 and 7.17. Shifts in the pedestals can make similar effects as the coherent noise, and should be kept as small as possible (shifts by 3 MeV per channel in the EM calorimeter can be problematic, due to the presence of significant number of channels). The pedestals in the EM calorimeter were stable below 1 MeV. The presamplers had problems with coherent noise during the 2008 data taking, but were fixed in 2009. The stability of the electronic noise was stable within ± 1 %, and showed good enough performance to meet the requirements from the physics analyses.

7.2 Problematic Channels in the ATLAS Calorimeters

Searches for problematic channels in the ATLAS calorimeters have been undergoing since long time using calorimeter specific calibration run and combined commissioning run data. So called the “dead” (not responding) and “hot” (noisy) channels must be identified to perform any meaningful measurements using the calorimeters. The “dead” channels form “holes” in the detectors, and underestimate the energy when particles penetrate through the regions. They can also lead to large fake E_T^{miss} when a bunch of high energy particles like jets accidentally pass the dead region. On the other hand, “hot” channels can obviously initiate fake high energy signals in the calorimeters, which will also disturb the triggers on top of energy measurements. Thus, the “hot” channels must be masked (their energy is forcibly set to zero or another fixed value as a flag). Figure 7.18 shows the η - ϕ map of masked problematic channels in LAr and TileCal. The numbers and percentages of masked cells in each partition is shown in Table 7.1.

The impact of hot channels on calorimeter clusters is shown in Figure 7.19 (the details on the cluster algorithm will be mentioned in the following section). A significant number of clusters were reconstructed, since hot channels can easily pass the energy threshold defined by the clustering algorithm. Their effects are too obvious in the energy distribu-

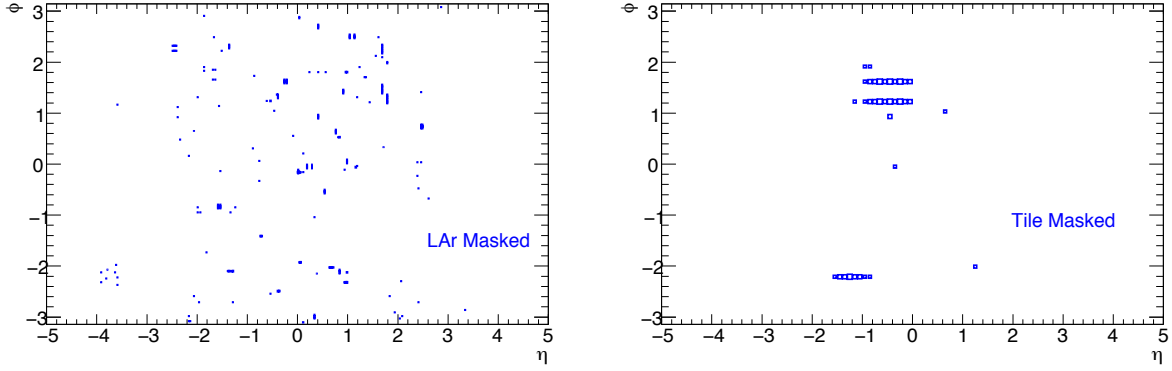


Figure 7.18: η - ϕ map of LAr (left) and TileCal (right) masked problematic channels.

Table 7.1: Numbers and percentages of masked problematic cells for each partition during 2008 Fall cosmic data taking period.

| | EM | Tile | HEC | FCAL |
|-----------|-------------|-----------|-------------|------------|
| All cells | 163968 | 5248 | 5632 | 3524 |
| Masked | 325 (0.2 %) | 66 (1.3%) | 12 (0.19 %) | 10 (0.3 %) |

tions as well. In the calorimeter reconstruction, so called the “masking” procedure can be performed on the identified problematic channels. For problematic LAr channels, the cell energy is overwritten as zero when the masking is turned on. For TileCal channels, the masking can take two different correction procedures in regards to the situation. When only one of the two PMT’s in a cell is identified as “bad”, only the remaining “good” PMT will be used for the energy reconstruction, namely its channel energy is multiplied by two to calculate the cell energy. If both PMT’s in a cell are problematic, then the cell energy is set to 1 MeV. This masking procedure will remove disastrous contributions from noisy channels, but further procedures are needed to recover the energy resolution degraded by the “holes” in the calorimeters. One of the straightforward ways to recover the energy lost in the dead (or masked) channels are to estimate the energy of the channels by taking the mean energy density from the neighboring cells [108]. Another method was proposed to make use of the Inner Detector tracks pointing to the dead channels [109].

The problematic channels were identified, categorized for their problematic issues, and stored in the ATLAS database. The list has been checked and updated throughout the data taking.

For the LAr channels, the bad channels are grouped into 15 categories (Tab. 7.2)[110] in regards to their problematic phenomena. They are also broadly grouped in three. The “deadPhys” and “deadReadout” channels are called the “Dead” cells. The “high-NoiseHG(MG,LG),” “unstabelNoiseHG(MG,LG),” “sporadicBurstNoise” channels are grouped as “Noisy” cells. The remaining bad channels are called the “Affected” cells.

In TileCal, the problematic channels are categorized as shown in Table 7.3.

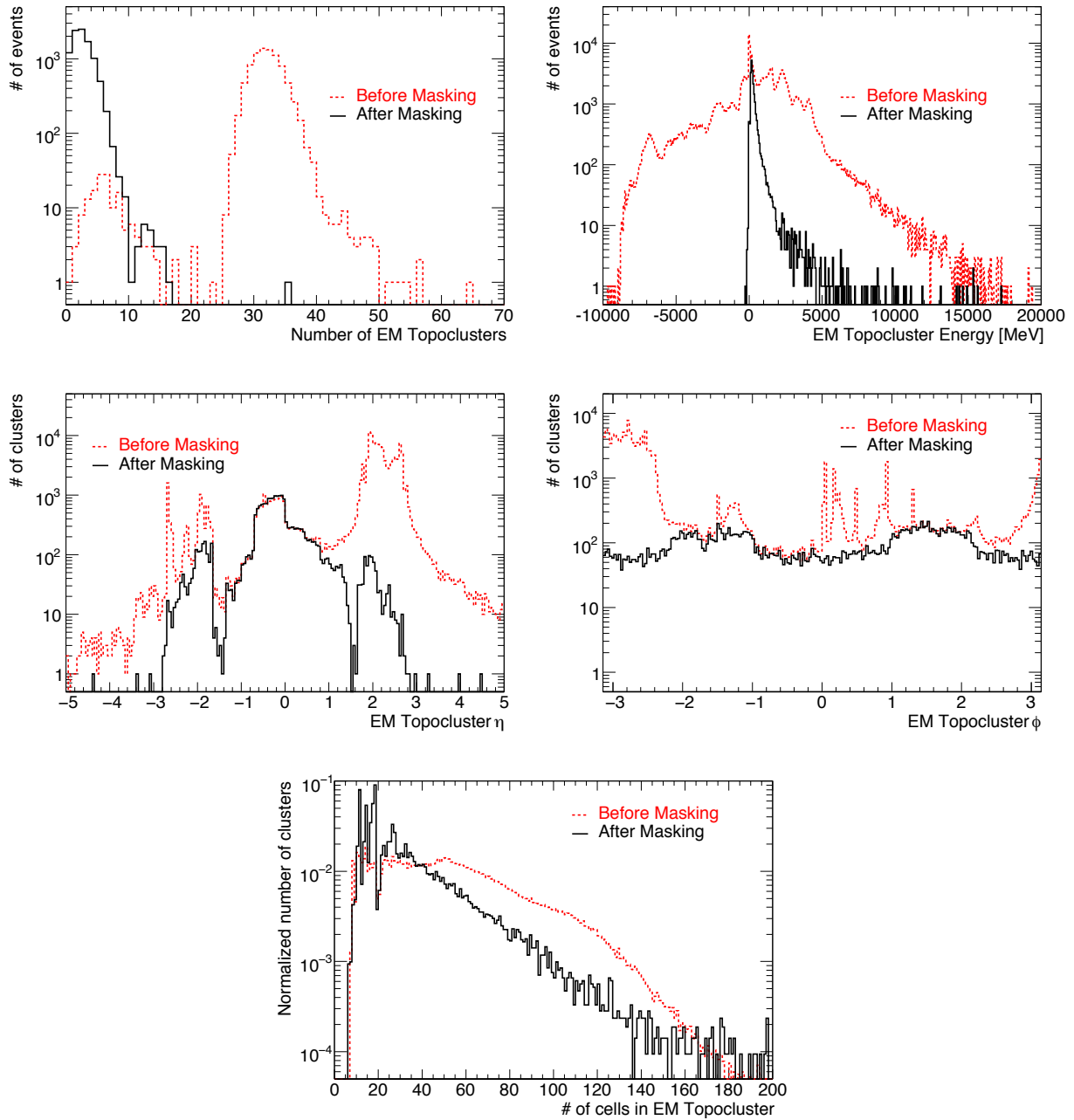


Figure 7.19: The distributions of EMTopoclusters in M5 run 29576 NIM0 stream. The reconstructed number of clusters (top left), the cluster energy (top right), pseudorapidity of the clusters (middle left), the ϕ of clusters (middle right), and the number of cells inside the clusters (bottom) are shown.

Table 7.2: Categories of the problematic LAr channels

| Category | Flag Name | Definition |
|----------|-------------------------|---|
| Dead | deadReadout | dead channels at the readout level |
| Dead | deadPhys | dead channels at the detector level |
| Noisy | highNoiseHG(MG,LG) | significantly noisy channels in high gain (medium, low gain) they should be considered for masking |
| Noisy | unstabelNoiseHG(MG,LG) | channels with instability respect to time |
| Noisy | sporadicBurstNoise | channels with sporadic bursts of noise observed during the cosmic runs |
| Affected | deadCalib | channels with significantly distorted calibration pulse |
| Affected | distorted | wave distortions of various types |
| Affected | lowNoiseHG(MG,LG) | noisy channels in high gain (medium, low) more than about 5 standard deviations from the expected noise not so noisy as to mask them |
| Affected | short | channels with shorts |
| Affected | peculiarCalibrationLine | channels with calibration problems (signals leaking in other channels) only in the low gain |
| Affected | missingFEB | FEB was missing in the readout for the channels |

Table 7.3: Categories of the problematic TileCal channels

| Level | Flag Name | Definition |
|---------|----------------------|---|
| ADC | GeneralMaskAdc | Unspecified ADC problems |
| ADC | ADCDead | ADC is dead |
| ADC | StuckBit | A bit is stuck (fixed at 1 or 0), in the ADC output, but no significant effect on the performance. |
| ADC | SevereStuckBit | A bit is stuck (fixed at 1 or 0), in the ADC output, manifesting significant effects on the performance. |
| ADC | DataCorruption | Digital data is corrupted (CRC, BCID, DMU memory parity errors, etc.) |
| ADC | SevereDataCorruption | Digital data is corrupted (CRC, BCID, DMU memory parity errors, etc.) The channels have to be masked. |
| ADC | VeryLargeHfNoise | The RMS of the ADC 7 sample distribution is very large |
| ADC | NoData | No data comes out of the ADC |
| ADC | WrongDspConfig | The online DSP configuration was not correct. |
| ADC | LargeHfNoise | The RMS of the ADC 7 sample distribution is very large |
| ADC | CorrelatedNoise | Correlation is observed among the ADC noise |
| ADC | LargeLfNoise | The RMS of the first sample distribution is large |
| ADC | NoCis | Problems identified in the long-term CIS calibration runs |
| ADC | BadCis | Channels with 5.2 pF capacitor problems. |
| Channel | Unspecified | Unspecified channel problems |
| Channel | NoPmt | The PMT is not read out or dead |
| Channel | NoHV | HV not applied to the PMT |
| Channel | WrongHV | A wrong HV value applied to the PMT |
| Channel | NoLaser | The PMT not receiving laser light |
| Channel | BadLaser | Laser light is too low or bright to perform good calibration |
| Channel | NoCesium | The PMT is not responding to the cesium scan |
| Channel | BadCesium | The response of the PMT to the cesium scan is too low or high |
| Channel | NoTiming | Not possible to set the dskew timing delay for the PMT |
| Channel | BadTiming | The PMT not well timed-in with the physics trigger |
| Trigger | TriggerGeneralMask | Unspecified trigger problems |
| Trigger | TriggerNoGain | The PMT of the 3-in-1 card is dead |
| Trigger | TriggerHalfGain | One of the two differential signals is broken so the channel is at 50% gain |
| Trigger | TriggerNoisy | The channel is too noisy, and must be disabled at the hardware-level |
| DSP | IgnoreInDsp | Data from the channels are not to be processed by the DSP when masked, but this flag does not save computing time and so not used |
| DSP | IgnoredInHlt | Channels to be masked for the HLT decision to avoid biasing events |

In the next section, the strategy to identify the problematic TileCal channels is proposed and investigated.

7.2.1 TileCal Bad Channel Search

In order to identify problematic channels in TileCal, searches were performed for the individual PMT's with noise levels exceeding the average distributions measured in the previous section. The criteria were developed to identify possible problematic channels [A.3.4.20], which are listed below.

- Noise values significantly deviating from the average
- Mean energy of a PMT significantly different from zero
- Large energy difference between PMT's in the same cell
- Large energy difference ratio of PMT's. This ratio is defined as the difference of the energies of 2 PMT's in a cell divided by the total cell energy. This quantity provides additional information when studying high energy deposits.
- Time difference of PMT's in the same cell (not considered here, but provides additional information, see Reference [122])
- Shape of the energy distribution significantly deviating from a Gaussian distribution

Examples are shown in Figure 7.20, 7.21, 7.22, 7.23 from M7 Week cosmic ray run 69373.

Figure 7.20 gives the measured noise of PMT 6 for all 64 Long-Barrel A (LBA) drawers. The correspondence of PMT numbers and the cells are shown in Figure 7.3. The PMT's with the same ID number are compared, because the electronic noise has η -dependence but basically uniform in ϕ as mentioned before (PMT number corresponds to η , and a drawer is a set of PMT's with the same ϕ values). Two channels are obviously noisier than average, and one exhibits a below-average noise. From the left plot, we can see the mean noise value and the spread of values for PMT 6 averaged over the LBA partition. By fitting this distribution with a Gaussian, we can define criteria to identify bad channels (e.g. channels deviating from the mean value by 5σ can be tracked in a potential bad channel list). The right plot shows the PMT noise values versus the drawer number, and this plot makes it easier to spot the problematic channels visually.

Figure 7.21 shows the mean energy of PMT 29 in the extended barrel A (EBA). The left plot shows the energy distributions of two PMT's, one of which is obviously problematic. Again, by plotting the mean energy per drawer number one can easily spot bad channels visually.

Figure 7.22 shows the energy difference of two PMT's in the same cell (PMT 3 and 4 in LBA) compared to those over all the drawers. The left plot shows two examples of the PMT energy difference, in which one has an unusual distribution with two peaks. The right plot provides a better visualization by correlating the PMT energy difference with

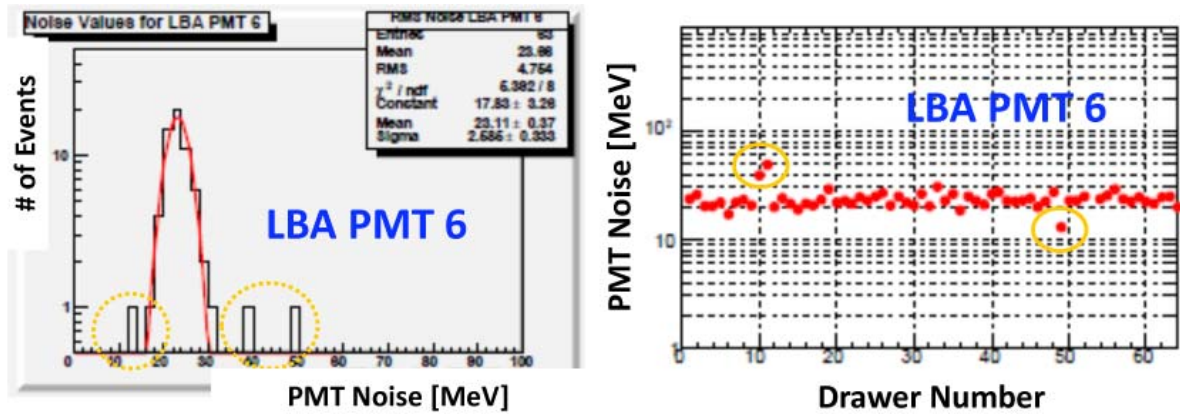


Figure 7.20: Noise values of LBA PMT 6 for each drawer in M7 run 69373 from the RNDM0 stream. The left plot shows the electronic noise distribution of PMT 6 for each drawer, while the right plot gives the electronic noise for PMT 6 versus drawer number.

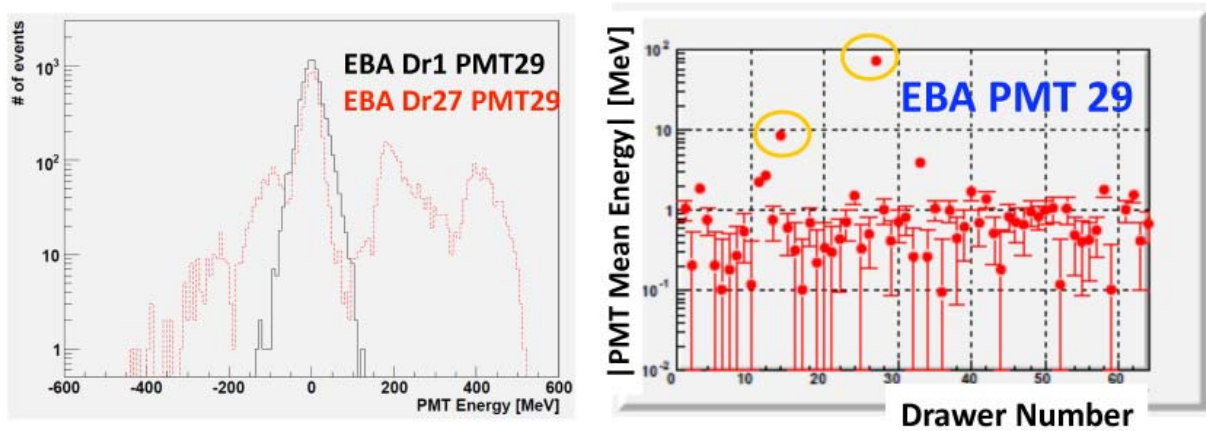


Figure 7.21: Mean energy of EBA PMT 29 in M7 run 69373 from the RNDM0 stream. The left plot gives examples of energy distributions for PMT 29 from 2 drawers, while the right plot shows the mean energy for PMT 29 versus drawer number.

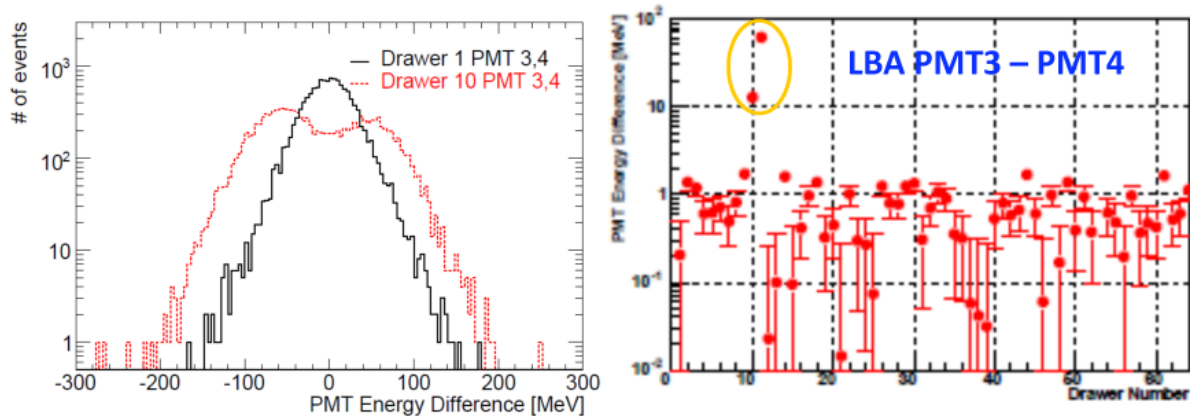


Figure 7.22: Energy difference of PMT's in the same cell (PMT 3 & 4 in LBA) in M7 run from the 69373 RNDM0 stream. The left plot gives examples of the energy difference between PMT 3 and 4, while the right plot shows the energy difference of PMT 3 and 4 versus drawer number

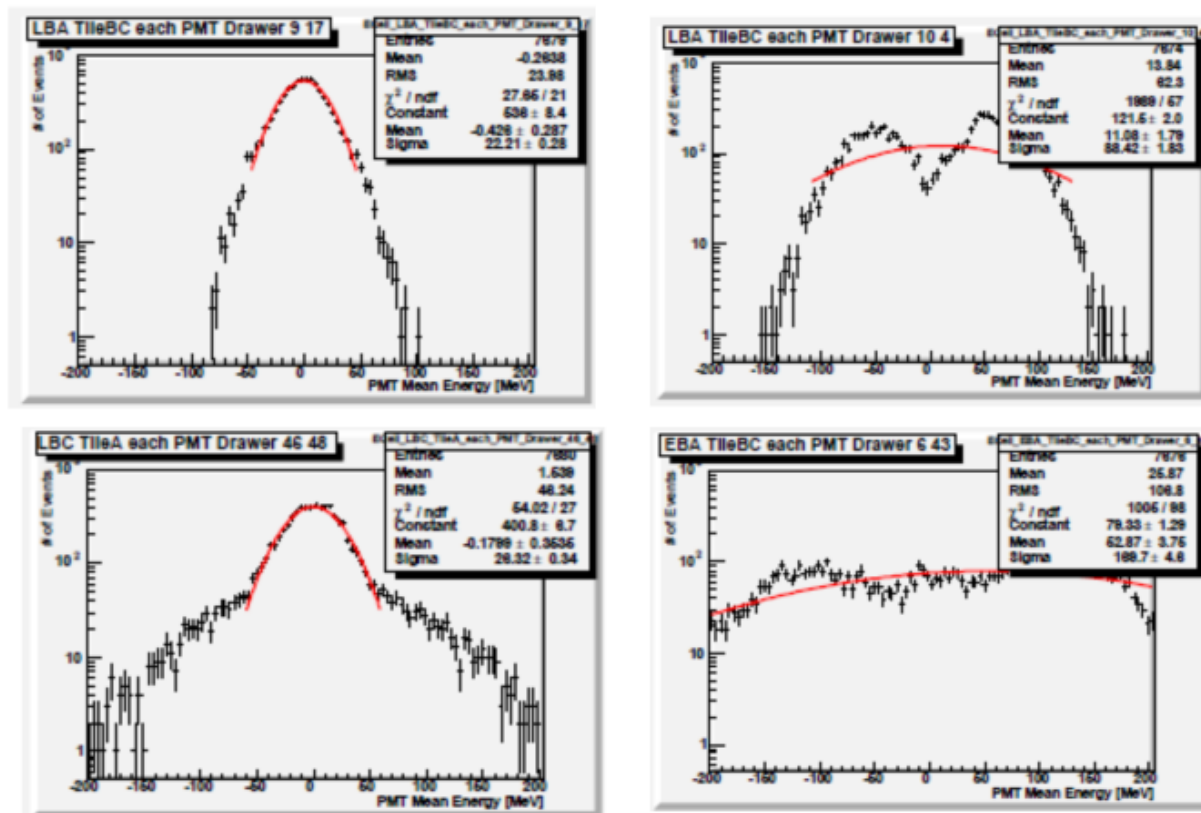


Figure 7.23: Energy distribution of PMT's. The upper right and lower right plots are for known bad channels.

drawer number. From this plot, we can only spot the “pairs” of problematic channels, but we need additional information (such as that mentioned above) to identify the individual bad channels.

Finally, Figure 7.23 shows the energy distribution for each PMT. The upper and lower left plots are good channels, (the lower left plot has large non-Gaussian tails, but some of the channels in $|\eta| \sim 1$ have this feature, which results in the increase in noise values in Figure 7.4). The upper right and lower right plots are for known bad channels.

By adopting the criteria mentioned above, we can identify potential bad channels. However, these criteria are not sensitive to coherent noise, or to channels which become noisy for a short period of time (noise bursts). For those cases, we need to develop a complementary strategy, such as using the fit quality of the signal pulse shape.

7.3 Performance of Calorimeter Clusters

There are two major calorimeter clustering algorithms in ATLAS [111]. They are referred to as a sliding window and a topological clustering (Topocluster) algorithm. Both types of clusters are standard inputs for jet reconstruction.

The sliding window algorithm exploits fixed size clusters, and shows robust performance. The topological clustering algorithm has better noise suppression, but relies heavily on the ATLAS noise database in order to consider the signal-to-noise ratio of each cell energy output. We will briefly review the methods of the both algorithms below.

7.3.1 Sliding Window Algorithm

There are two kinds of sliding window clusters used in ATLAS; electromagnetic (EM) clusters used for electron and photon reconstruction, and EM-hadronic combined clusters used for the tau lepton reconstruction and jet finding.

The ATLAS calorimeters are divided in the $\eta - \phi$ grid by a fixed size of $\Delta\eta \times \Delta\phi$.

The EM tower building starts from a size of $\Delta\eta \times \Delta\phi = 0.025 \times 0.025$, and they extend up to $|\eta| = 2.5$, which means that the EM calorimeter is divided into 51,200 grids. They will go through further procedures to be used for electron or photon reconstruction [111], but the EM towers are not considered in this thesis.

The combined towers exploits larger configuration size of $\Delta\eta \times \Delta\phi = 0.1 \times 0.1$, extending up to $|\eta| = 5.0$, thus $100 \times 64 = 6,400$ towers in total. Projective cells which completely fit inside the tower, are simply added to the tower energy. For projective cells with bin size larger than the tower (e.g. the D-layer cells of TileCal) and non-projective cells (e.g. cells in the Forward Calorimeter), only some fraction of the cells contribute to the tower (Figure 7.24). In such cases, weight is applied to each cell considering the fraction of volume inside the tower. During the tower building, no further corrections or calibrations are applied.

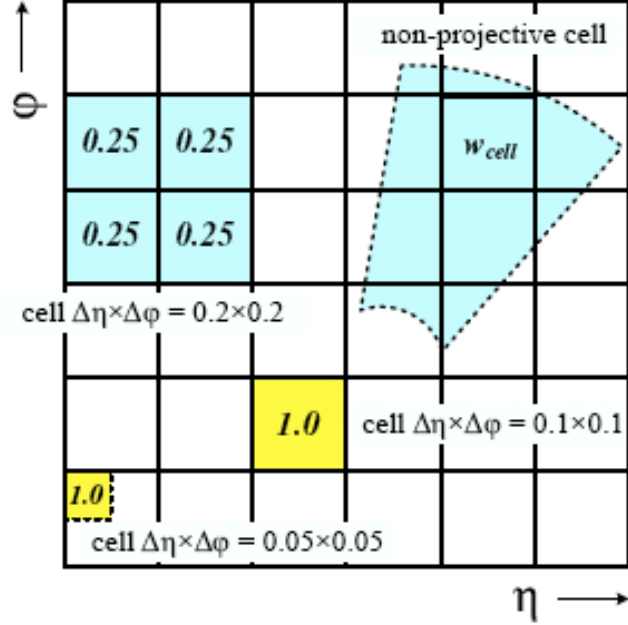


Figure 7.24: Contributions of calorimeter cells to combined towers shown in schematic $\eta - \phi$ grid.

7.3.2 Topological Clustering

The main idea of the topological clustering algorithm is to group cells in three-dimensions and over various calorimeter partitions, based on the significance of their energy deposits in each cell and its relationship among the adjacent cells [112]. In the topological clustering algorithm, cells are classified as “seeds”, “neighbors”, and “others” with respect to their significance above the expected noise levels. Cells whose absolute energy pass the $n_{\text{seed}}\sigma$ (σ is noise value of the cell) are defined as “seeds”. Cells adjacent to “seed” cells are called “neighbors” when their energy is larger than $n_{\text{neighbor}}\sigma$. “Neighbors” themselves can behave as new “seeds”, expanding the clusters by including their adjacent cells with $|E|/\sigma_{\text{neighbor}} > n_{\text{neighbor}}$. Cells bound to “neighbor” cells are defined as “others” when their energy exceeds $n_{\text{others}}\sigma$. Detailed criteria for merging and splitting of the clusters are explained in [112].

There are several types of Topological Clusters (Topoclusters). EMTopoclusters are reconstructed solely from cells in the EM calorimeter. “AllCalo” Topoclusters are reconstructed from all the calorimeter cells among EM and hadronic calorimeter, and are used as inputs for jet reconstruction and the E_T^{miss} calculation. Topoclusters reconstructed solely from TileCal were also used for the commissioning studies up to the Tier-0 reconstruction of the Fall 2008 data (Tier-0 is the initial Grid site located at CERN, responsible for storing the raw data from the experiments, and running the first reconstruction of data. See Acronyms and Terms for more details). The settings $(n_{\text{seed}}, n_{\text{neighbor}}, n_{\text{others}}) = (4, 2, 0)$ were used as the default for all types of Topoclusters in commissioning runs (and an additional $E_T > 0.1$ GeV cut was applied to EM Topocluster), though the threshold for

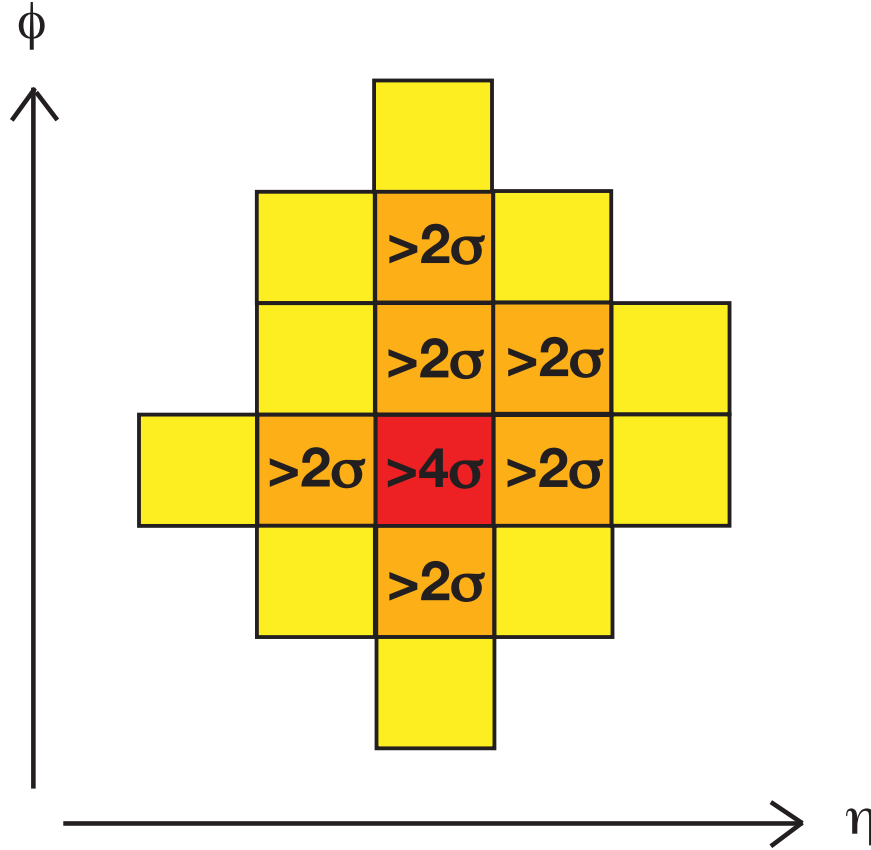


Figure 7.25: Schematic view of Topological Clustering algorithm. The red box indicates the “seed” cell, the orange boxes are “neighbors”, and the yellow boxes are “others” cells. Note that the actual clustering takes place in three dimensional directions.

EM Topoclusters were updated to $(n_{\text{seed}}, n_{\text{neighbor}}, n_{\text{others}}) = (4, 3, 0)$ with $E_T > 0.3$ GeV cut. Here, investigations were extensively done for Topoclusters using all the calorimeters with $(n_{\text{seed}}, n_{\text{neighbor}}, n_{\text{others}}) = (4, 2, 0)$ threshold.

7.3.3 Performance of Topoclusters in Random Stream Data

Topological clustering has a sophisticated noise suppression algorithm, but on the other hand, it is sensitive to the noise description in the database. Figure 7.26 shows the number of reconstructed TileCal Topoclusters in M5 run 29576 NIM0 stream in the Fall of 2007 (NIM0 stream consists of events triggered by the TileCal towers with coincidence in the top and bottom drawer, thus include many cosmic events). The blue line shows the number of reconstructed clusters with the noise values stored in the database. At that time, the noise values assumed in the Monte Carlo simulation were stored in the database and was also used for the real cosmic data (see the left figure in Figure 7.4). The red line and black lines show reconstructed number of clusters with the noise values measured from the same run (Gaussian σ used for the red line, and the RMS for the black line).

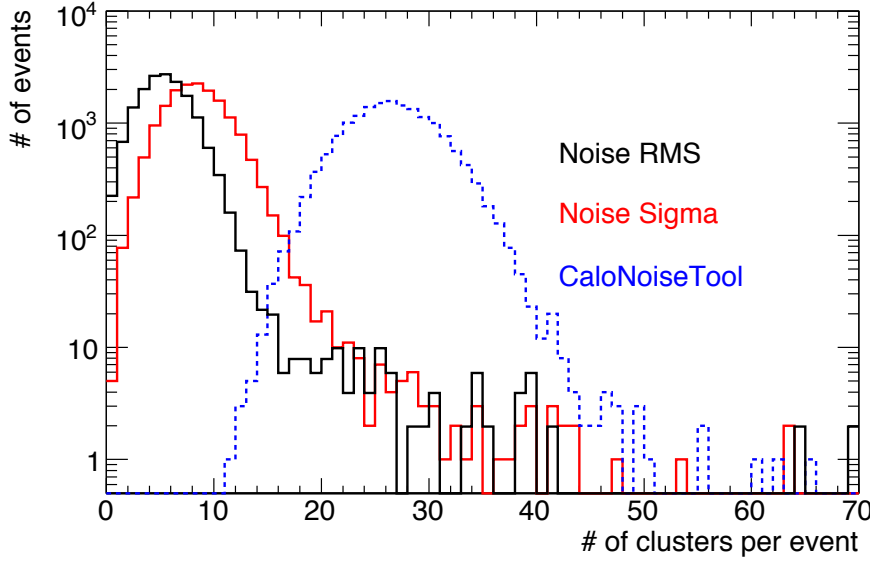


Figure 7.26: Sensitivity of Topoclusters to noise database. Number of reconstructed TileCal Topoclusters in M5 run 29576 NIM0 stream is shown.

From the penetration of a cosmic muon, two clusters should be reconstructed in average, even though there can be splitting of clusters due to geometrical effects. However, the mean number of reconstructed TileCal Topoclusters was 5.2 even when considering the RMS of the noise, which is more than twice the expectation. Such phenomena have been continuously observed in the commissioning data also for the combined Topoclusters (and will be mentioned again below).

As mentioned above, TileCal has been observing more reconstructed clusters than the expectation. Since the noisy channels are mostly identified and masked during the reconstruction, the source of extra clusters must have some other origin. It was found that those extra clusters were reconstructed due to the non-Gaussian tails in the TileCal cell energy distributions (Figure 7.27) [A.3.4.29].

The Topological Clustering algorithm makes use of the threshold considering the confidence level of the energy in each cell. The default algorithm extracts the noise values from the database, and simply multiply by the n_{seed} , n_{neighbor} , n_{other} to set the threshold. Due to the non-Gaussian tails in the TileCal cells, this linear relationship between the confidence level and $n \times \text{RMS}$ does not hold, underestimating the seed threshold by about 60 % at most (the left figure of Figure 7.28). Such effects can affect the cluster performance to a great extent, and can also degrade the resolution of $E_{\text{T}}^{\text{miss}}$ as will be mentioned in the next section. In order to reconstruct the topological clusters consistent with the expectation, the correct values for $n_{\text{seed}}\sigma$, $n_{\text{neighbor}}\sigma$, $n_{\text{other}}\sigma$ must be offered in regards to the real confidence levels.

Here, the default Topological Clustering algorithm was updated to extract the correct values of noise threshold, and was compared with the default reconstruction [A.3.4.29]. In Figure 7.29, the reconstructed numbers of Topoclusters are shown for various conditions.

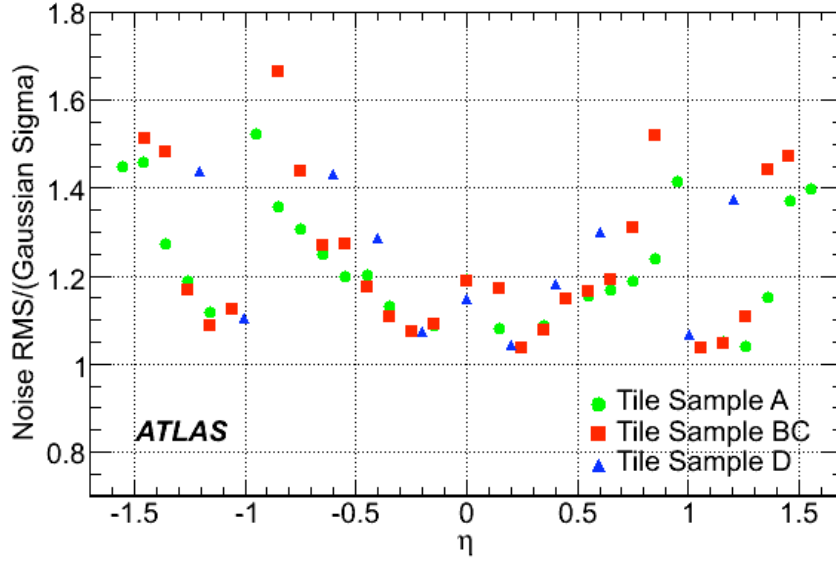


Figure 7.27: Ratio of the RMS and the Gaussian σ

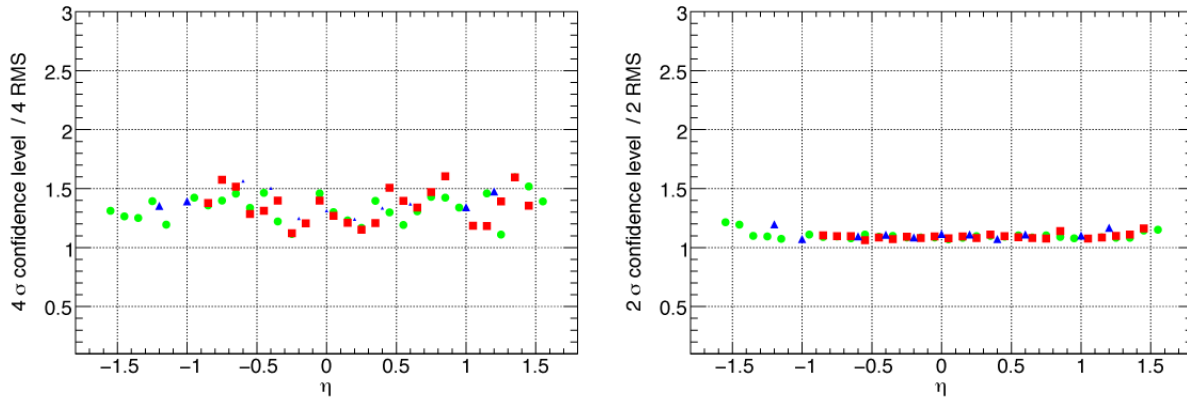


Figure 7.28: Ratio between the confidence level and the Gaussian sigma

Table 7.4: Mean of reconstructed number of Topoclusters in each calorimeter region

| | MC | Old Repro | Dec08 Repro | New Topo |
|-------|------|-----------|-------------|----------|
| Tile | 0.6 | 10.3 | 8.3 | 0.2 |
| EM | 9.5 | 23.9 | 15.9 | 15.9 |
| HEC | 0.4 | 2.5 | 0.4 | 0.4 |
| FCAL | 0.2 | 0.8 | 0.2 | 0.2 |
| Total | 10.8 | 38.0 | 25.0 | 17.0 |

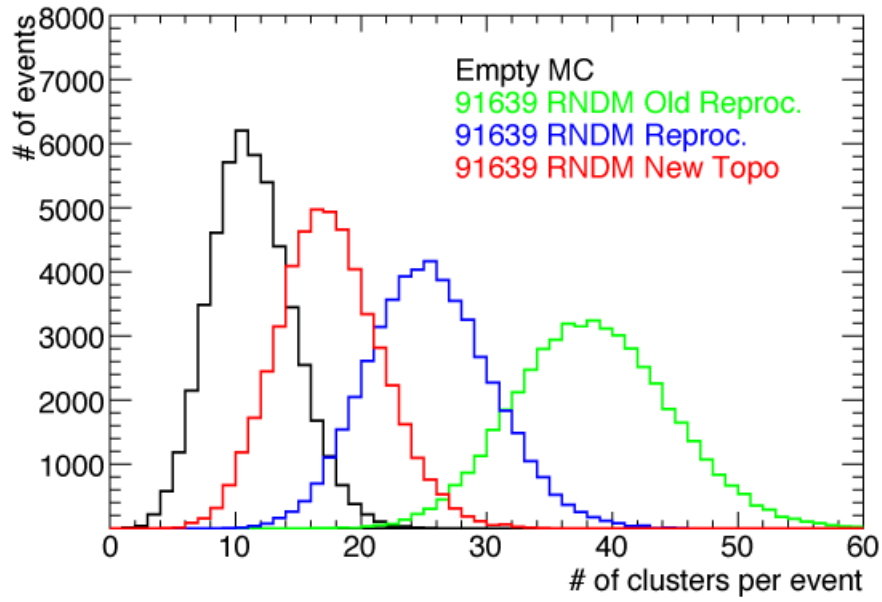


Figure 7.29: Number of reconstructed Topoclusters

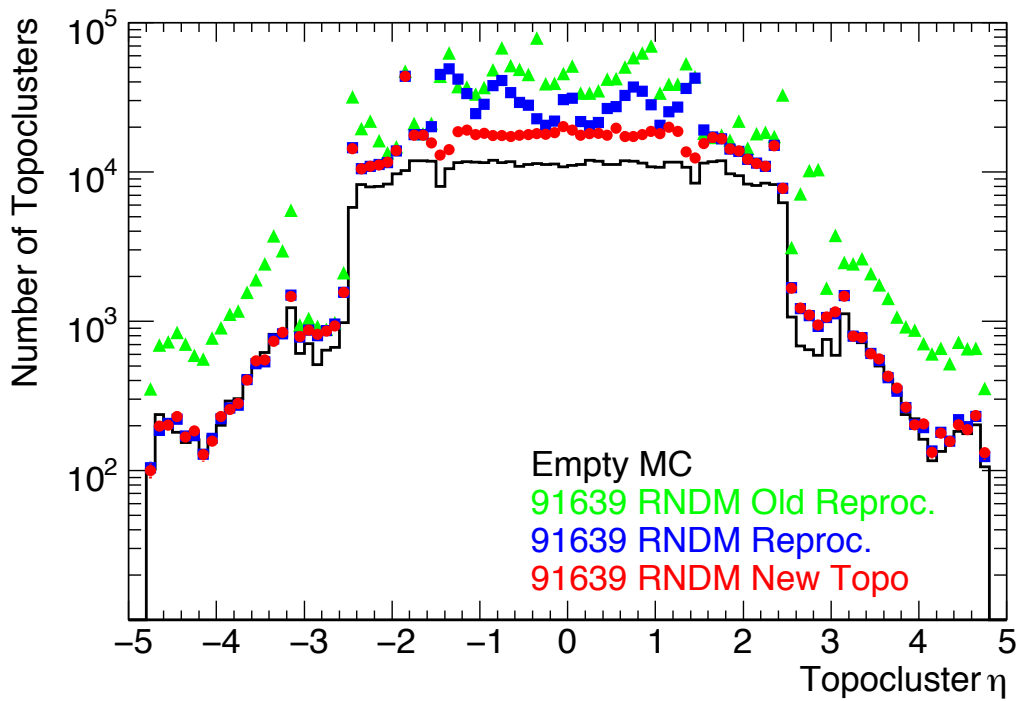


Figure 7.30: η distributions of reconstructed Topoclusters

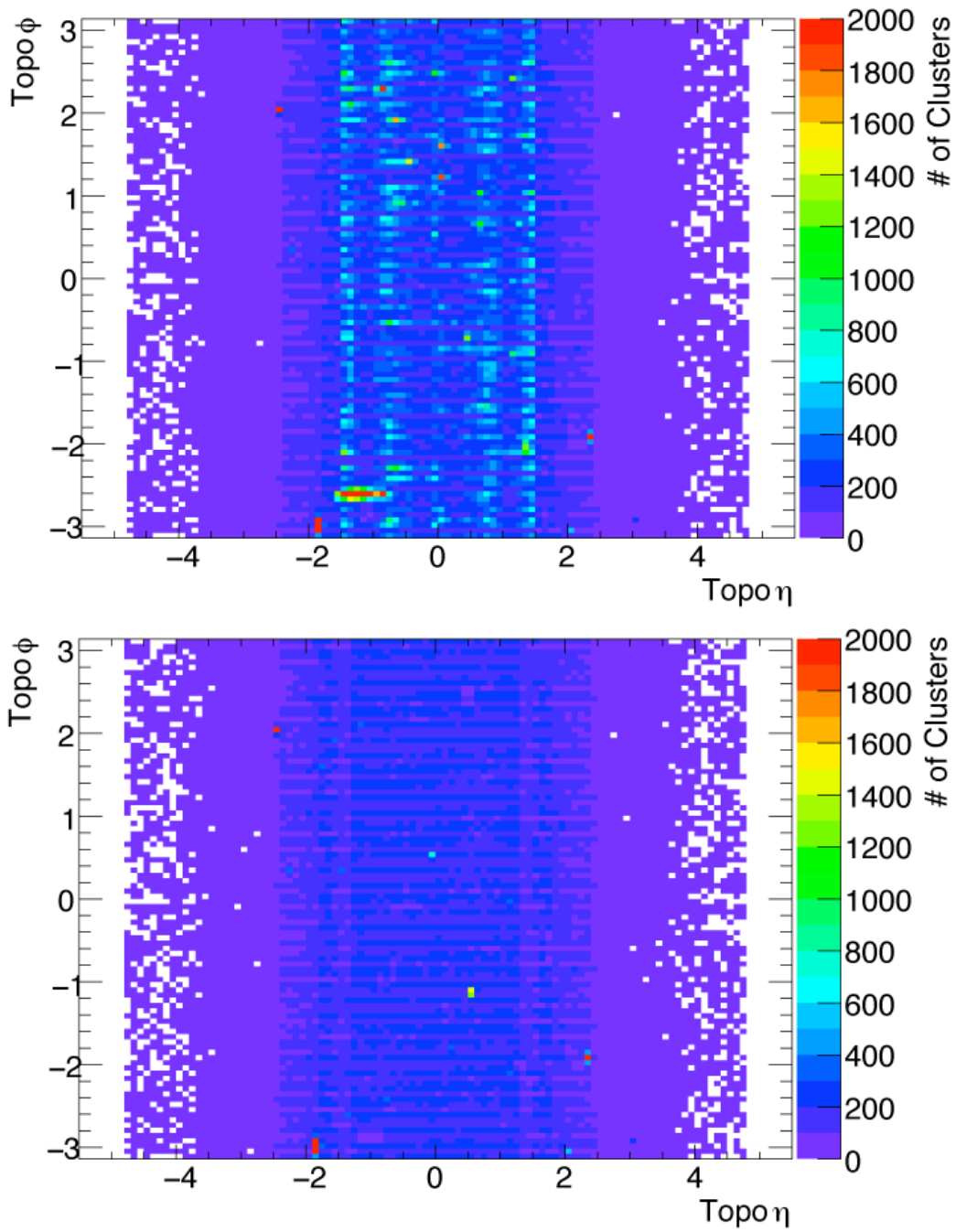


Figure 7.31: $\eta - \phi$ distributions in December 08 reprocessing data and new reconstruction

The green line shows the Tier-0 reconstruction of run 91639 RNDM stream data. When the Tier-0 reconstruction was done, the database was containing inconsistent noise values, and was underestimating them in the TileCal. The blue line shows the distribution from the December 2008 Tier-1 reprocessing. The correct noise values are stored in the database, and energy reconstruction in the LAr was improved, which resolved many of the pedestal shifts observed in the Tier-0 data. The red line shows the improvement after the updates in the Topocluster algorithm taking care of the non-Gaussian feature of the noise in TileCal. The black line shows the noise Monte Carlo samples, and is the expectation. There still remains some discrepancy in the number of reconstructed clusters, but it is mainly due to the slight pedestal shift in the LAr EM calorimeter and the HV problem observed in the presampler. The numbers are explicitly shown in Table 7.4, and shows that now the TileCal performance is greatly improved and well consistent with the expectation. The excess of reconstructed numbers of clusters and the improvement after the new Topocluster algorithm are obviously visible in Figure 7.30 and 7.31.

7.4 Performance of Missing E_T in Random Stream Data

Missing E_T (E_T^{miss}) is a variable which quantifies the imbalance of energy in the transverse plane. It provides indirect detection of weakly interacting particles such as neutrinos and possibly dark matters if they exist. Its performance is crucial for numerous measurements not only in the Standard Model phenomenon (W , $t\bar{t}$ decaying leptonically) but also for Higgs, supersymmetry, and extra dimension searches.

Here, the E_T^{miss} algorithm is briefly reviewed, and the performance of the calorimeter term of E_T^{miss} from the random stream data was investigated.

7.4.1 Missing E_T Algorithm in ATLAS

Two approaches exist in the E_T^{miss} algorithm in ATLAS; calorimeter cell-based and object-based algorithms. Here, the former will be explained and used.

The main components come from the calorimeter, muon, and the cryostat correction (correction for the energy lost when particles pass through the cryostat) term [23],

$$E_{x,y}^{\text{miss}} = E_{x,y}^{\text{miss,Calo}} + E_{x,y}^{\text{miss,Muon}} + E_{x,y}^{\text{miss,Cryo}} . \quad (7.5)$$

Several calibration schemes exist on top of the raw EM scale, in order to achieve good resolution. Various E_T^{miss} quantities with different calibration levels are defined in ATLAS (see Table C.1 in Appendix C). Here, the performance of the calorimeter terms of E_T^{miss} was investigated with the random stream data. The overview of the Missing E_T algorithm including the muon and cryostat terms in ATLAS is described in Appendix C.

Calorimeter Term in E_T^{miss}

The x and y components of the calorimeter term are calculated from the vector sum of energy in each cell.

$$E_{x,y}^{\text{miss,Calo}} = - \sum_{\text{cell}} E_{x,y}^{\text{cell}} \quad (7.6)$$

$$E_x^{\text{cell}} = E^{\text{cell}} \sin \theta \cos \phi \quad (7.7)$$

$$E_y^{\text{cell}} = E^{\text{cell}} \sin \theta \sin \phi \quad (7.8)$$

The angular directions of cells are defined from the central position of the cell. Eight categories exist in the ATLAS framework for the calorimeter term. Four of them are at the EM-scale, and the others are calibrated to the hadronic scale with H1-style or the Local Hadronic Calibration scheme [23]. Random stream data offers a useful training ground to validate the calorimeter term of the E_T^{miss} , and will be mentioned in the next section.

7.4.2 Performance of E_T^{miss} in Data and Its Improvement

Measurement of E_T^{miss} in random stream data allow us to understand the performance of noise term. Noise term becomes important when the high resolution of E_T^{miss} is required. Higgs decaying into di-tau is an example, since the resolution of E_T^{miss} will influence the resolution of the invariant mass of the two taus.

For this study, we produced toy Monte Carlo samples which assume incoherent Gaussian noise. The same noise RMS was taken from the ATLAS noise database for each channel. The comparison of data with the toy Monte Carlo allows for the validation of the E_T^{miss} performance.

MET_Base Algorithm

Figure 7.32 shows the distributions of Missing E_x and E_y from the random stream data and toy Monte Carlo. MET_Base algorithm was used for the figure. Fairly good consistency is observed, but slight shift in the mean of Missing E_y was found. This phenomenon matches with the pedestal shifts we have observed for some cells. Figure 7.33 shows the E_T^{miss} distribution from MET_Base algorithm. Large tail from the random stream data is due to the problematic coherent noise in the barrel presampler that we have been observing. After removing the contribution of the barrel presampler in the E_T^{miss} calculation, the consistency of E_T^{miss} between toy Monte Carlo and data becomes much better [103].

MET_Topo Algorithm

Although, the performance of MET_Base in random data was basically consistent with the expectation, it was found that that the resolution of missing E_x and E_y (and thus E_T^{miss}) in MET_Topo algorithm was largely degraded compared to the expectation (Figure 7.34

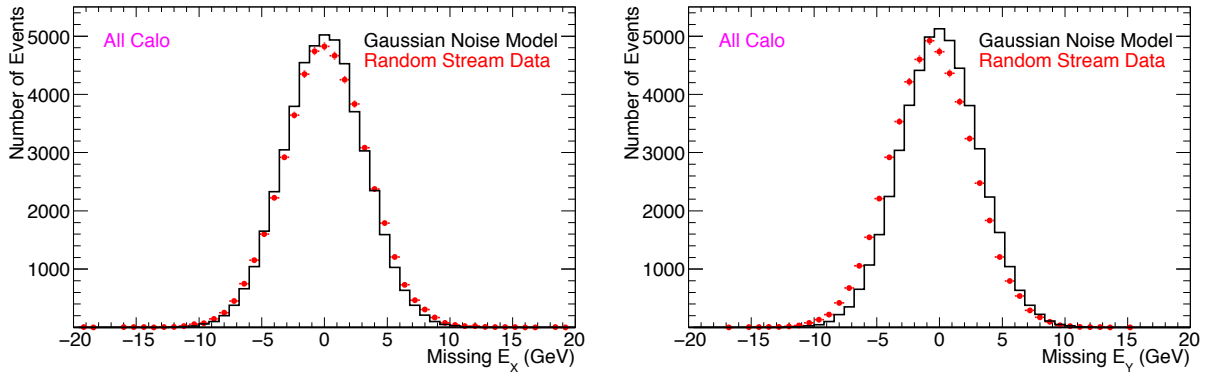


Figure 7.32: “MET_Base” Missing E_X and E_Y from random stream data and toy Monte Carlo samples from a Gaussian noise model. Black histograms show the distributions from toy Monte Carlo samples assuming incoherent Gaussian noise. Red points show the distributions from the random stream data.

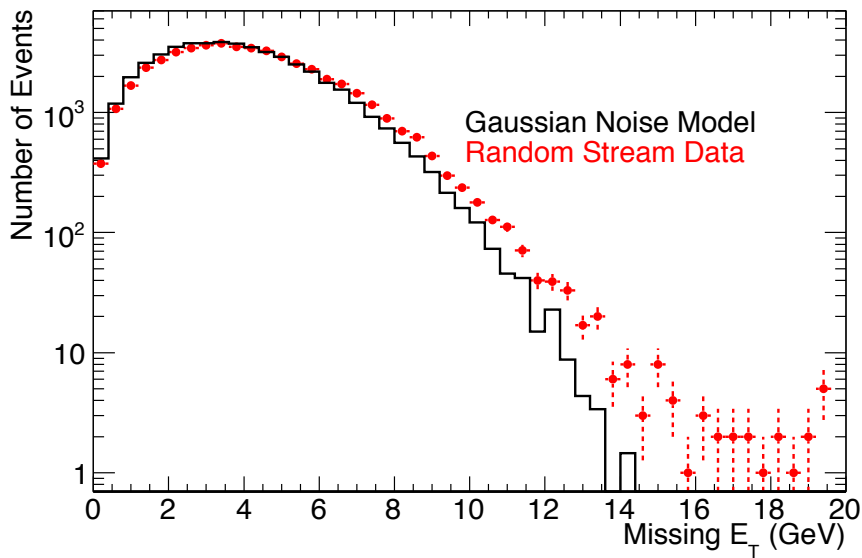


Figure 7.33: “MET_Base” E_T^{miss} from random stream data and toy Monte Carlo samples from a Gaussian noise model. Black histograms show the distributions from toy Monte Carlo samples assuming incoherent Gaussian noise. Red points show the distributions from the random stream data.

and 7.35). This degradation was largely due to the non-Gaussian shape of the electronic noise in TileCal as mentioned in the previous section for the Topocluster performance.

Figure 7.36 and 7.37 shows the improvement seen after the updated Topocluster algorithm was used. Tails still remain, which is coming from the non-Gaussian feature. Those tails cannot be simply removed by applying the correct noise threshold. Use of fit quality factor of the pulse shape in the channels may offer a way to remove such remaining outliers.

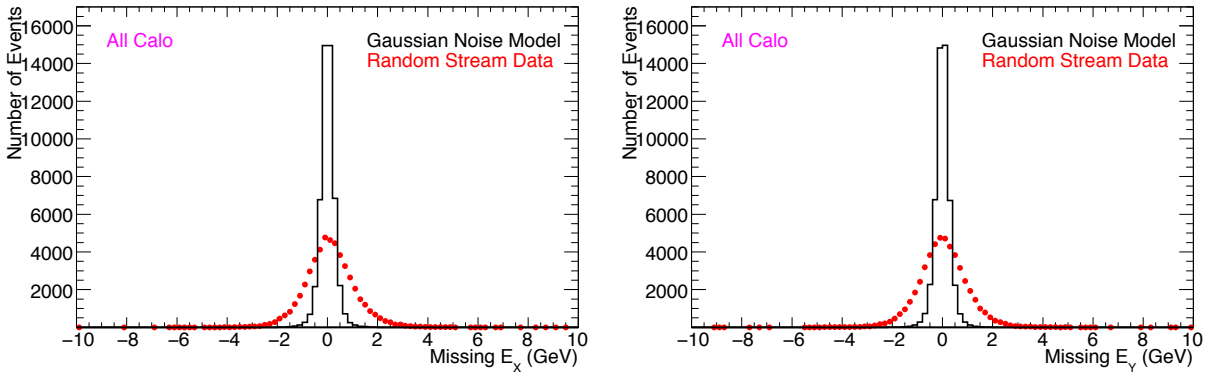


Figure 7.34: “MET_Topo” Missing E_X and E_Y from random stream data and toy Monte Carlo samples from a Gaussian noise model. Black histograms show the distributions from toy Monte Carlo samples assuming incoherent Gaussian noise. Red points show the distributions from the random stream data.

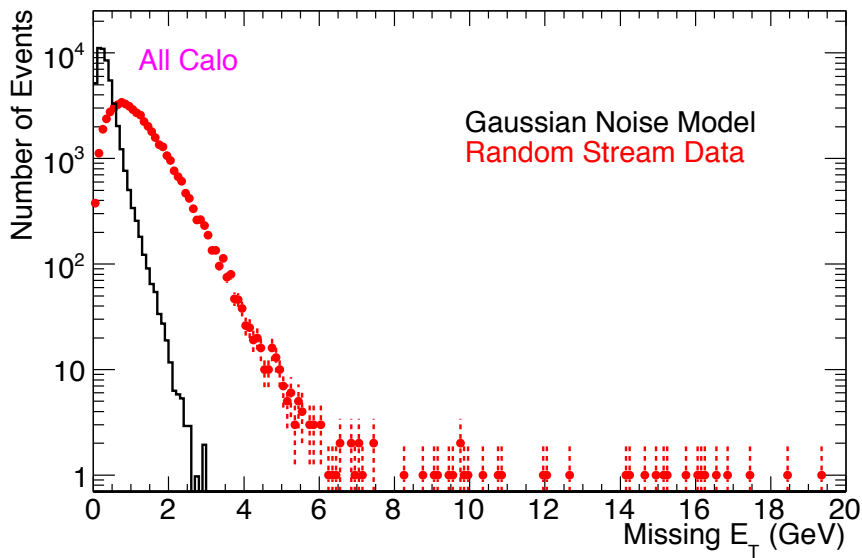


Figure 7.35: “MET_Topo” E_T^{miss} from random stream data and toy Monte Carlo samples from a Gaussian noise model. Black histograms show the distributions from toy Monte Carlo samples assuming incoherent Gaussian noise. Red points show the distributions from the random stream data.

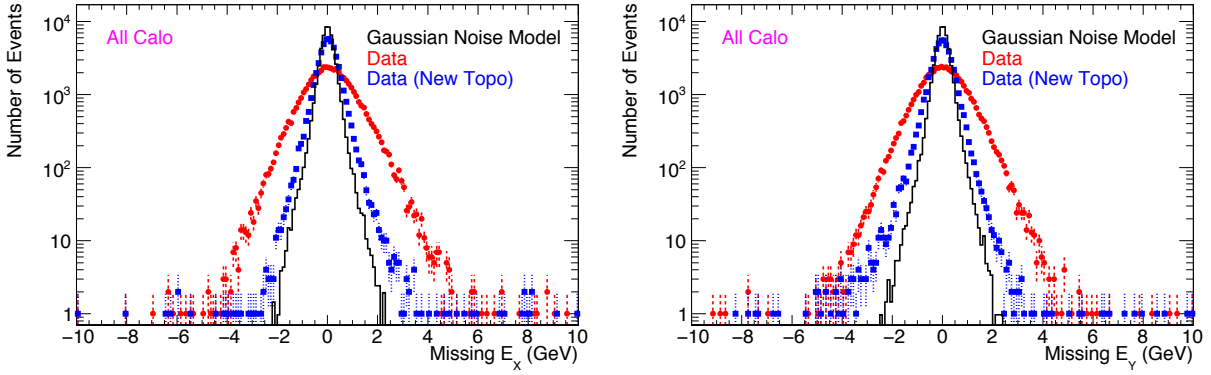


Figure 7.36: “MET_Topo” Missing E_X and E_Y from random stream data with and without updated Topocluster algorithm and toy Monte Carlo samples from a Gaussian noise model. Black histograms show the distributions from toy Monte Carlo samples assuming incoherent Gaussian noise. Red points show the distributions from the random stream data.

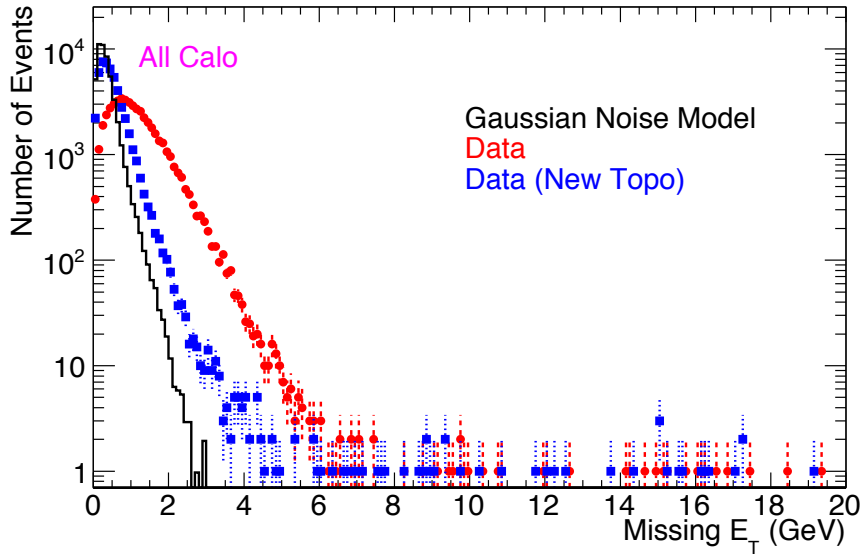


Figure 7.37: “MET_Topo” E_T^{miss} from random stream data with and without updated Topocluster algorithm and toy Monte Carlo samples from a Gaussian noise model. Black histograms show the distributions from toy Monte Carlo samples assuming incoherent Gaussian noise. Red points show the distributions from the random stream data.

Chapter 8

Calorimeter Measurement with Cosmic Ray Data

In this chapter, the performance of the ATLAS calorimeters was investigated with cosmic ray data. High energy deposits in the calorimeters have been continuously observed during the cosmic ray data taking, and the origin of such events were investigated. Monte Carlo simulation of cosmic muons reaching the ATLAS detector (including the interactions through the ground) was exploited to understand the data. Also, such high energy deposits in the calorimeters originate fakely reconstructed “jets” and large E_T^{miss} , and become background to the physics analyses using jets and E_T^{miss} .

In this chapter, we show that such contributions are well described by the Monte Carlo simulation and understood. Strategies to reject the non-collision background (so called the “cleaning”) will be discussed in Chapter 9.

8.1 Cosmic Rays

Cosmic rays are high energy particles traversing cosmic space. The “primary” cosmic rays originate and are accelerated by astrophysical sources. Electrons, protons, helium, and other heavier nuclei produced inside the stars belong to the category. Nuclei such as lithium, beryllium, and boron are produced by those particles interacting with interstellar gas. Antiprotons and positrons are also mostly produced through the interaction of those primary cosmic rays during the propagation. Neutral particles such as γ -rays and neutrinos compose important fraction of the cosmic rays as well. The energy of cosmic rays spreads over vast scales, but the acceleration mechanism is not yet fully understood.

When cosmic rays reach the earth, they undergo numerous interactions with the atmosphere, and generate secondary particles (these are often called as “secondary cosmic rays”). Incident protons and nuclei will initiate a hadron shower. Their products are grouped into three components: hadronic, muonic, and electromagnetic components (Figure 8.1). Muons originate from the decays of kaons and pions, and make up the largest fraction of the cosmic rays (except for the neutrinos) reaching the earth surface. Due to the penetration ability of muons, they are detected even at deep underground. The vertical fluxes of cosmic rays in the atmosphere is shown in Figure 8.2.

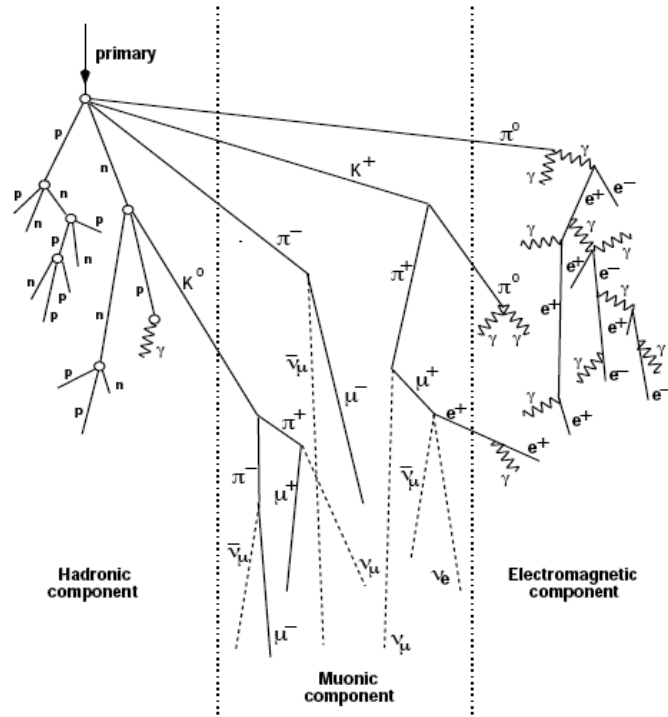


Figure 8.1: Schematic view of air shower development [117][118].

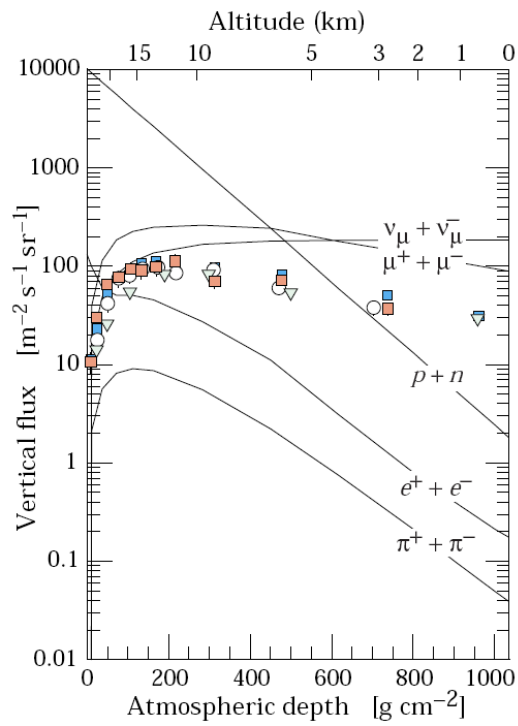


Figure 8.2: Vertical fluxes of cosmic rays in the atmosphere as a function of atmospheric depth [74].

Table 8.1: Profile of generated cosmic Monte Carlo simulation samples.

| Generated μ Momentum | Area (Z \times X) | Events | Expected Time Duration |
|--------------------------|------------------------|--------|------------------------|
| 10 - 100 GeV | 300 m \times 300 m | 33.4k | 134 s |
| 100 - 300 GeV | 600 m \times 600 m | 105k | 1.47×10^3 s |
| 300 GeV - 1 TeV | 1.5 km \times 1.5 km | 144k | 1.40×10^4 s |
| 1 - 3 TeV | 2 km \times 2 km | 145k | 2.16×10^5 s |
| 3 - 5 TeV | 3 km \times 3 km | 142k | 3.75×10^6 s |

8.2 Cosmic Monte Carlo Simulation in ATLAS

We produced cosmic Monte Carlo simulation samples to understand the performance of the calorimeters. Here, the overview of the simulation method is given.

The cosmic muons are generated at the ground level, with a fixed generation area (Figure 8.3). The muons are randomly generated according to the expected muon spectrum [115]. In this simulation, only single muon events were considered, and did not include air shower events. In this thesis, different areas were used for each momentum range (larger areas for high momentum muons; see Table 8.1) for two reasons. The first reason is that when cosmic muons have large energy, they will have more penetration power and can survive even for large incident angles and long traverse through the ground. Secondly, the flux of cosmic muons in large azimuthal angles tend to become more significant for high energy muons, because in order to produce such high energy muons from pion and kaon decays, those parent mesons must travel longer distance to decay due to the Lorentz boost (~ 55 km for muons with 1 TeV energy; the thickness of the earth troposphere is ~ 17 km) and tend to originate from mesons coming in large azimuthal angles.

In order to understand the effect of rock overburden for the propagation of cosmic muons, the simulation starts from the ground level, and takes into account the interaction of those cosmic muons inside the rock over ATLAS. The simulation also takes account of the two shafts (PX14 and PX16 in Figure 8.4) used for the transport of ATLAS detector units used during the construction era.

Since most of the muons simply generated by the expected spectrum and flux will miss the ATLAS detector, two event filtering algorithms were performed.

The first filtering algorithm requires the generated muons to point at a sphere centered at the interaction point with a fixed radius (25 meters in this thesis). The extrapolation to the sphere was done assuming a straight line from the generated point.

The second filtering algorithm is often called as the ‘‘volume filtering’’ and makes use of the Geant-4 hits in some specific ATLAS sub-detectors. Specifying the ‘‘detector volume,’’ for the simulation, the filtering will run to record only events with Geant-4 hits in the sub-detector. Here, the calorimeter volume (‘‘MuonEntryLayer’’) was used for the filtering, because the Monte Carlo samples were produced to compare with the L1Calo stream data (events triggered by the calorimeter towers).

In this thesis, Monte Carlo samples were produced in five separate slices in muon mo-

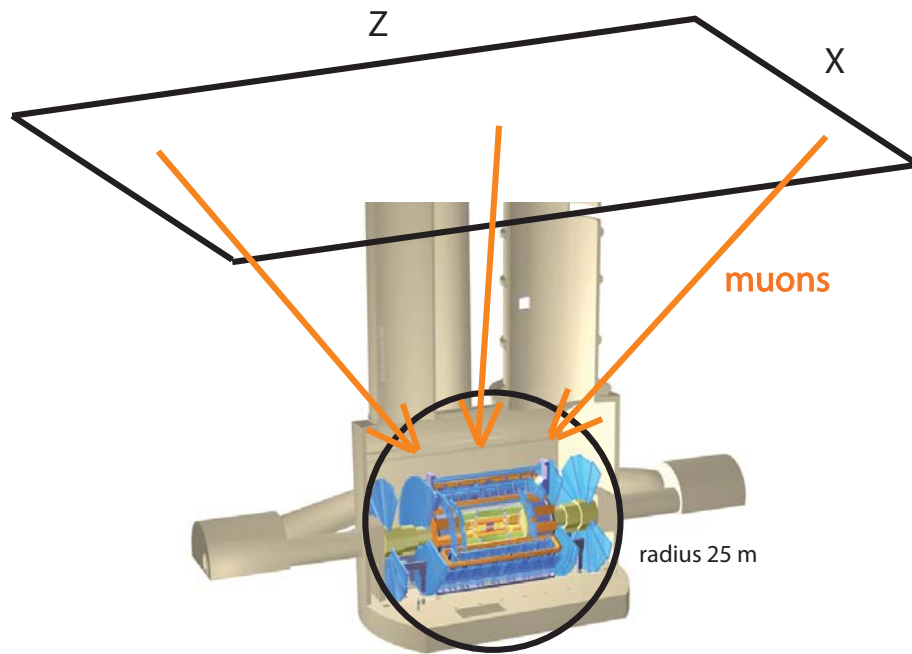


Figure 8.3: Schematic view of cosmic Monte Carlo simulation. A single cosmic muon is generated inside fixed area, and events are filtered to have the muon point to ATLAS.

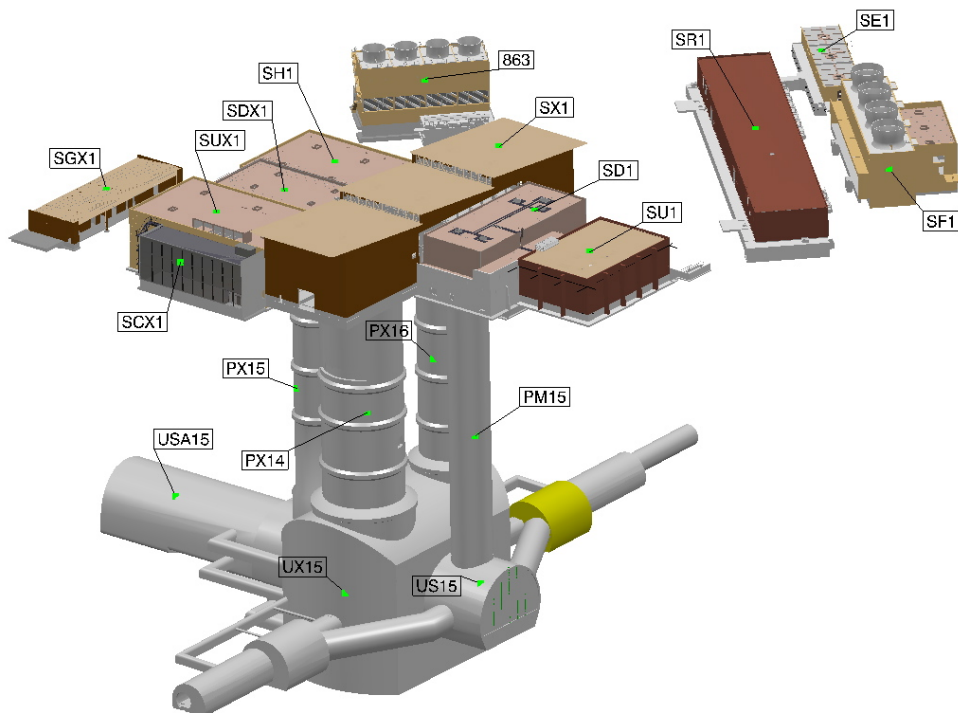


Figure 8.4: Layout of ATLAS cavern at Point 1. Surface buildings and access shafts (PX14, PX15, PX16) are shown.

mentum (10 - 100 GeV, 100 - 300 GeV, 300 GeV - 1 TeV, 1 - 3 TeV, 3 - 5 TeV) [A.3.4.42], in order to provide enough statistics even in high momentum tails.

Figure 8.5 shows the Z-X distributions (Z: the direction of the beam line, X: direction pointing to the center of the LHC ring, Y: direction pointing perpendicular to the ground) of the generated muons which survived the filtering. The effects from the shafts are visible for low energy cosmic muons (the upper left figure). Considering the thickness of the ATLAS overburden (~ 100 m), the expected “cut-off” of muons reaching the detector is around 50 GeV [116]. The cut-off momentum is visible in the simulated momentum distribution of muons reaching the detector (Figure 8.7). Thus, for low energy muons, the most-likely way for them to reach the detector is by passing the shaft and avoid the interactions with materials. The effects of the shafts were confirmed also from the real cosmic data (Figure 8.6), where the impact points of cosmic muons at the ground level are estimated from the extrapolation of muon tracks reconstructed by RPC hits [106]. On top of the two large shafts used for the detector transport (PX14 and PX16), effects from two small elevator shafts (PX15 and PM15) were visible in the real data. These small shafts are currently not included in the cosmic simulation (planned to be included in newer Athena versions). Since the shafts make significant effects mostly on low energy muons, and also considering the small size of the elevator shafts, their impact will not be critical for the current studies, which the main emphasis is on high energy cosmic muons depositing large energy in the calorimeters.

Figure 8.8 shows the momentum distribution of Muon Spectrometer tracks from cosmic run 91890 L1Calo stream and Monte Carlo simulation samples. Run 91890 was one of the long runs with good quality of the muon spectrometer and other detector conditions. Since, the trigger simulation is currently not included in the cosmic Monte Carlo samples, only events with a jet with $E_T > 20$ GeV were considered in the plot to avoid trigger effects. The Monte Carlo simulation samples from each muon momentum slices were merged considering the flux, and normalized to data by entries. The shape of the distribution is well described by the simulation. We will further look into the calorimeter information with the cosmic ray data and Monte Carlo simulation in the following sections.

8.3 High Energy Events from Cosmics

High energy deposits in the ATLAS calorimeters from cosmic rays have been observed for several years, as reported in the previous notes [96][119]. These energy deposits, ranging from tens of GeV up to several TeV, can arise from noisy channels, air shower events, and muons undergoing a hard bremsstrahlung in the calorimeters. An additional source of “fake” energy deposit can include an incorrect signal reconstruction due to errors in the calibration or a distorted pulse shape. In the following section we investigate high energy events in recent cosmic ray runs and discuss their possible origins.

In Figure 8.9, the distribution of the total transverse energy of all calorimeter cells with energy larger than twice the electronic noise (so called “Sum E_T ” in Athena MET_Base algorithm), were calculated and shown for run 90272 L1Calo stream. This run was an overnight run with good detector quality on September 28, 2008, with the time duration

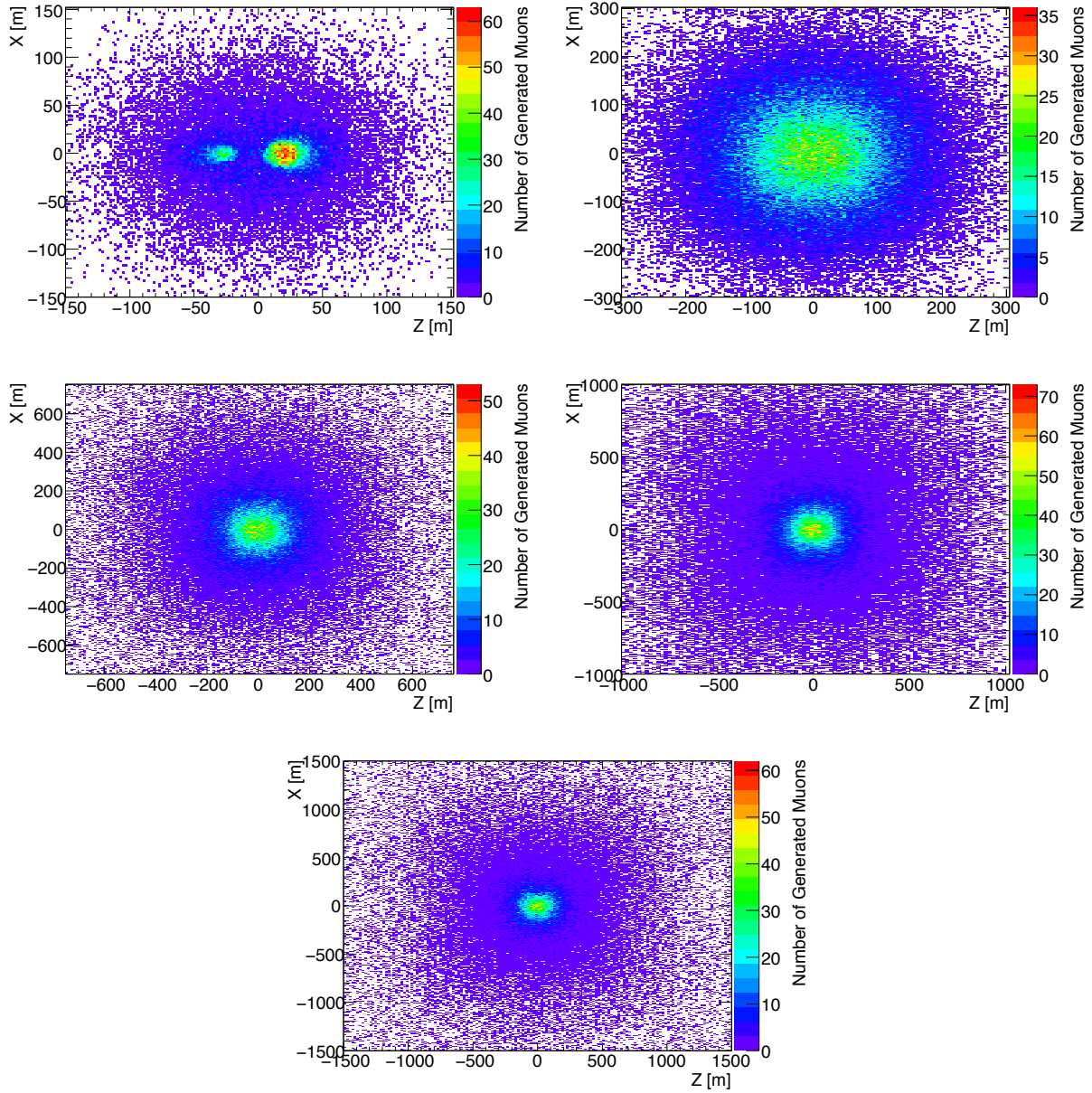


Figure 8.5: Origin of cosmic muons at the surface in the Monte Carlo simulation. Each figure consists of different muon momentum ranges; 10 - 100 GeV (upper left), 100 - 300 GeV (upper right), 300 GeV - 1 TeV (middle left), 1 - 3 TeV (middle right), and 3 TeV - 5 TeV (bottom).

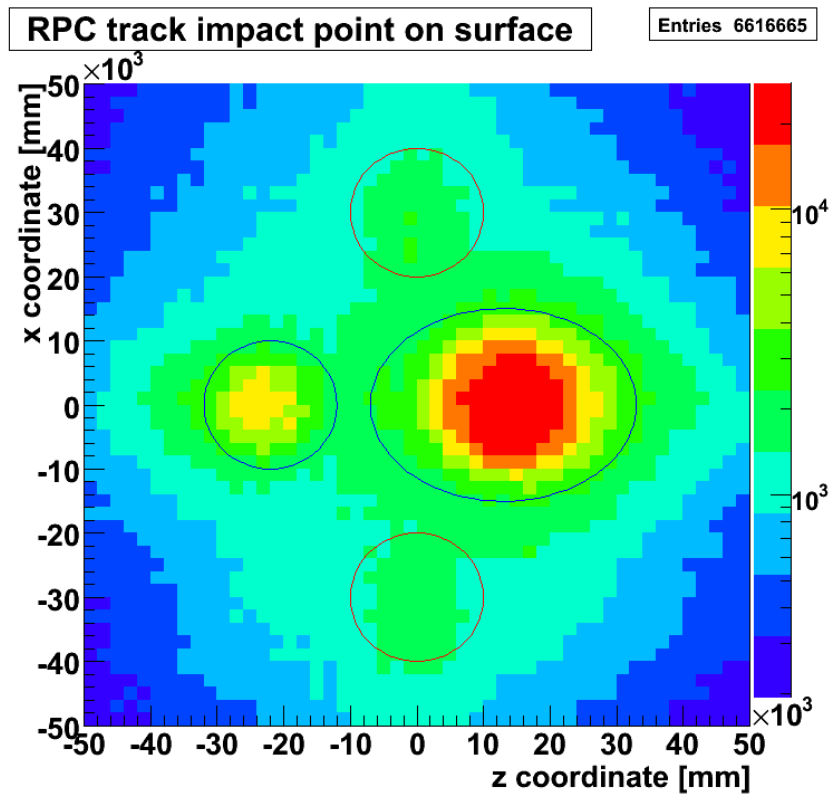


Figure 8.6: Impact point of cosmic muons on surface from the cosmic ray data, estimated from the extrapolation of muon tracks reconstructed by RPC hits [106].

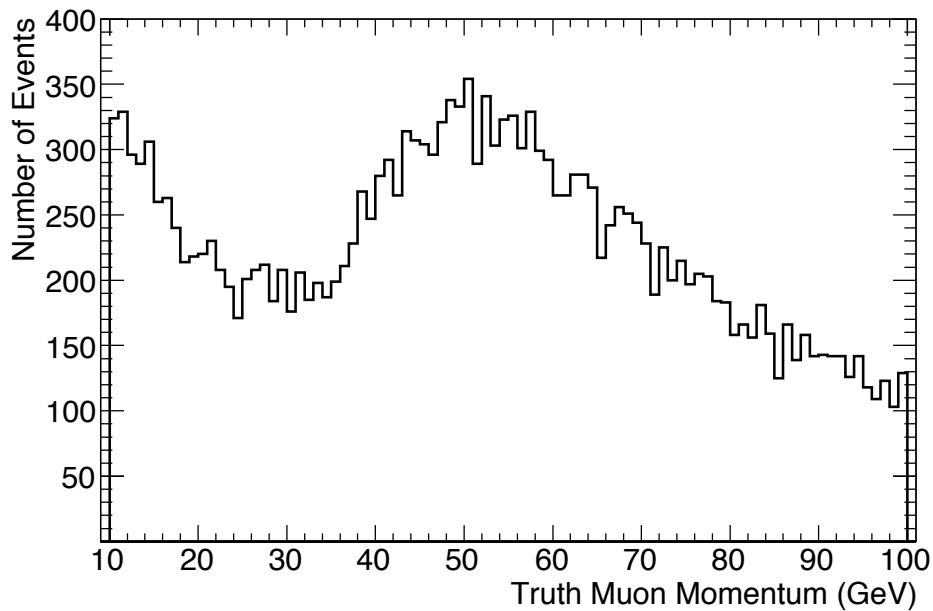


Figure 8.7: Momentum of generated muons that reached the ATLAS detector. A cut-off around 50 GeV is visible in the distribution.

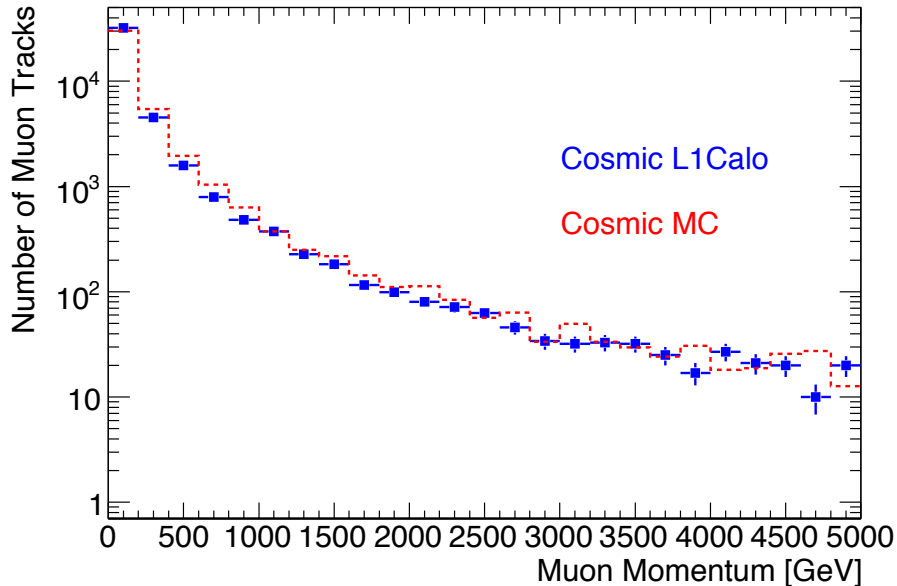


Figure 8.8: Momentum distribution of stand-alone muon spectrometer tracks in cosmic data run 91890 L1Calo stream and cosmic Monte Carlo samples. Cosmic Monte Carlo is normalized to data by entries.

of 16 hours, having 350k events recorded in the L1Calo stream. Only events with a jet ($E_T > 20$ GeV) were included in the figures in order to consider the trigger effects in the simulation as well.

Cosmic Monte Carlo samples are produced in the way mentioned in the previous section. The simulation only considers single muon events, and does not generate any air showers. From the simulation, we confirmed that the TeV energy deposit is actually possible from a single cosmic muon [A.3.4.42]. These high energy deposits in the calorimeters are due to the hard bremsstrahlung from high energy muons (will be explicitly shown in Section 8.4.2). There was a discrepancy of about 7 % in the absolute event rate between the cosmic Monte Carlo simulation and real data. This is rather a good consistency considering that the uncertainty in the previous measurements of cosmic ray flux are large [116]. The Monte Carlo samples in Figure 8.9 are normalized to data by the entries. The same normalization factor was applied to the corresponding plots in various calorimeter regions (Figure 8.10). The triggered event rate in the stream is summarized in Table 8.2. TeV events were recorded in 6×10^{-4} Hz, which is about 2 events per hour. The shape of the distributions are in good agreement throughout various energy regions.

Figure 8.11 is an event display of one of the high energy events from run 90272 L1Calo stream, in which an energy deposit of more than 1 TeV was recorded. In the event display, the green lines show the muon segments. The muon segments in X-Y view (the left figure in Figure 8.11) are pointing to the interaction point, due to the lack of RPC ϕ hits. The yellow boxes indicate energy deposits in the Tile Calorimeter. The direction of the reconstructed jet is shown by the gray marker. The light blue dotted line is the direction

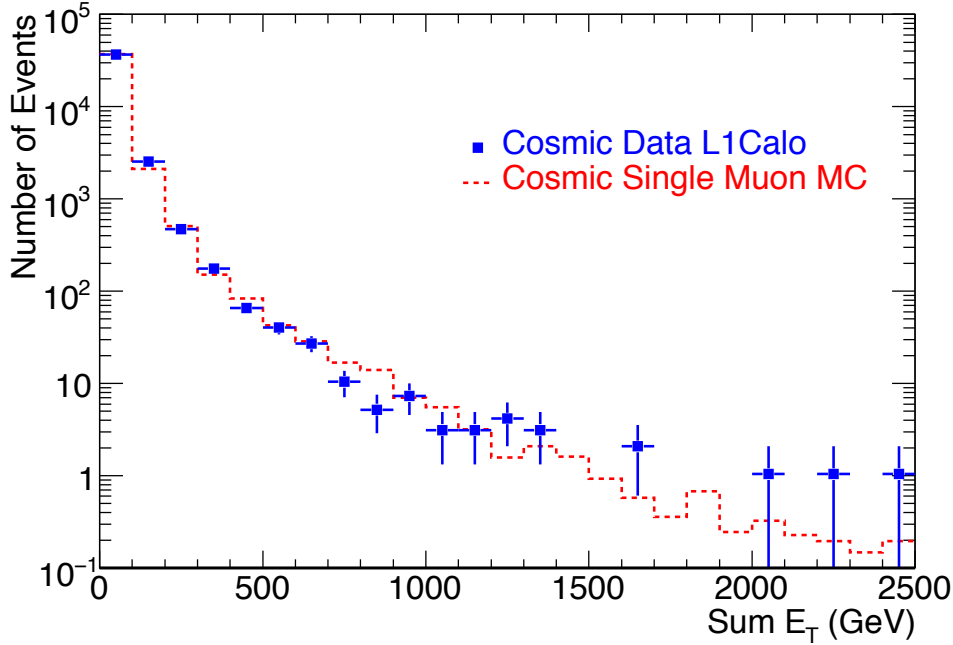


Figure 8.9: Sum E_T distribution from cosmic ray data and Monte Carlo simulation. Run 90272 L1Calo stream data is compared with the cosmic Monte Carlo samples normalized to the data by entries. Energy is calibrated at the EM scale.

of E_T^{miss} . The highlights in the MDT indicate hits (yellow for any hits, and orange when tracks are reconstructed). No track was reconstructed in the inner detector for this event. The R-Z projection is shown in the right figure of Figure 8.11, where the energy deposit in the calorimeter is clearly seen along the muon path. This event most likely arose from a muon undergoing a hard bremsstrahlung. Such events can fake new physics signals such as “monojet” candidates, or even multi-jet signatures when overlapped with QCD events. Figure 8.12 shows an example of air shower events from the same run and stream. Air shower events also contribute to the high energy tail of the Sum E_T distributions, and can initiate a fake multi-jet signature. Such events can be identified by the presence of numerous numbers of reconstructed muon segments. We explore strategies to tag and remove those non-collision background in Section 9.1.3.

8.4 Test of Object Reconstruction in the Calorimeters

8.4.1 Topological Clusters in Cosmic Ray Data

The number of clusters per event reconstructed from cosmic ray data is shown in Figure 8.13. During M5 runs, the electronic noise in LAr was overestimated in the database;

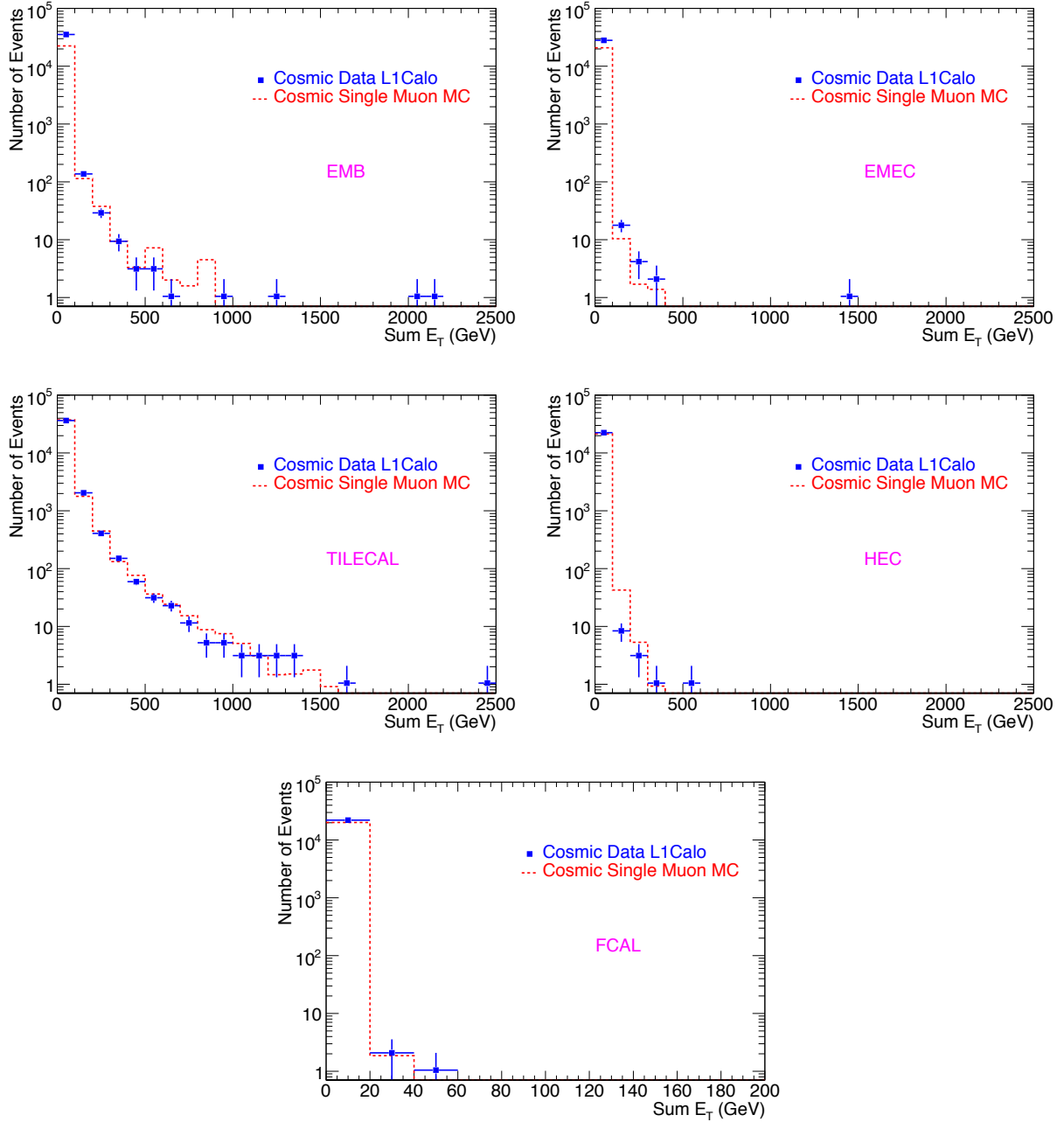


Figure 8.10: Sum E_T distribution in each calorimeter partition in run 90272 L1Calo stream. Energy is calibrated at the EM energy scale. From the upper left, distributions from LAr EM Barrel, LAr EM End-cap, TileCal, LAr hadron End-cap, LAr Forward, are shown. The normalization factor for the Monte Carlo samples are the same as the one used in Figure 8.9

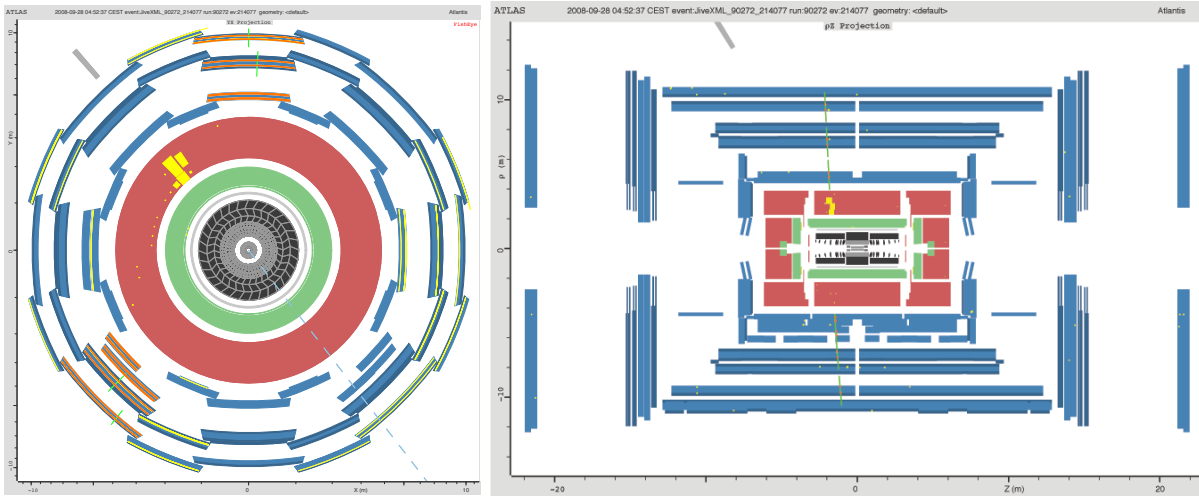


Figure 8.11: A TeV event in run 90272 L1Calo stream.

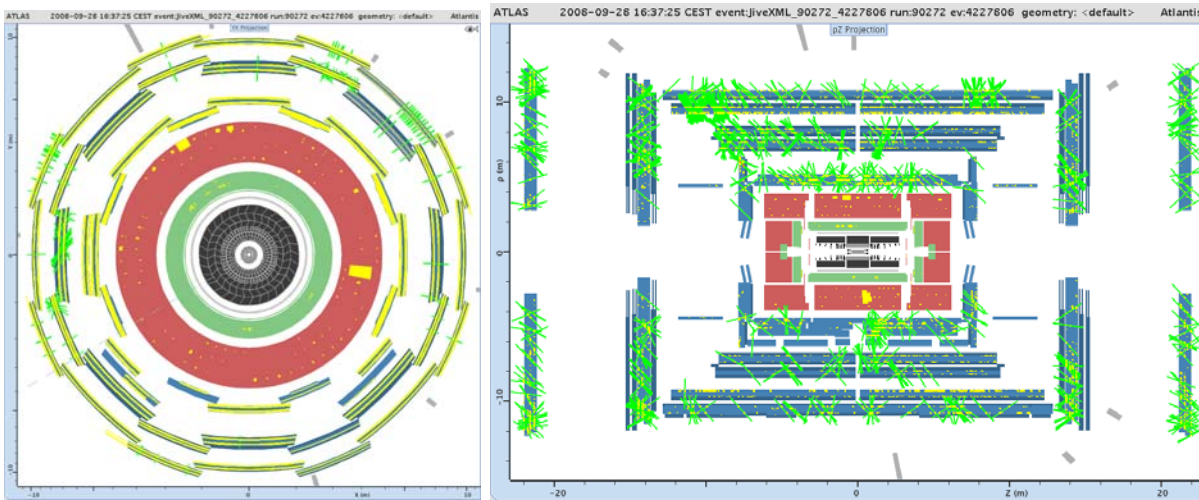


Figure 8.12: An air shower event in run 90272 L1Calo stream.

Table 8.2: Triggered event rate of high energy events in run 90272 L1Calo stream

| Sum E_T | Overall Rate [Hz] | TileCal Rate [Hz] | LAr EM Rate [Hz] |
|-----------------|--------------------------------|--------------------------------|----------------------------------|
| 20 - 50 GeV | 2.689 ± 0.007 | 1.181 ± 0.005 | $(6.8 \pm 0.1) \times 10^{-2}$ |
| 50 - 100 GeV | 0.320 ± 0.002 | 0.173 ± 0.002 | $(1.11 \pm 0.04) \times 10^{-2}$ |
| 100 - 500 GeV | $(9.0 \pm 0.1) \times 10^{-2}$ | $(6.5 \pm 0.1) \times 10^{-2}$ | $(3.6 \pm 0.3) \times 10^{-3}$ |
| 500 GeV - 1 TeV | $(2.2 \pm 0.2) \times 10^{-3}$ | $(2.0 \pm 0.2) \times 10^{-3}$ | $(1.0 \pm 0.4) \times 10^{-4}$ |
| > 1 TeV | $(6 \pm 1) \times 10^{-4}$ | $(5 \pm 1) \times 10^{-4}$ | $(7 \pm 3) \times 10^{-5}$ |

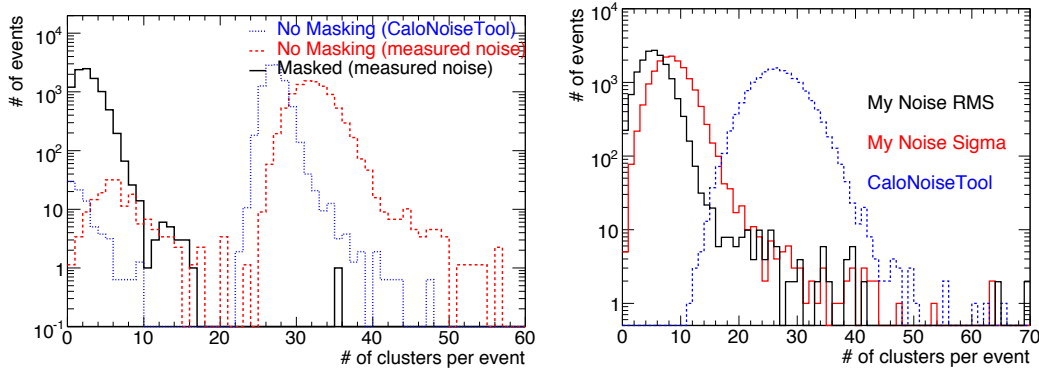


Figure 8.13: The number of EMTopoclusters in M5 run 29576 NIM0 stream (left). The number of Tile Topoclusters per event in the same run and stream (right).

thus by using the correctly-measured noise had the effect of increasing the number of clusters. After masking bad LAr channels, the number of EMTopoclusters significantly decreased, close to the level expected from Monte Carlo simulation.

In TileCal, bad channels were masked in the default reconstruction. In contrast to LAr, the electronic noise for TileCal was underestimated in the database, and the number of Tile Topoclusters significantly decreased after the correctly-measured noise values were used. A slight difference was observed when the noise in TileCal was defined as the sigma of from a Gaussian fit compared to the RMS of the cell energy distribution. This is due to the fact that the cell energy distribution in TileCal has non-Gaussian tails, as mentioned in Section 7.1. In that case, we recommend the use of the RMS of the cell energy distribution for TileCal cluster reconstruction.

From our investigation, we find that:

- Fake Topoclusters are formed from bad channels (noisy channels), because those channels become “seeds”.
- Wrongly-estimated noise values in the database significantly affect the number of reconstructed clusters per event.

The energy distribution of Tile Topoclusters is shown in Figure 8.14 for M5 run 29576, using both TGC-triggered events and TileCal-triggered events (NIM0 stream; this stream

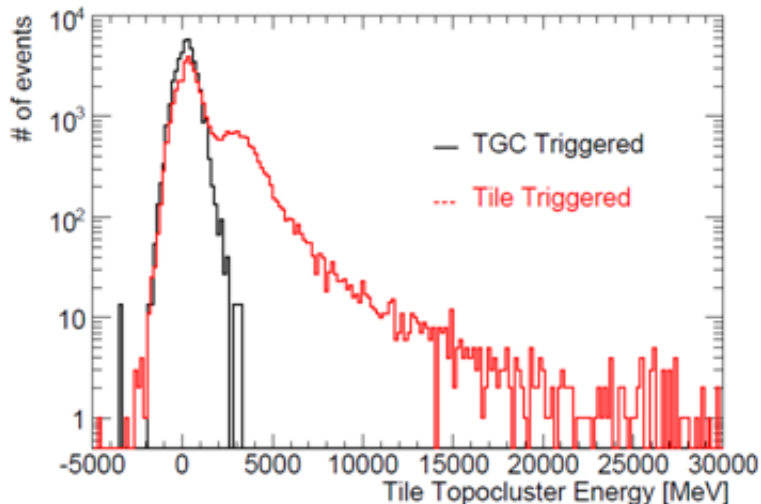


Figure 8.14: Energy of Tile Topoclusters for M5 run 29576, for both TGC-triggered and Tile-triggered events.

was later merged with CosmicMuons stream in Fall 2008 data). The distribution from TGC-triggered events is normalized to that from the NIM0 stream to compare the shape of the distributions. Here, the TileCal cluster energies from TGC-triggered events are found to be almost pedestal-like, since those events rarely hit TileCal due to the geometry of the trigger. Thus, a clear separation of clusters originating from noise and those formed from muon energy deposits is observed. A peak around 3 GeV was observed in Tile Topoclusters from the NIM0 stream, which is consistent with what we expect from muon energy deposits in TileCal.

8.4.2 Jet Reconstruction With Cosmic Ray Data

Jets are highly collimated bundles of hadrons (and their decay products) produced by the fragmentations of quarks and gluons. The performance of jet reconstruction is crucially important for Standard Model measurements such as jet cross sections, as well as for new physics searches (Supersymmetric particle search, Higgs particle search, extra-dimensional black holes, etc.) Here, the jet reconstruction schemes used in ATLAS are briefly reviewed, and their performance is shown.

Jet Algorithms in ATLAS

There are several jet finding schemes implemented in ATLAS: fixed cone jet finder, sequential recombination such as k_T algorithms, and etc. [23] Each jet finding schemes make use of calorimeter clusters as inputs and scan the calorimeters and form a jet. Combined towers and Topoclusters are the standard inputs to jet reconstruction. An overview of jet reconstruction in ATLAS is shown in Figure 8.15.

In the fixed cone jet finder, all cluster inputs are sorted in decreasing order of their transverse momenta p_T . When the cluster with the highest p_T is above the seed threshold

($p_T > 1$ GeV), all the clusters within the defined cone size R_{cone} are combined with the seed. A new direction is calculated from the sum of the four-momenta from all the combined clusters, and combining the surrounding clusters will be iteratively done until the new seed is stable and stays the same as the one before the iteration. When the jet is stable, the next iteration will start with the next-leading clusters passing the seed threshold. Such procedures continue until all the inputs are considered for jet reconstruction. Cone size of 0.7 has been proposed for the QCD dijet studies, and smaller cone size of 0.4 has been used in Top and supersymmetric search studies, where events tend to be more crowded and have more jets.

“Jets” in Cosmic Ray Data

“Fake jet” can be formed from calorimeter noise, bad channels, and cosmic rays. Running jet reconstruction on cosmic ray events is an important approach to validate the reconstruction software and study the jet algorithm performance at an early stage before collision data are available. Fake jets from the effects mentioned above have been observed in the real cosmic data, and understanding their properties will lead to the development of possible quality cuts on jets. (Note that here we refer to “jet” as the results of running reconstruction algorithms on cosmic ray data, not to be confused with the real hadron jets that will result from proton-proton collisions.)

In Figure 8.16, the number of reconstructed jets with an $E_T > 7$ GeV cut is shown for 2 cone sizes ($R = 0.4$ and 0.7) and 2 types of input (combined towers and Topoclusters). $E_T > 7$ GeV is the default transverse energy threshold used for jet containers in the ATLAS data model. Figure 8.17 shows the same distributions, except that the threshold is raised to $E_T > 20$ GeV, which is the standard transverse energy cut applied for physics analyses. The triggered event rate of reconstructed jets are also summarized in Table 8.3 (for TopoJets with cone size 0.4 and $E_T > 20$ GeV).

In Figure 8.18, the distribution of reconstructed jet transverse energy is shown for CosmicMuons and L1Calo stream. In the CosmicMuons and L1Calo streams, a larger number of jets was reconstructed compared to the RNDM stream. This gives the first indication that additional fake jets can be initiated by the energy deposits of cosmic ray muons. Figure 8.19 confirms the hypothesis, since the reconstructed jets are found to be concentrated around $\phi \sim \pm\pi/2$ for the CosmicMuons stream, which is triggered by the RPC and TGC. In the L1Calo stream, jets populated the entire $\eta - \phi$ region (Figure 8.20). This is due to the fact that L1Calo does not require such a top-bottom coincidence, but rather simply an energy deposit over threshold in the entire calorimeter.

Multi-jet events are also observed in the CosmicMuons and L1Calo streams. These events are likely formed by air shower events, which is supported by the observation of multiple hits in the muon spectrometer system. An example event display of such an event is shown in Figure 8.12.

Finally, comparison of jet transverse energy distributions from run 90272 L1Calo stream and cosmic Monte Carlo simulation samples was done for Cone4H1TowerJets and Cone4H1TopoJets (Figure 8.21). The normalization factor extracted from Figure 8.9 was used, and the distributions were well consistent for both the TowerJets and TopoJets.

Jet Reconstruction Sequences

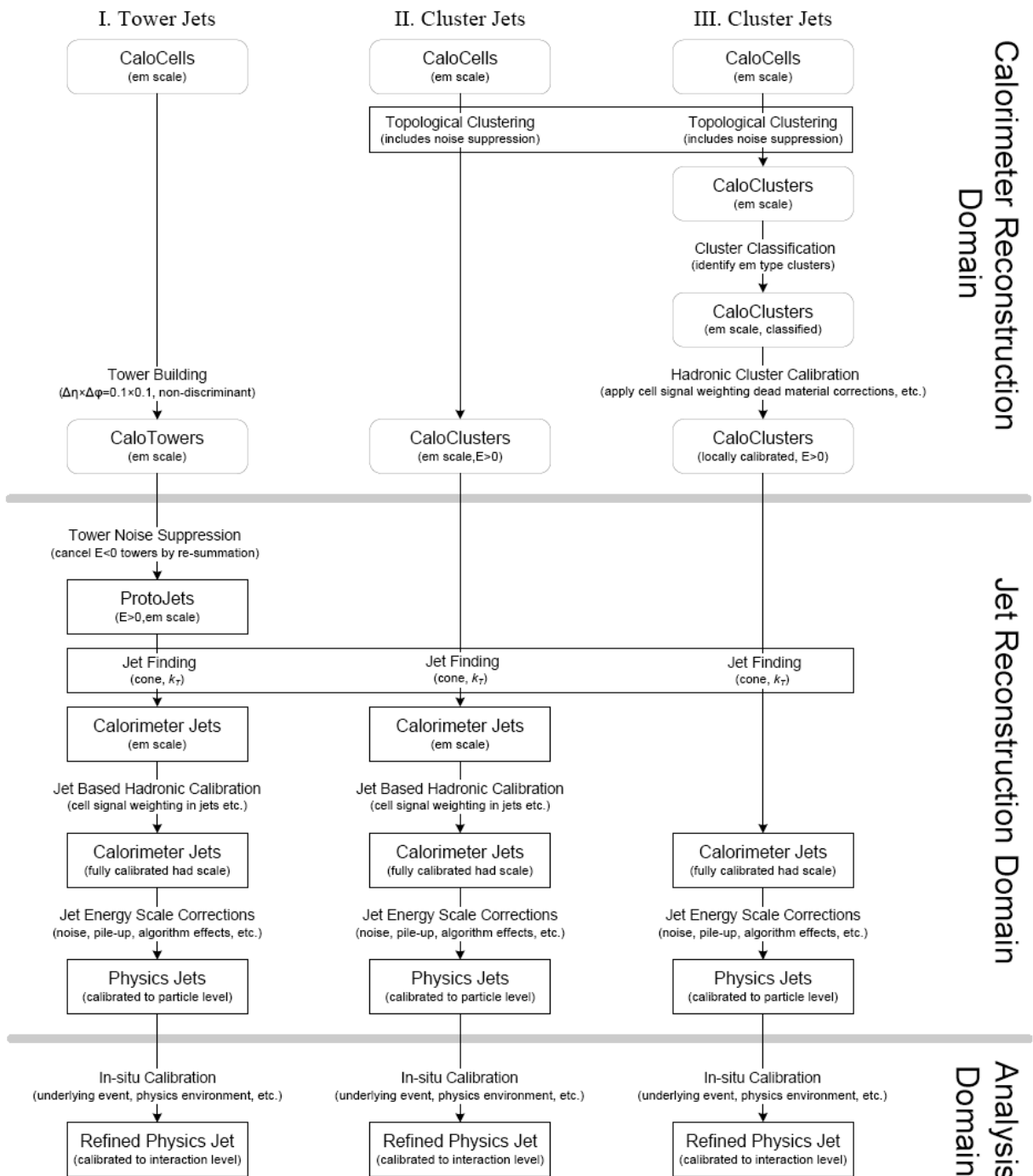


Figure 8.15: Schematic overview of jet reconstruction in ATLAS.

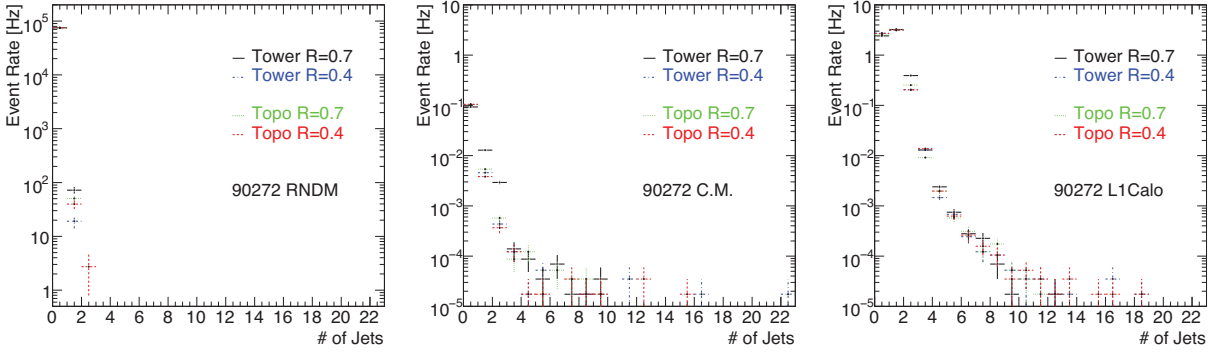


Figure 8.16: Number of reconstructed cone-algorithm jets ($E_T > 7$ GeV) for various cluster input and cone size, in run 90272 for RNDM stream (left), CosmicMuons stream (center), and L1Calo stream (right).

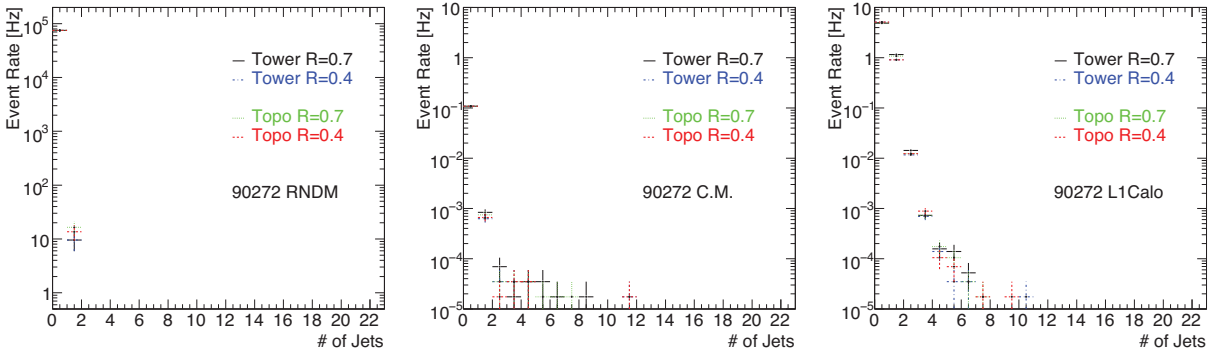


Figure 8.17: Number of reconstructed cone-algorithm jets ($E_T > 20$ GeV) for various cluster input and cone size, in run 90272 for RNDM stream (left), CosmicMuons stream (center), and L1Calo stream (right).

Table 8.3: Triggered event rate for numbers of TopoJets per event (cone size 0.4 and $E_T > 20$ GeV) in run 90272.

| Number of Jets | L1Calo stream [Hz] | CosmicMuons stream [Hz] |
|----------------|----------------------------------|----------------------------|
| 0 | 5.146 ± 0.009 | 0.109 ± 0.001 |
| 1 | 0.909 ± 0.004 | $(7 \pm 1) \times 10^{-4}$ |
| 2 | $(1.23 \pm 0.05) \times 10^{-2}$ | $(2 \pm 2) \times 10^{-5}$ |
| ≥ 3 | $(1.1 \pm 0.1) \times 10^{-4}$ | $(9 \pm 4) \times 10^{-5}$ |

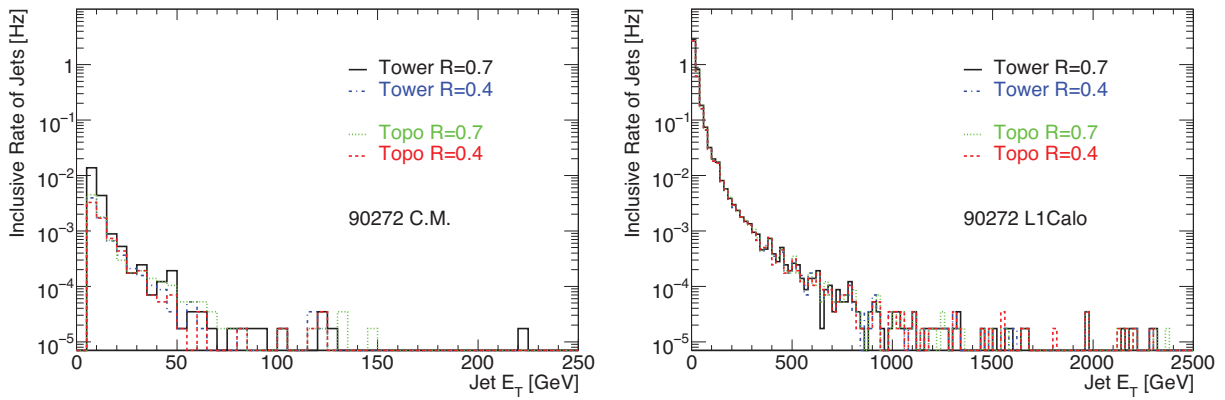


Figure 8.18: Transverse energy of reconstructed jets in post-M8 run 90272 for three different trigger streams. Jets with $E_T > 7$ GeV are shown.

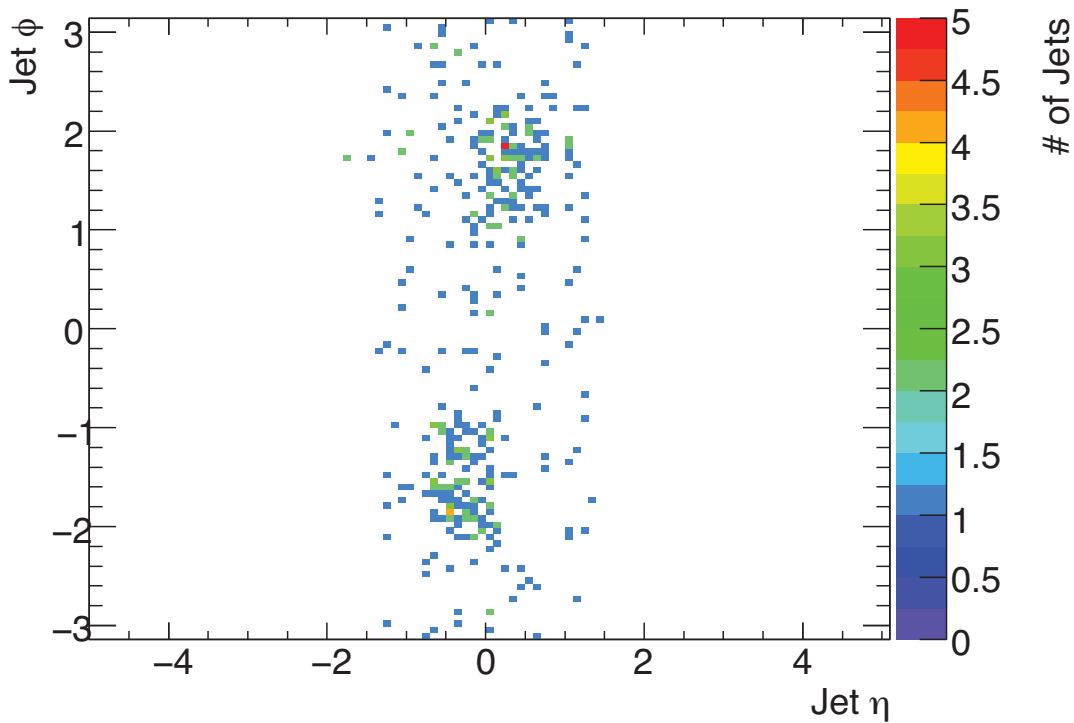


Figure 8.19: Reconstructed jets' η - ϕ distribution for post-M8 run 90272 CosmicMuons stream, showing TowerJets with cone size 0.4 and $E_T > 7$ GeV (left), TopoJets with cone size 0.4 and $E_T > 7$ GeV (right).

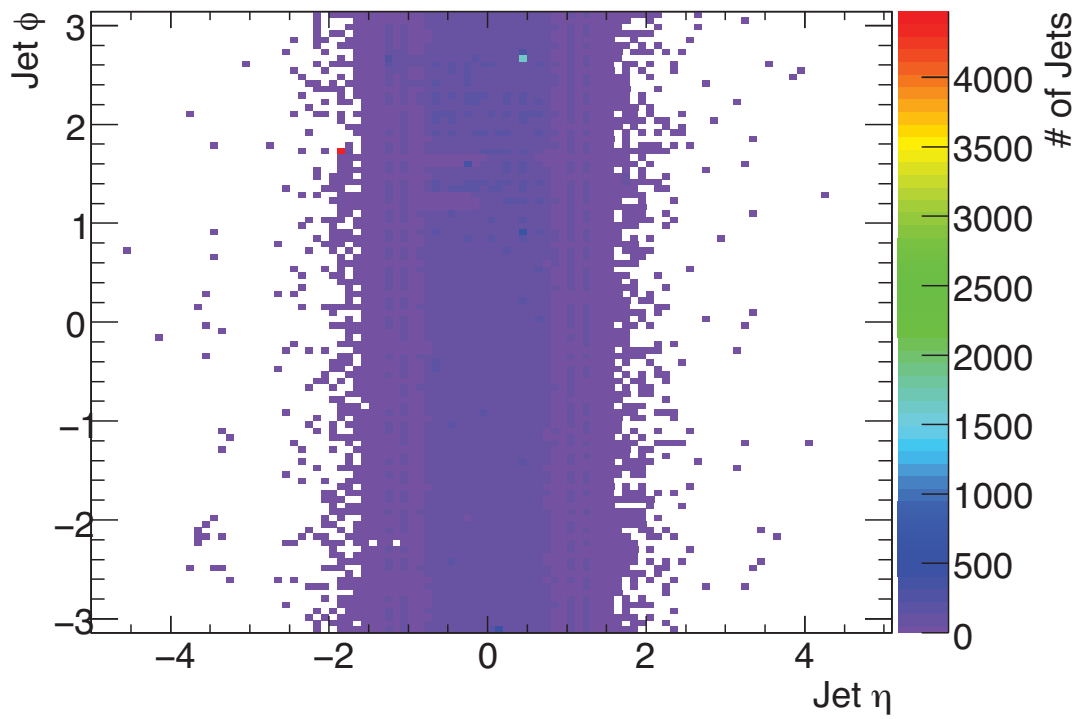


Figure 8.20: Reconstructed jets' η - ϕ distribution for post-M8 run 90272 L1Calo stream, showing TowerJets with cone size 0.4 and $E_T > 7$ GeV (left), and TopoJets with cone size 0.4 and $E_T > 7$ GeV (right).

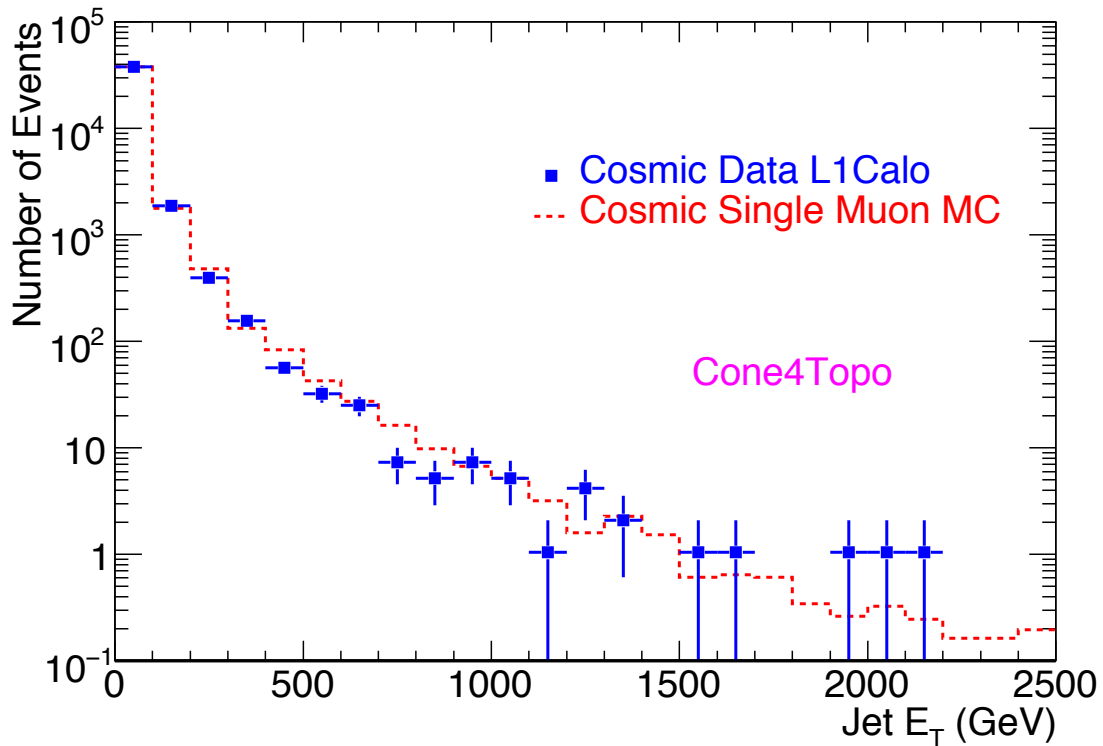
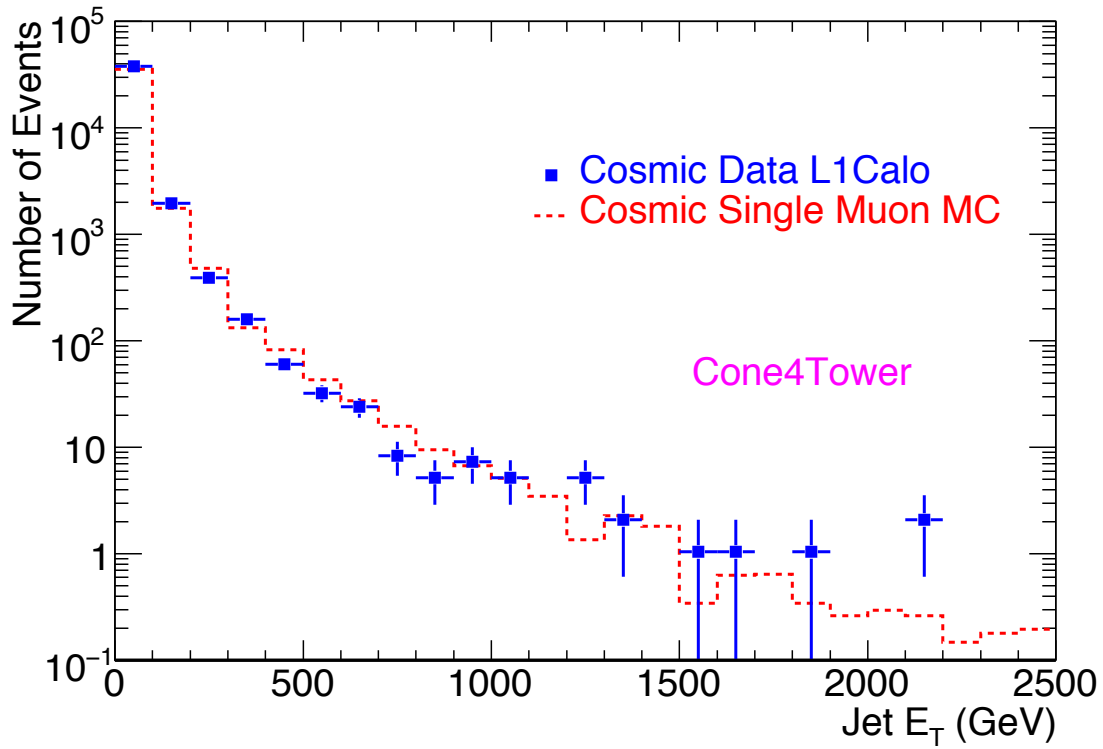


Figure 8.21: Comparison of Jet distributions in run 90272 L1Calo stream with cosmic Monte Carlo samples for TowerJet (top) and TopoJet (bottom). The normalization factor in Figure 8.9 was used.

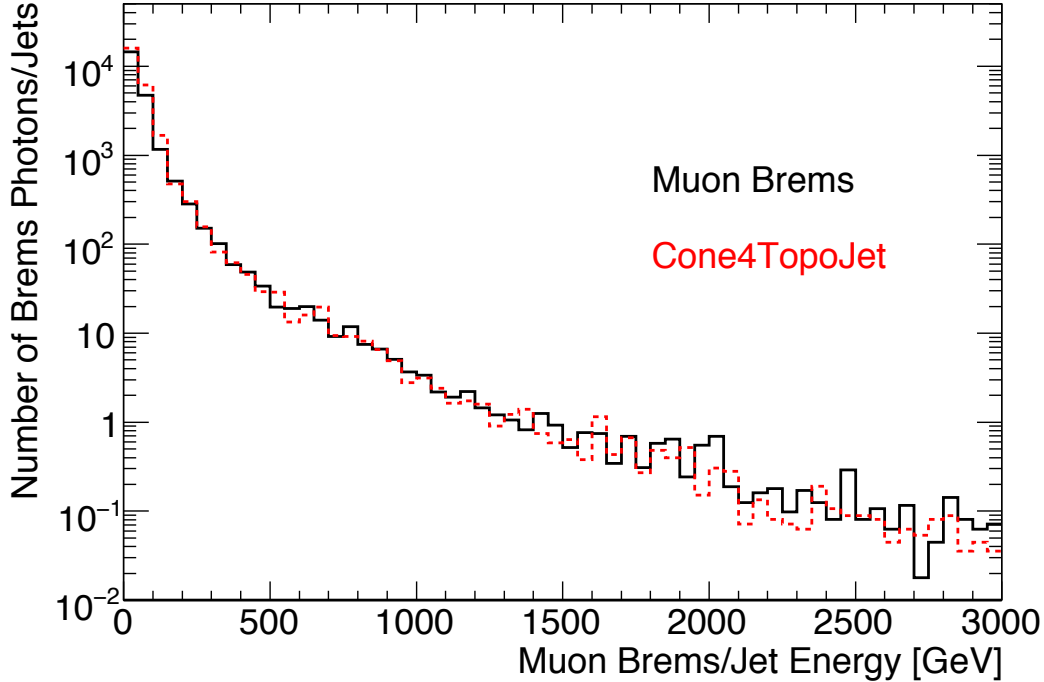


Figure 8.22: Comparison of energy distributions of bremsstrahlung photons from cosmic muons and reconstructed “fake” jets in cosmic Monte Carlo samples.

Figure 8.22 compares the energy distributions of “fake jets” reconstructed from calorimeter clusters and the bremsstrahlung photons from the muons in the cosmic Monte Carlo simulation. Using the Monte Carlo’s generation profile, photons emitted from the cosmic muons within the calorimeter volume were considered in the figure. Through this comparison, it was confirmed that the “fake jets” mostly originates from hard bremsstrahlung photons from the cosmic muons, since the energy distributions of the bremsstrahlung photons and the fakely reconstructed jets are very well consistent including the normalization. The small discrepancy in the lower energy region is due to the feature of jet reconstruction, such as the splitting or merging of the reconstructed objects.

8.4.3 Missing Transverse Energy Reconstruction Using Cosmic Ray Data

As mentioned in the previous chapter, E_T^{miss} is a variable which indicates the magnitude of energy imbalance in the plane perpendicular to the beam axis. In order to make use of this variable for physics measurements, we must control any sources that lead to a “fake” E_T^{miss} .

In previous notes [119], we found that electronic failures in the calorimeter front-end electronic can easily generate tens of GeV of E_T^{miss} and that cosmic ray air showers and cosmic ray muons undergoing hard bremsstrahlung can generate hundreds of GeV of

E_T^{miss} . Figure 8.23 shows E_T^{miss} distributions from run 90272 L1Calo stream with the MET_Base and MET_Topo algorithm. Cosmic Monte Carlo samples are normalized to the data with the same normalization factor mentioned before. Only events with a jet ($E_T > 20$ GeV) were included in the figures in order to consider the trigger effects in the simulation as well. Good agreement between data and Monte Carlo was observed. Figure 8.24 shows a 2-dimensional plot of Sum E_T versus E_T^{miss} from an M8 run [96]. Since we are looking at cosmic events (and some contribution from noisy channels), there is a strong correlation between Sum E_T and E_T^{miss} . This indicates that the high energy deposits from cosmic and/or unmasked noisy channels in the calorimeters are responsible for the large E_T^{miss} values, as expected.

These sources of fake E_T^{miss} can be a serious background to Standard Model measurements and in searches for new physics. Initial cleaning cuts to remove such sources of fake E_T^{miss} , such as those based on calorimeter timing [122]-[128], were studied, together with cuts on the calorimeter electromagnetic fraction, F_{em} in the previous note [119]. Investigations on these cleaning cuts will be described in detail in Section 9.1.3.

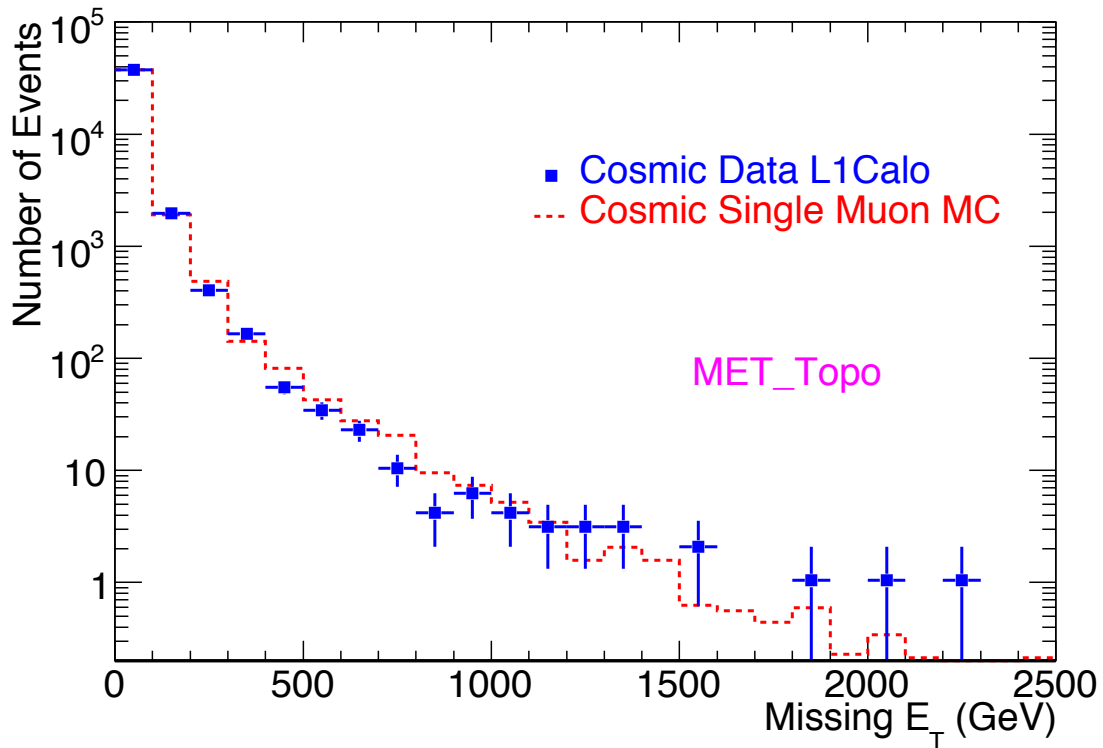
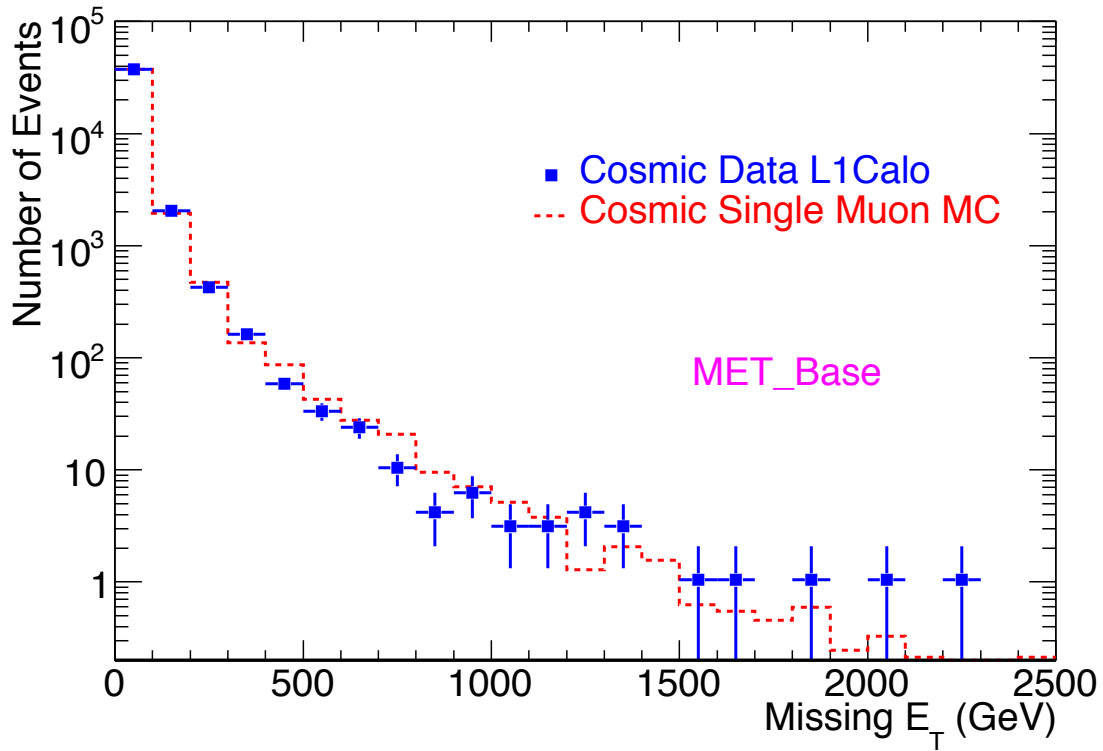


Figure 8.23: E_T^{miss} from MET_Base algorithm (top) and MET_Topo algorithm (bottom) in post-M8 run 90272 triggered by the L1Calo. Cosmic Monte Carlo samples are normalized to data using the same factor as in Figure 8.9.

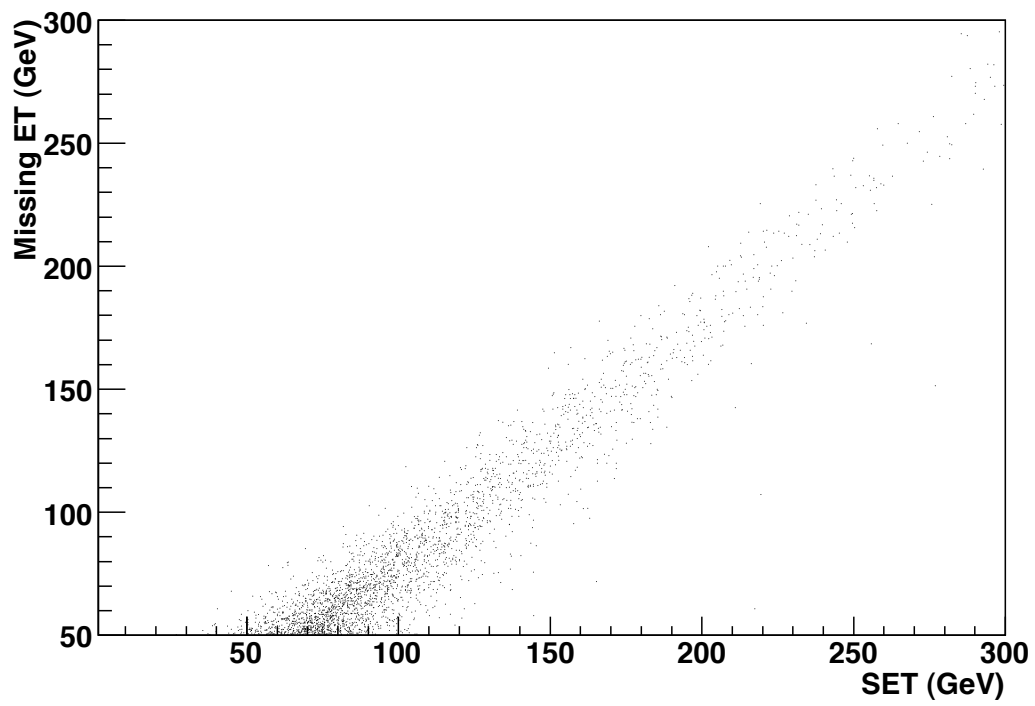


Figure 8.24: Sum E_T vs E_T^{miss} as measured in M8 run 77585.

Chapter 9

Quality of Calorimeter Objects

As described in Chapter 7 and 8, detector failures, cosmic rays and other non-collision backgrounds can originate high-energy in the calorimeters, and deteriorate the energy measurement during the collision data taking. Such contributions will be obstacles to physics analyses using the calorimeters. Thus, it is of great importance that we develop strategies to identify and remove such effects from the non-collision background. Here, the quality of reconstructed calorimeter objects was proposed at various stages of event reconstruction; from the channel-level, cluster-level, and to the jet and event-level.

The most ideal strategy is to identify the channels affected by non-collision sources, and recover the correct energy. However, such strategy is not always possible due to the difficulty in identifying the origin of the background, and also in recovering the correct energy especially in case of overlaps of cosmic muons or beam halos. The offline rejection of non-collision background by applying cuts on quality variables of calorimeter objects is often called “cleaning.” This is rather a fall back solution to discard the physics objects or even events which seem to be contaminated with non-collision background. This strategy was highly used in the Tevatron experiments, and played a very important role especially in the new physics searches using jets and E_T^{miss} .

The rejection power and the efficiency of those cleaning cuts were investigated in this chapter. Note that choice of quality cuts and their optimal thresholds are analysis-dependent. This chapter is dedicated to show the possible cleaning cuts to be used in various analyses, and is not intended to fix the strategies. An adoption of these cleaning cuts for monojet search is discussed in Chapter 11.

The first half of the chapter is dedicated to the investigations with pure cosmic events. However, the rejection power and signal efficiency of those cleaning cuts can change when the energy deposits from cosmic or beam halo muons overlap with collision events (e.g. Minimum Bias, QCD di-jet), and the rate of such overlap is dependent on the luminosity. The software algorithm called the “Event Overlay,” which allows to combine two different events (in this case, a cosmic ray event and Monte Carlo event) and run the reconstruction, was used for the study. The latter half of the chapter shows the performance of the cleaning cuts under such “overlaid” conditions.

9.1 Quality Variables and Cleaning Cuts

In order to discriminate the signal and background, we searched for useful variables which successfully tag and reject the background and still keep the signals with high efficiency. Background rejection can be performed at the various stages of reconstruction of energy deposits in the calorimeters, and the variables to be used for cleaning cuts can be categorized as the following,

- Channel-level qualities: identification of problematic channels, quality factor of the pulse shape fit from calorimeter channels.
- Cluster-level qualities: energy fraction of the cell with the highest energy (or 2 highest energy cells) inside Topoclusters, timing information from Topoclusters, other geometrical features.
- Jet-level qualities: electromagnetic (EM) energy fraction, number of associated tracks, number of clusters and cells in jets.
- Event-level qualities (used for “ E_T^{miss} cleaning”): timing information, jets’ E_T weighted-average of EM fraction, numbers of tracks, clusters, or cells.

Here, we concentrate on jet, and event-level quality, which are crucially important for new physics searches using jets and E_T^{miss} (e.g. SUSY, extra dimensions). We have developed series of “data cleaning cuts,” which can be performed at various stages of event reconstruction and analysis. Note that the validity of cleaning cuts highly depends on the physics analyses as previously mentioned and their event signatures, and thus some of the cleaning cuts can be powerful tools for some analyses but can be inappropriate for others (will be mentioned again in the following sections).

9.1.1 Jet-level quality

Here, some quality cuts which can be useful for “cleaning” fake jets, will be mentioned.

Jet Electromagnetic Fraction

The electromagnetic (EM) fraction is an example of a powerful cleaning cut, and has been used in the previous experiments at the Tevatron. The EM fraction can be defined as the ratio of the energy deposited in the EM calorimeters to the total energy. The first attempt of using the EM fraction for removing cosmic ray backgrounds in ATLAS can be found in [119], in which the EM fraction was calculated not within a single jet, but by adding all the cell energies above a given threshold (the calorimeter EM fraction).

Here, we consider the EM fraction in jets. The jet EM fraction is calculated for each as:

$$\text{Jet EM Fraction} = \frac{(\text{Sum of Energy Deposit in jet in EMB, EMEC})}{(\text{Sum of Energy Deposit in jet for all layers})} \quad (\text{for jet } |\eta| < 3.2) \quad (9.1)$$

Table 9.1: Definition of QCD dijet Monte Carlo samples at the center-of-mass energy of 10 TeV.

| Sample | Leading parton p_T [GeV] | xsec |
|--------|----------------------------|---------------------|
| J1 | 17 - 35 | 0.859 mb |
| J2 | 35 - 70 | 56.15 μb |
| J3 | 70 - 140 | 3.24 μb |
| J4 | 140 - 280 | 150.9 nb |
| J5 | 280 - 560 | 5.18 nb |
| J6 | 560 - 1120 | 0.11 nb |

If we also consider forward jets, the definition should be extended using the first (electromagnetic) sampling layer of the Forward Calorimeter (FCAL):

$$\text{Jet EM Fraction} = \frac{(\text{Sum of Energy Deposit in jet in EMB, EMEC, FCAL0})}{(\text{Sum of Energy Deposit in jet for all layers})} \quad (9.2)$$

For fake jets arising from cosmic ray muons undergoing a hard bremsstrahlung, we expect that the EM fraction will be concentrated around zero or one. This is due to the fact that the energy deposit from bremsstrahlung is highly concentrated in a small region, and thus only in the EM or hadronic calorimeter. For jets originating from electronic noise, we expect that most of the jet energy is isolated in a particular channel or group of nearby channels. In this case, the EM fraction should also be concentrated around around zero or one, depending on whether those channels were in the EM or hadronic calorimeters.

The jet EM fraction from run 90272 is shown in Figure 9.1 for both Cone4H1TowerJets (jets reconstructed by the ATLAS cone algorithm with the cone size of 0.4 and the combined towers as inputs) and Cone4H1TopoJets (jets from the ATLAS cone algorithm with the cone size 0.4 and the Topoclusters as inputs). The jet EM fraction from cosmic L1Calo stream, cosmic Monte Carlo and the QCD dijet Monte Carlo samples are shown in the figure. The details of cosmic Monte Carlo samples were already mentioned in Chapter 8. The QCD dijet Monte Carlo samples are produced in slices considering the leading parton transverse momentum (Table 9.1), to cover adequate statistics even in the high energy range as well. They are called “JX” (X=0~8) samples, where X denotes the “Xth slice” of the QCD dijet samples. J1 to J6 samples are considered in the figure. Jets with transverse energy larger than 20 GeV are shown, and the energy is at the EM scale.

The jet EM fraction from the L1Calo streams is mostly concentrated around 0 or 1 as expected, and they are consistent with the cosmic Monte Carlo simulation. QCD dijet has a large EM fraction value with the peak around 0.8, and thus a clear separation is seen between fake jets from cosmics and the “real” QCD jets.

Note that the negative EM fraction and EM fraction larger than 1 originate from noise with negative energy. Cone4H1TowerJets tend to have larger tails aside the peaks due to the fact that combined towers are more likely to include noise contributions inside jets, compared to Cone4H1Topoclusters. Slight discrepancy between the cosmic data and Monte Carlo for Cone4H1TowerJets (the left plot of Figure 9.1) is due to the electronic

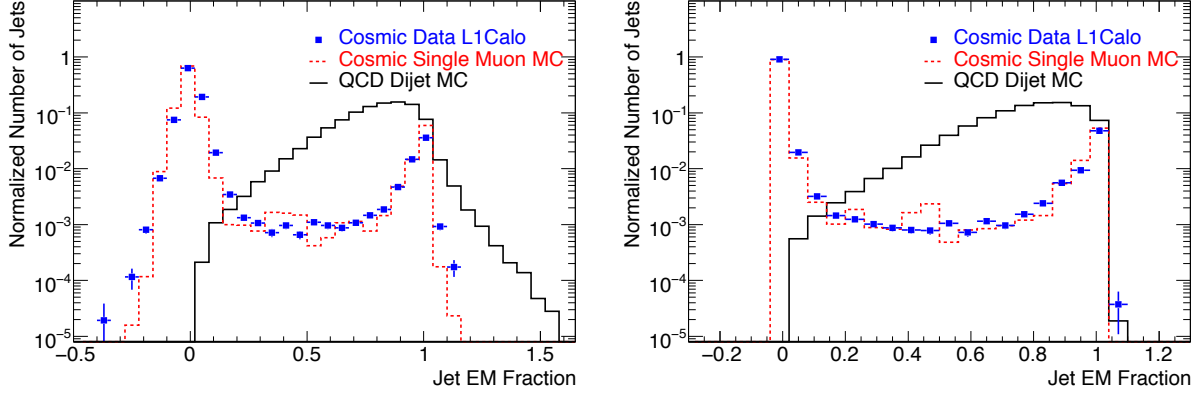


Figure 9.1: Jet EM fraction from Tower jets with cone size 0.4 (left) and Topocluster jets with cone size 0.4 (right) in post-M8 run 90272 and QCD di-jet Monte Carlo samples. Only jets with $E_T > 20$ GeV are shown here.

noise values (especially TileCal) higher in the data than the Monte Carlo. Apart from the effect, the consistency of data and Monte Carlo is very good.

In Figure 9.2, the jet EM fractions are shown for various calorimeter regions. As seen from the plots, the jet EM fraction is effective in all the calorimeter regions including the forward region.

The correlation plots of jet EM fraction and jets' transverse energy from both Tower-Jets and TopoJets are shown in Figure 9.2 for cosmic L1Calo stream and cosmic Monte Carlo. As seen from the plots, most fake jets are concentrated in low E_T region with EM fraction around 0. Note that high E_T jets tend to have better concentration on jet EM fraction 0 or 1, which confirms the validity of the cleaning cuts.

Table 9.2 and 9.3 shows the breakdown of jets remaining after a series of cuts on the jet EM fraction (thus shows the rejection power and efficiency). The low EM fraction cut definitely removes most of the fake jets coming from the noise or cosmics, and still provides good efficiency for the “real” QCD jets. A cut on EM fraction 0.2 removes more than 90% of the reconstructed jets (with $E_T > 20$ GeV) in cosmic runs, but efficiency for the QCD jets remains to be more than 99%. On top of that, a cut on the upper EM fraction also removes additional background [121]. However, an upper EM fraction cut also tends to lower the efficiency of the real QCD jets unlike a lower EM fraction cut. Electrons identified as jets can also be removed by the upper EM fraction cut, so some cares must be taken in case of adopting the upper EM fraction cut. Fake jets with mid-EM fraction values are something that cannot be rejected by the EM fraction cut. Those jets originate when a cosmic muon radiates a bremsstrahlung around the boundary region of the EM and hadronic calorimeter; a cosmic muon forms multiple clusters from hadrons originated from muon's photonuclear interaction; or when there are significant amounts of energy over the whole calorimeter due to air showers (Figure 9.4). For fake jets with mid-EM fraction, other complementary quality cuts will be applied, which are mentioned in the following sections.

Table 9.2: The breakdown of the ratio of jets remaining after different cut values on the EM fraction from run 90272 for Cone4H1TowerJets ($E_T > 20$ GeV). Bad channels are not masked in RNDM stream events. Only statistical errors were considered.

| Cut | L1Calo stream | J3 | J6 |
|--------|--------------------|--------------------|--------------------|
| > 0.05 | $16.6 \pm 0.2\%$ | $99.99 \pm 2e-3\%$ | $99.99 \pm 3e-3\%$ |
| > 0.10 | $8.7 \pm 0.1\%$ | $99.96 \pm 4e-3\%$ | $99.95 \pm 6e-3\%$ |
| > 0.15 | $7.4 \pm 0.1\%$ | $99.89 \pm 7e-3\%$ | $99.87 \pm 9e-3\%$ |
| > 0.20 | $7.1 \pm 0.1\%$ | $99.75 \pm 0.01\%$ | $99.71 \pm 0.01\%$ |
| > 0.25 | $6.9 \pm 0.1\%$ | $99.51 \pm 0.02\%$ | $99.40 \pm 0.02\%$ |
| > 0.30 | $6.8 \pm 0.1\%$ | $99.13 \pm 0.02\%$ | $98.90 \pm 0.03\%$ |
| < 0.85 | $94.2 \pm 0.1\%$ | $65.58 \pm 0.01\%$ | $78.57 \pm 0.1\%$ |
| < 0.90 | $94.5 \pm 0.1\%$ | $78.56 \pm 0.09\%$ | $87.75 \pm 0.08\%$ |
| < 0.95 | $95.21 \pm 0.09\%$ | $89.31 \pm 0.07\%$ | $94.22 \pm 0.06\%$ |
| < 1.0 | $98.15 \pm 0.06\%$ | $97.07 \pm 0.04\%$ | $98.47 \pm 0.03\%$ |

Table 9.3: The breakdown of the ratio of jets remaining after different cut values on the EM fraction from run 90272 for Cone4H1TopoJets ($E_T > 20$ GeV). Bad channels are not masked in RNDM stream events. Only statistical errors were considered.

| EMF Cut | L1Calo stream | J3 | J6 |
|---------|--------------------|--------------------|--------------------|
| > 0.05 | $8.2 \pm 0.1\%$ | $99.98 \pm 3e-3\%$ | $99.98 \pm 3e-3\%$ |
| > 0.10 | $7.7 \pm 0.1\%$ | $99.95 \pm 5e-3\%$ | $99.94 \pm 7e-3\%$ |
| > 0.15 | $7.5 \pm 0.1\%$ | $99.86 \pm 8e-3\%$ | $99.85 \pm 0.01\%$ |
| > 0.20 | $7.4 \pm 0.1\%$ | $99.69 \pm 0.01\%$ | $99.68 \pm 0.01\%$ |
| > 0.25 | $7.3 \pm 0.1\%$ | $99.41 \pm 0.02\%$ | $99.34 \pm 0.02\%$ |
| > 0.30 | $7.2 \pm 0.1\%$ | $98.98 \pm 0.02\%$ | $98.81 \pm 0.03\%$ |
| < 0.85 | $93.9 \pm 0.1\%$ | $68.6 \pm 0.1\%$ | $79.6 \pm 0.1\%$ |
| < 0.90 | $94.2 \pm 0.1\%$ | $80.98 \pm 0.08\%$ | $88.50 \pm 0.08\%$ |
| < 0.95 | $94.96 \pm 0.09\%$ | $90.97 \pm 0.06\%$ | $94.66 \pm 0.06\%$ |
| < 1.0 | $98.21 \pm 0.06\%$ | $98.70 \pm 0.02\%$ | $99.30 \pm 0.02\%$ |

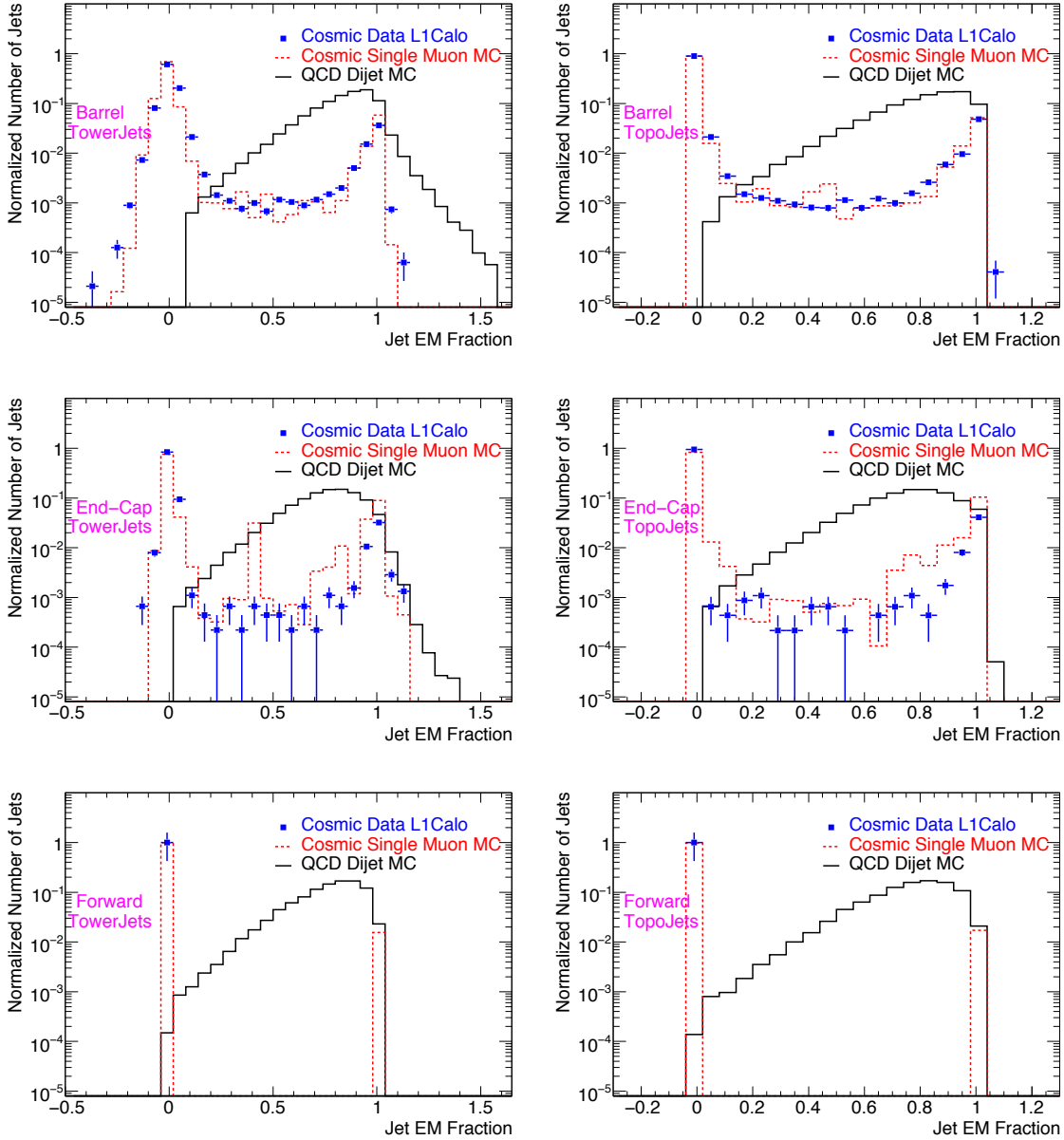


Figure 9.2: Jet EM fraction from Tower jets with cone size 0.4 (left) and Topocluster jets with cone size 0.4 (right) in post-M8 run 90272 and QCD di-jet Monte Carlo samples for each calorimeter region. Only jets with $E_T > 20$ GeV are shown here.

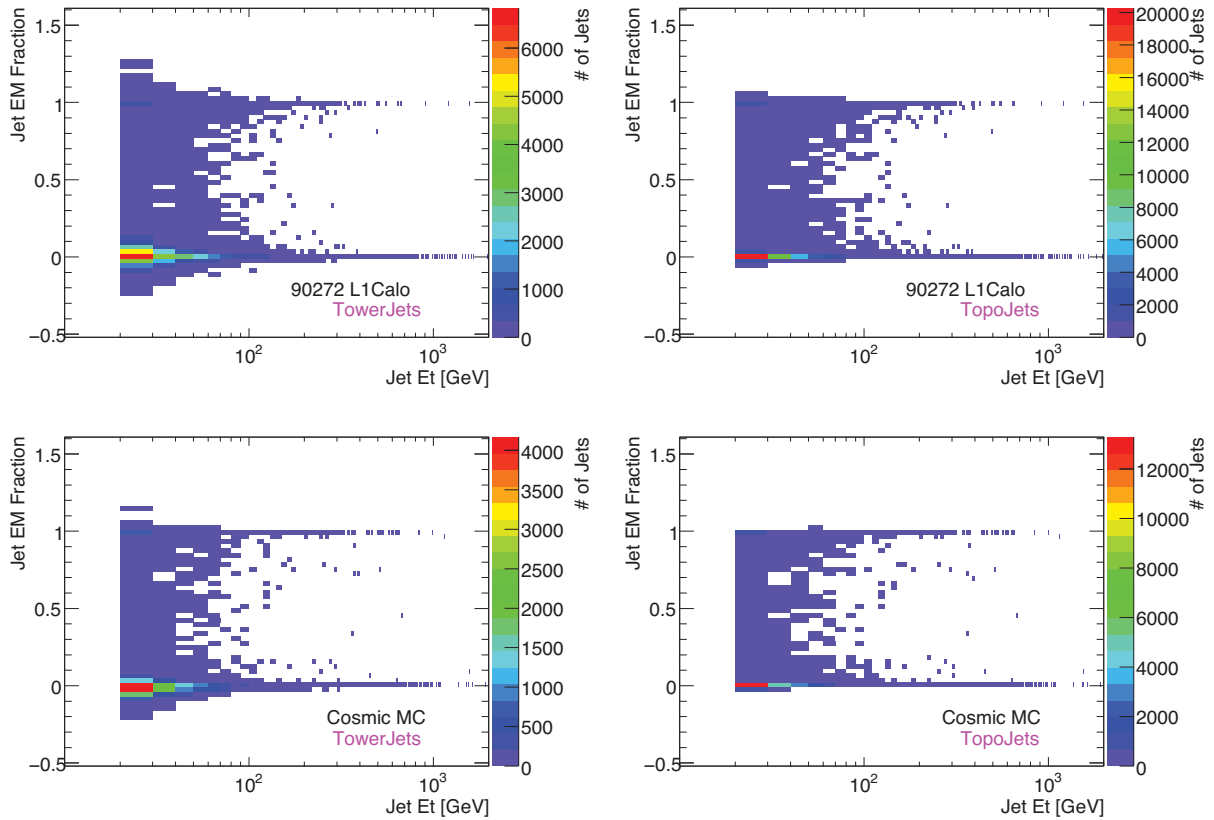


Figure 9.3: Correlation plots of transverse energy of jets and jet EM fraction for TowerJets with cone size 0.4 (left) and TopoJets with cone size 0.4 (right) in post-M8 run 90272 and cosmic Monte Carlo samples. Only jets with $E_T > 20$ GeV are shown here.

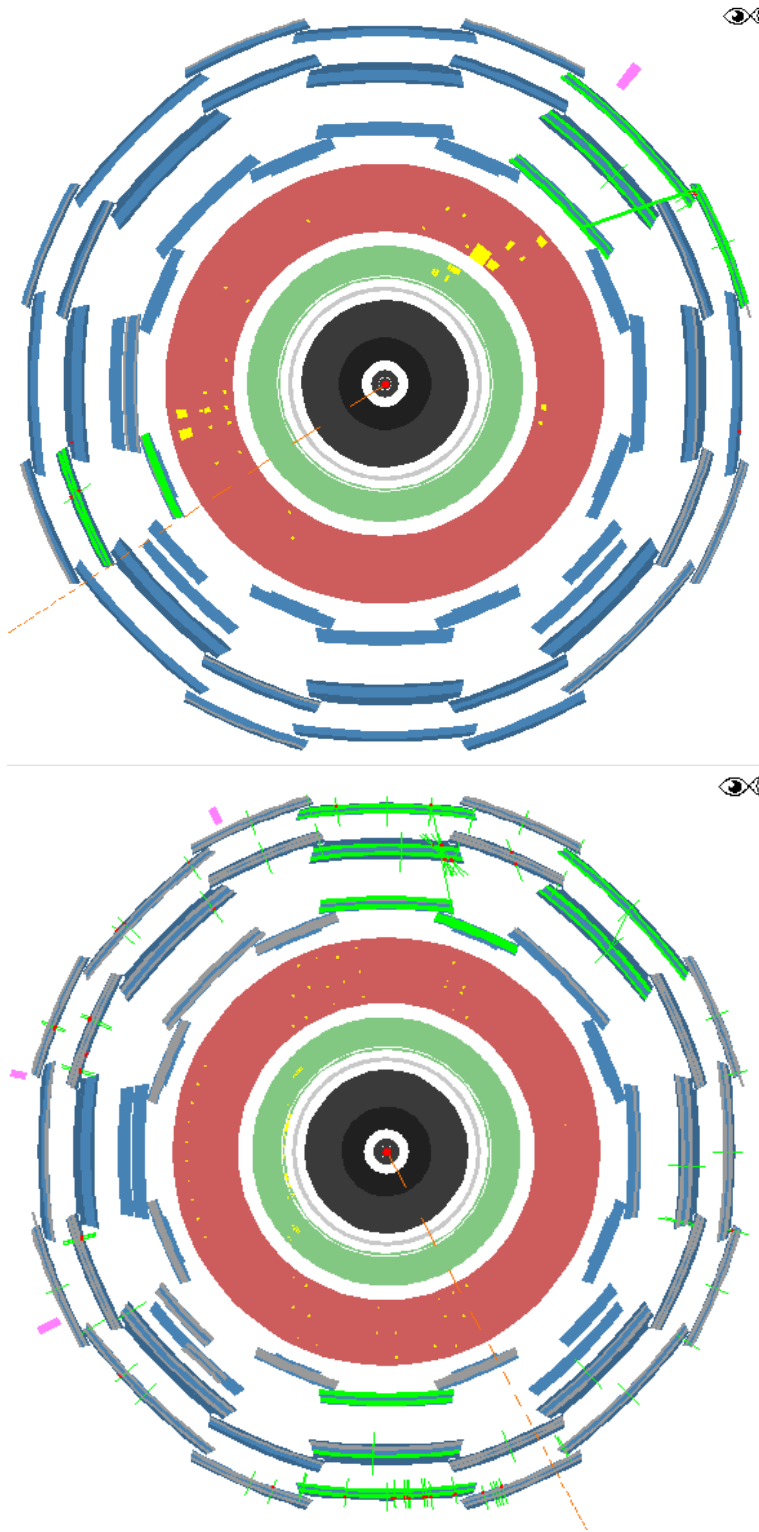


Figure 9.4: Examples of events with mid-EM fraction. The upper figure shows a jet originated from a single muon, and the lower figure shows an air shower event.

Number of Associated Tracks in Jets

The number of Inner Detector tracks matching to jets also provides useful information to discriminate the QCD and fake jets. QCD jets tend to have many tracks associated with them, due to the fact that numbers of charged hadrons are inside the jets. On the other hand, fake jets generated from noise or problematic channels will not have tracks associated to them except for accidental association of unrelated tracks. Jets produced from a single cosmic muons should contain only one track, or may not have any track associated to them when the cosmic muons are non-projective (do not pass near the interaction point). Jets generated from air shower events may have more tracks inside jets, but even those jets have far less associated tracks compared to the QCD jets.

Here, the Inner Detector tracks (called the “TrackParticleCandidate” in the ATLAS analysis framework) were considered for the track association. In cosmic run data, the Inner Detector tracks were not assumed to be coming from the interaction point, but as passing downward through the detector, and thus were reconstructed using the whole inner detector hits (a single track passes through the top and bottom module of the detector; see Figure 9.5). All the ϕ values in the cosmic tracks are set as negative, since they are going downward. In this study, the motivation is to understand the effects of cosmic tracks during the collision data taking, so the track reconstruction was re-done in the cosmic data with the same criteria as those during the collision data taking. In such criteria, two tracks can originate from a single muon, each track reconstructed from the interaction point, one track going upward and the other traversing downward.

The number of reconstructed Inner Detector tracks with the collision settings are shown in Figure 9.6. The upper left plot shows the number from cosmic run 90272 IDCosmic stream, and the upper right plot shows the one from the L1Calo stream of the same run. The lower plot is from the QCD dijet Monte Carlo. The number of tracks are shown for the default reconstruction, and after applying some cuts on the number of hits in the silicon detectors. Most tracks only have TRT hits, and they do not have η information or do not have reliable η values due to the detector feature (straws running parallel to the beam direction). Such tracks cannot be used for jet association. In order to have reliable $\eta - \phi$ information, we required one hit in the Pixel B-layer (which is the innermost layer, closest to the interaction point) and at least five hits in the whole silicon. Applying the cuts, almost no tracks are reconstructed in the cosmic data. The L1Calo stream has far less number of tracks than the IDCosmic stream, because many cosmic muons triggered by the Level-1 Calorimeter trigger do not pass near the interaction point, whereas the IDCosmic stream tend to have more tracks since the Level-2 Inner Detector trigger is used.

When tracks were within the cone size of jets (0.4) in regards to $dR = \sqrt{\Delta\eta^2 + \Delta\phi^2}$, they were regarded as associated to jets.

In Figure 9.7, number of tracks in jets are shown for both TowerJets and TopoJets with cone size 0.4. Clear separation of fake jets from cosmic events and QCD jets are observed. Table 9.4 shows breakdowns of the ratio of jets remaining after cuts with number of associated tracks. As seen from there, even a requirement of single associated track removes most of the fake jets with good efficiency on QCD jets.

Although, cleaning cuts using the number of tracks seem to show powerful fake re-

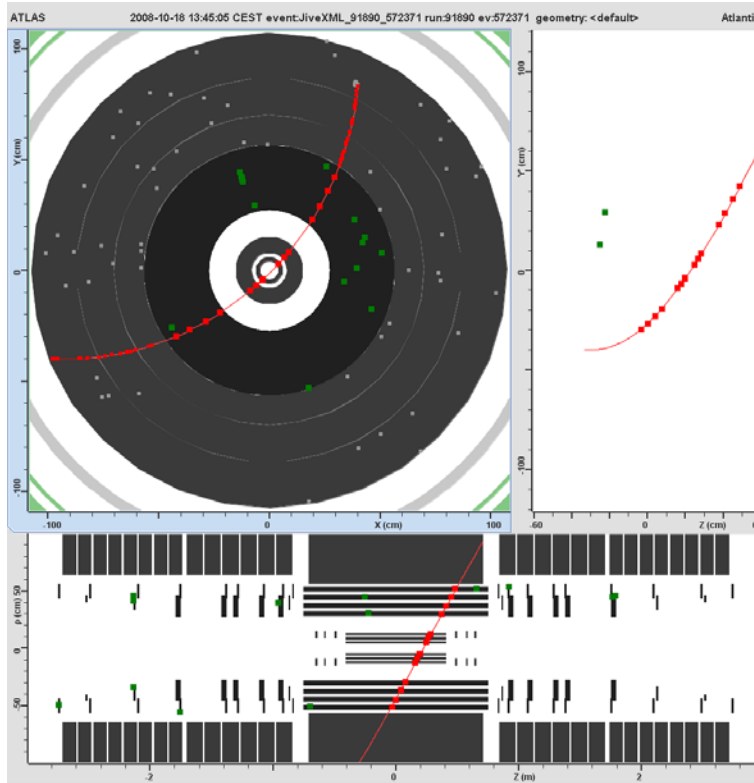


Figure 9.5: Inner Detector event display from cosmic run 90270 with solenoidal magnetic field on. The red line shows the reconstructed Inner Detector track and points show the hits in the detector [106].

jection power, the performance is deteriorated when we start to consider cosmic muons overlapping high cross section collision events such as the Minimum Bias or the QCD dijets. Under such circumstances, even the fake jets tend to have larger number of associated tracks which is due to the accidental overlap of tracks coming from the collision events. In such cases, additional information from tracks, such as “charge fraction” of jets can be useful to remove backgrounds. It is defined as

$$\text{Charge Fraction} = \frac{\sum_i^{\text{tracks}} P_T^{(i)}}{\text{Jet } E_T} \quad (9.3)$$

and was used in Tevatron experiments. The performance of this variable under cosmic-collision overlap condition will be mentioned in Section 9.2.

Number of Clusters in Jets

Number of calorimeter clusters in jets is expected to have discrimination power on real and fake jets as well. This is called “jet size” in the ATLAS software. For TowerJets, jet size is the number of combined towers inside the jets, whereas the number of Topoclusters inside the jets corresponds to the jet size for TopoJets.

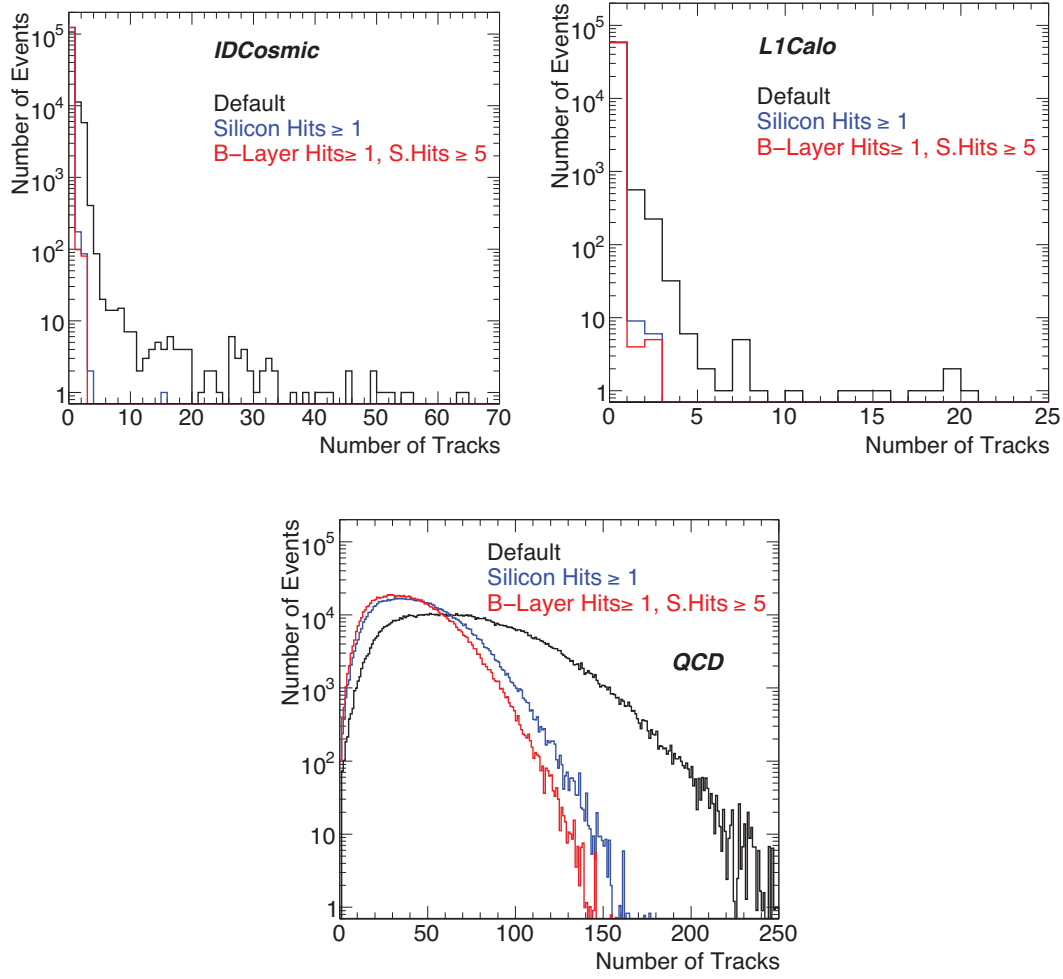


Figure 9.6: Number of Tracks in cosmic data and QCD dijet Monte Carlo. The upper left plot shows the number from cosmic run 90272 IDCosmic stream, and the upper right plot shows the one from the L1Calo stream of the same run. The lower plot is from the QCD dijet Monte Carlo.

Table 9.4: The breakdown of the ratio of jets remaining after different cut values on the number of associated tracks in jets from post-M8 run 90272 (for Cone4H1TopoJets with a cone size of 0.4 and $E_T > 20$ GeV, $|\eta| < 2.5$). Only statistical errors were considered.

| Cut | L1Calo stream | IDCosmic | J3 |
|----------|-----------------------|-----------------------|--------------------|
| ≥ 1 | $0 \pm \text{---} \%$ | $0.15 \pm 0.06\%$ | $99.67 \pm 0.02\%$ |
| ≥ 2 | $0 \pm \text{---} \%$ | $0 \pm \text{---} \%$ | $98.37 \pm 0.04\%$ |
| ≥ 3 | $0 \pm \text{---} \%$ | $0 \pm \text{---} \%$ | $95.02 \pm 0.06\%$ |
| ≥ 4 | $0 \pm \text{---} \%$ | $0 \pm \text{---} \%$ | $89.00 \pm 0.09\%$ |
| ≥ 5 | $0 \pm \text{---} \%$ | $0 \pm \text{---} \%$ | $80.4 \pm 0.1\%$ |

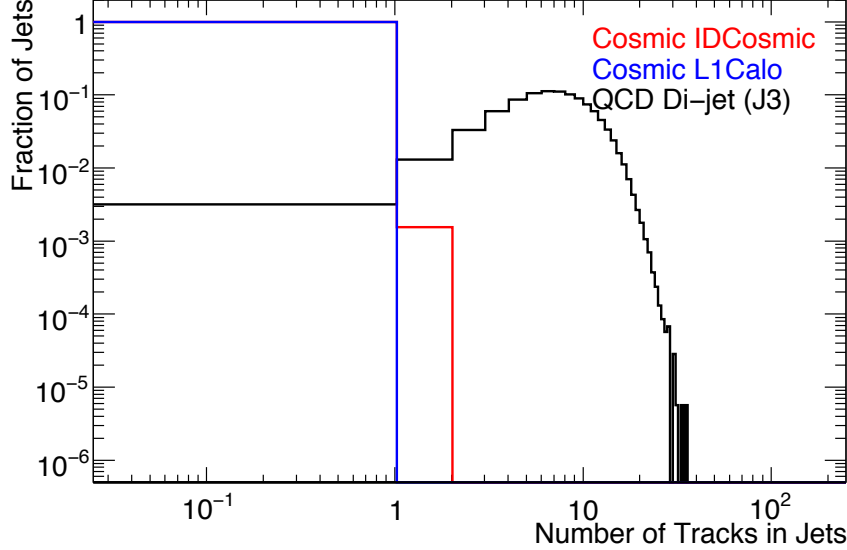


Figure 9.7: Numbers of tracks associated with Cone4H1TopoJets with cone size 0.4 in run 90272, cosmic and QCD di-jet Monte Carlo samples. Only jets with $E_T > 20$ GeV and $|\eta| < 2.5$ are shown here.

Figure 9.8 shows the number of clusters for Cone4H1TopoJets. The number of clusters for TopoJets seems to be useful for jet cleaning. This is due to the fact that jets originated from noisy channels or cosmic muons tend to have only a few numbers of Topoclusters. On the other hand, Topoclusters have a good correlation with the number of particles in QCD jets, which leads to a clear separation in jet size. About 1 Topocluster corresponds to 1.6 MC Truth stable particles passing the calorimeter [23]. (e.g. π^0 's are not counted, but the two photons from their decays are counted)

We need to investigate the effect of calorimeter geometry on this quantity as well, since the cluster reconstruction is severely affected by calorimeter geometry such as the granularity. Figure 9.9 shows the distributions of the number of clusters in Cone4H1TopoJets in various calorimeter regions, such as the barrel ($|\eta| < 1.5$), end-cap ($1.5 < |\eta| < 3.2$). Good separation between fake and real jets are observed in Cone4H1TopoJets for the barrel and the end-cap. Here, we investigate the breakdown of TopoJets within $|\eta| < 3.2$, as shown in Table 9.5. A cut on the number of clusters in TopoJets removes most of the fake jets, and still maintains good efficiency on the QCD jets. However, like other cleaning cuts, the performance needs to be confirmed under overlapping condition of cosmics and collision events, which will be mentioned in Section 9.2.

Number of Cells in Jets

Number of cells inside Topoclusters or jets can also provide useful information to perform a clean-up. Jets formed from noisy channels or cosmic ray muons undergoing hard bremsstrahlung tend to have low number of cells, whereas QCD jets have a large number of cells inside jets due to contributions from the large number of particles [94]. In

Table 9.5: The ratio of jets remaining after different cut values on the jet size from post-M8 run 90272 (for Cone4H1TopoJets with a cone size of 0.4 and $E_T > 20$ GeV, $|\eta| < 3.2$). Only statistical errors were considered.

| Cut | L1Calo stream | J3 | J6 |
|------|-------------------|--------------------|--------------------|
| > 2 | $28.1 \pm 0.2\%$ | $99.64 \pm 0.01\%$ | $99.82 \pm 0.01\%$ |
| > 4 | $3.23 \pm 0.08\%$ | $97.61 \pm 0.03\%$ | $98.77 \pm 0.03\%$ |
| > 6 | $0.59 \pm 0.03\%$ | $92.60 \pm 0.04\%$ | $95.66 \pm 0.05\%$ |
| > 8 | $0.20 \pm 0.02\%$ | $84.49 \pm 0.08\%$ | $89.32 \pm 0.08\%$ |
| > 10 | $0.07 \pm 0.01\%$ | $73.03 \pm 0.1\%$ | $78.97 \pm 0.1\%$ |
| > 15 | $0.01 \pm 5e-3\%$ | $36.17 \pm 0.1\%$ | $42.17 \pm 0.1\%$ |

Table 9.6: Mean number (RMS in parenthesis) of cells in jets ($E_T > 20$ GeV) in di-jet Monte Carlo samples

| Type of Jets | J1 | J3 | J6 |
|--------------------|----------------------------|-----------------------------|-------------------------|
| TopoJets (R = 0.4) | $723 \pm 1(362.0 \pm 0.8)$ | $1202 \pm 1(559.8 \pm 0.9)$ | $1930 \pm 2(905 \pm 2)$ |

Table 9.7: The breakdown of the ratio of jets remaining after different cut values on the number of cells in jets from post-M8 run 90272 (for TopoJets with a cone size of 0.4, $E_T > 20$ GeV, and $|\eta| < 3.2$).

| Cut | L1Calo stream | J3 | J6 |
|-------|-------------------|---------------------|---------------------|
| > 50 | $91.2 \pm 0.1\%$ | $99.999 \pm 7e-4\%$ | $99.999 \pm 7e-4\%$ |
| > 100 | $80.0 \pm 0.2\%$ | $99.98 \pm 3e-3\%$ | $99.99 \pm 3e-3\%$ |
| > 150 | $63.2 \pm 0.2\%$ | $99.87 \pm 8e-3\%$ | $99.95 \pm 6e-3\%$ |
| > 200 | $47.4 \pm 0.2\%$ | $99.52 \pm 0.02\%$ | $99.79 \pm 0.01\%$ |
| > 300 | $25.5 \pm 0.2\%$ | $97.40 \pm 0.04\%$ | $98.95 \pm 0.03\%$ |
| > 400 | $13.1 \pm 0.1\%$ | $94.56 \pm 0.05\%$ | $97.94 \pm 0.04\%$ |
| > 500 | $6.5 \pm 0.1\%$ | $92.14 \pm 0.06\%$ | $97.024 \pm 0.04\%$ |
| > 600 | $3.38 \pm 0.08\%$ | $89.58 \pm 0.07\%$ | $95.82 \pm 0.05\%$ |
| > 700 | $1.93 \pm 0.06\%$ | $86.15 \pm 0.08\%$ | $94.06 \pm 0.06\%$ |

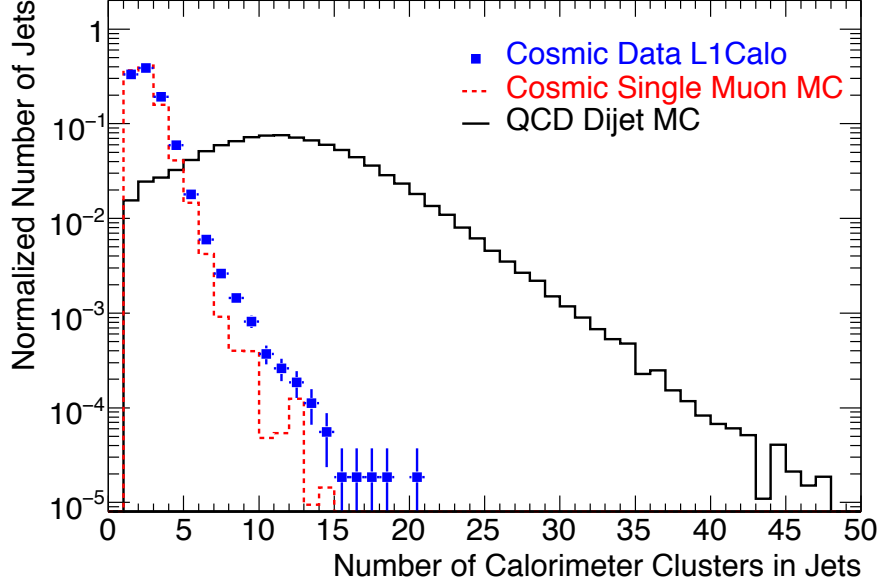


Figure 9.8: Number of clusters in Cone4H1TopoJets (jet with cone size 0.4 and Topoclusters as inputs) from run 90272 L1Calo stream and QCD di-jet Monte Carlo samples. Only jets with $E_T > 20$ GeV are shown here.

Figure 9.10, a difference in the number of cells inside TopoJets is observed between jets reconstructed from cosmic ray events and those from di-jet Monte Carlo samples. Good separation is seen in TopoJets between reconstructed jets from cosmic events and QCD jets. However, large numbers of cells in jets were observed in a few cosmic ray events. It was confirmed from Figure 9.11 in Section 9.1.1 that these were mainly coming from LAr EM calorimeter. These can be due to sporadic noise bursts in the calorimeter.

The number of cells inside TowerJets seems to have little discrimination power, regardless of the calorimeter region, which may be due to the similar reason mentioned for the jet size. As shown in Table 9.7, for real jets, higher the jet energy, the large the number of cells reconstructed inside jets (also mentioned in [94]). The breakdown of ratio of jets remaining after various cuts on the number of cells is shown in Table 9.7.

Correlation of Jet Quality

As mentioned in the previous sections, several quality cuts are proposed. We expect that each of them perform a removal of fake contributions in complementary ways. Here, we look at the correlation of quality variables. In Figure 9.11, it is obvious that most jets are concentrated around jet EM fraction 0 and small number of tracks, clusters, and cells. Note that most jets with mid-EM fraction also tend to have small numbers of tracks and clusters. This shows that these quality cuts are performing complementary “cleaning.” Jets with large tremendous numbers of cells in run 90272 L1Calo stream seems to generate in LAr EM region, as Jet EM fraction shows. However, even for those jets, numbers of tracks and clusters remain small, so these two variables may perform

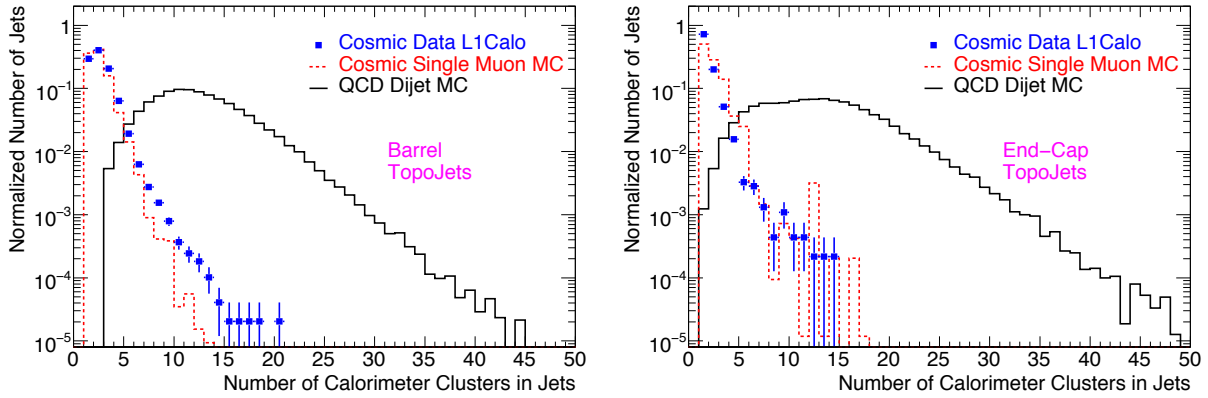


Figure 9.9: Number of clusters in Cone4H1TopoJets in run 90272 L1Calo stream and QCD di-jet Monte Carlo samples in the barrel (upper figure) and the end-cap (lower figure). Only jets with $E_T > 20$ GeV are shown here.

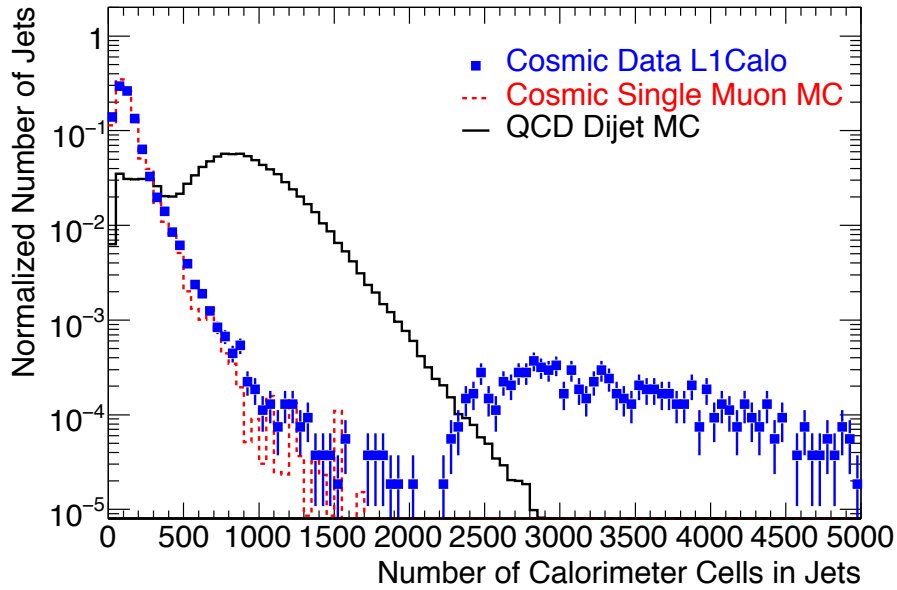


Figure 9.10: Number of cells in Cone4H1TopoJets from run 90272 L1Calo stream and QCD di-jet Monte Carlo samples. Only jets with $E_T > 20$ GeV are shown here.

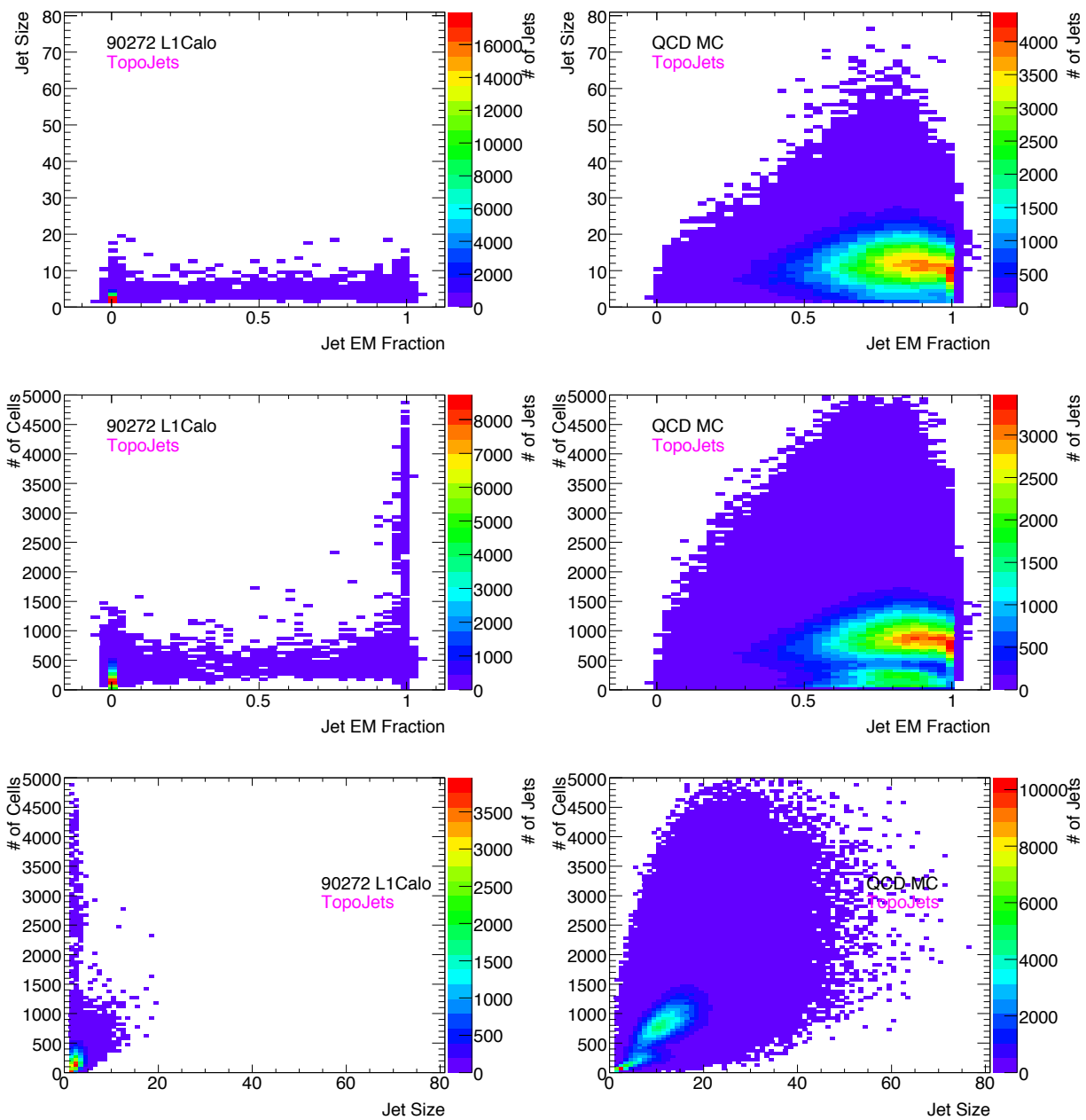


Figure 9.11: Correlation of jet quality variables for post-M8 run 90272 L1Calo stream and QCD Monte Carlo.

better fake removal than the numbers of cells.

Preliminary look at the overall “cleaning” of jets will be mentioned again in Section 9.1.3.

9.1.2 Event-level Quality

In the previous sections, quality of jets were mentioned. “Event cleaning” is a fake removal procedure performed at the event level. This is the most stringent cut to be performed during the analyses, since the event itself is discarded when the contamination from non-collision sources is identified, rather than only removing the reconstructed objects. This approach is very important and crucial for new physics searches using large E_T^{miss} (and possibly accompanying jets), and is often called the “ E_T^{miss} cleaning.” Many of the event-level quality can be provided from jet information (see 9.1.2). Here, we also investigate on the timing information from TileCal using the time-of-flight.

Event-level Quality from Jet Information

As mentioned above, jet information can provide quality cuts even at the event-level. Taking the weighted-average by jet transverse energy of the previously mentioned jet quality will also be a good possibility for event-level quality, and is useful for physics analyses with multi-jet events. Such a quality using information from jets’ EM fraction is called the event EM fraction derived as below.

$$\text{Event EM Fraction} = \frac{\sum_{jet} EMF_{jet} \times E_{Tjet}}{\sum_{jet} E_{Tjet}} \quad (9.4)$$

It is calculated event-by-event to remove backgrounds with large fake E_T^{miss} . This quantity was used in the analyses at Tevatron experiments to remove events with large fake E_T^{miss} . Figure 9.12 shows the event EM fraction calculated from Cone4H1TowerJets and Cone4H1TopoJets with $E_T > 20$ GeV. A clear separation is seen between cosmic ray events and real QCD di-jet events using this variable. However, this quantity can be smeared when the transverse energy of fake jet(s) are comparable or smaller than the other real QCD jets. In such a case, an alternative and more stringent cut is to reject events when there is at least one jet not fulfilling the quality requirement. Which strategy to take depends on the physics analysis and its motivation.

The same calculation performed for number of tracks, clusters, and cells (replace EMF_{jet} by these quantities in equation 9.4) may also serve as event-level quantities for the cleaning as shown in Figure 9.12.

9.1.3 Cleaning for Pure Cosmic Events

Here, we show a result of applying cleaning cuts for jets. Note that the pure cosmic events were analyzed in the plot and either contributions from electronic noise or cosmic rays show up. The performance of cleaning cuts on cosmic ray overlapping collision events will be mentioned in Section 9.2.

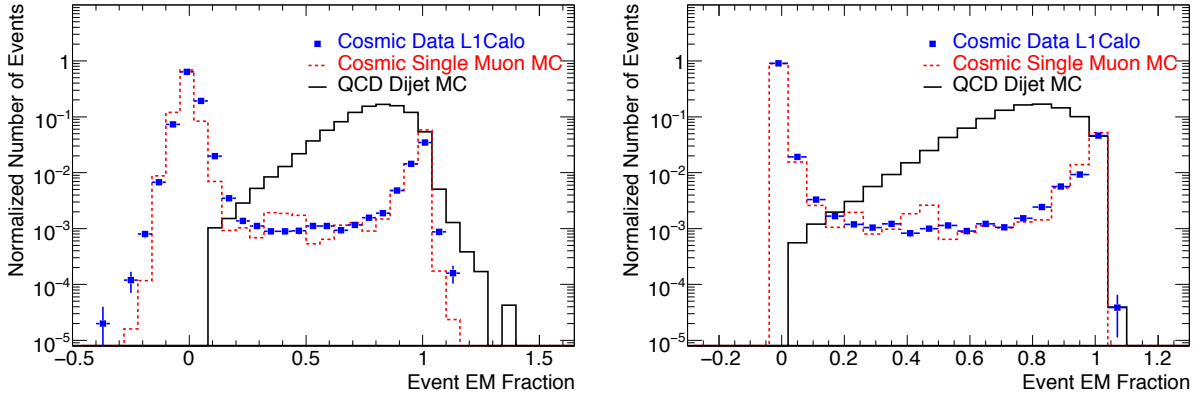


Figure 9.12: Event quality from jet information. Left side shows quality derived from TowerJets with cone size 0.4 and right side shows quality calculated from TopoJets with cone size 0.4 in post-M8 run 90272, cosmic Monte Carlo and QCD di-jet Monte Carlo samples. Jets with $E_T > 20$ GeV are used for the calculations.

Figure 9.1.3 shows a result on jet cleaning for post-M8 run 90272 L1Calo stream and cosmic Monte Carlo samples for Cone4H1TopoJets. Quality cuts with EM fraction and number of clusters in jets were considered. The actual values used for the selection are as follows.

- Cone4H1TopoJets with EM fraction < 0.2 or > 0.97 were rejected.
- Cone4H1TopoJets with jet size ≤ 6 were rejected.

9.2 Event Overlay Studies

In the previous section, jet and E_T^{miss} quality were studied with pure cosmic ray events. It is not obvious whether those cleaning cuts remain to be valid when cosmic ray muons overlap with physics events with large cross sections (such as Minimum Bias and QCD di-jet events). Here, so called “Event Overlay” algorithm developed in ATLAS was used to study such cases. The algorithm has originally been developed for the pile-up studies.

9.2.1 Event Overlay Algorithm

The algorithm allows to read and mix events from various streams at the Geant-4 “Hits”-level. The number of events to mix can be set arbitrarily. It can combine not just Monte Carlo events, but also real events or mixture of several Monte Carlo and real events. This algorithm allows to investigate not just the effects of the pile-up, but also the overlap of non-collision sources on the signal events.

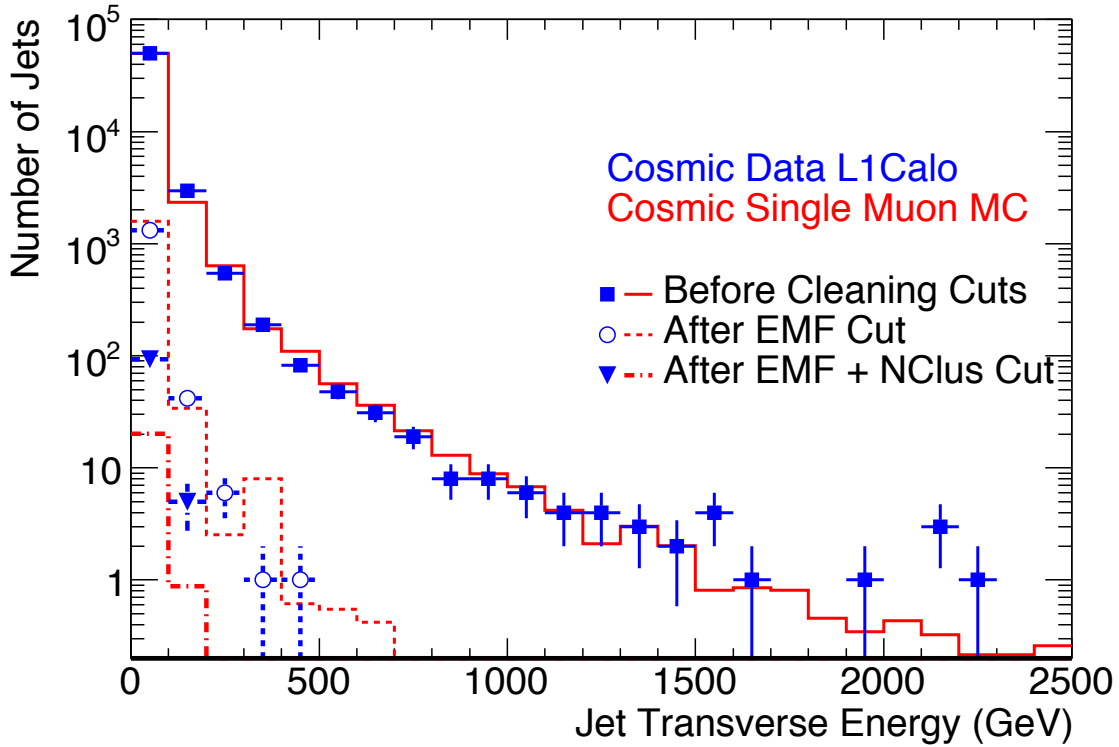


Figure 9.13: Preliminary cleaning on TowerJets and TopoJets with cone size 0.4 in post-M8 run 90272 L1Calo stream and cosmic Monte Carlo samples.

9.2.2 Investigations on Event Overlap of Cosmic Rays on Collision Events

The event overlay was done for the cosmic ray data and the high cross section Monte Carlo events, such as the Minimum Bias and QCD dijet samples.

Figure 9.14 shows the jet EM fraction from cosmic-Minimum Bias mixed samples and cosmic-J3 mixed samples. The blue lines show what we observed in the pure cosmic data, whereas the red lines show the EM fraction from fake jets originated from cosmics under overlaid conditions. The black line show the EM fraction of the QCD jets under overlaid conditions. The determination of whether the jets originated from cosmics or the real QCD jets was done using the Monte Carlo generator’s information. The ATLAS framework provides so called the “TruthJets” where the jet algorithm runs among the particles at the generator’s level with a particular cone size, and offers the “true” jet information without any detector effects. In the overlaid samples, the generator’s information remains even after the Monte Carlo events are mixed with real data. Thus, matching between the reconstructed jets in the mixed data, and “TruthJets” were performed to categorize them into “fake jets” originated from cosmics, and the real QCD jets coming from the partons’ fragmentations and hadronizations. The breakdown of the rejection power of

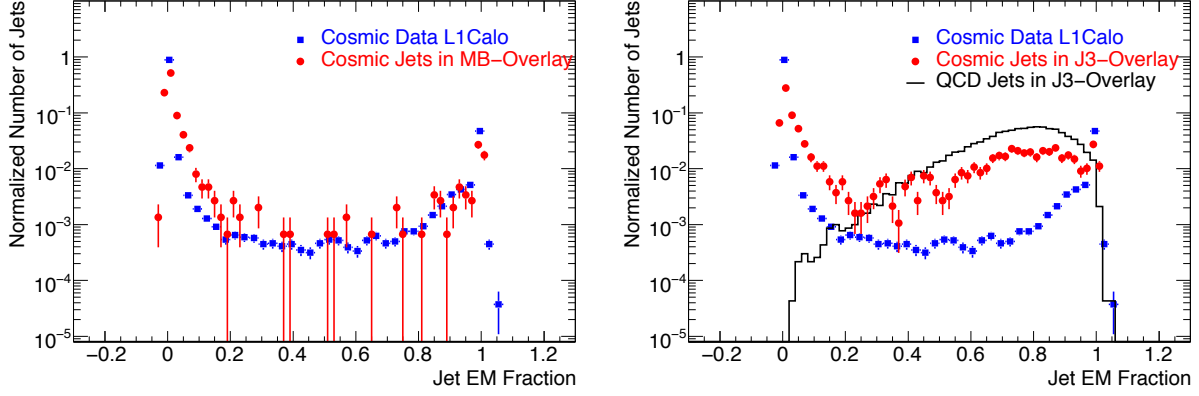


Figure 9.14: Jet EM fraction in overlaid samples; cosmic L1Calo on Minimum Bias events (left) and cosmic L1Calo on QCD dijet J3 events (right).

Table 9.8: The breakdown of the ratio of jets remaining after different cut values on the EM fraction for Cone4H1TopoJets ($E_T > 20$ GeV) in pure cosmic L1Calo stream, overlaid cosmic samples on Minimum Bias and QCD dijet J3 Monte Carlo samples. Only statistical errors were considered.

| EMF Cut | L1Calo stream | Cosmic jets on MB | Cosmic jets on J3 | QCD jets in cosmic-on-J3 |
|---------|--------------------|-------------------|-------------------|--------------------------|
| > 0.05 | $8.2 \pm 0.1\%$ | $13.6 \pm 0.9\%$ | $54 \pm 1\%$ | $99.98 \pm 9e-3\%$ |
| > 0.10 | $7.7 \pm 0.1\%$ | $9.2 \pm 0.7\%$ | $47 \pm 1\%$ | $99.92 \pm 0.02\%$ |
| > 0.15 | $7.5 \pm 0.1\%$ | $8.1 \pm 0.7\%$ | $45 \pm 1\%$ | $99.82 \pm 0.03\%$ |
| > 0.20 | $7.4 \pm 0.1\%$ | $7.8 \pm 0.7\%$ | $43 \pm 1\%$ | $99.59 \pm 0.04\%$ |
| > 0.25 | $7.3 \pm 0.1\%$ | $7.4 \pm 0.7\%$ | $43 \pm 1\%$ | $99.34 \pm 0.05\%$ |
| > 0.30 | $7.2 \pm 0.1\%$ | $7.2 \pm 0.7\%$ | $42 \pm 1\%$ | $98.9 \pm 0.7\%$ |
| < 0.85 | $93.9 \pm 0.1\%$ | $93.7 \pm 0.6\%$ | $86.2 \pm 0.8\%$ | $74.4 \pm 0.3\%$ |
| < 0.90 | $94.2 \pm 0.1\%$ | $94.3 \pm 0.6\%$ | $91.0 \pm 0.7\%$ | $86.5 \pm 0.2\%$ |
| < 0.95 | $94.96 \pm 0.09\%$ | $95.2 \pm 0.6\%$ | $94.6 \pm 0.5\%$ | $95.2 \pm 0.1\%$ |
| < 1.0 | $98.21 \pm 0.06\%$ | $98.3 \pm 0.3\%$ | $98.9 \pm 0.2\%$ | $99.78 \pm 0.03\%$ |

Table 9.9: The breakdown of the ratio of jets remaining after different cut values on the number of clusters in Cone4H1TopoJets ($E_T > 20$ GeV) in pure cosmic L1Calo stream, overlaid cosmic samples on Minimum Bias and QCD dijet J3 Monte Carlo samples. Only statistical errors were considered.

| EMF Cut | L1Calo stream | Cosmic jets on MB | Cosmic jets on J3 | QCD jets in cosmic-on-J3 |
|---------|-------------------|-------------------|-------------------|--------------------------|
| > 2 | $28.1 \pm 0.2\%$ | $53 \pm 1\%$ | $83.2 \pm 0.9\%$ | $99.76 \pm 0.03\%$ |
| > 4 | $3.23 \pm 0.08\%$ | $17 \pm 1\%$ | $61 \pm 1\%$ | $97.8 \pm 0.1\%$ |
| > 6 | $0.59 \pm 0.03\%$ | $6.3 \pm 0.6\%$ | $47 \pm 1\%$ | $92.9 \pm 0.2\%$ |
| > 8 | $0.20 \pm 0.02\%$ | $2.1 \pm 0.4\%$ | $38 \pm 1\%$ | $84.7 \pm 0.2\%$ |
| > 10 | $0.07 \pm 0.01\%$ | $0.8 \pm 0.2\%$ | $32 \pm 1\%$ | $73.2 \pm 0.3\%$ |
| > 15 | $0.01 \pm 5e-3\%$ | $0.8 \pm 0.2\%$ | $32 \pm 1\%$ | $73.2 \pm 0.3\%$ |

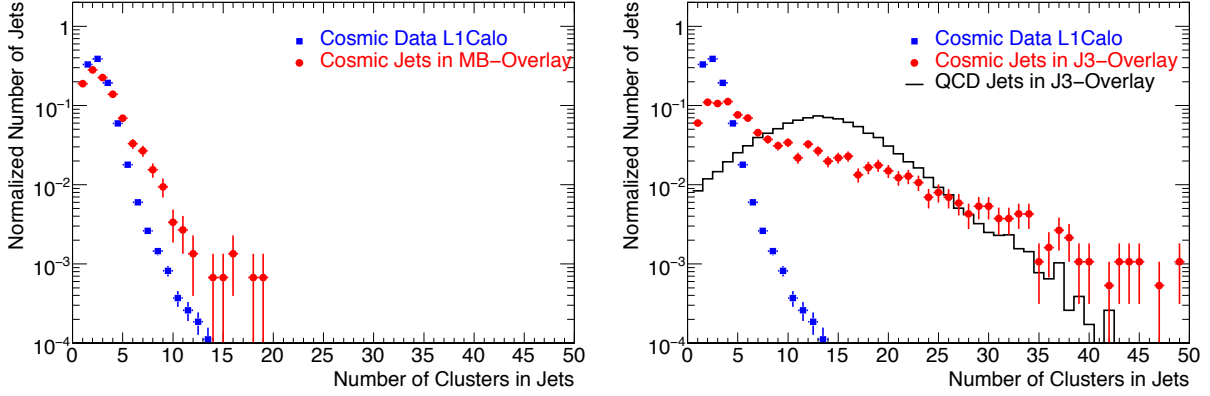


Figure 9.15: Number of Topoclusters in overlaid samples; cosmic L1Calo on Minimum Bias events (left) and cosmic L1Calo on QCD dijet J3 events (right).

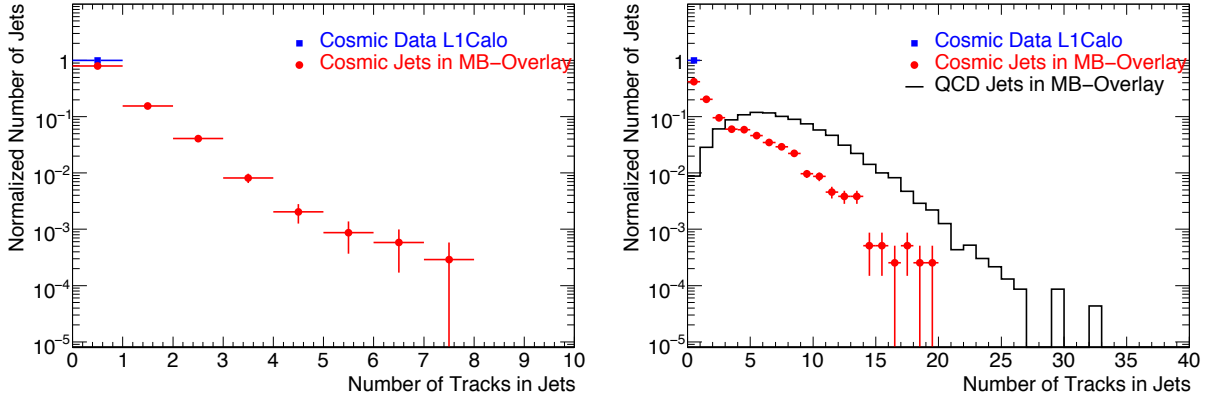


Figure 9.16: Number of associated tracks in jets in overlaid samples; cosmic L1Calo on Minimum Bias events (left) and cosmic L1Calo on QCD dijet J3 events (right).

Table 9.10: The breakdown of the ratio of jets remaining after different cut values on the number of associated tracks for Cone4H1TopoJets ($E_T > 20$ GeV) in pure cosmic L1Calo stream, overlaid cosmic samples on Minimum Bias and QCD dijet J3 Monte Carlo samples. Only statistical errors were considered.

| EMF Cut | L1Calo stream | Cosmic jets on MB | Cosmic jets on J3 | QCD jets in cosmic-on-J3 |
|----------|-----------------------|-------------------|-------------------|--------------------------|
| ≥ 1 | $0 \pm \text{---} \%$ | $20.8 \pm 0.7\%$ | $58.2 \pm 0.8\%$ | $99.12 \pm 0.06\%$ |
| ≥ 2 | $0 \pm \text{---} \%$ | $5.3 \pm 0.4\%$ | $38.0 \pm 0.8\%$ | $96.3 \pm 0.1\%$ |
| ≥ 3 | $0 \pm \text{---} \%$ | $1.2 \pm 0.2\%$ | $28.4 \pm 0.7\%$ | $90.2 \pm 0.2\%$ |
| ≥ 4 | $0 \pm \text{---} \%$ | $0.4 \pm 0.1\%$ | $22.4 \pm 0.7\%$ | $81.4 \pm 0.3\%$ |
| ≥ 5 | $0 \pm \text{---} \%$ | $0.17 \pm 0.07\%$ | $16.5 \pm 0.6\%$ | $70.6 \pm 0.3\%$ |

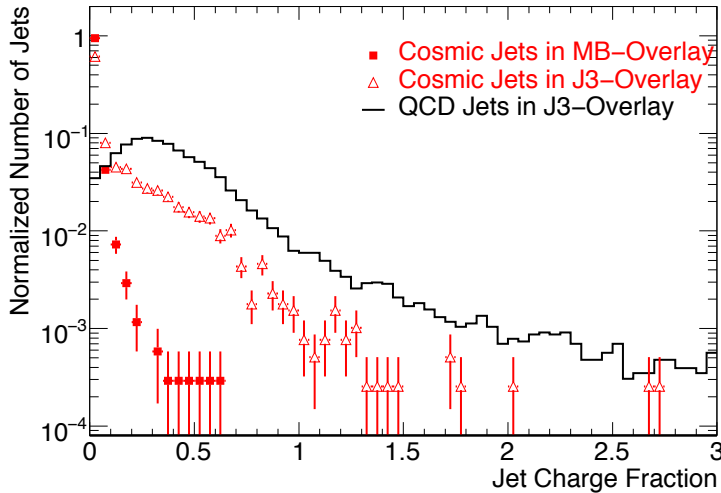


Figure 9.17: Jet charge fraction in overlaid samples; jet originated from cosmic muons in cosmic L1Calo on Minimum Bias events (red square), cosmic L1Calo on QCD dijet J3 events (red open triangle), and from QCD jets in cosmic L1Calo on QCD dijet J3 events (black).

the fake jets and the efficiency of the QCD jets are shown in Table 9.11. The cleaning cut by the EM fraction still remains to be very effective when cosmic muons overlap with a single Minimum Bias event, rejecting more than 90 % of the fake jets when EM fraction cut of 0.1 (or tighter) is used. The pile-up of a single Minimum Bias event in average corresponds to the luminosity of $5 \times 10^{32} \text{cm}^{-2} \text{s}^{-1}$. However, the performance is degraded when cosmic muons overlap with more “crowded” events such as the QCD dijet with high energy (here, J3 is the example).

Figure 9.15 shows the number of clusters in Cone4H1TopoJets from cosmic-Minimum Bias mixed samples and cosmic-J3 mixed samples. The color convention is the same as Figure 9.14. The performance of cleaning cuts is slightly degraded as in the case of the jet EM fraction for cosmic-Minimum Bias mixed events (Table 9.9), but it still removes more than 90 % of the fake jets and keeps more than 90 % of efficiency for QCD jets. For cosmic-J3 mixed events, only 50 % of the fake jets are removed.

The information from the Inner Detector tracks will provide further cleaning, as mentioned in the previous section. The number of associated tracks in jets and the charge fraction defined in equation (9.3) are shown in Figure 9.16 and 9.17.

Table 9.11: The breakdown of the ratio of jets remaining after different cut values on the charge fraction for Cone4H1TopoJets ($E_T > 20$ GeV) in pure cosmic L1Calo stream, overlaid cosmic samples on Minimum Bias and QCD dijet J3 Monte Carlo samples. Only statistical errors were considered.

| EMF Cut | L1Calo stream | Cosmic jets on MB | Cosmic jets on J3 | QCD jets in cosmic-on-J3 |
|-------------|-----------------------|-------------------|-------------------|--------------------------|
| ≥ 0.01 | $0 \pm \text{---} \%$ | $19.4 \pm 0.7\%$ | $56.6 \pm 0.8\%$ | $99.0 \pm 0.07\%$ |
| ≥ 0.05 | $0 \pm \text{---} \%$ | $5.6 \pm 0.4\%$ | $38.4 \pm 0.8\%$ | $96.5 \pm 0.1\%$ |
| ≥ 0.1 | $0 \pm \text{---} \%$ | $1.4 \pm 0.2\%$ | $30.4 \pm 0.7\%$ | $91.9 \pm 0.2\%$ |
| ≥ 0.15 | $0 \pm \text{---} \%$ | $0.6 \pm 0.1\%$ | $25.9 \pm 0.7\%$ | $85.6 \pm 0.2\%$ |
| ≥ 0.2 | $0 \pm \text{---} \%$ | $0.3 \pm 0.1\%$ | $21.5 \pm 0.7\%$ | $78.0 \pm 0.3\%$ |

Part III

**Prospects towards New Physics
Search**

Chapter 10

Searches for New Physics with Jets and E_T^{miss} Event Topologies

The current status of the ATLAS calorimeters were investigated and understood with the real commissioning data as mentioned in the previous chapters.

In the next chapters, the strategies to search for the physics beyond the Standard Model were investigated with jets and E_T^{miss} event topologies. Jets and E_T^{miss} event topologies offer important search modes for many physics models beyond the Standard Model as will briefly be mentioned in the next section. Jets and E_T^{miss} highly depend on the performance of the calorimeters, but the commissioning studies of the calorimeters indicate that the detector is in a stable condition, and we are ready to proceed into the performance studies of the physics objects and to the physics analyses.

In Chapter 11, we investigate the monojet event topology, which is an important channel to search for the Large Extra Dimensions. In order to perform successful searches, understandings of the detector performance and the rate of the Standard Model and non-collision background are highly essential. We were able to understand the effects from the problematic calorimeter channels, and also the cosmic background from the real data.

In Chapter 12, prospects towards multi-jet plus E_T^{miss} event topology are described. Since the uncertainty of multi-jet processes are still large for the Monte Carlo simulations, data-driven methods to estimate the Standard Model background are indispensable. The ways to perform the estimations were proposed. The expected rate of cosmic background was estimated with the real cosmic data and also the event overlay technique with cosmic data and QCD multi-jet Monte Carlo simulation.

Note that in Part III, the studies are fully done with Monte Carlo simulation, except for parts related to the cosmic background.

In this chapter, the overview of searches with jets and E_T^{miss} is given, and the definitions and criteria of physics objects and algorithms used in Chapter 11 and 12 will be mentioned.

10.1 Jets & E_T^{miss} Signatures from New Physics

In this thesis, we are motivated to develop search strategies for physics beyond the Standard Model with jets and E_T^{miss} . As mentioned in Chapter 1, SUSY and extra dimensional models predict weakly-interacting particles (neutralinos for many of the SUSY models, and KK-gravitons for Large Extra Dimensions model) which are good candidates for the dark matter in the universe. Thus, the searches using E_T^{miss} are highly important. Due to the feature of hadron colliders, and also from the properties of particle production, and/or the decays of produced new particles, high p_T jets are expected to accompany in events with SUSY particles or KK-gravitons.

10.1.1 SUSY Search Modes in ATLAS

Event topology-based searches allow for model-independent searches for SUSY. The following modes are considered in ATLAS,

- No-lepton search mode
- One-lepton search mode
- Opposite-sign dilepton search mode
- Same-sign dilepton search mode
- Multi-lepton search mode

The search modes are considered with various jet multiplicity (usually starting from two high p_T jets, up to three or four). Search modes with b-jets or hadronic τ 's may also provide additional sensitivity for the SUSY searches. Monojet signatures may arise from some of the AMSB SUSY, or split SUSY models as will be briefly mentioned in Chapter 11.

Among the search modes, no-lepton and one-lepton search modes have the largest discovery reach among various mSUGRA parameters [23][129], and thus highly important for early data analyses. However, observations in various search modes allow us to narrow down the candidates of new physics, once excess(es) are found in some of the search modes, as excesses themselves do not carry significant amount of information about their physics origin.

In Chapter 12, we concentrate on the investigations of no-lepton search mode, because it is one of the most important channel for the discovery. The most challenging part of the no-lepton search mode is the estimation of background. Strategies to perform successful prediction will be mentioned in the chapter.

10.2 Physics Objects and Algorithms

Identification criteria including isolation and overlap removal were mentioned below for each object.

10.2.1 Electrons

Electrons are reconstructed and identified using the inner detector and LAr electromagnetic calorimeter by so called the “eGamma” algorithm [23]. The basic concept is to match the tracks from the Inner Detector to the clusters in the EM calorimeter. The “eGamma” algorithm is actually an inclusive term for three algorithms; an algorithm exploiting calorimeter clusters as the seeds (the algorithm for high p_T electrons), an algorithm using the Inner Detector tracks (for low p_T electrons), or the one specifically used for forward electrons with no requirement on the matching of tracks to the calorimeter. Here, the transverse momentum of an electron is required to be larger than 20 GeV, and the absolute value of pseudorapidity η to be less than 2.5. On top of the basic identification criteria (such as track fit quality, shower shape in the calorimeter), isolation conditions are required to avoid identifying electrons originating from b-jets. The transverse energy in a cone of $\Delta R (= \sqrt{\Delta\eta^2 + \Delta\phi^2}) < 0.2$ from the electrons is required to be smaller than 10 GeV. When electrons are within $0.2 < \Delta R < 0.4$ from a jet, they are discarded, since they are likely to have originated from b-jets (in case of $\Delta R < 0.2$, the electron is kept and the overlapping jet is discarded since they are very likely coming from the same electron).

10.2.2 Muons

So called the STACO algorithm [23][52] was used for the muon reconstruction. It makes use of a statistical combination of tracks reconstructed in the Muon Spectrometer and the Inner Detector. The tracks in the Muon Spectrometer and the Inner Detector were matched correspondingly with a requirement of a reasonable matching quality (here, $\chi^2 < 100$ is required). The transverse energy inside a cone of $\Delta R < 0.2$ from muons is required to be smaller than 10 GeV. When muons are within $\Delta R < 0.4$ from a jet, they are discarded, since they are likely to have originated from b-jets.

10.2.3 Jets

Jets reconstructed with the seeded Cone algorithm were used. The details of jet reconstruction were previously mentioned in Section 8.4.2. Here, jets reconstructed from Topoclusters as inputs by the ATLAS cone algorithm with the cone size 0.4 (“Cone4H1TopoJets”) are used for the analysis.

10.2.4 Missing E_T

As frequently mentioned in this thesis, E_T^{miss} is the imbalance of energy (momentum, to be precise) in the transverse plane. Due to the feature of the hadron collider, the energy in the z direction is not balanced, because only fractions of the energy of incoming protons are carried by the interacting partons (and the energy of the partons are unknown for each event).

E_T^{miss} carries important information for weakly interacting particles (neutrinos and possibly new particles such as LSP’s and KK particles), and thus very important for

searches of physics beyond the Standard Model (needless to mention its importance for the Standard Model measurements).

The algorithm of E_T^{miss} and its categories were mentioned in Sec. 7.4.1 and Appendix C. Here, “MET_Final” was used in the analysis. It is a calorimeter cell-based E_T^{miss} , with corrections applied for the muon contribution and the energy lost in the cryostat.

10.2.5 b-Tagging

b-Tagging is the identification of jets originating from the hadronization of b-quarks. The tagging of b-jets is especially important for Top physics, Higgs searches, and searches for SUSY.

The identification of b-jets are performed using their features that is quite different from jets originating from lighter quarks. Such features are,

- Long lifetime of hadrons containing a b quark ($c\tau \sim 450 \mu\text{m}$). Presence of displaced vertices are expected.
- Hard fragmentation. A b-hadron carries large fraction of the original momentum of the b quark.
- Relatively large mass of b-hadrons. Decay products of b-hadrons have large transverse momentum from the jet axis.

The first feature indicate that the reconstruction of ID tracks and measurement of their impact parameters are highly important. Also, the presence of leptons in jets can complementarily used for the tagging when semi-leptonic decays occur from b-hadrons. In this thesis, the standard b-tagging algorithm in ATLAS using the combination of information from the impact parameter of ID tracks associated with jets, and the presence of secondary vertex is used. Weights are defined and calculated from the likelihood ratios, and a cut is used to tag b-jets. Figure 10.1 shows the b-tagging weight for b-jets, c-jets, and light flavor jets. In this thesis, jets with weights larger than 3 are defined as b-jets. Currently, the performance of b-tagging is evaluated from Monte Carlo simulations, but it will be measured from data during the actual data taking by using QCD di-jet and $t\bar{t}$ events.

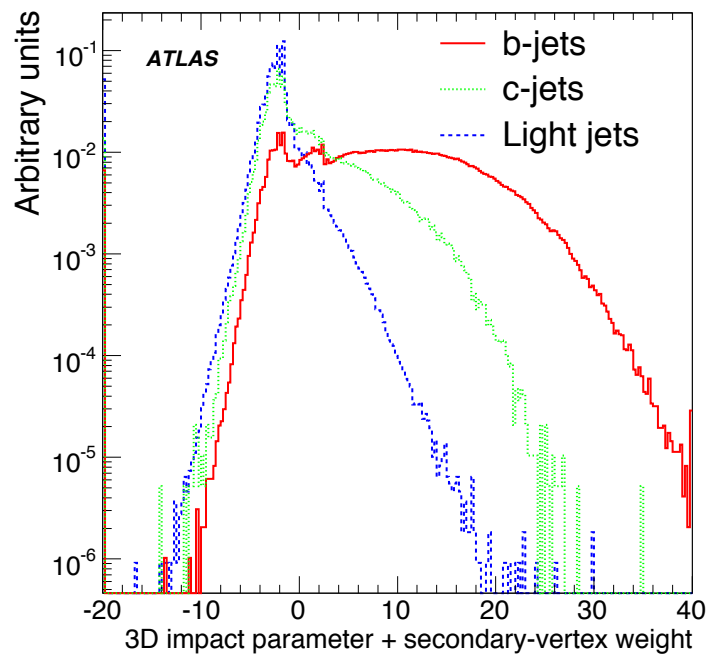


Figure 10.1: Distribution of jet b-tagging weight for b-jets (red), c-jets (green), and light flavor jet (blue) [23].

Chapter 11

Monojet Search for the Large Extra Dimensions

In the previous chapter, the quality of calorimeter objects was extensively investigated with both pure and MC-overlaid cosmic events. Those cleaning cuts using quality variables are crucial for physics measurements using jets and E_T^{miss} . Here, we estimated the contribution of cosmic background to various event signature with jet(s) and E_T^{miss} ; from monojet to multi-jet plus large E_T^{miss} . These event signatures are expected in various new physics models; from the Supersymmetry, the Large Extra Dimensions, Leptoquarks, and Heavy Vector Bosons, for example. The contribution on the Standard Model background was investigated in detail in the previous studies [23][130]. Here, the first data-driven studies on the cosmic background is shown, and the strategy to cope with such background is proposed.

In Section 10.2, the definition and identification criteria of physics objects used in the analyses were mentioned. In this chapter, the emphasis is on the monojet search where non-collision background can significantly affect the analyses, and the Large Extra Dimensions (LED) model [27] with KK-graviton emissions was taken as a benchmark for the monojet search.

11.1 Monojet Signature from the Large Extra Dimensions

Previous studies of the Standard Model background in monojet search are mentioned in [137][138]. Here, we show the first investigation in ATLAS on the contribution of cosmic background to monojet signature using the real data, and its effects on the Large Extra Dimensions search. Sherpa [139] Monte Carlo generator was used for the signal production, which has a robust framework to generate the spin-2 KK-gravitons using the matrix-element calculator AMEGIC++ [140][141].

A brief overview of real KK-Graviton emission processes in the Large Extra Dimensions model is given in Section 11.1.1. The profile of Monte Carlo samples used in this study is mentioned in Section 11.2. Section 11.3 shows investigations on the effects of

selection cuts and cosmic background in the monojet search.

11.1.1 Real KK-Graviton Emission in Large Extra Dimensions Model

As mentioned in Chapter 2, according to the Large Extra Dimension model, the Planck scale can be as low as the TeV-scale due to the presence of the extra dimensions (the number of the extra dimensions is described as δ in the following text). The small observed value of the Newton's constant may be due to the existence of a large compactified volume of the extra dimensions [27]. The interactions of the Kaluza-Klein excitations of the gravitons can be described by a 4-dimensional effective field theory [142]. The effects of those KK-excitations from the LED model can manifest themselves in several event signatures such as “jet + E_T^{miss} (monojet)”, “photon + E_T^{miss} ,” by emission of KK-gravitons (Figure 11.1) or excess of dijet or a lepton pair productions in the high energy tail (virtual KK-graviton exchange). Those signals were extensively searched in the previous experiments at the LEP [31]-[34] and the Tevatron [35]-[39]. The current exclusion limit is around 1 TeV for most numbers of extra dimensions (Figure 2.6). Here, we consider the monojet signature originating from the KK-graviton emissions.

In the LED model, the rate of graviton emission is enhanced by the large phase space of the Kaluza-Klein modes, and counteract the suppression from M_P . The KK-graviton modes have masses $|\mathbf{n}|/R$ (\mathbf{n} : a δ -dimensional vector with components indicating the KK-excitation level in each extra dimension, R : size of the compactified extra dimensions), and the mass splitting Δm of the KK-modes is described as,

$$\Delta m \sim \frac{1}{R} = M_D \left(\frac{M_D}{\bar{M}_P} \right)^{2/\delta} \sim \left(\frac{M_D}{\text{TeV}} \right)^{\frac{\delta+2}{2}} 10^{\frac{12\delta-31}{\delta}} \text{ eV} \quad (11.1)$$

$$\bar{M}_P = M_P / \sqrt{8\pi} . \quad (11.2)$$

For small numbers of extra dimensions, the mass splitting is far below the energy resolution of the detector (4 meV for $M_D = 2$ TeV, $\delta = 2$; 160 keV for $M_D = 2$ TeV, $\delta = 4$ for example). For such small numbers of extra dimensions (and thus large R), the sum over Kaluza-Klein modes can be replaced by a continuous integral. Considering a hypersphere with a unit radius in δ dimensions, the number of modes between n and $n + dn$ ($|\mathbf{n}|$ is written as n for simplicity) can be written as,

$$dN = \frac{2\pi^{\delta/2}}{\Gamma(\delta/2)} n^{\delta-1} dn . \quad (11.3)$$

This equation can be rewritten in terms of $m (= n/R)$, the mass of a Kaluza-Klein mode,

$$dN = \frac{2\pi^{\delta/2}}{\Gamma(\delta/2)} \frac{\bar{M}_P^2}{M_D^{2+\delta}} m^{\delta-1} dm . \quad (11.4)$$

Thus, the differential cross section for inclusive KK-graviton production is described as,

$$\frac{d^2\sigma}{dt dm} = \frac{2\pi^{\delta/2}}{\Gamma(\delta/2)} \frac{\bar{M}_P^2}{M_D^{2+\delta}} m^{\delta-1} \frac{d\sigma_m}{dt} , \quad (11.5)$$

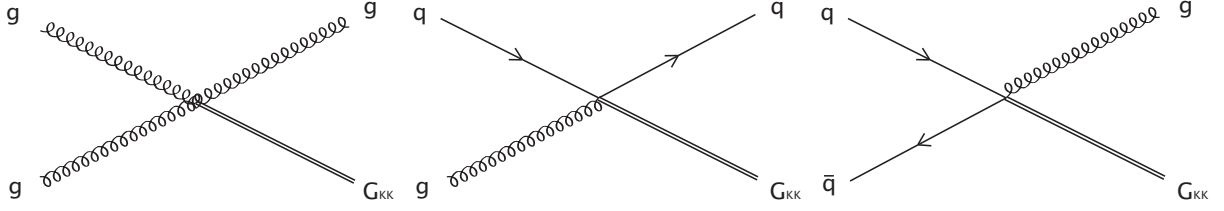


Figure 11.1: Leading order Feynman diagrams of KK-graviton emission with monojet signature.

where t is the Mandelstam variable and m corresponds to the mass of the KK-graviton. For the monojet signature the leading order diagrams are as shown in Figure 11.1, and the differential cross section for each process is,

$$\frac{d\sigma_m}{dt}(gg \rightarrow gG_{\text{KK}}) = \frac{\alpha_s}{36} \frac{1}{s\bar{M}_P^2} F_1(t/s, m^2/s), \quad (11.6)$$

$$\frac{d\sigma_m}{dt}(qg \rightarrow qG_{\text{KK}}) = \frac{\alpha_s}{96} \frac{1}{s\bar{M}_P^2} F_2(t/s, m^2/s), \quad (11.7)$$

$$\frac{d\sigma_m}{dt}(q\bar{q} \rightarrow gG_{\text{KK}}) = \frac{3\alpha_s}{16} \frac{1}{s\bar{M}_P^2} F_3(t/s, m^2/s), \quad (11.8)$$

where t and s follow the standard definition of the Mandelstam variables. The F_1, F_2 , and F_3 functions will be explicitly shown in Appendix D. Thus, in order to calculate the differential cross section for monojet signature, an integral should be taken in regards to m . The upper limit of the integral is typically taken as M_D , and this approach was adopted here as well.

11.2 Monte Carlo Simulation Samples and Data

As mentioned in the previous section, SHERPA (version 1.1.3) was used for the signal production. Three processes (Figure 11.1) were inclusively generated. Figure 11.2 shows the cross section of ADD monojet processes in SHERPA as a function of the number of extra dimensions. The cross sections shown in the figure are after a cut on the leading parton ($p_T > 80$ GeV) was applied. Cross sections for $M_D=2,3,4$ TeV are shown. Here, we will use four samples shown in Table 11.2. The cut on $\sqrt{\hat{s}} < M_D$ was applied for the summation of KK-graviton excitations in each sample (the calculation was based on [142])

For the Standard Model background, Z/W+jets (separate samples for $Z(\rightarrow \nu\bar{\nu})$, $Z(\rightarrow e^+e^-)$, $Z(\rightarrow \mu^+\mu^-)$, and $Z(\rightarrow \tau^+\tau^-)$), $t\bar{t}$, single top and QCD dijets were considered. The information for each sample is shown in Table E.2 in Appendix . QCD dijet samples were generated in momentum slices as mentioned in the table and Section 9.1.1.

Real cosmic data and cosmic data overlaid on the Minimum Bias Monte Carlo samples were used to estimate the contribution of cosmic background.

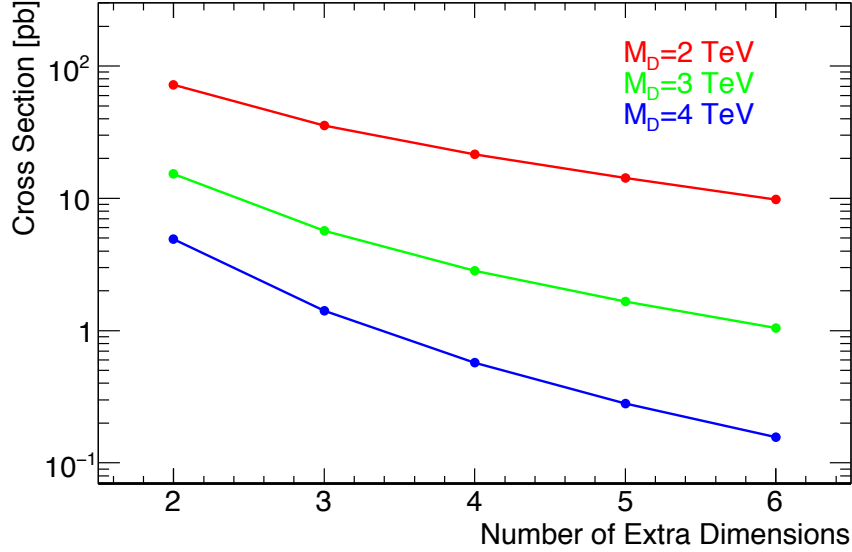


Figure 11.2: Cross section of LED monojet processes in SHERPA as a function of the number of extra dimensions. Cut on the leading parton ($p_T > 80$ GeV) is applied. Cross sections for $M_D=2,3,4$ TeV are shown.

Table 11.1: Cross section of LED processes in SHERPA. Cut on the leading parton ($p_T > 80$ GeV) is applied.

| Planck Scale M_D | δ | xsec [pb] |
|--------------------|----------|---------------------|
| 2 TeV | 2 | 72.42 ± 0.12 |
| 2 TeV | 6 | 9.810 ± 0.015 |
| 4 TeV | 2 | 4.897 ± 0.008 |
| 4 TeV | 6 | 0.1562 ± 0.0002 |

11.3 Event Selection

Search for the Large Extra Dimensions in the monojet channel is one of the effective ways, and has a good sensitivity to the signals if they exist.

Considering the kinematics of the processes, the events are expected to have the following features,

- Absence of leptons
- High p_T monojet
- Large E_T^{miss}

Here, we will investigate on the trigger effects and useful selection cuts to perform searches in the monojet signature.

11.3.1 Trigger Menus for the Monojet Search

Here, we consider trigger menus “lumi1E31_no_Bphysics_no_prescale” in the Monte Carlo samples (reconstructed with Athena version 14.2.25.9), which are intended for $10^{31}\text{cm}^{-2}\text{s}^{-1}$ luminosity. The prescales are not considered in the simulation itself, so the proposed prescales are implemented by hand in the analyses when needed (in such cases, it will explicitly be mentioned in the text). The menus have minor differences from what are currently proposed (see Table 4.1), but the differences are not significant in the following studies.

The trigger menus without prescales useful for the monojet searches are “EF_J265 (leading jet $p_T > 265$ GeV),” “EF_J350 (leading jet $p_T > 350$ GeV),” and “EF_j70_xe30 (leading jet $p_T > 70$ GeV and $E_T^{\text{miss}} > 30$ GeV).” Trigger menus with lower thresholds and prescales will allow for estimating the trigger efficiencies in data-driven ways. The trigger efficiencies from the jet trigger menus as a function of the leading jet transverse momentum are shown in Figure 11.3. The QCD dijet Monte Carlo samples are used in the figure. E_T^{miss} trigger efficiencies as a function of E_T^{miss} are shown in Figure 11.4 for various E_T^{miss} algorithms. We used MET_Final for the analysis here.

In order to reduce the trigger effects in the analyses as much as possible, the cut on the leading jet p_T is preferable to be more than about 300 GeV for EF_J265 and 400 GeV for EF_350. For EF_j70_xe30, the cut on the leading jet p_T should be larger than about 100 GeV and E_T^{miss} to be larger than 80 GeV.

11.3.2 Absence of Reconstructed Leptons

Since no leptons exist in the leading-order diagrams of KK-graviton emissions, it is appropriate to reject events with leptons, which will remove large fraction of $W(\rightarrow l\nu)$ and $Z(\rightarrow \tau^+\tau^-) + \text{jet}$ events. In QCD dijets and LED samples, electrons can fakely be reconstructed from jets in a low rate.

In Figure 11.5, the numbers of reconstructed electrons are shown for events with the leading jet $p_T > 100$ GeV for three different selection criteria of electron reconstructions (which are mentioned as “loose,” “medium,” and “tight”). Here, we take leading jet $p_T > 100$ GeV cut as a starting benchmark. The breakdown of events remaining after an electron veto for each criteria is shown in Table 11.2. Reconstructing electrons with loose selection criteria and rejecting events with such electrons do not significantly reduce the sensitivity to the LED signals (reduction by about a few percent), but reduces background by a few tens of percent compared to the case with tighter electron selection criteria. Thus, it is preferable to use loose electron selection criteria to veto more Standard Model background.

Due to the same reason as the electrons, events with muons should be rejected for the monojet search. Well isolated “combined muons” (reconstructed by the combination of Inner Detector and Muon Spectrometer tracks) originate from $Z/W + \text{jets}$ events where the bosons decay into muon(s) or tau(s) consecutively decaying into muon(s). Requiring absence of combined muons will reject large amount of $Z(\rightarrow \mu^+\mu^-)+\text{jets}$ and $W(\rightarrow \mu\nu)+\text{jets}$.

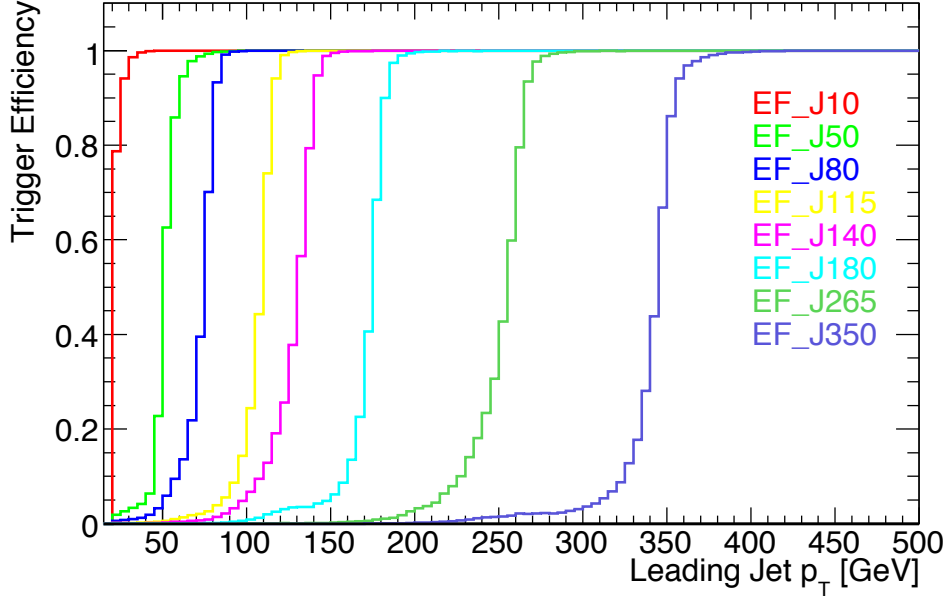


Figure 11.3: Efficiency of jet triggers at the Event Filter level as a function of the leading jet transverse momentum. The efficiencies from QCD dijet Monte Carlo samples are shown in the figure.

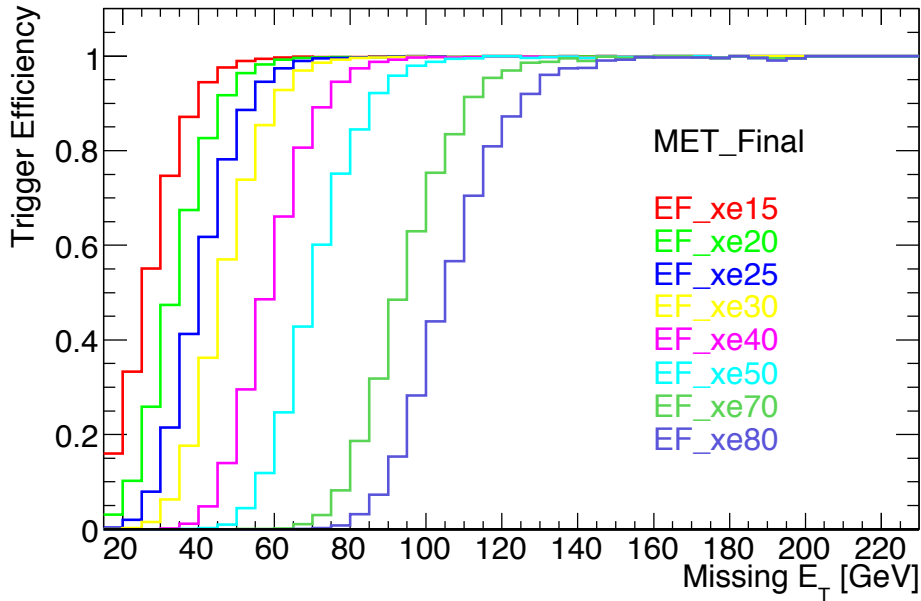


Figure 11.4: Efficiency of E_T^{miss} triggers at the Event Filter level as a function of E_T^{miss} . The efficiencies from $Z(\rightarrow \nu\bar{\nu}) + \text{jets}$ Monte Carlo samples are shown in the figure. MET_Final is used for the E_T^{miss} algorithm.

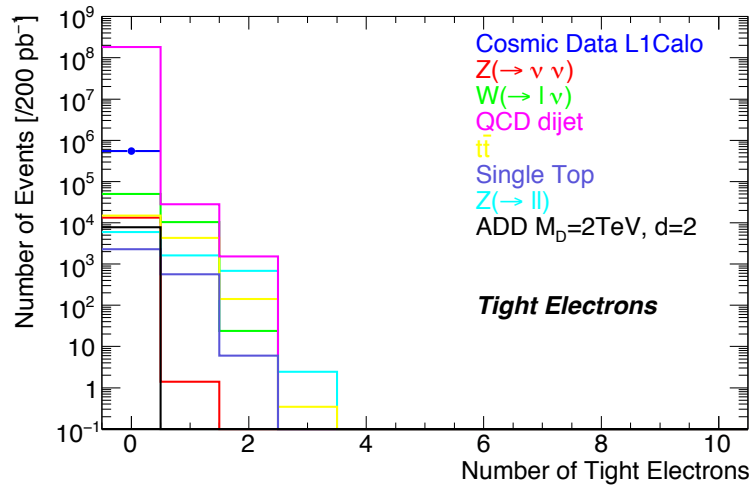
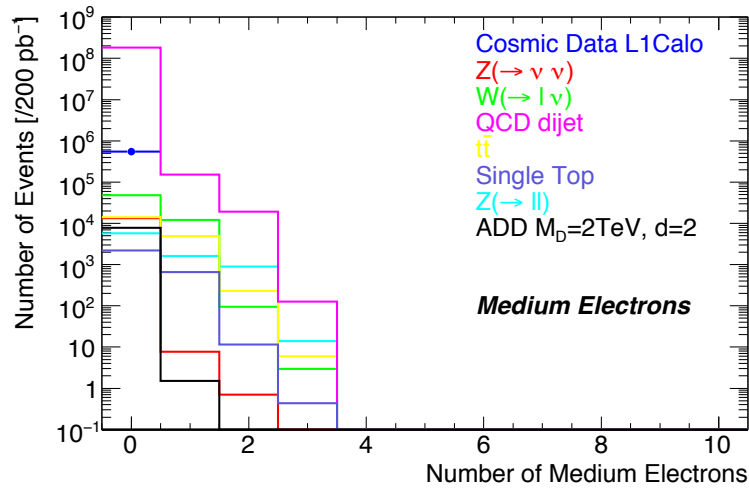
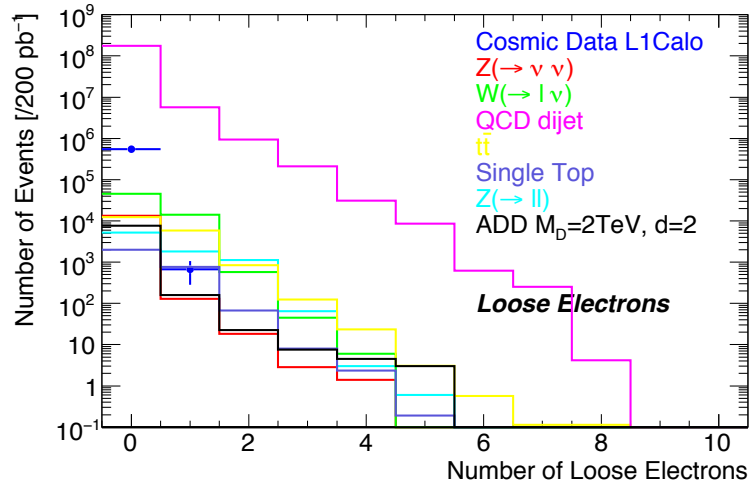


Figure 11.5: Number of reconstructed electrons (left: loose IsEM, center: medium IsEM criteria, right: tight IsEM) from LED KK-graviton signals and background (for events with the leading jet $p_T > 100 \text{ GeV}$). The distributions are normalized to 200 pb^{-1} .

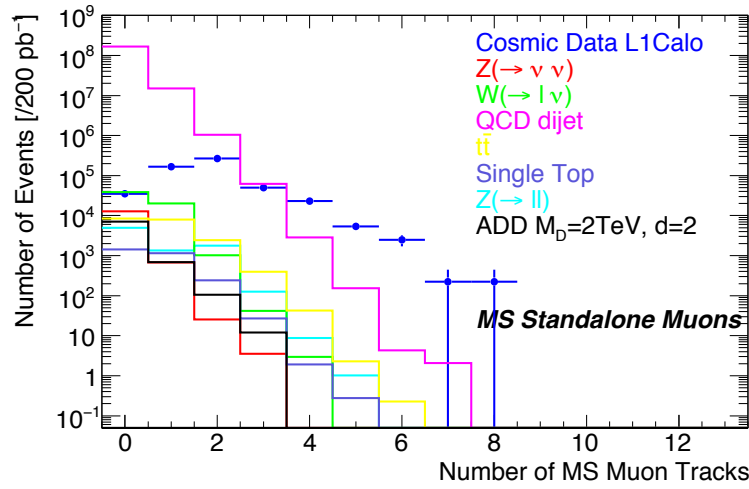
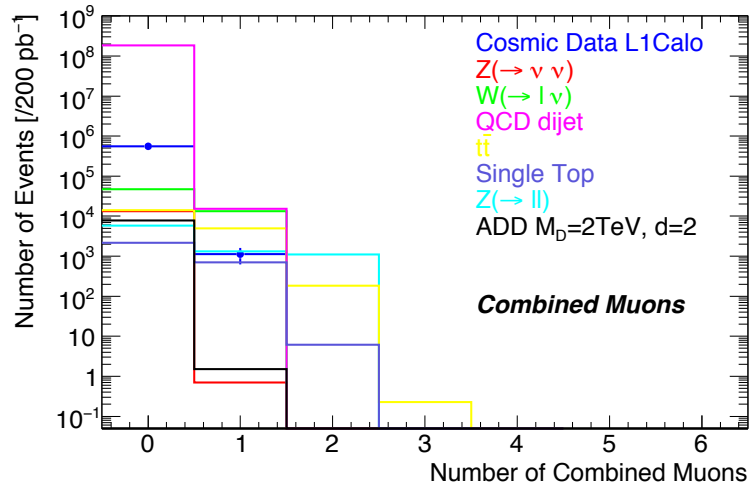


Figure 11.6: Number of reconstructed combined and MS-standalone muons from LED KK-graviton signals and background (for events with the leading jet $p_T > 100$ GeV). The distributions are normalized to 200 pb^{-1} .

On top of combined muons, standalone Muon Spectrometer (MS) tracks provide additional background rejection. Figure 11.6 shows the numbers of reconstructed combined and stand-alone Muon Spectrometer tracks. Table 11.3 shows the breakdown of number of events without combined or MS-standalone muons.

The utmost motivation to require the absence of standalone MS tracks is to reject the cosmic background. Most of the cosmic muons are non-projective (not passing near the interaction point), and will not be reconstructed as combined tracks, but are very often reconstructed as standalone MS tracks. As obvious from Table 11.3, the cosmic background is reduced by a factor of 16. Also, this selection cut further removes $Z(\rightarrow \mu^+\mu^-)+\text{jets}$ and $W(\rightarrow \mu\nu)+\text{jets}$, when the muons failed the combined muon reconstruction but tagged as MS-standalone muon tracks. Another byproduct of this rejection scheme is that it also rejects events with pion “punch-through’s” from jets’ shower leakage, where such leakage forms tracks in the muon spectrometer. Events with punch-throughs have badly reconstructed $E_{\text{T}}^{\text{miss}}$, so it is appropriate to reject such events for both signals and background.

11.3.3 Selection Cuts on Jets

The most important cut to be applied to jets is the second-leading jet veto. Whereas $Z(\rightarrow \nu\bar{\nu})+\text{jets}$ and most of the $W(\rightarrow \tau\nu)$ jets are irreducible background, QCD dijet events can significantly be reduced by selection cuts on jets. Among those selection cuts, the second leading jet veto is the most important strategy.

Figure 11.7 and 11.8 show the leading and second-leading jet distributions. There are significant contributions from QCD dijets and cosmic rays as expected, which surpass the signals without any specific considerations. There are no significant difference in the pseudorapidity (η) distributions in the signals and background, but it is meaningful to select jets in the central region to avoid the cracks ($1.37 < \eta < 1.52$) in the calorimeters, which one of the dijet can be lost and fake monojet signals.

Since the second-leading jets tend to be soft for the KK-graviton emission processes, a veto on the second-leading jets still keeps high efficiency of the signals, but significantly removes the QCD dijet background (however, too tight a veto also reduces the signals by some factor so the cut should be balanced considering both effects).

11.3.4 Non-collision Background Rejection

The jet EM fraction (EMF) is a useful discrimination variable to reject non-collision background as mentioned in the previous chapter. Figure 11.10 shows the distributions of jet EM fraction for signals and background. Rejecting events which has low EM fraction values of the leading jet removes significant amount of cosmic background when a hard muon bremsstrahlung occurs in TileCal. Applying higher cut on the jet EM fraction not just removes remaining background from the cosmic muons when the bremsstrahlung takes place in LAr EM calorimeter, but also rejects events with an electron failing to be identified and reconstructed as a jet (e.g. background from $W(\rightarrow e\nu)$ events).

The jet charge fraction (CHF) is another variable to successfully reject non-collision

Table 11.2: Number of events with no reconstructed electrons (only events with the leading jet $p_T > 100$ GeV are counted below). Integrated luminosity is assumed to be 200 pb^{-1} .

| Sample | No Loose Electron | No Medium Electron | No Tight Electron |
|---|-----------------------------------|-----------------------------------|----------------------------------|
| LED $M_D = 2, \delta = 2$ | 7662 ± 88 | 7859 ± 89 | 7860 ± 89 |
| LED $M_D = 2, \delta = 6$ | 520 ± 23 | 536 ± 23 | 536 ± 23 |
| LED $M_D = 4, \delta = 2$ | 263 ± 16 | 273 ± 17 | 272 ± 17 |
| LED $M_D = 4, \delta = 6$ | 10 ± 3 | 10 ± 3 | 10 ± 3 |
| Cosmic | $(5.512 \pm 0.007) \times 10^5$ | $(5.518 \pm 0.007) \times 10^5$ | $(5.518 \pm 0.007) \times 10^5$ |
| QCD Dijet | $(1.7631 \pm 0.0001) \times 10^8$ | $(1.8303 \pm 0.0001) \times 10^8$ | $(1.832 \pm 0.0001) \times 10^8$ |
| $t\bar{t}$ | 12357 ± 111 | 14114 ± 119 | 14825 ± 122 |
| $Z(\rightarrow \nu\bar{\nu})+\text{jets}$ | 13252 ± 115 | 13395 ± 116 | 13402 ± 116 |
| $Z(\rightarrow e^+e^-)+\text{jets}$ | 787 ± 28 | 945 ± 31 | 1127 ± 34 |
| $Z(\rightarrow \mu^+\mu^-)+\text{jets}$ | 2327 ± 48 | 2384 ± 49 | 2401 ± 49 |
| $Z(\rightarrow \tau^+\tau^-)+\text{jets}$ | 2099 ± 46 | 2362 ± 49 | 2417 ± 49 |
| $W(\rightarrow e\nu_e)+\text{jets}$ | 9015 ± 95 | 10310 ± 102 | 11799 ± 109 |
| $W(\rightarrow \mu\nu_\mu)+\text{jets}$ | 18763 ± 137 | 19078 ± 138 | 19135 ± 138 |
| $W(\rightarrow \tau\nu_\tau)+\text{jets}$ | 17438 ± 132 | 18537 ± 136 | 18739 ± 137 |
| Single Top | 2002 ± 45 | 2184 ± 47 | 2280 ± 48 |

Table 11.3: Number of events with no reconstructed muons (only events with the leading jet $p_T > 100$ GeV are counted below). Integrated luminosity is assumed to be 200 pb^{-1} .

| Sample | No Combined Muon | No MS-standalone Muon |
|---|-----------------------------------|-----------------------------------|
| LED $M_D = 2, \delta = 2$ | 7859 ± 89 | 7052 ± 84 |
| LED $M_D = 2, \delta = 6$ | 536 ± 23 | 484 ± 22 |
| LED $M_D = 4, \delta = 2$ | 273 ± 17 | 242 ± 16 |
| LED $M_D = 4, \delta = 6$ | 10 ± 3 | 9 ± 3 |
| Cosmic | $(5.507 \pm 0.007) \times 10^5$ | 35205 ± 188 |
| QCD Dijet | $(1.8318 \pm 0.0001) \times 10^8$ | $(1.6706 \pm 0.0001) \times 10^8$ |
| $t\bar{t}$ | 14091 ± 119 | 8423 ± 92 |
| $Z(\rightarrow \nu\bar{\nu})+\text{jets}$ | 13402 ± 116 | 12696 ± 113 |
| $Z(\rightarrow e^+e^-)+\text{jets}$ | 3184 ± 56 | 3022 ± 55 |
| $Z(\rightarrow \mu^+\mu^-)+\text{jets}$ | 283 ± 17 | 71 ± 8 |
| $Z(\rightarrow \tau^+\tau^-)+\text{jets}$ | 2348 ± 49 | 1890 ± 43 |
| $W(\rightarrow e\nu_e)+\text{jets}$ | 21234 ± 146 | 20195 ± 142 |
| $W(\rightarrow \mu\nu_\mu)+\text{jets}$ | 7008 ± 84 | 2593 ± 51 |
| $W(\rightarrow \tau\nu_\tau)+\text{jets}$ | 18438 ± 136 | 16075 ± 127 |
| Single Top | 2144 ± 46 | 14400 ± 38 |

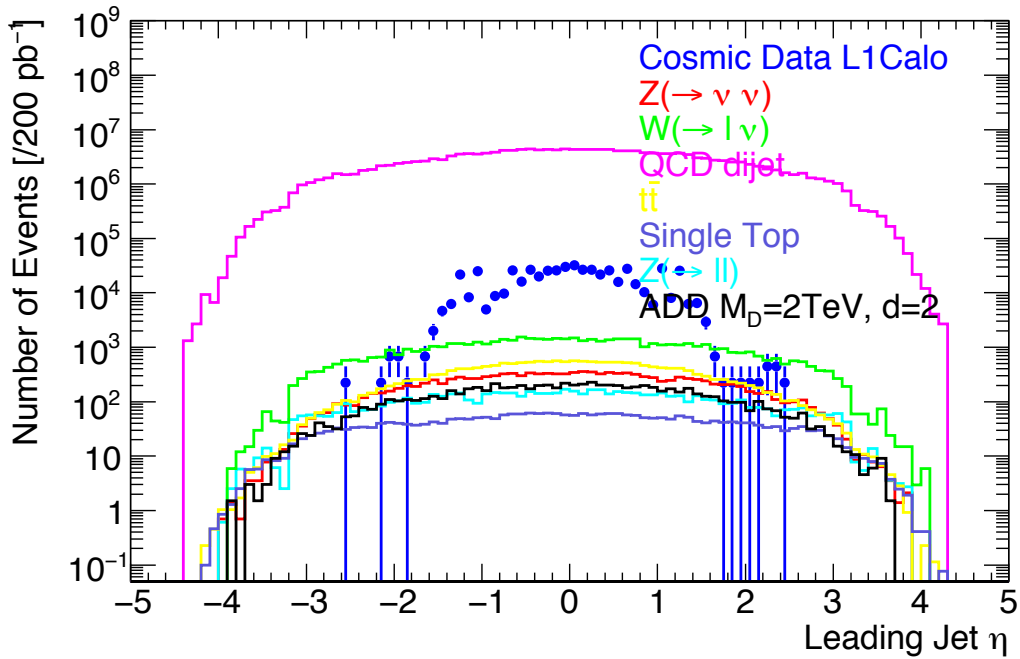
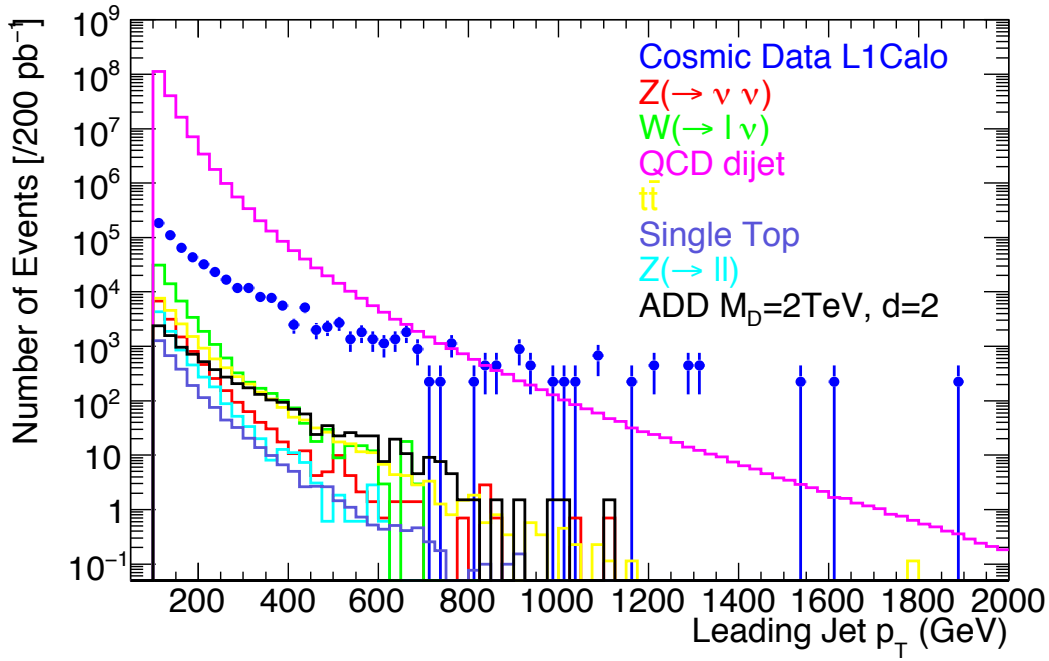


Figure 11.7: Leading jet distributions of LED KK-graviton signals and background ($p_T > 100\text{GeV}$). The left figure shows the transverse momentum and the right shows the pseudorapidity. The distributions are normalized to 200 pb⁻¹.

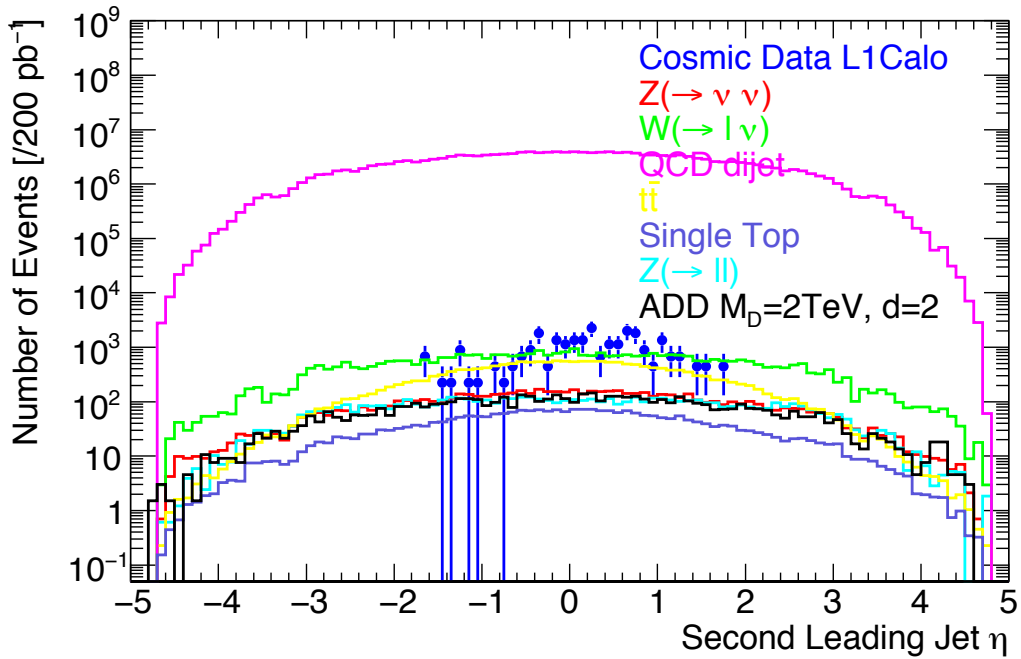
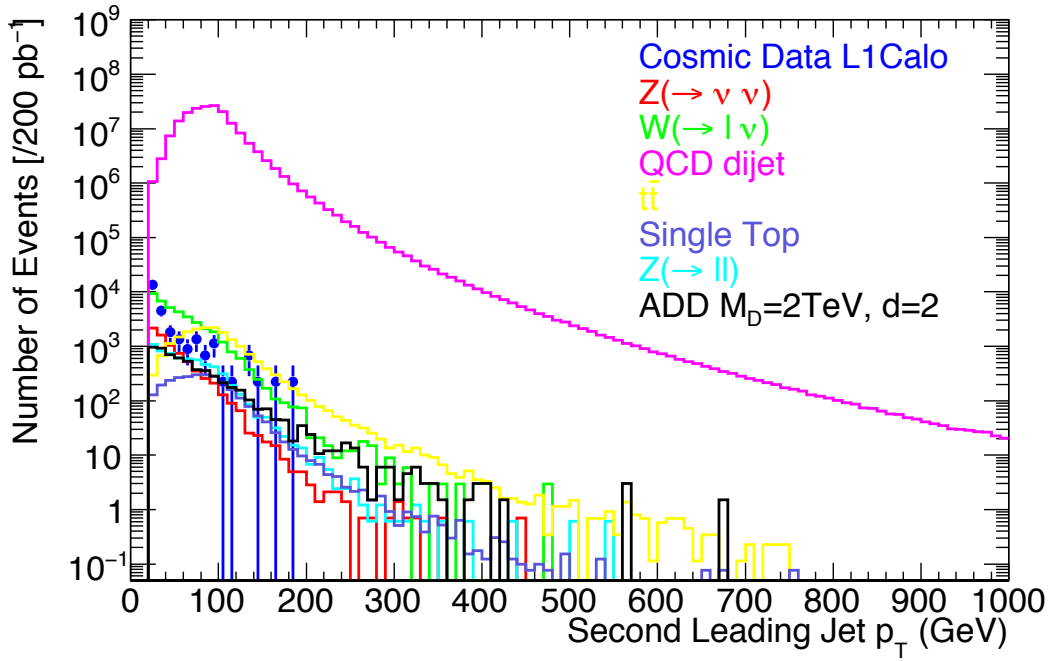


Figure 11.8: Second leading jet distributions of LED KK-graviton signals and background (when leading jet $p_T > 100\text{GeV}$). The left figure shows the transverse momentum and the right shows the pseudorapidity. The distributions are normalized to 200pb^{-1} .

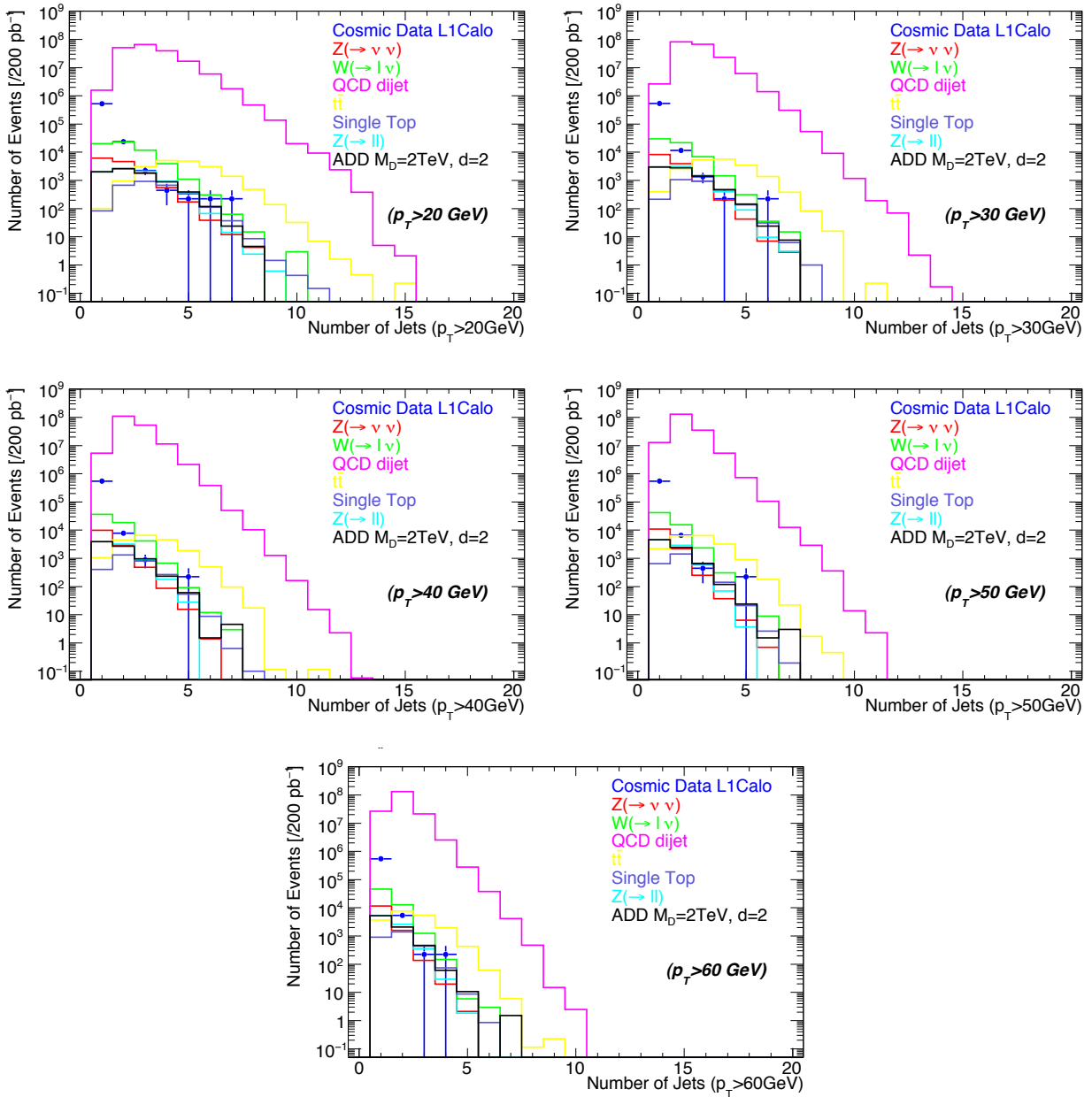


Figure 11.9: Number of jets with $p_T > 20$ GeV (upper left), 30 GeV (upper right), 40 GeV (middle left), 50 GeV (middle right), and 60 GeV (bottom) for events with the leading jet $p_T > 100$ GeV. The distributions are normalized to 200 pb^{-1} .

Table 11.4: Number of events with second leading jet veto (only events with the leading jet $p_T > 100$ GeV are counted below). Integrated luminosity is assumed to be 200 pb^{-1} .

| Sample | veto 20 GeV | veto 30 GeV | veto 40 GeV |
|---|---------------------------------|---------------------------------|---------------------------------|
| LED $M_D = 2, \delta = 2$ | 2032 ± 45 | 2989 ± 55 | 3913 ± 63 |
| LED $M_D = 2, \delta = 6$ | 118 ± 11 | 185 ± 14 | 241 ± 16 |
| LED $M_D = 4, \delta = 2$ | 66 ± 8 | 100 ± 10 | 129 ± 11 |
| LED $M_D = 4, \delta = 6$ | 2 ± 1 | 3 ± 2 | 4 ± 2 |
| Cosmic | $(5.249 \pm 0.007) \times 10^5$ | $(5.384 \pm 0.007) \times 10^5$ | $(5.429 \pm 0.007) \times 10^5$ |
| QCD Dijet | $(1.567 \pm 0.001) \times 10^6$ | $(2.628 \pm 0.002) \times 10^6$ | $(5.424 \pm 0.002) \times 10^6$ |
| $t\bar{t}$ | 101 ± 10 | 395 ± 20 | 1066 ± 33 |
| $Z(\rightarrow \nu\bar{\nu})+\text{jets}$ | 8273 ± 91 | 4136 ± 64 | 9872 ± 99 |
| $Z(\rightarrow e^+e^-)+\text{jets}$ | 647 ± 25 | 1067 ± 33 | 1345 ± 37 |
| $Z(\rightarrow \mu^+\mu^-)+\text{jets}$ | 1035 ± 32 | 1452 ± 38 | 1746 ± 42 |
| $Z(\rightarrow \tau^+\tau^-)+\text{jets}$ | 295 ± 17 | 550 ± 23 | 806 ± 28 |
| $W(\rightarrow e\nu_e)+\text{jets}$ | 6592 ± 81 | 9831 ± 99 | 12046 ± 110 |
| $W(\rightarrow \mu\nu_\mu)+\text{jets}$ | 8696 ± 93 | 11775 ± 109 | 13936 ± 118 |
| $W(\rightarrow \tau\nu_\tau)+\text{jets}$ | 4950 ± 70 | 8022 ± 90 | 10505 ± 102 |
| Single Top | 84 ± 9 | 213 ± 15 | 407 ± 20 |

| Sample | veto 50 GeV | veto 60 GeV |
|---|-----------------------------------|-----------------------------------|
| LED $M_D = 2, \delta = 2$ | 4612 ± 70 | 5227 ± 72 |
| LED $M_D = 2, \delta = 6$ | 290 ± 17 | 336 ± 18 |
| LED $M_D = 4, \delta = 2$ | 157 ± 13 | 177 ± 13 |
| LED $M_D = 4, \delta = 6$ | 5 ± 2 | 6 ± 2 |
| Cosmic | $(5.447 \pm 0.007) \times 10^5$ | $(5.460 \pm 0.007) \times 10^5$ |
| QCD Dijet | $(1.2829 \pm 0.0004) \times 10^7$ | $(2.6637 \pm 0.0005) \times 10^7$ |
| $t\bar{t}$ | 2200 ± 47 | 3699 ± 61 |
| $Z(\rightarrow \nu\bar{\nu})+\text{jets}$ | 10912 ± 104 | 11663 ± 108 |
| $Z(\rightarrow e^+e^-)+\text{jets}$ | 1605 ± 40 | 1835 ± 43 |
| $Z(\rightarrow \mu^+\mu^-)+\text{jets}$ | 1938 ± 44 | 2076 ± 46 |
| $Z(\rightarrow \tau^+\tau^-)+\text{jets}$ | 1103 ± 33 | 1347 ± 37 |
| $W(\rightarrow e\nu_e)+\text{jets}$ | 13758 ± 117 | 15193 ± 123 |
| $W(\rightarrow \mu\nu_\mu)+\text{jets}$ | 15464 ± 124 | 16652 ± 129 |
| $W(\rightarrow \tau\nu_\tau)+\text{jets}$ | 12449 ± 112 | 14125 ± 119 |
| Single Top | 645 ± 25 | 914 ± 30 |

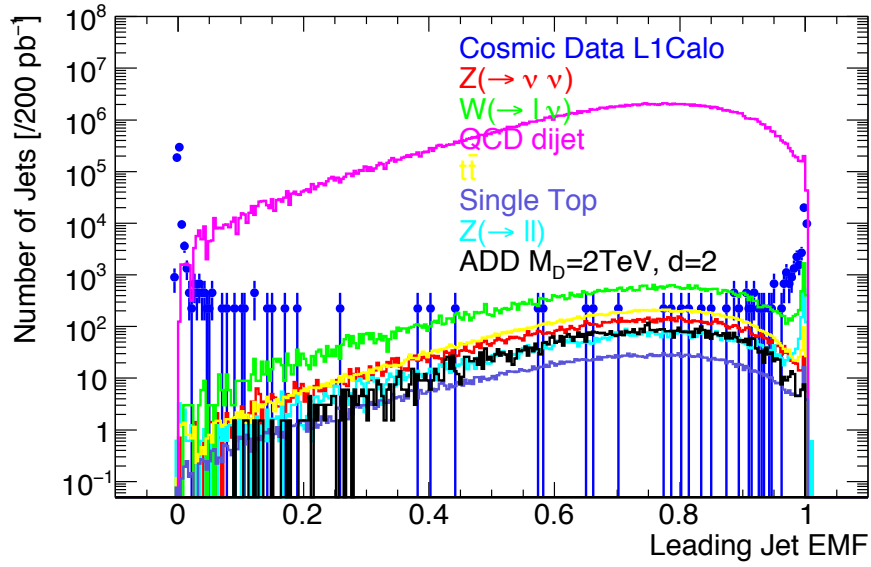


Figure 11.10: EM fraction of leading jet from LED KK-graviton signals and background (when leading jet $p_T > 100\text{GeV}$). The distributions are normalized to 200 pb^{-1} .

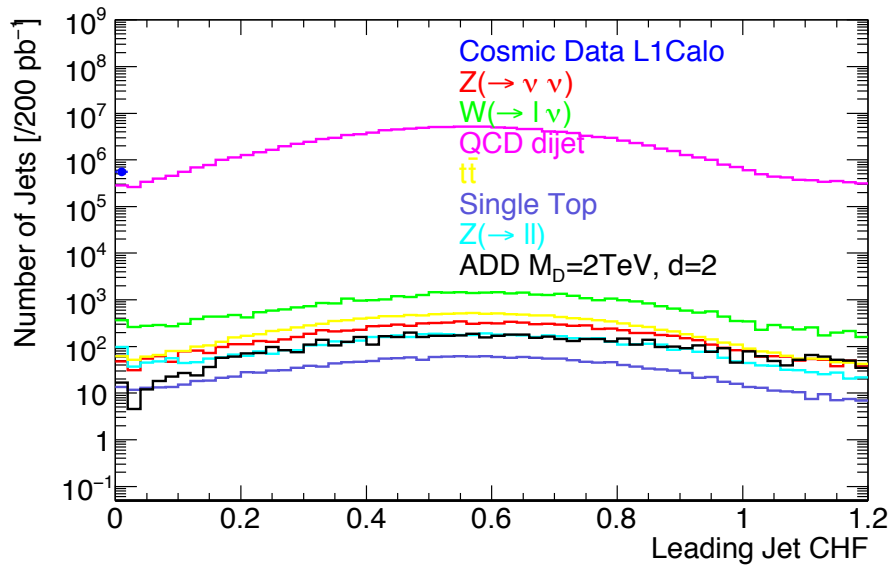


Figure 11.11: Charge fraction of leading jet from LED KK-graviton signals and background (when leading jet $p_T > 100\text{GeV}$). The distributions are normalized to 200 pb^{-1} .

background. Figure 11.11 shows the distributions of charge fraction of the leading jets for signals and background. As fake jets reconstructed from cosmic muon energy deposits have almost no Inner Detector tracks associated to the jets, the charge fraction is steeply concentrated around 0.

Table 11.6 shows the breakdown of numbers after the EM fraction cut ($0.15 < \text{leading jet EMF} < 0.95$) and charge fraction cut (leading jet CHF > 0.1).

11.3.5 Event Selection

Here, the following cuts were used for the event selection.

- Cut 1: No lepton (e, μ)
- Cut 2: Leading jet $p_T > 200$ GeV, $|\eta| < 1.2$
- Cut 3: $E_T^{\text{miss}} > 250$ GeV
- Cut 4: second leading jet veto: second leading jet $p_T < 50$ GeV
- Cut 5: $\Delta\phi(\text{second leading jet}, E_T^{\text{miss}}) > 0.15$
- Cut 6: No jet within $\Delta R < 0.1$ from dead or masked channels
- Cut 7: No tracks in the muon spectrometer
- Cut 8: Jet EM fraction > 0.15
- Cut 9: Jet Charge Fraction > 0.1

The E_T^{miss} distributions after each cut are shown in Figure 11.12 (from the upper left; Cut 2 is applied, and remaining cuts are additionally applied one by one). The non-existence of leptons are required, since the physics process of the LED KK-graviton emissions does not include a lepton. The leading jet is expected to have a large transverse momentum, since it is recoiled against an LED KK-graviton with mass of TeV order. Only the leading jet in the barrel region is required to avoid fake background from the QCD dijet, where one of the jets is badly reconstructed due to detector features such as the crack region. A cut on E_T^{miss} is applied, which is a straightforward requirement from the characteristics of the physics process. A veto on the second leading jet is required in order to avoid dijets with E_T^{miss} , which can originate from calibration uncertainty or other systematic effects. Cut 5-7 are the “cleaning cuts” for non-collision background rejection. Since the standard identification of muons in ATLAS requires a good combination of reconstructed tracks from the Inner Detector and the Muon Spectrometer, most of the cosmic muons fail the criteria due to the fact that not many cosmic muons pass the Inner Detector. Cut 5 take such an effect into account, and removes events with tracks from the muon spectrometer. Cut 5 significantly removes the cosmic background, but still a non-negligible amount of background remains. This is due to the fact that a large fraction of high energy cosmic muons have a large azimuthal angle, and do not leave enough hits to be well reconstructed in the muon spectrometer. On top of the angular characteristics, cosmic muons reach the

detector with a large in-coincidence to the bunch crossing. Such a large timing offsets of the hits in the muon spectrometer often leads to the non-reconstruction of muon tracks. This phenomenon was actually observed in the cosmic data in the Fall of 2008.

After all the event selection and cleaning cuts, the most dominant cosmic background is mostly removed and are under control. This result indicates the successful understandings and treatment of the cosmic background.

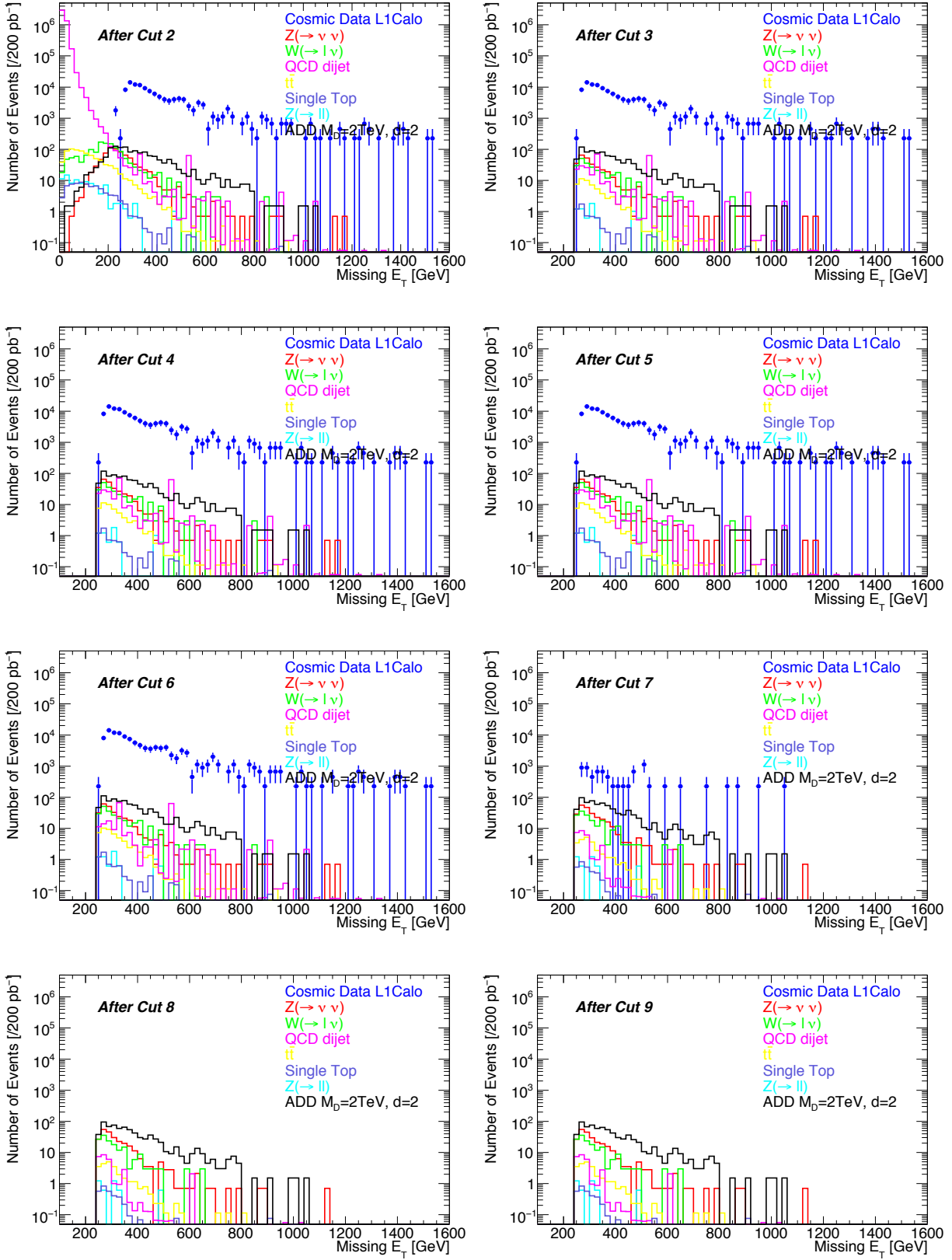


Figure 11.12: Expected E_T^{miss} distributions in monojet signature assuming the integrated luminosity of 200 pb^{-1} .

Table 11.5: Number of events after EM fraction and charge fraction cuts (only events with the leading jet $p_T > 100$ GeV are counted below). Integrated luminosity is assumed to be 200 pb^{-1} .

| Sample | EM Fraction Cut | Charge Fraction Cut |
|---|-----------------------------------|-----------------------------------|
| LED $M_D = 2, \delta = 2$ | 7709 ± 88 | 7234 ± 85 |
| LED $M_D = 2, \delta = 6$ | 526 ± 23 | 510 ± 23 |
| LED $M_D = 4, \delta = 2$ | 269 ± 16 | 251 ± 16 |
| LED $M_D = 4, \delta = 6$ | 10 ± 3 | 10 ± 3 |
| Cosmic | 7624 ± 87 | 448 ± 21 |
| QCD Dijet | $(1.7892 \pm 0.0001) \times 10^8$ | $(1.6047 \pm 0.0001) \times 10^8$ |
| $t\bar{t}$ | 18632 ± 137 | 17843 ± 134 |
| $Z(\rightarrow \nu\bar{\nu})+\text{jets}$ | 13002 ± 114 | 12169 ± 110 |
| $Z(\rightarrow e^+e^-)+\text{jets}$ | 2218 ± 47 | 2303 ± 48 |
| $Z(\rightarrow \mu^+\mu^-)+\text{jets}$ | 2330 ± 48 | 2194 ± 47 |
| $Z(\rightarrow \tau^+\tau^-)+\text{jets}$ | 2521 ± 50 | 2378 ± 49 |
| $W(\rightarrow e\nu_e)+\text{jets}$ | 17974 ± 134 | 17557 ± 133 |
| $W(\rightarrow \mu\nu_\mu)+\text{jets}$ | 18498 ± 136 | 17170 ± 131 |
| $W(\rightarrow \tau\nu_\tau)+\text{jets}$ | 19040 ± 138 | 17670 ± 133 |
| Single Top | 2743 ± 52 | 2323 ± 48 |

Table 11.6: Number of events remaining after each selection cuts for background processes. Integrated luminosity is assumed to be 200 pb^{-1} .

| | $Z(\nu\nu) + j$ | $W(\tau\nu)+j$ | tt | single-t | $W(e\nu, \mu\nu)+j$ | $Z(l\ell)+j$ |
|----------|-----------------|----------------|--------------|------------|---------------------|--------------|
| Cut 1, 2 | 763 ± 28 | 798 ± 28 | 800 ± 28 | 78 ± 9 | 581 ± 24 | 98 ± 10 |
| Cut 3 | 309 ± 18 | 164 ± 13 | 58 ± 8 | 7 ± 3 | 107 ± 10 | 7 ± 3 |
| Cut 4 | 309 ± 18 | 164 ± 13 | 58 ± 8 | 7 ± 3 | 107 ± 10 | 7 ± 3 |
| Cut 5 | 309 ± 18 | 164 ± 13 | 58 ± 8 | 7 ± 3 | 107 ± 10 | 7 ± 3 |
| Cut 6 | 293 ± 17 | 164 ± 13 | 55 ± 7 | 7 ± 3 | 107 ± 10 | 7 ± 3 |
| Cut 7 | 266 ± 16 | 125 ± 11 | 26 ± 5 | 3 ± 2 | 54 ± 7 | 4 ± 2 |
| Cut 8 | 262 ± 16 | 119 ± 11 | 25 ± 5 | 3 ± 2 | 48 ± 7 | 4 ± 2 |
| Cut 9 | 257 ± 16 | 119 ± 11 | 25 ± 5 | 3 ± 2 | 48 ± 7 | 4 ± 2 |

| | Cosmic | QCD |
|----------|---------------------------------|---------------------------------|
| Cut 1, 2 | $(1.267 \pm 0.004) \times 10^5$ | $(4.519 \pm 0.002) \times 10^6$ |
| Cut 3 | $(1.249 \pm 0.004) \times 10^5$ | 297 ± 17 |
| Cut 4 | $(1.249 \pm 0.004) \times 10^5$ | 297 ± 17 |
| Cut 5 | $(1.249 \pm 0.004) \times 10^5$ | 297 ± 17 |
| Cut 6 | $(1.222 \pm 0.003) \times 10^5$ | 241 ± 16 |
| Cut 7 | 8745 ± 94 | 30 ± 6 |
| Cut 8 | $0 \pm \text{—}$ | 30 ± 5 |
| Cut 9 | $0 \pm \text{—}$ | 30 ± 5 |

Table 11.7: Number of events remaining after each selection cuts for the LED signals. Integrated luminosity is assumed to be 200 pb^{-1} .

| | $M_D = 2, \delta = 2$ | $M_D = 2, \delta = 6$ | $M_D = 4, \delta = 2$ | $M_D = 4, \delta = 6$ |
|----------|-----------------------|-----------------------|-----------------------|-----------------------|
| Cut 1, 2 | 1446 ± 38 | 112 ± 11 | 51 ± 7 | 3 ± 2 |
| Cut 3 | 974 ± 31 | 74 ± 9 | 34 ± 6 | 2 ± 1 |
| Cut 4 | 974 ± 31 | 74 ± 9 | 34 ± 6 | 2 ± 1 |
| Cut 5 | 974 ± 31 | 74 ± 9 | 34 ± 6 | 2 ± 1 |
| Cut 6 | 925 ± 30 | 71 ± 8 | 32 ± 6 | 2 ± 1 |
| Cut 7 | 769 ± 28 | 63 ± 8 | 26 ± 5 | 2 ± 1 |
| Cut 8 | 762 ± 28 | 62 ± 8 | 26 ± 5 | 2 ± 1 |
| Cut 9 | 757 ± 28 | 62 ± 8 | 26 ± 5 | 2 ± 1 |

Chapter 12

Multi-jet plus E_T^{miss} Search for R-parity Conserving SUSY Models

Searches for R-parity conserving SUSY models with “multi-jet plus E_T^{miss} ” event topology is one of the standard strategies, as mentioned in Chapter 10. In such models, squarks and gluinos are copiously produced at the LHC, and those SUSY particles emit jets through cascade decays down to the lightest SUSY particles (LSP’s).

In ATLAS, the “multi-jet plus E_T^{miss} ” searches are further categorized into several channels (see Section 10.1.1). The searches are separately done for various multiplicities of reconstructed leptons (here, electrons and muons). Presence of reconstructed hadronic taus, or b-jets are also optionally used for the inclusive searches. Among those search channels, no-lepton search mode (no reconstructed electrons or muons in the event topology) and one-lepton search mode (one reconstructed electrons or muons) have high discovery potentials, and are especially considered for searches with early data.

Here, we investigate the contribution of the Standard Model and non-collision background to the event topology, especially without reconstructed electrons or muons (so called the “No-lepton search mode” in ATLAS). Data-driven methods to estimate the background are developed. We also consider the systematic effects (especially coming from the calorimeters) on the analysis, and show sensitivity to some of the benchmark mSUGRA signals considered in ATLAS. The profile of the benchmark SUSY signals are mentioned in the next section.

12.1 Data-Driven Methods for Background Estimation

In order to perform successful searches for new physics (in this case, SUSY), the background from the Standard Model (SM) processes must be well understood. Since uncertainties of the cross sections of SM processes are quite large especially for multi-jet events, and our knowledge is poor of the parton distribution functions, underlying event and parton showering at the LHC energy scale. Also, knowledge of detector performance will also be a large source of uncertainty, especially during the early data taking. Thus,

it is more reliable to predict the SM background from the real data as much as possible, rather than fully relying on Monte Carlo simulations.

In data-driven methods, we make use of so called the “standard candles” or the “control samples,” which we have well understandings of the events, and extrapolate them in some ways to estimate background. For example, it is quite straightforward to tag Z +jets events by requiring dilepton and its invariant mass near the Z mass. Due to the same kinematic properties of $Z(\rightarrow l^+l^-)$ +jets and $Z(\rightarrow \nu\bar{\nu})$ +jets, $Z(\rightarrow \nu\bar{\nu})$ background for No-lepton search mode can be predicted from tagged events of $Z(\rightarrow l^+l^-)$ +jets by removing the dilepton and apply the appropriate normalization factor.

The major advantages of data-driven methods are that we do not have to rely on the Monte Carlo predictions including the shape of distributions and the normalization, and many of the crucial uncertainties of Monte Carlo simulations are disentangled in data-driven methods, including detector performance.

The data-driven methods are particularly important in early data analyses. Here, we propose and validate data-driven methods to estimate major Standard Model background for the no-lepton search mode under the assumption of the integrated luminosity of 200 pb^{-1} .

12.2 Monte Carlo Simulation Samples and Data

For SUSY signals, we considered the ATLAS benchmark points for mSUGRA models. The Monte Carlo simulation samples were generated by HERWIG with JIMMY’s multiparton interaction model. The mass inputs for the SUSY particles were derived from Isasugra [144]. Table 12.2 shows the cross section and parameters of the benchmark mSUGRA points in ATLAS.

The profile of Monte Carlo simulation samples are mentioned in Appendix E. For electroweak process background such as Z/W + jets, the Monte Carlo generator Alpgen [145] was used with the HERWIG and JIMMY to accommodate parton showers and multiparton interaction. Alpgen treats the hard component of parton emission by explicitly including it in the matrix element (up to five parton emissions by the matrix elements are processed by Alpgen; see Appendix E), and the remaining soft parton emission is covered by the parton shower. On top of it, the “matching” procedure was used to avoid overlaps among samples with different parton multiplicity, because a simple combination of matrix element and the parton shower can “double count” the same event. Alpgen with matching procedure is expected to better describe multi-jet processes compared to the ones simply generated by the parton shower. $t\bar{t}$ and QCD multi-jet processes were respectively generated with MC@NLO and Pythia.

12.3 Trigger Menus for the Multi-jet Search

On top of “EF_j70_xe30” trigger (mentioned in Section 11.3; it triggers for events with leading jet E_T larger than 70 GeV and E_T^{miss} larger than 30 GeV), unprescaled jet+ E_T^{miss} trigger “EF_2j42_xe30” and multi-jet triggers “EF_3J60” and “EF_4J45” are useful for the

Table 12.1: Cross section and profile of the benchmark SUSY mSUGRA samples

| MC Sample | xsec [pb] | M_0 [GeV] | $M_{1/2}$ [GeV] | A_0 [GeV] | $\tan\beta$ | $\text{sgn}(\mu)$ |
|-----------|-----------|-------------|-----------------|-------------|-------------|-------------------|
| SU1 | 2.42 | 70 | 350 | 0 | 10 | + |
| SU3 | 5.46 | 100 | 300 | -300 | 6 | + |
| SU4 | 107.4 | 200 | 160 | -400 | 10 | + |
| SU6 | 1.23 | 320 | 375 | 0 | 50 | + |
| SU8 | 1.79 | 210 | 360 | 0 | 40 | + |

Table 12.2: Particle mass spectrum for the benchmark mSUGRA points [23]. The masses are in GeV.

| Particle | SU1 | SU3 | SU4 | SU6 | SU8 |
|--------------------|--------|--------|--------|--------|--------|
| \tilde{d}_L | 764.90 | 636.27 | 419.84 | 870.79 | 801.16 |
| \tilde{u}_L | 760.42 | 631.51 | 412.25 | 866.84 | 797.09 |
| \tilde{b}_1 | 697.90 | 575.23 | 358.49 | 716.83 | 690.31 |
| \tilde{t}_1 | 572.96 | 424.12 | 206.04 | 641.61 | 603.65 |
| \tilde{d}_R | 733.53 | 610.69 | 406.22 | 840.21 | 771.91 |
| \tilde{u}_R | 735.41 | 611.81 | 404.92 | 842.16 | 773.69 |
| \tilde{b}_2 | 722.87 | 610.73 | 399.18 | 779.42 | 743.09 |
| \tilde{t}_2 | 749.46 | 650.50 | 445.00 | 797.99 | 766.21 |
| \tilde{e}_L | 255.13 | 230.45 | 231.94 | 411.89 | 325.44 |
| $\tilde{\nu}_e$ | 238.31 | 216.96 | 217.92 | 401.89 | 315.29 |
| $\tilde{\tau}_1$ | 146.50 | 149.99 | 200.50 | 181.31 | 151.90 |
| $\tilde{\nu}_\tau$ | 237.56 | 216.29 | 215.53 | 358.26 | 296.98 |
| \tilde{e}_R | 154.06 | 155.45 | 212.88 | 351.10 | 253.35 |
| $\tilde{\tau}_2$ | 256.98 | 232.17 | 236.04 | 392.58 | 331.34 |
| \tilde{g} | 832.33 | 717.46 | 413.37 | 894.70 | 856.45 |
| $\tilde{\chi}_1^0$ | 136.98 | 117.91 | 59.84 | 149.57 | 142.45 |
| $\tilde{\chi}_2^0$ | 263.64 | 218.60 | 113.48 | 287.97 | 273.95 |
| $\tilde{\chi}_3^0$ | 466.44 | 463.99 | 308.94 | 477.23 | 463.55 |
| $\tilde{\chi}_4^0$ | 483.30 | 480.59 | 327.76 | 492.23 | 479.01 |
| $\tilde{\chi}_1^+$ | 262.06 | 218.33 | 113.22 | 288.29 | 274.30 |
| $\tilde{\chi}_2^+$ | 483.62 | 480.16 | 326.59 | 492.42 | 479.22 |
| h^0 | 115.81 | 114.83 | 113.98 | 116.85 | 116.69 |
| H^0 | 515.99 | 512.86 | 370.47 | 388.92 | 430.49 |
| A^0 | 512.39 | 511.53 | 368.18 | 386.47 | 427.74 |
| H^+ | 521.90 | 518.15 | 378.90 | 401.15 | 440.23 |

searches.

12.4 Event Selection for No-lepton Search Mode

In order to investigate on the no-lepton search mode, and start from the standard benchmark selection cuts used in ATLAS with slight modifications. The event selection is mentioned below.

- No isolated electrons and muons
- **High jet multiplicity expected from SUSY signals by cascade decays of squarks and gluinos:**
 - Cut 1: Number of jets > 3 , Leading jet $p_T > 100$ GeV
 - Cut 2: Second leading jet $p_T > 50$ GeV
 - Cut 3: Third leading jet $p_T > 50$ GeV
- **Large E_T^{miss} from LSP, and $E_T^{\text{miss}}/M_{\text{eff}}$ cut ($M_{\text{eff}} = E_T^{\text{miss}} + \sum_{i=1}^3 p_T^{\text{jet}(i)}$) for the suppression of QCD background:**
 - Cut 4: $E_T^{\text{miss}} > 100$ GeV
 - Cut 5: $E_T^{\text{miss}}/M_{\text{eff}} > 0.2$
- **Rejection of QCD background by the angular correlation of jets and E_T^{miss} :**
 - Cut 6: $0.3 < \Delta\phi(\text{leading jet}, E_T^{\text{miss}}) < \pi - 0.3$
 - Cut 7: $0.2 < \Delta\phi(2^{\text{nd}} \text{ leading jet}, E_T^{\text{miss}}) < \pi - 0.2$
 - Cut 8: $0.2 < \Delta\phi(3^{\text{rd}} \text{ leading jet}, E_T^{\text{miss}}) < \pi - 0.2$

The effective mass M_{eff} is roughly proportional to the mass of produced SUSY particles [53]. The cut “ $E_T^{\text{miss}} > 0.2M_{\text{eff}}$ ” is used to reject QCD background, because fake E_T^{miss} tends to increase when jets’ energies are larger. The cuts on the angular difference of jets and E_T^{miss} are also used to suppress QCD background.

Figure 12.1 shows the E_T^{miss} distributions of the SUSY signals and the Standard Model background after each selection cut. The distributions of E_T^{miss} and effective mass are shown in Figure 12.2 for the SUSY signal and the Standard Model background. The breakdown of number of events remaining after the SUSY event selection is shown in Table 12.3 and 12.4. As is obvious from the tables, $Z, W, t\bar{t}$, and QCD backgrounds contribute almost equally to the no-lepton search, but in the high E_T^{miss} region, QCD background is less significant compared to the other background.

In the next section, we investigate on the methods to estimate the background in data-driven ways.

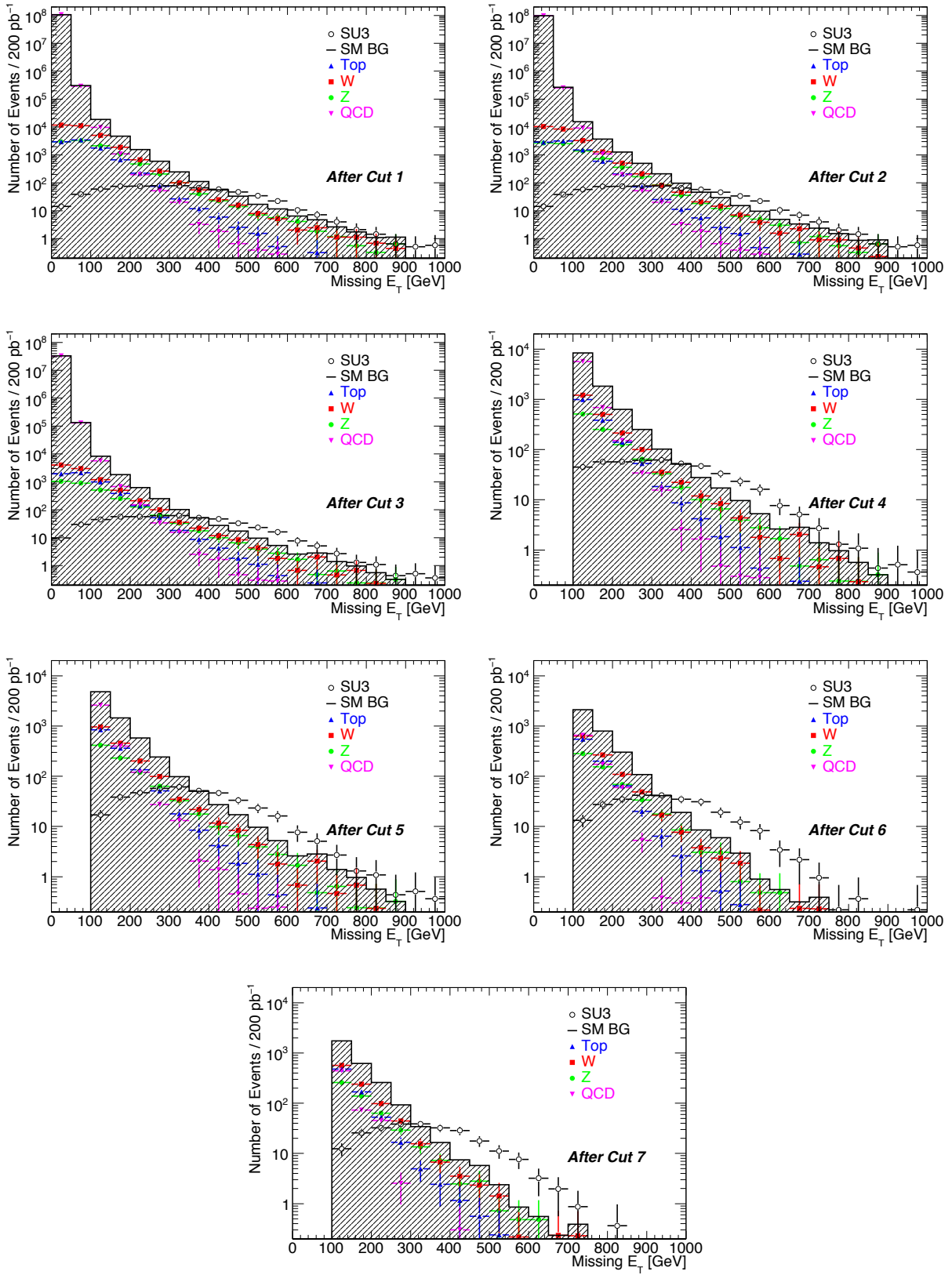


Figure 12.1: E_T^{miss} distributions of SUSY signals and Standard Model background after selection cuts assuming the integrated luminosity of 200 pb^{-1} .

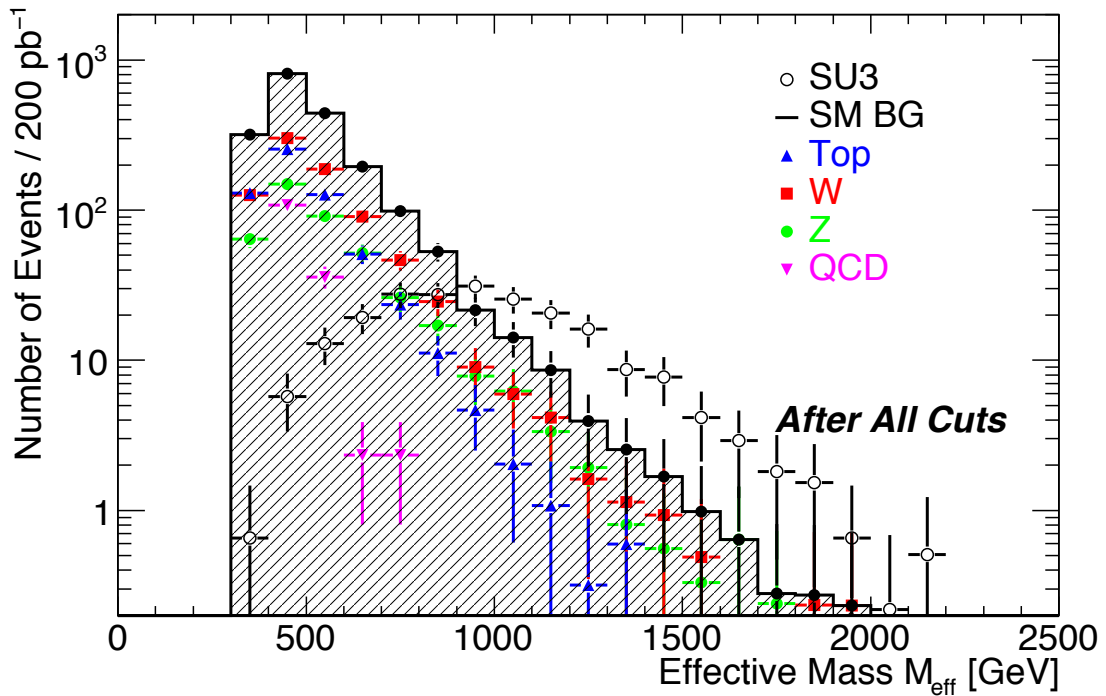
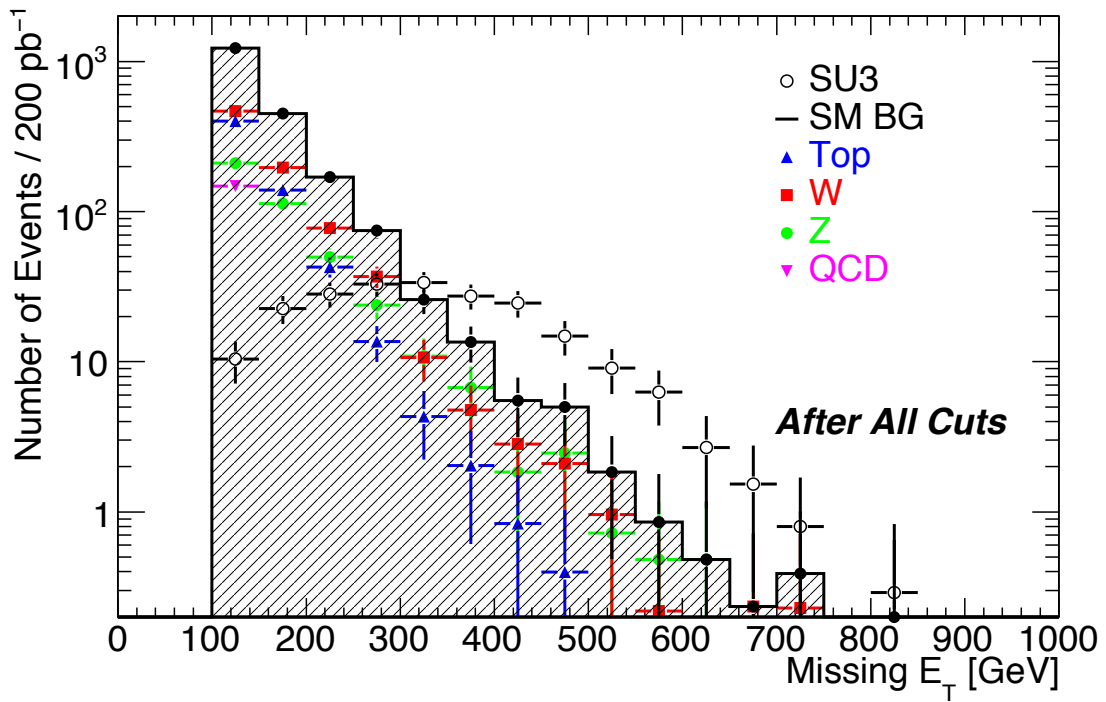


Figure 12.2: E_T^{miss} (top) and effective mass (bottom) distributions after No-lepton Mode selection cuts for SUSY signals and Standard Model background.

Table 12.3: Breakdown of events after event selection of no-lepton search mode for integrated luminosity of 200 pb^{-1} .

| Cut | Z | W | $t\bar{t}$ | QCD |
|--------------------------------------|-------------------------------|-------------------------------|---------------|-----------------------------------|
| After Cut 1 | $(1.04 \pm 0.01) \times 10^4$ | $(3.09 \pm 0.02) \times 10^4$ | 9207 ± 96 | $(1.0678 \pm 0.0001) \times 10^8$ |
| After Cut 2 | 8018 ± 90 | $(2.45 \pm 0.02) \times 10^4$ | 8471 ± 92 | $(9.722 \pm 0.001) \times 10^7$ |
| After Cut 3 | 2971 ± 55 | 9203 ± 96 | 5680 ± 75 | $(3.2943 \pm 0.0006) \times 10^7$ |
| After Cut 4 | 1032 ± 32 | 2118 ± 46 | 1604 ± 40 | 6569 ± 81 |
| After Cut 5 | 904 ± 30 | 1801 ± 42 | 1422 ± 38 | 3180 ± 56 |
| After Cut 6 | 575 ± 24 | 1089 ± 33 | 841 ± 29 | 892 ± 30 |
| After Cut 7 | 518 ± 23 | 979 ± 31 | 725 ± 27 | 565 ± 24 |
| After All Cuts | 422 ± 21 | 801 ± 28 | 606 ± 25 | 148 ± 12 |
| All Cuts & $E_T^{\text{miss}} > 300$ | 24 ± 5 | 22 ± 5 | 8 ± 3 | $— \pm —$ |

Table 12.4: Breakdown of events after event selection of no-lepton search mode for integrated luminosity of 200 pb^{-1} .

| Cut | SU1 | SU3 | SU4 | SU6 | SU8 |
|--|--------------|--------------|-------------------------------|--------------|--------------|
| After Cut 1 | 246 ± 16 | 683 ± 26 | $(1.14 \pm 0.01) \times 10^4$ | 146 ± 12 | 227 ± 15 |
| After Cut 2 | 242 ± 16 | 668 ± 26 | $(1.10 \pm 0.01) \times 10^4$ | 144 ± 12 | 222 ± 15 |
| After Cut 3 | 185 ± 14 | 514 ± 23 | 8600 ± 93 | 116 ± 11 | 171 ± 13 |
| After Cut 4 | 174 ± 13 | 474 ± 22 | 5933 ± 77 | 110 ± 10 | 162 ± 13 |
| After Cut 5 | 153 ± 12 | 412 ± 20 | 5102 ± 71 | 94 ± 10 | 140 ± 12 |
| After Cut 6 | 98 ± 10 | 273 ± 17 | 3321 ± 58 | 59 ± 8 | 90 ± 9 |
| After Cut 7 | 92 ± 10 | 252 ± 16 | 2980 ± 55 | 54 ± 7 | 83 ± 9 |
| After All Cuts | 77 ± 9 | 216 ± 15 | 2532 ± 25 | 46 ± 7 | 71 ± 8 |
| All Cuts & $E_T^{\text{miss}} > 300 \text{ GeV}$ | 51 ± 7 | 122 ± 11 | 246 ± 16 | 32 ± 6 | 49 ± 7 |

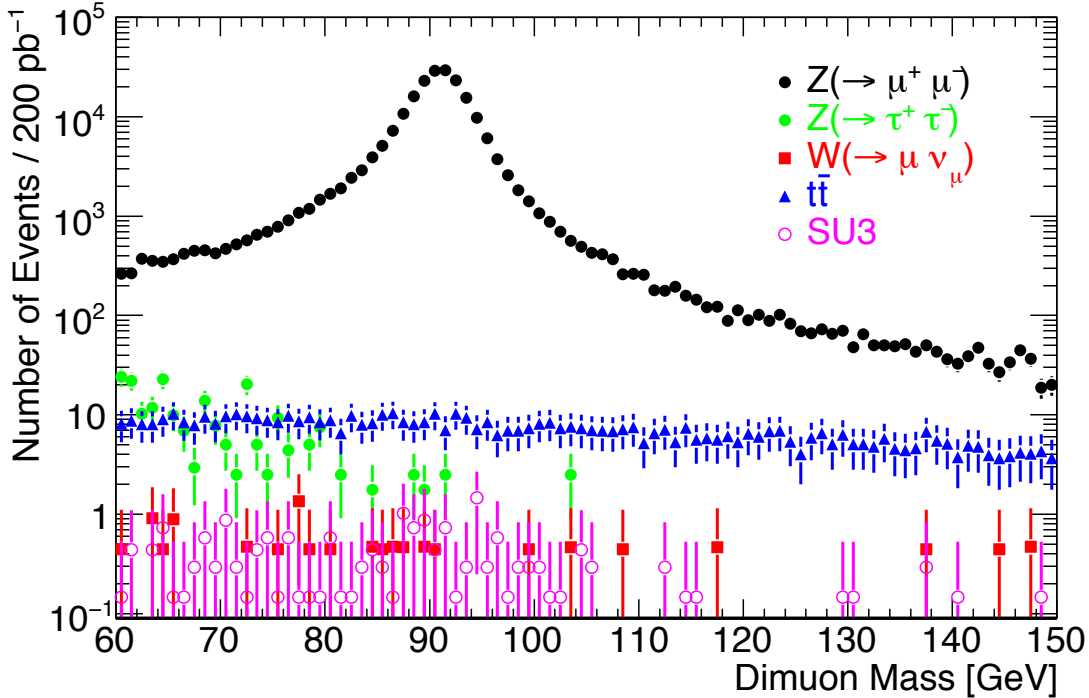


Figure 12.3: Invariant mass of dimuons for integrated luminosity of 200 pb^{-1} .

12.5 Estimation of Background

Major background to the all-hadronic multi-jet search consists of $Z(\rightarrow \nu\bar{\nu})+\text{jets}$, $W+\text{jets}$, $t\bar{t}$, and QCD multi-jet events as mentioned in the previous section. Since the theoretical uncertainty of multi-jet processes from perturbative QCD is still large, major background should be estimated by data-driven ways using well-known references. We will call such well-known references as “control samples.”

12.5.1 $Z(\rightarrow \nu\bar{\nu})+\text{jets}$ Background

One of the straightforward ways to estimate $Z(\rightarrow \nu\bar{\nu})+\text{jets}$ background is to use $Z(\rightarrow l^+l^-)+\text{jets}$ events, where l 's are electrons or muons. Here, we use the muon channel for the investigation. $Z(\rightarrow \mu^+\mu^-)$ events are fairly background free once the invariant mass of the dimuons are required (Figure 12.3). However, small contamination is expected from $t\bar{t}$ events and possibly SUSY signals. Contributions from $Z(\rightarrow \tau^+\tau^-)$, $W(\rightarrow \mu\nu_\mu)$, and QCD are negligible.

$Z(\rightarrow \nu\bar{\nu})$ and $Z(\rightarrow \mu^+\mu^-)$ events share the same kinematic properties, so tagging $Z(\rightarrow l^+l^-)+\text{jets}$ events and calculating $E_{\text{T}}^{\text{miss}}$ without considering the dilepton will basically reproduce the distributions of $Z(\rightarrow \nu\bar{\nu})+\text{jets}$ events. However, the identification efficiency and acceptance effects for the leptons in $Z(\rightarrow l^+l^-)+\text{jets}$ events should be taken care of, in order to correctly reproduce $Z(\rightarrow \nu\bar{\nu})+\text{jets}$ background.

Two methods were considered in ATLAS within the approach mentioned above. One

is fully using the $Z(\rightarrow l^+l^-)+\text{jets}$ events to reproduce $Z(\rightarrow \nu\bar{\nu})+\text{jets}$ background. We call this approach the ‘‘Replace Method.’’ This method was investigated by the author for the first time in ATLAS [A.3.4.1] [A.3.4.2]. The other method uses the shape of the $Z(\rightarrow l^+l^-)+\text{jets}$ Monte Carlo simulation, but uses normalization obtained from data to cope with the uncertainty of cross section [A.3.4.6] [A.3.4.7] [A.3.4.9]. We will describe these method in more detail below.

Replace Method

In the former method, $Z(\rightarrow \mu^+\mu^-)+\text{jets}$ events are tagged and directly used for the estimation. Muon trigger ‘‘mu10’’ ($p_T > 10$ GeV threshold; without prescale for low luminosity running) was considered for the events. $Z(\rightarrow \mu^+\mu^-)+\text{jets}$ events are selected by requiring two reconstructed leptons with invariant mass in the Z mass window (here $81 < M_Z < 101$ GeV). When reconstructing E_T^{miss} , the muons are removed from the calculation in order to reproduce the distributions for $Z(\rightarrow \nu\bar{\nu})$ background. Several corrections are needed to reproduce $Z(\rightarrow \nu\bar{\nu})$ distributions from $Z(\rightarrow \mu^+\mu^-)$ events, in order to recover the muon trigger efficiency, identification efficiency and acceptance effects for the leptons. They can be obtained by the following way,

$$N_{Z(\rightarrow \nu\bar{\nu})}(E_T^{\text{miss}}) = \frac{N_{Z(\rightarrow l^+l^-)}(E_T^{\text{miss}})}{\left[1 - (1 - \varepsilon_{l^+}^{\text{trig}})(1 - \varepsilon_{l^+}^{\text{trig}})\right] \varepsilon_{l^+}^{\text{reco}} \varepsilon_{l^-}^{\text{reco}}} \times C(p_T(Z)) \times \frac{\text{BR}(Z(\rightarrow \nu\bar{\nu}))}{\text{BR}(Z(\rightarrow l^+l^-))}. \quad (12.1)$$

First of all, the trigger efficiency $\varepsilon_l^{\text{trig}}$ should be considered. In this equation, $\varepsilon_l^{\text{trig}}$ is slightly different from the standard definition of the trigger efficiency. Here, we need to know the efficiency that the trigger fires for the events with a ‘‘reconstructed muon.’’ The trigger efficiency for such conditions is shown in Figure 12.4 as a function of p_T, η , and ϕ respectively. The dips in the trigger efficiency are coming from the gaps of muon trigger chambers for η , and from the presence of eight-fold toroidal magnets for ϕ . After the trigger efficiency correction, the identification efficiency should also be considered (Figure 12.5). Regions with inferior efficiency are due to the same reason as the trigger efficiency for ϕ and η . The decrease of efficiency in high p_T is due to the isolation conditions (transverse energy around $\Delta R < 0.1$ from the muon is required to be less than 10 GeV). Both trigger and muon identification efficiencies will be estimated from data by the tag-and-probe method [23] (will not be mentioned in this thesis).

$C(p_T(Z))$ is a function of Z p_T and corrects for the acceptance effects of the leptons ($p_T > 20$ GeV, $|\eta| < 2.5$) and kinematic effects (invariant mass requirement for the dilepton). In this thesis, correction terms for the trigger efficiency, identification efficiency, and kinematic correction were inclusively considered (Figure 12.6).

Finally, branching ratios of $Z(\rightarrow \nu\bar{\nu})$ and $Z(\rightarrow l^+l^-)$ is considered.

Figure 12.7 shows the data-driven estimation of E_T^{miss} and effective mass distributions from $Z(\rightarrow \nu\bar{\nu})$ background.

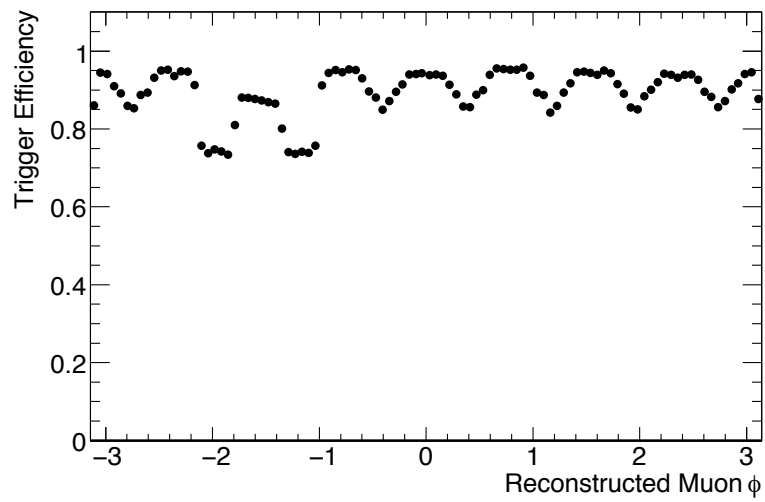
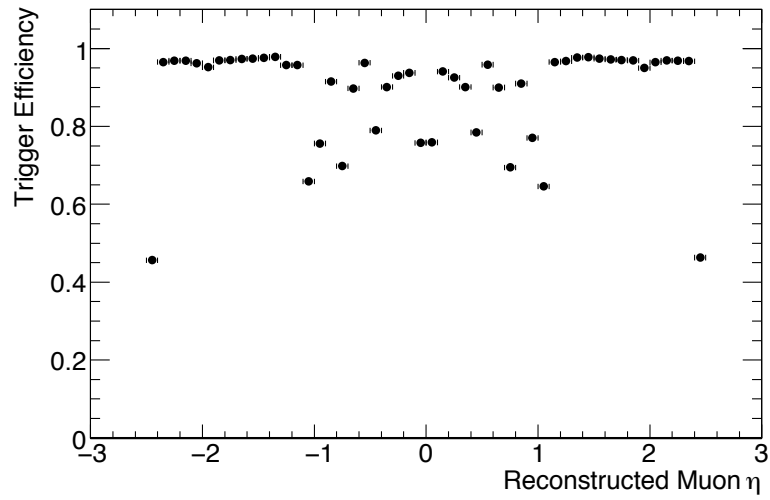
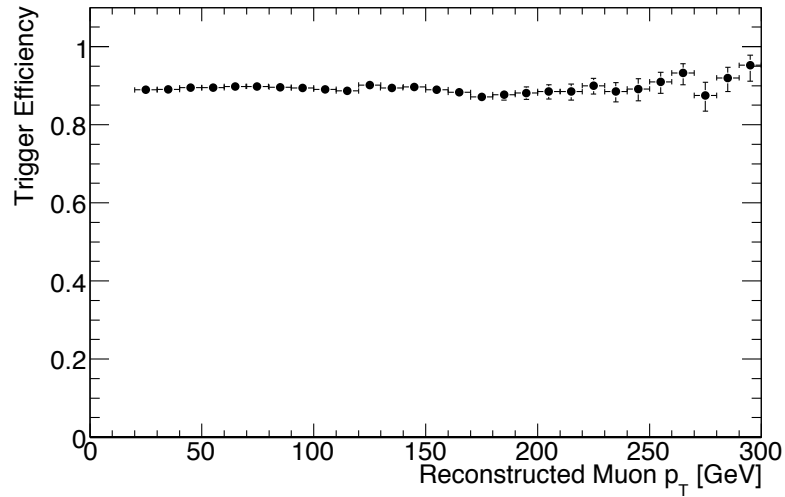


Figure 12.4: Trigger efficiency of reconstructed muons as a function of muon p_T (top), η (middle), ϕ (bottom).

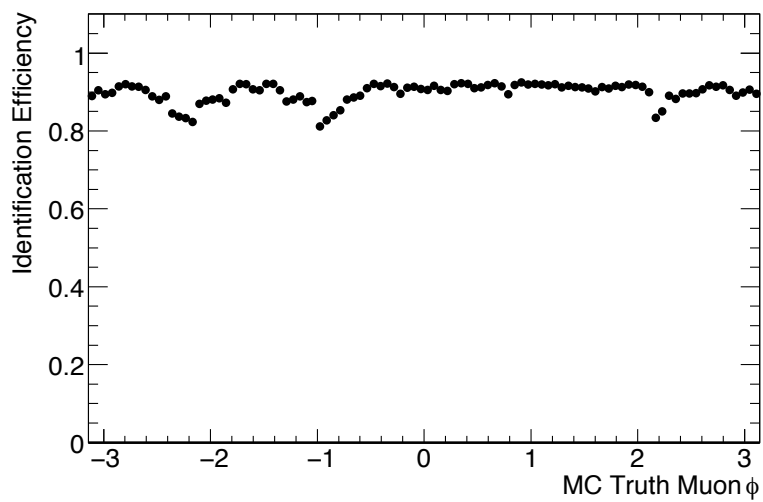
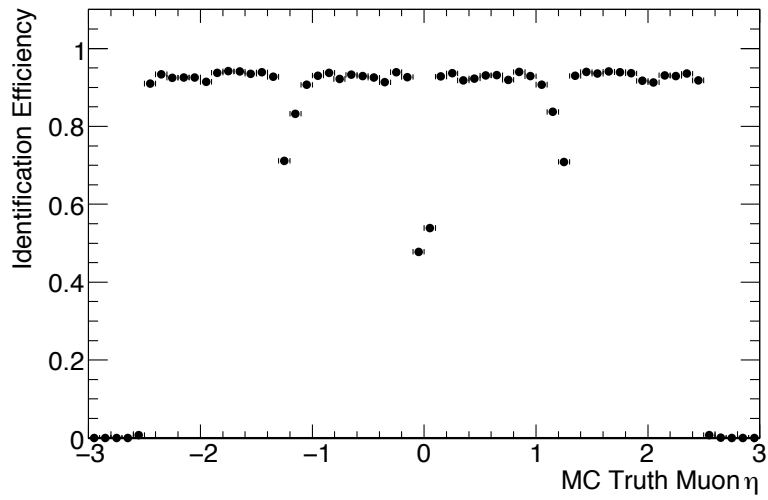
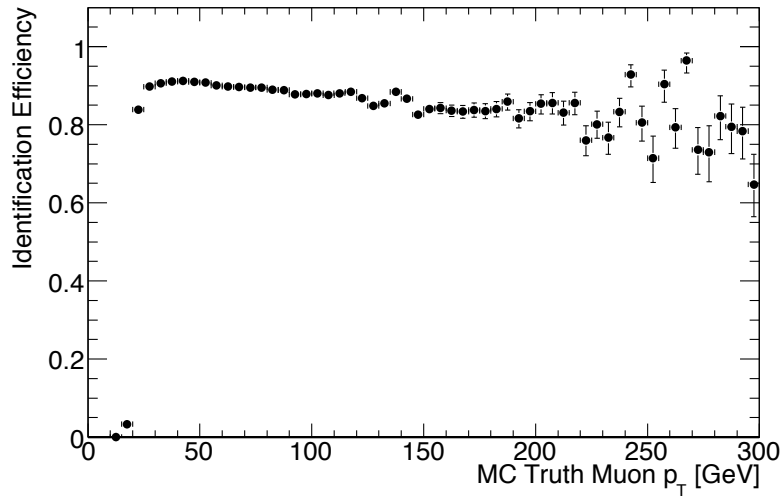


Figure 12.5: Identification efficiency of muons as a function of muon p_T (top), η (middle), ϕ (bottom).

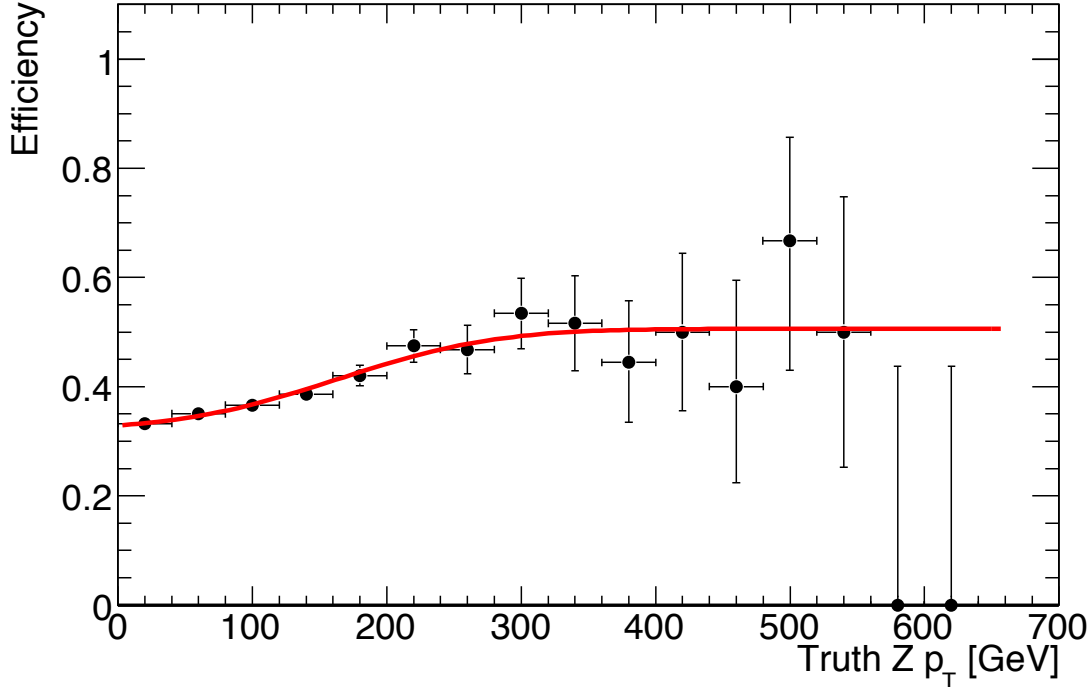


Figure 12.6: Efficiency of Z reconstruction using dimuons as a function of p_T .

Estimation using Monte Carlo Simulation Samples

The latter estimation method for $Z(\rightarrow \nu\bar{\nu})$ background exploits the shape of distributions from the Monte Carlo, in order to cope with the limited statistics of $Z(\rightarrow l^+l^-)+\text{jets}$ data.

The validation of Monte Carlo is preceded by comparing distributions with $Z(\rightarrow l^+l^-)$ data tagged by dilepton invariant mass. Once the Monte Carlo is tuned, and the normalization factor needed to correct for the cross section uncertainty is also extracted.

Since, Monte Carlo is fully used except for the normalization, various uncertainties must be estimated from the data and considered. Uncertainties from the jets and E_T^{miss} (energy scale and resolution) have the largest impact on the background estimation.

An example of estimation for the case center-of-mass energy 14 TeV and 1 fb^{-1} integrated luminosity is shown in Appendix F. Estimation of E_T^{miss} scale and resolution can also be estimated from $Z(\rightarrow l^+l^-)$ events, and are mentioned in Appendix F.

12.5.2 $W+\text{jets}$ Background

The largest component of $W+\text{jets}$ background for no-lepton search mode comes from $W(\rightarrow \tau\nu_\tau)+\text{jets}$, where τ is decaying hadronically. The remaining contributions come from $W(\rightarrow \tau\nu_\tau)+\text{jets}$ with τ decaying leptonically and the lepton is not identified, or $W(\rightarrow e\nu_e)$ or $W(\rightarrow \mu\nu_\mu)+\text{jets}$ with electrons or muons going out-of-acceptance or not identified due to isolation criteria or etc. (Table 12.6).

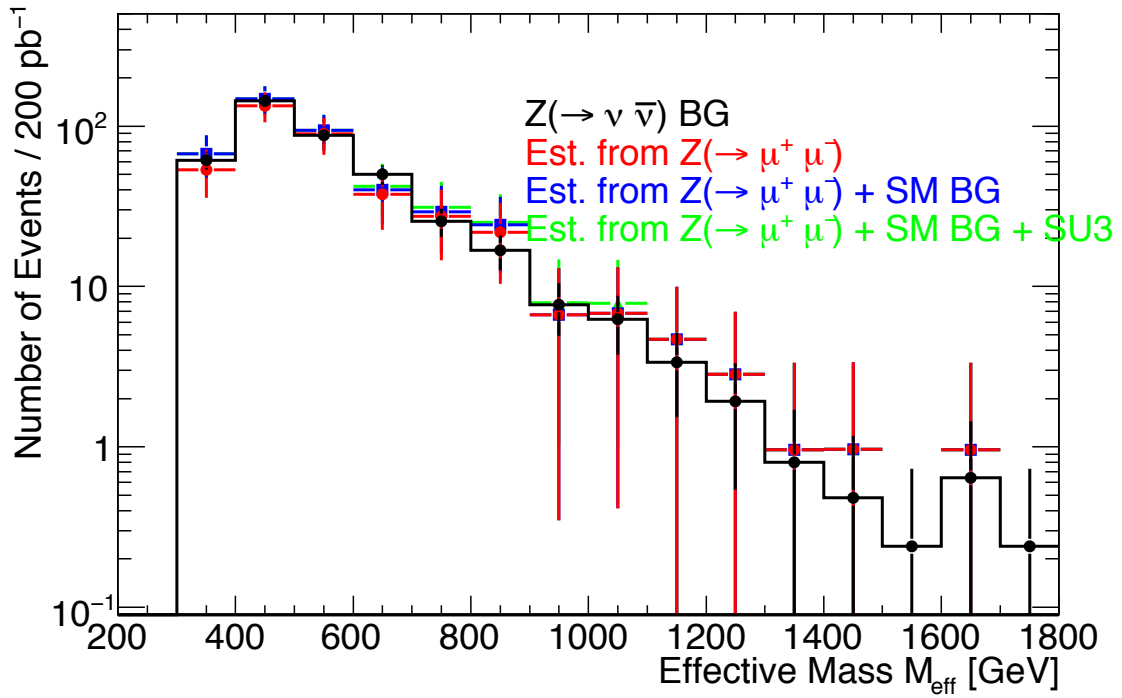
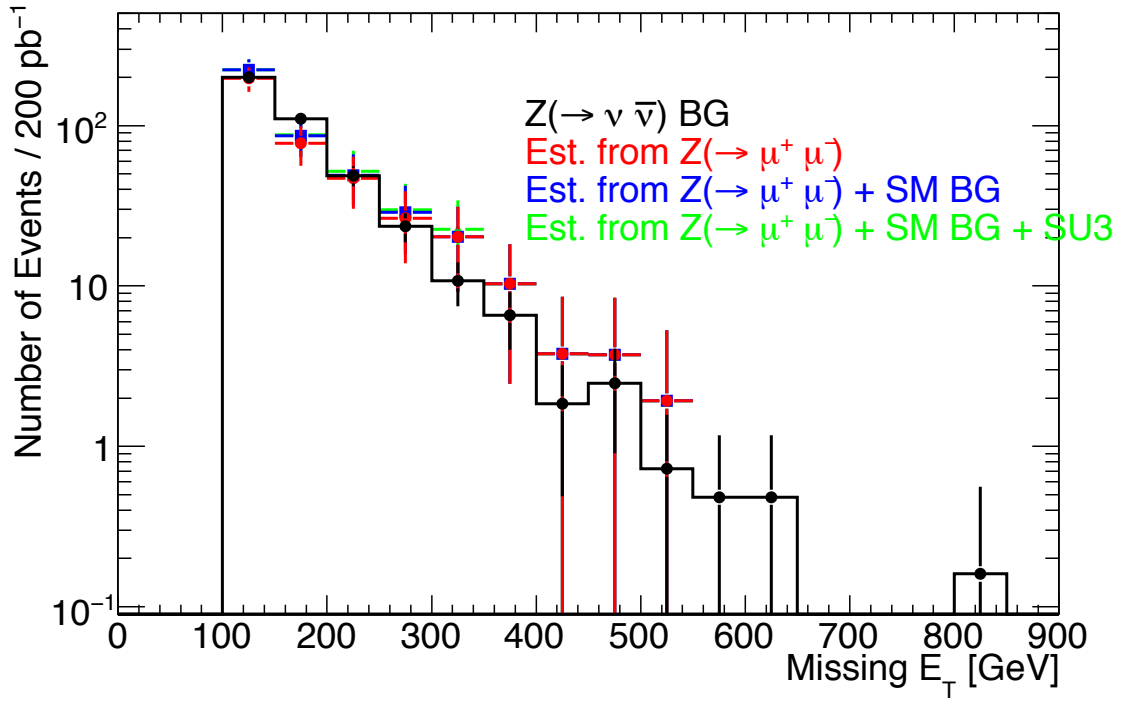


Figure 12.7: Estimation of $Z(\rightarrow \nu\bar{\nu})$ background using $Z(\rightarrow \mu^+\mu^-)$ events (top: E_T^{miss} , bottom: effective mass). Estimations from pure $Z(\rightarrow \mu^+\mu^-)$ (red), with other Standard Model background (blue), and with other Standard Model background and SUSY signal contamination (green) are shown.

Table 12.5: Number of events of $Z(\rightarrow \nu\bar{\nu})$ background and data-driven estimation from $Z(\rightarrow \mu^+\mu^-)$.

| BG & Estimation | $E_T^{\text{miss}} > 100 \text{ GeV}$ | $E_T^{\text{miss}} > 300 \text{ GeV}$ |
|--|---------------------------------------|---------------------------------------|
| $Z(\rightarrow \nu\bar{\nu})$ | 406 ± 20 | 24 ± 5 |
| Estimation from $Z(\rightarrow \mu^+\mu^-)$ | 388 ± 48 | 40 ± 15 |
| Est. from $Z(\mu^+\mu^-)$ & SM BG | 426 ± 51 | 40 ± 15 |
| Est. from $Z(\mu^+\mu^-)$ & SM BG & SU1 contami. | 429 ± 51 | 41 ± 16 |
| Est. from $Z(\mu^+\mu^-)$ & SM BG & SU3 contami. | 434 ± 51 | 42 ± 16 |
| Est. from $Z(\mu^+\mu^-)$ & SM BG & SU4 contami. | 476 ± 53 | 49 ± 17 |
| Est. from $Z(\mu^+\mu^-)$ & SM BG & SU6 contami. | 428 ± 51 | 41 ± 16 |
| Est. from $Z(\mu^+\mu^-)$ & SM BG & SU8 contami. | 427 ± 51 | 41 ± 16 |

Table 12.6: Origin of W background to no-lepton search mode.

| Origin | Fraction |
|---|----------|
| τ within acceptance | 47.8 % |
| τ out of acceptance | 17.6 % |
| e, μ within acceptance but unidentified | 7.4 % |
| e, μ out of acceptance | 27.1 % |

Data-driven Estimation

Since the largest component of W +jets background comes from the $W(\rightarrow \tau\nu_\tau)$, the kinematics of those events are the same as $W(\rightarrow e\nu_e)$ and $W(\rightarrow \mu\nu_\mu)$ +jets with electrons and muons identified. Such background with τ within the acceptance ($p_T > 20 \text{ GeV}$ and $|\eta| < 2.5$) can be estimated from the following control samples. Here, we consider two types of control samples with the following criteria (basically the same as no-lepton search mode selection except for those related to leptons).

- **Control Sample I**

- **Requirement of one lepton in order to select W 's with leptonic decays:** Presence of one electron or muon with $p_T > 20 \text{ GeV}$ and $|\eta| < 2.5$, and passing isolation criteria: $E_T(\Delta R < 0.2) < 10 \text{ GeV}$
- **Avoidance of the signal region of the SUSY one-lepton search mode:** transverse mass $M_T < 100 \text{ GeV}$
- **Rejection of $t\bar{t}$ events (W-purification):** no b-tagged jets
- **SUSY selection cuts to match the kinematic properties of the control sample as the no-lepton search mode background:**

Table 12.7: Number of events of $W(\rightarrow \tau\nu_\tau)$ background with τ in the acceptance and estimation.

| BG & Estimation | $E_T^{\text{miss}} > 100 \text{ GeV}$ | $E_T^{\text{miss}} > 300 \text{ GeV}$ |
|--|---------------------------------------|---------------------------------------|
| $W(\rightarrow \tau\nu_\tau)$ No Lepton BG | 362 ± 19 | 13 ± 4 |
| Estimation from $W(\rightarrow \mu\nu_\mu)$ Control Sample | 346 ± 21 | 9 ± 4 |
| Est. from W with $t\bar{t}$ contami. | 397 ± 23 | 10 ± 4 |
| Est. from W with $t\bar{t}$ & SU1 contami. | 401 ± 23 | 13 ± 4 |
| Est. from W with $t\bar{t}$ & SU3 contami. | 402 ± 23 | 13 ± 4 |
| Est. from W with $t\bar{t}$ & SU4 contami. | 464 ± 25 | 14 ± 4 |
| Est. from W with $t\bar{t}$ & SU6 contami. | 399 ± 23 | 11 ± 4 |
| Est. from W with $t\bar{t}$ & SU8 contami. | 398 ± 23 | 11 ± 4 |

- * At least four jets with $p_T > 50 \text{ GeV}$ and $|\eta| < 2.5$, and at least one of them with $p_T > 100 \text{ GeV}$
- * $E_T^{\text{miss}} > 100 \text{ GeV}$ and $E_T^{\text{miss}} > 0.2M_{eff}$
- * $0.3 < \Delta\phi(\text{jet1}, E_T^{\text{miss}}) < \pi - 0.3$, $0.2 < \Delta\phi(\text{jet2}, E_T^{\text{miss}}) < \pi - 0.2$, $0.2 < \Delta\phi(\text{jet3}, E_T^{\text{miss}}) < \pi - 0.2$

• Control Sample II

- Basically the same as Control Sample I, but the lepton is replaced as a “jet,” and included in the effective mass calculation if it is among the three leading “jets.” The same event selection is applied other than the lepton-jet replacement.

Before using the information from b-tagging, the one lepton control samples mostly consist of $t\bar{t}$ with semi-leptonic decays and leptonically decaying W events. For the estimation of W background, the control samples should be purified into W -only samples. Here, we use b-tagging to separate W and $t\bar{t}$ events. Due to the presence of two b-jets in $t\bar{t}$ events and low presence of b-jets in W +jets events, the separation of W and $t\bar{t}$ events can be performed with high efficiency and rejection power (94% $t\bar{t}$ -rejection for 75% b-tag efficiency).

Considering the lepton identification efficiency, b-tagging efficiency, and efficiency coming from the cut on the transverse mass of the one-lepton control samples, the no-lepton $W(\rightarrow \tau\nu_\tau)$ background with τ within the acceptance can be estimated with Control Sample II (Figure 12.10).

Also, no-lepton background originating from $W(\rightarrow e\nu_e)$ or $W(\rightarrow \mu\nu_\mu)$ with electrons or muons within acceptance but not identified, can be estimated from Control Sample I considering the lepton identification efficiency, b-tagging efficiency, and efficiency (Figure 12.9).

For no-lepton background originating from leptons out of acceptance, information from the Monte Carlo simulation is needed. The strategy to estimate such background will not be mentioned here.

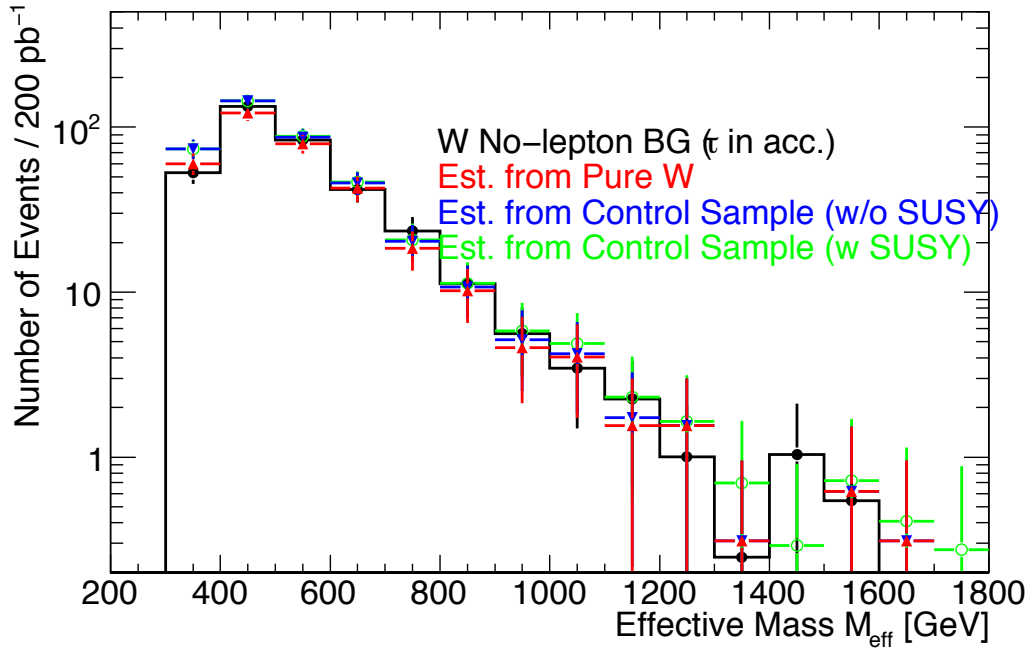
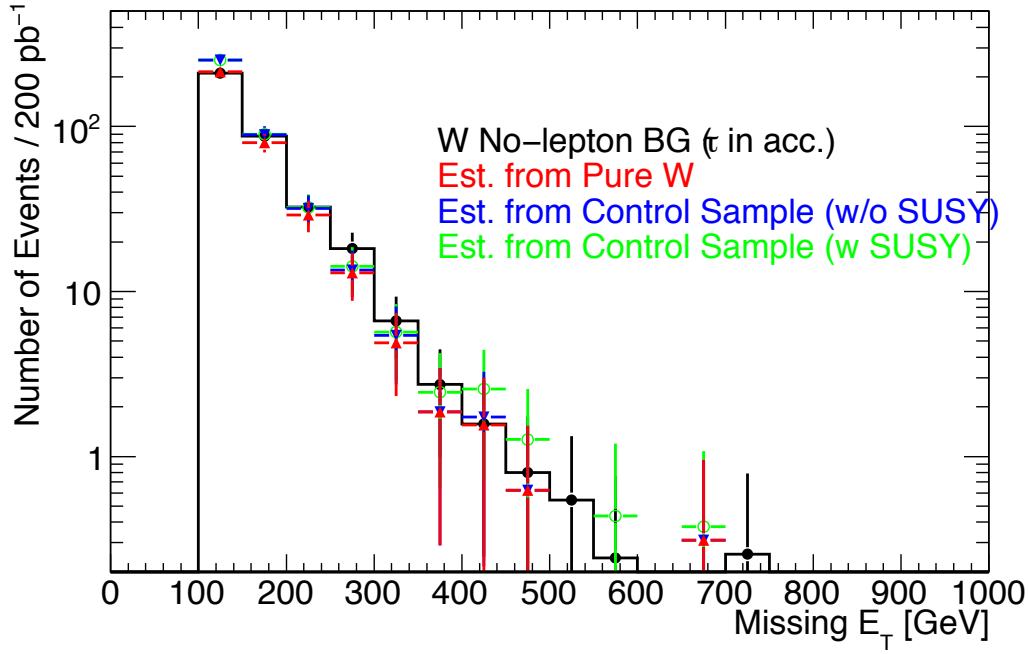


Figure 12.8: Estimation of $W(\rightarrow \tau\nu_\tau)$ background using one-lepton control samples (top: E_T^{miss} , bottom: effective mass). Estimations from pure $W(\rightarrow \mu\nu_\mu)$ control samples (red), with $t\bar{t}$ contamination (blue), and with $t\bar{t}$ and SUSY signal contamination are shown.

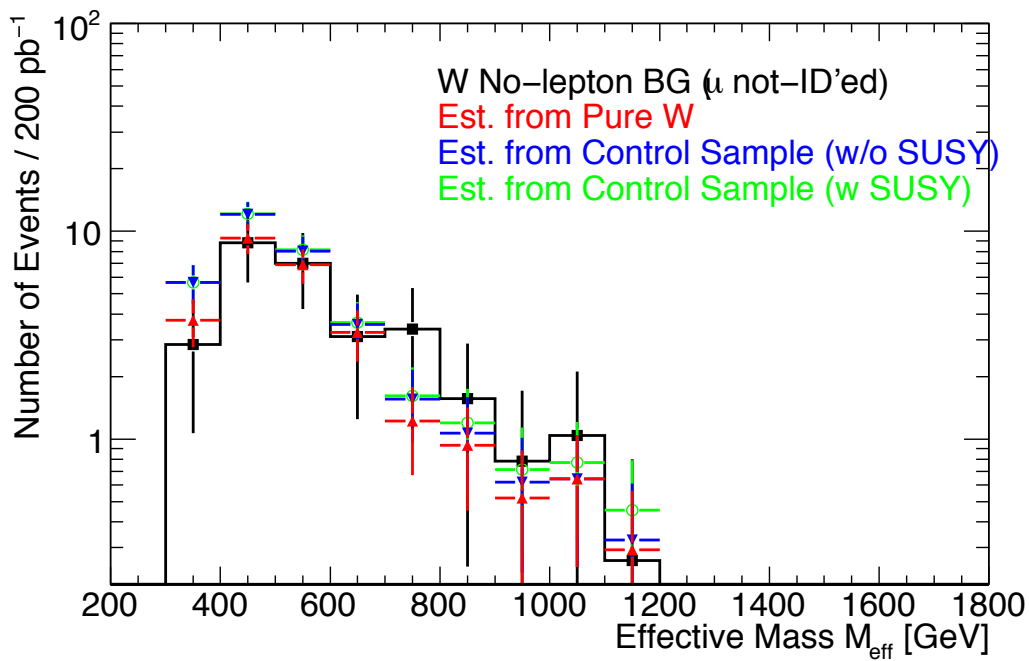
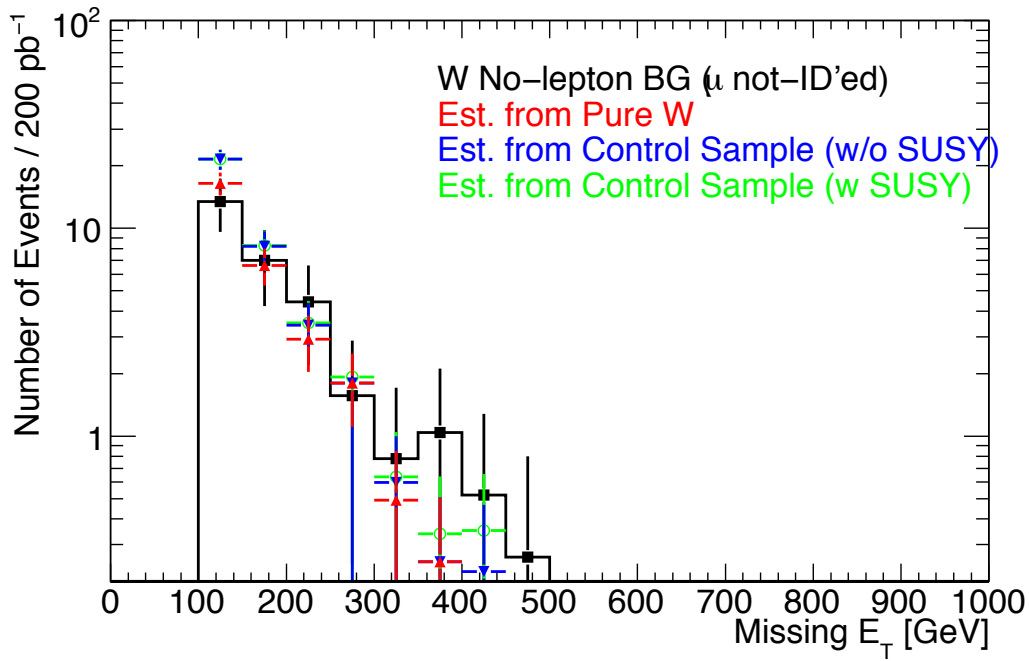


Figure 12.9: Estimation of $W(\rightarrow \mu\nu_\mu)$ no-lepton background using $W(\rightarrow \mu\nu_\mu)$ one-lepton control samples (top: E_T^{miss} , bottom: effective mass). Estimations from pure $W(\rightarrow \mu\nu_\mu)$ control samples (red), with $t\bar{t}$ contamination (blue), and with $t\bar{t}$ and SUSY signal contamination are shown.

Table 12.8: Number of events of $W(\rightarrow \mu\nu_\mu)$ no-lepton background with μ in the acceptance and estimation from one-lepton control samples.

| BG & Estimation | $E_T^{\text{miss}} > 100 \text{ GeV}$ | $E_T^{\text{miss}} > 300 \text{ GeV}$ |
|---|---------------------------------------|---------------------------------------|
| $W(\rightarrow \mu\nu_\mu)$ No Lepton BG with μ in acc. | 29 ± 5 | 3 ± 2 |
| Estimation from $W(\rightarrow \mu\nu_\mu)$ Control Sample | 29 ± 3 | 1.0 ± 0.6 |
| Est. from W with $t\bar{t}$ contami. | 36 ± 3 | 1.2 ± 0.6 |
| Est. from W with $t\bar{t}$ & SU1 contami. | 37 ± 3 | 1.6 ± 0.7 |
| Est. from W with $t\bar{t}$ & SU3 contami. | 37 ± 3 | 1.8 ± 0.7 |
| Est. from W with $t\bar{t}$ & SU4 contami. | 47 ± 4 | 2.0 ± 0.7 |
| Est. from W with $t\bar{t}$ & SU6 contami. | 36 ± 3 | 1.4 ± 0.6 |
| Est. from W with $t\bar{t}$ & SU8 contami. | 36 ± 3 | 1.3 ± 0.6 |

Estimation using Monte Carlo Simulation Samples

The Monte Carlo method used for $Z(\rightarrow \nu\bar{\nu})$ background can also be expanded to the estimation of W +jets background. Since gluons in protons mainly contribute to the multi-jet processes associating W productions, the same normalization factor is expected to be valid to apply on W +jets background (and it was confirmed by investigating the dependence of Z/W +jets Monte Carlo on various parameters).

12.5.3 $t\bar{t}$ +jets Background

Main component of $t\bar{t}$ +jets background is the semi-leptonic decay events where the leptons are tau's most of which are decaying hadronically. The remaining $t\bar{t}$ +jets background is due to the non-identified electron or muon [A.3.4.4].

The background can be estimated in a data-driven way using semi-leptonic $t\bar{t}$ +jets events with an identified electron or muon. The one-lepton control samples with b-tagged events can be used. The event selection for the $t\bar{t}$ one-lepton control sample is shown below.

- **Control Sample Ib**

- **Requirement of one lepton in order to select W 's with leptonic decays:** Presence of one electron or muon with $p_T > 20 \text{ GeV}$ and $|\eta| < 2.5$, and passing isolation criteria: $E_T(\Delta R < 0.2) < 10 \text{ GeV}$
- **Avoidance of the signal region of the SUSY one-lepton search mode:** transverse mass $M_T < 100 \text{ GeV}$
- **Rejection of W events (selection of $t\bar{t}$ events):** Presence of at least one b-tagged jet
- **SUSY selection cuts to match the kinematic properties of the control sample as the no-lepton search mode background:**

Table 12.9: Origin of $t\bar{t}$ background to no-lepton search mode.

| Origin | Fraction |
|---|----------|
| τ within acceptance | 53.4 % |
| τ out of acceptance | 20.9 % |
| e, μ within acceptance but unidentified | 8.5 % |
| e, μ out of acceptance | 17.1 % |

Table 12.10: Number of events of $t\bar{t}$ no-lepton background with τ inside the acceptance and estimation from one-lepton control samples.

| BG & Estimation | $E_T^{\text{miss}} > 100 \text{ GeV}$ | $E_T^{\text{miss}} > 300 \text{ GeV}$ |
|--|---------------------------------------|---------------------------------------|
| $t\bar{t}$ No-lepton BG with τ in acc. | 286 ± 17 | 4 ± 2 |
| Estimation from $t\bar{t}$ One-lepton Control Sample | 219 ± 10 | 2 ± 2 |
| Est. from $t\bar{t}$ with W contamination | 253 ± 18 | 4 ± 2 |
| Est. from $t\bar{t}$ with W & SU1 contami. | 255 ± 18 | 6 ± 3 |
| Est. from $t\bar{t}$ with W & SU3 contami. | 259 ± 18 | 6 ± 3 |
| Est. from $t\bar{t}$ with W & SU4 contami. | 423 ± 18 | 10 ± 4 |
| Est. from $t\bar{t}$ with W & SU6 contami. | 255 ± 18 | 5 ± 3 |
| Est. from $t\bar{t}$ with W & SU8 contami. | 254 ± 18 | 5 ± 3 |

- * At least four jets with $p_T > 50 \text{ GeV}$ and $|\eta| < 2.5$, and at least one of them with $p_T > 100 \text{ GeV}$
- * $E_T^{\text{miss}} > 100 \text{ GeV}$ and $E_T^{\text{miss}} > 0.2M_{eff}$
- * $0.3 < \Delta\phi(\text{jet1}, E_T^{\text{miss}}) < \pi - 0.3$, $0.2 < \Delta\phi(\text{jet2}, E_T^{\text{miss}}) < \pi - 0.2$,
 $0.2 < \Delta\phi(\text{jet3}, E_T^{\text{miss}}) < \pi - 0.2$

• Control Sample IIb

- Basically the same as Control Sample Ib, but the lepton is replaced as a “jet,” and included in the effective mass calculation if it is among the three leading “jets.” The same event selection is applied other than the lepton-jet replacement.

Here, we use these control samples for the estimation. Without the use of b-tagging, $t\bar{t}$ +jets events can also be selected by reconstructing top quark masses in the leptonic and hadronic parts [146]. Here, we will only mention the strategy with using the b-tagging.

The no-lepton $t\bar{t}$ background from semileptonic decay with an electron or muon within the acceptance but unidentified can be estimated with Control Sample Ib (Figure 12.10), whereas the no-lepton $t\bar{t}$ background from semileptonic decay with a τ within the acceptance can be estimated with Control Sample IIb (Figure 12.10).

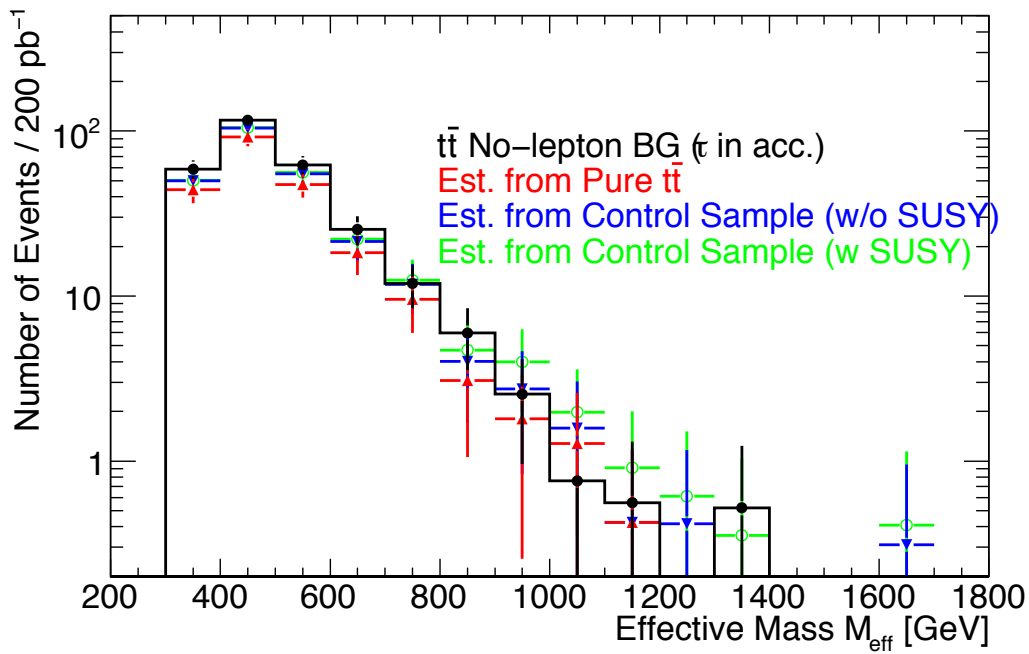
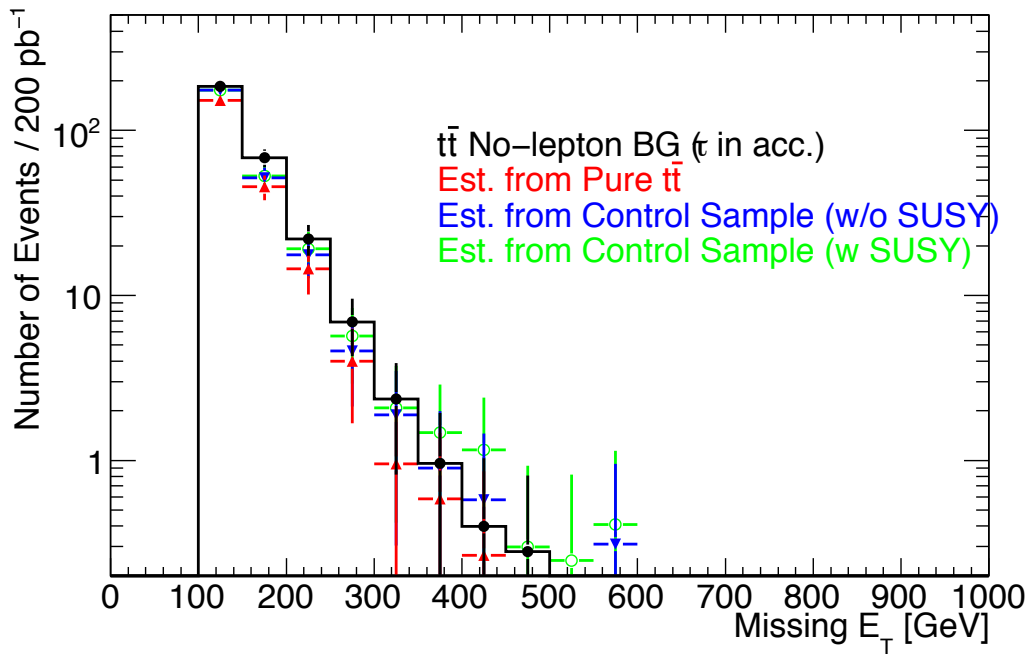


Figure 12.10: Estimation of $t\bar{t}(\rightarrow b\bar{b}\tau\nu_\tau qq)$ background using $t\bar{t}(\rightarrow b\bar{b}\mu\nu_\mu qq)$ one-lepton control samples (top: E_T^{miss} , bottom: effective mass).

12.5.4 QCD Multi-jet Background

QCD multi-jet events ideally do not have significantly large E_T^{miss} . Thus, QCD events become background to the no-lepton search mode, only when those events have large E_T^{miss} originated due to some reason. The origins of large E_T^{miss} in QCD background can be ascribed to the following sources:

- b-jets
- Jet mis-measurement
- Shower leakage
- Detector problems (E_T^{miss} formed from dead channels)

In either cases, peculiar feature of QCD background is that E_T^{miss} is highly correlated to the direction of a jet. After rejecting events with high angular correlation of jets and E_T^{miss} , the QCD background becomes very small in the interesting region for SUSY (set as $E_T^{\text{miss}} > 300$ GeV in ATLAS).

12.5.5 Non-collision Background

Non-collision sources such as cosmic rays and beam halo particles can deposit large amount of energy when traversing the calorimeters by hard bremsstrahlung as continuously mentioned in the previous chapters. However, it is not trivial how much of such backgrounds will actually contaminate the data and affect the analyses during the collision data taking. Considering the fact that the calorimeter signals last over several bunch crossings ($O(100)$ ns) and the time resolution of L1Calo trigger is coarse and only identifies which bunch crossing (25 ns interval) the event belongs to, cosmic muons will basically be triggered with the same rate as currently observed in cosmic ray runs [131] [132] (Cosmic muons generate fake jets with $p_T > 20$ GeV at the rate of about 2 Hz).

Thus, the effects from non-collision background can be grouped into two categories,

- Non-collision sources firing the trigger by themselves.
- Non-collision backgrounds overlapping collision events which have already been triggered.

Air shower events can fire the trigger, and also clear multi-jet event selections by themselves without overlapping collision events.

The estimation of background originating from cosmic overlaps on collision events was done with the event overlay technique mentioned in Section 9.2. In order to estimate the cross section of overlap effects, it was assumed that the cosmic muons have meaningful effects on the energy reconstruction of the calorimeters when they were within two bunch crossings from the collision events (± 50 ns). The amount of such background was estimated from this assumption and the cross section of the collision events. Due to the fact that the rate of high energy cosmic muons with a hard bremsstrahlung overlapping QCD dijet events is rare, none of the cosmic-overlaid events passed the SUSY event selection.

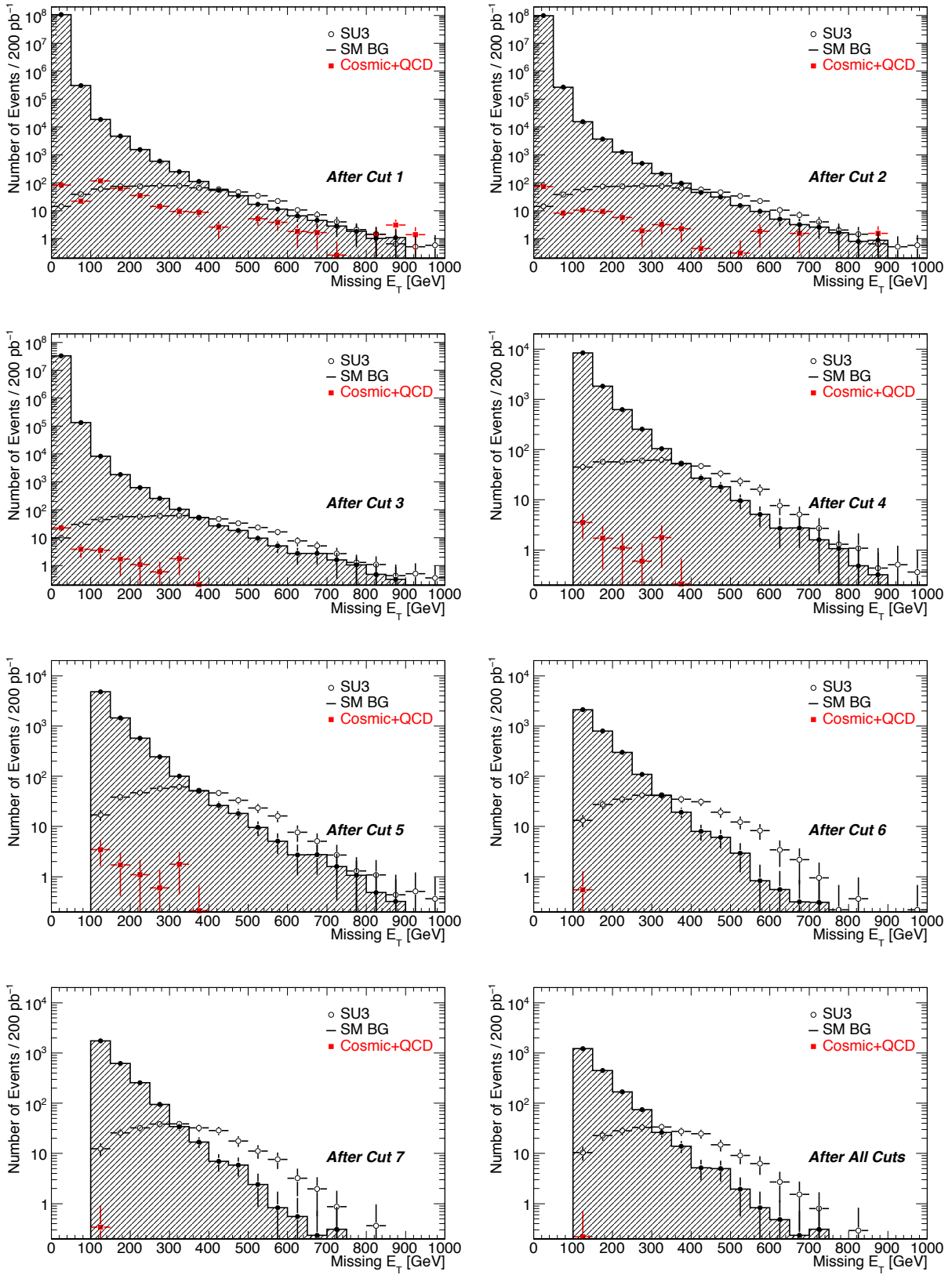


Figure 12.11: E_T^{miss} distributions of SUSY signals and Standard Model background after selection cuts assuming the integrated luminosity of 200 pb^{-1} .

Table 12.11: Breakdown of the Standard Model background and cosmic-QCD overlay events after event selection of no-lepton search mode for integrated luminosity of 200 pb⁻¹.

| Cut | SM BG | Cosmic+QCD |
|----------------|-----------------------------------|---------------|
| After Cut 1 | $(1.0682 \pm 0.0001) \times 10^8$ | 378 ± 19 |
| After Cut 2 | $(9.726 \pm 0.001) \times 10^7$ | 122 ± 11 |
| After Cut 3 | $(3.2943 \pm 0.0006) \times 10^7$ | 36 ± 6 |
| After Cut 4 | $(1.132 \pm 0.001) \times 10^5$ | 9 ± 3 |
| After Cut 5 | 7299 ± 85 | 9 ± 3 |
| After Cut 6 | 3389 ± 58 | 0.7 ± 0.9 |
| After Cut 7 | 2785 ± 53 | 0.5 ± 0.7 |
| After All Cuts | 1971 ± 44 | 0.4 ± 0.6 |

With the same assumption on the event overlap, (0.4 ± 0.6) events/200 pb⁻¹ are expected in the multi-jet signature from the cosmic overlaps. Thus, the overlaps of cosmic muons on QCD multi-jet events are almost negligible in No-lepton search mode, but even such background can be further rejected by the use of cleaning cuts mentioned in Chapter 9.

12.6 Systematic Uncertainties

For Monte Carlo-based estimation, systematic uncertainties arise from vast amount of components. For purely Monte Carlo issues, the systematics originate from the renormalization scale, description of the parton distribution function (PDF), factorization scale, description of gluon radiation, hadronization and decays, and effects from multi-parton interactions. Some additional systematics arise in case of Alpgen related to the matching procedure. Some of the systematics mentioned above have previously been investigated with Z +jets Monte Carlo simulation samples [A.3.4.3], [A.3.4.5].

Detector and performance effects such as the calorimeter response (which affects the energy scale and resolution of jets and E_T^{miss}), trigger efficiency and object reconstruction and identification efficiency also contribute to the systematics.

However, in case of data-driven estimation, most of the above systematics are disentangled. Needless to say the absence of Monte Carlo systematics, but many of the systematics from the detector performance are also absent, especially the jet and E_T^{miss} systematics, since the output from data is directly used for the estimation. For data-driven estimations, major uncertainties come from the methods themselves (e.g. presence of background contamination in the control samples, uncertainty of extrapolations if any).

Here, we will review in Section 12.6.1 the source of systematics for each data-driven estimation method mentioned in this chapter. The effects of jet and E_T^{miss} systematics on the signal and background selection efficiency will be mentioned in Section 12.6.2.

Table 12.12: Systematic uncertainties expected for data-driven estimation of $Z(\rightarrow \nu\bar{\nu})$ background for 200 pb^{-1} .

| Source | Uncertainty |
|--------------------------------|----------------|
| Muon trigger efficiency | 0.5 % |
| Muon identification efficiency | 2 % |
| Kinematic corrections | not considered |
| Statistical | 12.3 % |
| Effects from BG & SUSY signals | 12.0 % |

12.6.1 Systematics in Data-driven Methods

In this section, we investigate the systematic uncertainties from the data-driven methods themselves.

Systematics of $Z(\rightarrow \nu\bar{\nu})$ Background Estimation

First of all, for estimating $Z(\rightarrow \nu\bar{\nu})$ background, the systematic uncertainty originates from components in equation (12.1), the muon trigger efficiency, muon identification efficiency, and kinematic correction for the acceptance effects. The systematics from trigger efficiency is quite small. It can be estimated from data using tag-and-probe method and uncertainty less than 0.5 % will be achieved with 50 pb^{-1} of integrated luminosity [23]. Here, we assume 0.5 % even for 200 pb^{-1} analyses, to be conservative. This uncertainty should be considered separately for each muon p_T bins, but here we considered uniform uncertainty over various p_T regions with tight assumption. Similar uncertainty is expected for the reconstruction efficiency using the tag-and-probe method. Here, we assume overall uncertainty of reconstruction efficiency to be 2 % to be conservative (~ 1 % expected from previous studies [23] for 100 pb^{-1} in p_T range of 20 to 70 GeV). The systematics of $C(p_T(Z))$ will not be considered here. The jet and E_T^{miss} systematics do not contribute to the uncertainty of the method itself, but only affect the selection efficiency of $Z(\rightarrow \nu\bar{\nu})$ background, and thus will not be considered here, but mentioned in Section 12.6.2. Thus, the major systematic uncertainty is from the background contribution of $t\bar{t}$ and SUSY signals. For low mass SUSY case (SU4), the uncertainty becomes large. Here, we show SU3 as the benchmark for the effects of signal contamination in Table 12.12. Considering the systematics mentioned here, the number of events remaining after no-lepton search mode selection can be estimated by 17.3 % (and 37.9 % for the region of $E_T^{\text{miss}} > 300 \text{ GeV}$).

Systematics of W Background Estimation

For estimation $W(\rightarrow \tau\nu_\tau)$ no-lepton background with τ in the acceptance, the systematics of data-driven method arise from the lepton reconstruction efficiency, b-tag efficiency, cut efficiency using the transverse momentum, effects of substitution of the τ with a

Table 12.13: Systematic uncertainties expected for data-driven estimation of $W(\rightarrow \tau\nu_\tau)$ background with τ in acceptance for 200 pb^{-1} .

| Source | Uncertainty on BG |
|--------------------------------|--------------------------|
| Muon trigger efficiency | 0.5 % |
| Muon identification efficiency | 2 % |
| b-tagging efficiency | 3 % |
| Selection eff. using M_T | not considered but small |
| Statistical | 6.1 % |
| Effects from BG & SUSY signals | 15.9 % |

Table 12.14: Systematic uncertainties expected for data-driven estimation of $W(\rightarrow \mu\nu_\mu)$ background with μ in acceptance but unidentified for 200 pb^{-1} .

| Source | Uncertainty on BG |
|--------------------------------|--------------------------|
| Muon trigger efficiency | 0.5 % |
| Muon identification efficiency | 2 % |
| b-tagging efficiency | 3 % |
| Selection eff. using M_T | not considered but small |
| Statistical | 10.3 % |
| Effects from BG & SUSY signals | 27.4 % |

lepton, and background in the control sample. The uncertainty of cut efficiency with transverse momentum is rather small and will not be considered here. We assume the same systematics for the lepton reconstruction efficiency as mentioned above. The b-tagging efficiency will be estimated from $t\bar{t}$ data with the precision of less than 5 % with 100 pb^{-1} integrated luminosity [23], thus we assume 5 % uncertainty. When the b-tag efficiency fluctuate by 5 %, the amount of $t\bar{t}$ contamination change by less than 3 %. Thus, we conservatively assume 5 % fluctuation of contamination in the pure-W control samples. We will not consider the systematics of substitution of τ 's at the moment. Under such assumption, the number of events remaining after no-lepton search mode selection can be estimated by 17.4 % (and 62.9 % for the region of $E_T^{\text{miss}} > 300 \text{ GeV}$; note the small statistics in this region; 13 events expected). Table 12.13 shows the uncertainty from each contribution.

Similarly, the $W(\rightarrow \mu\nu_\mu)$ no-lepton background with the muon in acceptance but unidentified, can be estimated by 29.5 % (and 100 % for the region of $E_T^{\text{miss}} > 300 \text{ GeV}$; note the small statistics in this region; 3 events expected). Table 12.14 shows the uncertainty from each component.

Table 12.15: Systematic uncertainties expected for data-driven estimation of $t\bar{t}(\rightarrow b\bar{b}\tau\nu_\tau qq)$ background with τ in acceptance for 200 pb^{-1} .

| Source | Uncertainty on BG |
|--------------------------------|--------------------------|
| Muon trigger efficiency | 0.5 % |
| Muon identification efficiency | 2 % |
| b-tagging efficiency | 3 % |
| Selection eff. using M_T | not considered but small |
| Limitation of method | 30.1 % |
| Statistical | 4.6 % |
| Effects from BG | 18.3 % |

Systematics of $t\bar{t}$ Background Estimation

For estimation $t\bar{t}(\rightarrow b\bar{b}\tau\nu_\tau qq)$ no-lepton background with τ in the acceptance, the same systematics should be considered as the $W(\rightarrow \tau\nu_\tau)$ no-lepton background (Table 12.15). Since a deviation is seen for this data-driven method even for the pure $t\bar{t}$ control samples, the discrepancy was included in the systematic uncertainty. This background will be estimated by 36.0 % (and 245 % for the region of $E_T^{\text{miss}} > 300 \text{ GeV}$; 4 events expected).

The important component of the Standard Model background can be estimated with data-driven method as mentioned in this chapter. For the remaining background (which only dominate about 7 % in $E_T^{\text{miss}} > 300 \text{ GeV}$ region) which were not estimated by the data-driven method), we extract the numbers from the Monte Carlo to check the realistic significance mentioned in Section 12.7 with the normalization uncertainty of 20 %.

The overall number of events in the interesting region ($E_T^{\text{miss}} > 300 \text{ GeV}$ region) after the SUSY no-lepton search mode selection can be estimated as 67 ± 23 events (the actual value is 54 ± 7) in case of the presence of SU3.

12.6.2 Systematics from Jet and E_T^{miss} Performance

Various uncertainties from the performance of the detector and reconstructed objects highly affect the background and signal tagging efficiency. Here, we concentrate on the uncertainties arising from the calorimeters, namely those from jet and E_T^{miss} energy scale and resolution. We will not consider the systematics of jet algorithms themselves, such as the splitting and merging effects on reconstructed jets. The effects of these uncertainties will not propagate into the uncertainty in data-driven methods, but should be considered for Monte Carlo-based estimation and investigation on the selection efficiency of expected SUSY signals.

The performance of jets and E_T^{miss} will be validated with early data, and their energy scale and resolution will be estimated.

The energy scale of jets will be evaluated with the p_T balance of γ +jets and Z +jets events, which were adopted at the Tevatron as well. In the previous studies in ATLAS,

the jet energy scale is expected to be calibrated and evaluated within about 1 % with 100 pb^{-1} except for very low p_T jets and up to 300-500 GeV range [23][147]-[150]. Here, we investigate two cases, a realistic and slightly conservative case of 2 % uncertainty and a pessimistic case of 5 %.

The energy resolution of jets can be estimated in-situ using the p_T balance of dijet events. About 1 % precision can be achieved with 100 pb^{-1} for an η bin size of 0.1 and up to about 500 GeV of p_T [23] [151]. Here, uncertainty of a realistic case (2 %) and a pessimistic case (5 %) were assumed and investigated.

The performance of E_T^{miss} will be validated with data. Minimum Bias and QCD multijet events allow for the evaluation of E_T^{miss} resolution. The estimation of E_T^{miss} scale performance will be done with $Z(\rightarrow e^+e^-)$ and $Z(\rightarrow \mu^+\mu^-)$ by replacing the dilepton, $Z(\rightarrow \tau^+\tau^-)$ by measuring the invariant mass of the τ 's with collinear approximation of the emitted ν_τ , $W(\rightarrow l\nu)$ by using the shape of the transverse mass, and $t\bar{t}$ events with semileptonic decays using the invariant mass. These events allow for the estimation of E_T^{miss} performance with various event topologies. E_T^{miss} scale is expected to be estimated within about 1 - 2 % with 200 pb^{-1} data [23]. Here, we considered 2 % and 5 % E_T^{miss} scale uncertainty for the systematics studies. For E_T^{miss} resolution, we adopted 5 % and 10 % uncertainty for the studies.

Although the four systematics mentioned here are highly related and not independent (especially the jet and E_T^{miss} scale), we considered each effect separately and also totally (with jet and E_T^{miss} scale correlating and shifting in the same direction with the same ratio).

Investigation on the Selection Efficiencies

Effects of jet and E_T^{miss} systematics on the selection efficiency were investigated here. The energy scale were simply forced to shift by $\pm 2\%$ or $\pm 5\%$ (thus four sets of trials) in the offline analysis to see their effects. The impact of degraded resolution was considered here by independent smearing the jet p_x and p_y by a Gaussian of 2 or 5 % spread (so the direction was also smeared accordingly). The systematics of E_T^{miss} was treated in the offline analysis in the same way.

Table 12.16 and 12.18 show the breakdown of number of the Standard Model background and SUSY signal events remaining after the no-lepton search mode event selection with the consideration of various jet and E_T^{miss} systematics mentioned above. For ‘‘Overall Scale Up (2)’’ and ‘‘Overall Scale Down (2)’’ in the tables, the jet and E_T^{miss} scale was treated in a correlated way; shifted in the same direction with the same amount $\pm 2\%$ ($\pm 5\%$), and also the resolution was degraded by 2 % (5 %) for jets and 5 % (10 %) for E_T^{miss} (here, the resolution was degraded for both the ‘‘Up’’ and ‘‘Down’’ cases). Table 12.17 and 12.19 show the uncertainties from the overall systematics just mentioned. The impact of the uncertainties of jet and E_T^{miss} resolution is rather small (about 1 %) for both the background and SUSY signals. The uncertainty is slightly larger for the low mass case (SU4). On the other hand, the outcome of shifts in the energy scale of jets and E_T^{miss} is quite large for the Standard Model background (about 10 %). Note that QCD background mostly originates from fake E_T^{miss} , and thus it is from the tail of the jet and E_T^{miss} performance, which explains the small sensitivity to the jet and E_T^{miss} systematics

Table 12.16: Breakdown of events after event selection of no-lepton search mode for integrated luminosity of 200 pb^{-1} . Effects of jet and E_T^{miss} systematics were investigated.

| Cut | Z | W | $t\bar{t}$ | QCD |
|-------------------------------|--------------|---------------|--------------|--------------|
| After All Cuts | 422 ± 21 | 801 ± 28 | 606 ± 25 | 148 ± 12 |
| Jet Scale +2% | 440 ± 21 | 840 ± 29 | 630 ± 25 | 150 ± 12 |
| Jet Scale +5% | 471 ± 22 | 896 ± 30 | 668 ± 26 | 112 ± 11 |
| Jet Scale -2% | 407 ± 20 | 764 ± 28 | 582 ± 24 | 153 ± 12 |
| Jet Scale -5% | 380 ± 20 | 716 ± 27 | 545 ± 23 | 153 ± 12 |
| Jet Reso +2% | 425 ± 21 | 801 ± 28 | 605 ± 25 | 150 ± 12 |
| Jet Reso +5% | 421 ± 21 | 804 ± 28 | 605 ± 25 | 115 ± 11 |
| E_T^{miss} Scale +2% | 436 ± 21 | 836 ± 29 | 638 ± 25 | 153 ± 12 |
| E_T^{miss} Scale +5% | 460 ± 21 | 890 ± 30 | 681 ± 26 | 153 ± 12 |
| E_T^{miss} Scale -2% | 406 ± 20 | 764 ± 28 | 575 ± 24 | 150 ± 12 |
| E_T^{miss} Scale -5% | 384 ± 20 | 707 ± 27 | 529 ± 23 | 112 ± 11 |
| E_T^{miss} Reso +5% | 424 ± 21 | 808 ± 28 | 610 ± 25 | 150 ± 12 |
| E_T^{miss} Reso +10% | 427 ± 21 | 815 ± 29 | 615 ± 25 | 186 ± 14 |
| Overall Scale Up | 461 ± 21 | 886 ± 30 | 665 ± 26 | 150 ± 12 |
| Overall Scale Up 2 | 514 ± 23 | 1006 ± 31 | 754 ± 27 | 227 ± 15 |
| Overall Scale Down | 391 ± 20 | 735 ± 27 | 555 ± 24 | 150 ± 12 |
| Overall Scale Down 2 | 347 ± 19 | 640 ± 25 | 485 ± 22 | 154 ± 12 |

Table 12.17: Uncertainty of selection efficiency from jet and E_T^{miss} systematics for the Standard Model background, derived from the numbers in the ‘‘Overall Scale’’ rows in Table 12.16.

| Cut | Z | W | $t\bar{t}$ | QCD |
|---------------------------|--------|--------|------------|--------|
| Uncertainty | +9.2% | +10.6% | +9.7% | +1.4% |
| | -7.3% | -8.2% | -8.4% | --- |
| Uncertainty (pessimistic) | +21.8% | +25.6% | +24.4% | +53.4% |
| | -17.8% | -20.1% | -20.0% | --- |

Table 12.18: Breakdown of SUSY signal events after event selection of no-lepton search mode for integrated luminosity of 200 pb^{-1} . Effects of jet and E_T^{miss} systematics were investigated.

| Cut | SU1 | SU3 | SU4 | SU6 | SU8 |
|-------------------------------|----------------|------------------|-------------------|----------------|----------------|
| Default | 77.7 ± 8.8 | 215.9 ± 14.7 | 2534.4 ± 50.3 | 46.4 ± 6.8 | 71.2 ± 8.4 |
| Jet Scale +2% | 77.6 ± 8.8 | 216.7 ± 14.7 | 2556.2 ± 50.6 | 46.4 ± 6.8 | 71.4 ± 8.5 |
| Jet Scale +5% | 77.7 ± 8.8 | 218.6 ± 14.8 | 2583.7 ± 50.8 | 46.1 ± 6.8 | 71.2 ± 8.4 |
| Jet Scale -2% | 77.7 ± 8.8 | 216.6 ± 14.7 | 2503.8 ± 50.0 | 46.4 ± 6.8 | 71.2 ± 8.4 |
| Jet Scale -5% | 77.5 ± 8.8 | 213.5 ± 14.6 | 2451.2 ± 49.5 | 46.5 ± 6.8 | 71.4 ± 8.4 |
| Jet Reso +2% | 78.0 ± 8.8 | 215.4 ± 14.7 | 2534.4 ± 50.3 | 46.2 ± 6.8 | 71.2 ± 8.4 |
| Jet Reso +5% | 78.4 ± 8.9 | 215.4 ± 14.7 | 2524.0 ± 50.2 | 45.8 ± 6.8 | 70.7 ± 8.4 |
| E_T^{miss} Scale +2% | 78.4 ± 8.9 | 218.6 ± 14.8 | 2583.6 ± 50.8 | 46.9 ± 6.8 | 71.8 ± 8.5 |
| E_T^{miss} Scale +5% | 79.3 ± 8.9 | 221.2 ± 14.9 | 2649.0 ± 51.5 | 47.6 ± 6.9 | 72.8 ± 8.5 |
| E_T^{miss} Scale -2% | 76.6 ± 8.8 | 214.3 ± 14.6 | 2482.1 ± 49.8 | 45.9 ± 6.8 | 70.8 ± 8.4 |
| E_T^{miss} Scale -5% | 75.2 ± 8.7 | 210.3 ± 14.5 | 2397.9 ± 49.0 | 45.2 ± 6.7 | 69.7 ± 8.3 |
| E_T^{miss} Reso +5% | 77.7 ± 8.8 | 216.2 ± 14.7 | 2534.1 ± 50.3 | 46.2 ± 6.8 | 70.9 ± 8.4 |
| E_T^{miss} Reso +10% | 77.2 ± 8.8 | 216.2 ± 14.7 | 2533.8 ± 50.3 | 46.0 ± 6.8 | 71.4 ± 8.4 |
| Overall Scale Up | 78.7 ± 8.9 | 218.9 ± 14.8 | 2603.9 ± 51.0 | 46.7 ± 6.8 | 71.4 ± 8.5 |
| Overall Scale Up 2 | 80.1 ± 8.9 | 223.7 ± 15.0 | 2697.4 ± 51.9 | 46.9 ± 6.8 | 72.7 ± 8.5 |
| Overall Scale Down | 77.1 ± 8.8 | 213.0 ± 14.6 | 2452.1 ± 49.5 | 45.7 ± 6.8 | 70.1 ± 8.4 |
| Overall Scale Down 2 | 75.6 ± 8.7 | 208.3 ± 14.4 | 2325.4 ± 48.2 | 44.6 ± 6.7 | 69.1 ± 8.3 |

Table 12.19: Uncertainty of selection efficiency from jet and E_T^{miss} systematics for the SUSY signals, derived from the numbers in the ‘‘Overall Scale’’ rows in Table 12.18.

| Cut | SU1 | SU3 | SU4 | SU6 | SU8 |
|---------------------------|-------|-------|-------|-------|-------|
| Uncertainty | +1.3% | +1.4% | +2.7% | +0.6% | +0.3% |
| | -0.8% | -1.3% | -3.2% | -1.5% | -1.5% |
| Uncertainty (pessimistic) | +3.1% | +3.6% | +6.4% | +1.1% | +2.1% |
| | -2.7% | -3.5% | -8.2% | -3.9% | -2.9% |

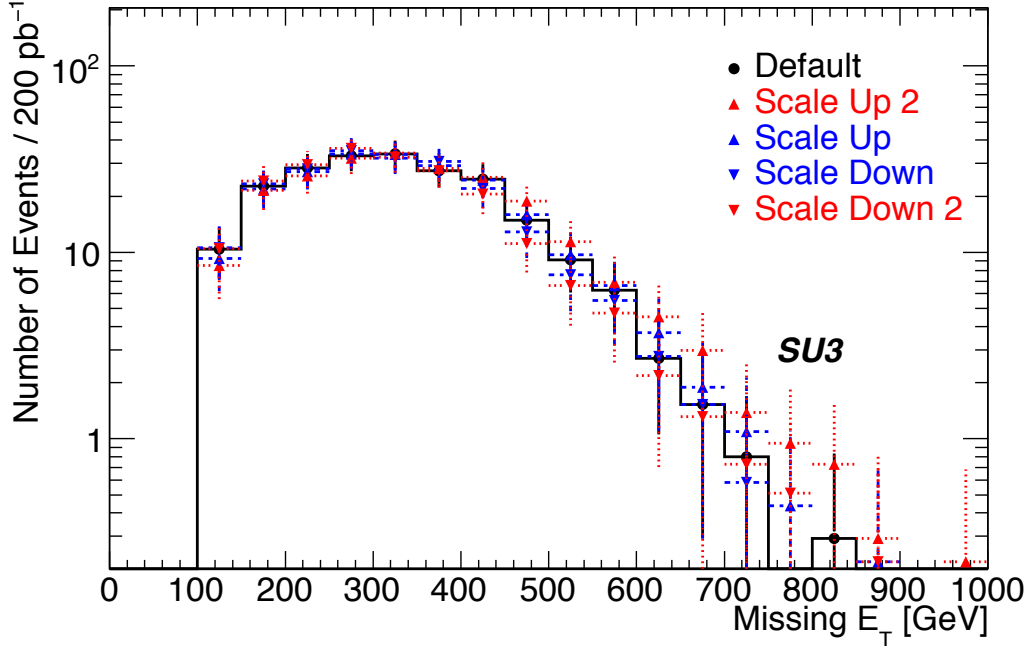


Figure 12.12: Effects of jet and E_T^{miss} systematics on E_T^{miss} distribution of SU3 signals under the integrated luminosity of 200 pb^{-1} . The definition of systematics assumed is mentioned in the text.

considered here. For QCD background, special consideration is needed to consider the effects from the tails of jet and E_T^{miss} performance, but we will not consider this issue in this thesis.

For SUSY signals, the uncertainty of selection efficiency arising from jet and E_T^{miss} systematics is small. This is due to the fact that many of the signal events are well above the selection thresholds, and not significantly influenced by the shifts in jets' transverse momenta and E_T^{miss} . Thus, for SUSY signals more important uncertainties originate from the Monte Carlo systematics which directly affect the cross section. Figure 12.12 shows the E_T^{miss} distribution from the default condition and with systematic shifts in the jet and E_T^{miss} performance.

12.7 Background Subtraction and Signal Significance

The estimation of the Standard Model background was performed in the previous sections with considerations on the systematic effects. Figure 12.13 and 12.14 show E_T^{miss} and effective mass distributions for the Standard Model background, estimated background with systematic uncertainties considered, and the total background and signals (uncertainties of the signal selection efficiency were included). Here, we assumed that the overall normalization of the background was the same as what we have in the Monte Carlo simulation samples. For SU3, an excess is observed in the tails. On the other hand, for SU4,

an excess is observed in almost all the range of distributions due to the low mass scale of SUSY. The background is now estimated, and can be subtracted from the observed distributions.

Some approaches can be considered for measurements in inclusive analyses; one is the measurement of the peak of effective mass distribution, and the other is simply counting the excess of the number of events from the background. Here, we briefly investigate on both approaches.

12.7.1 Effective Mass Distributions

When an excess is observed, the peak of M_{eff} distribution will give some indications on the produced SUSY particles, because the peak is known to be roughly proportional to $M_{SUSY}(= \min(\tilde{g}, \tilde{u}_R))$ [53]. Figure 12.15 shows the effective mass distribution in case of SU4 signals for a case of an ideal background estimation (perfect background subtraction with only statistical uncertainty) and more realist background subtraction with data-driven methods and systematic uncertainties considered. The peak of the effective mass for SU4 was 573 ± 6 GeV for ideal case and 591 ± 28 GeV in this study, and thus reproducing the actual value within the uncertainty (Figure 12.15). For SU3 case, the peak was measured as 988 ± 135 GeV (929 ± 24 GeV for ideal case). For other benchmark points, we need more statistics to measure the peak of the effective mass.

12.7.2 Number Counting Approach

An excess from the expected background should first of all be considered whether it is significant or not. It will eventually allow for the measurement of the cross section once a model is assumed with a careful treatment on the signal contamination in background, but we will not investigate this issue here. Comparing the excess in various SUSY search modes will allow us to narrow down the possible SUSY models matching the observation. Here, we will investigate how much significance is expected in the no-lepton search mode for the benchmark SUSY signals for 200 pb^{-1} with realistic background estimation.

Here, we adopt the definition of signal significance used in the previous studies [23]. Considering the Poisson statistics due to the feature of rare events, the probability p to observe N events or above can be expressed as,

$$p = A \int_0^\infty db G(b; N_b, \delta N_b) \sum_{i=N}^\infty \frac{e^{-b} b^i}{i!}, \quad (12.2)$$

where A is the normalization factor to set the total probability to unity, b is the expected number of events for the Poisson distribution, G is a Gaussian with mean N_b and standard deviation of δN_b . Finally, the probability can be converted to the signal significance $Z\sigma$, which Z is expressed as,

$$Z = \sqrt{2} \operatorname{erf}^{-1}(1 - 2p). \quad (12.3)$$

The uncertainty of the signal selection efficiency coming from jet and E_T^{miss} systematics were considered in the calculation as well.

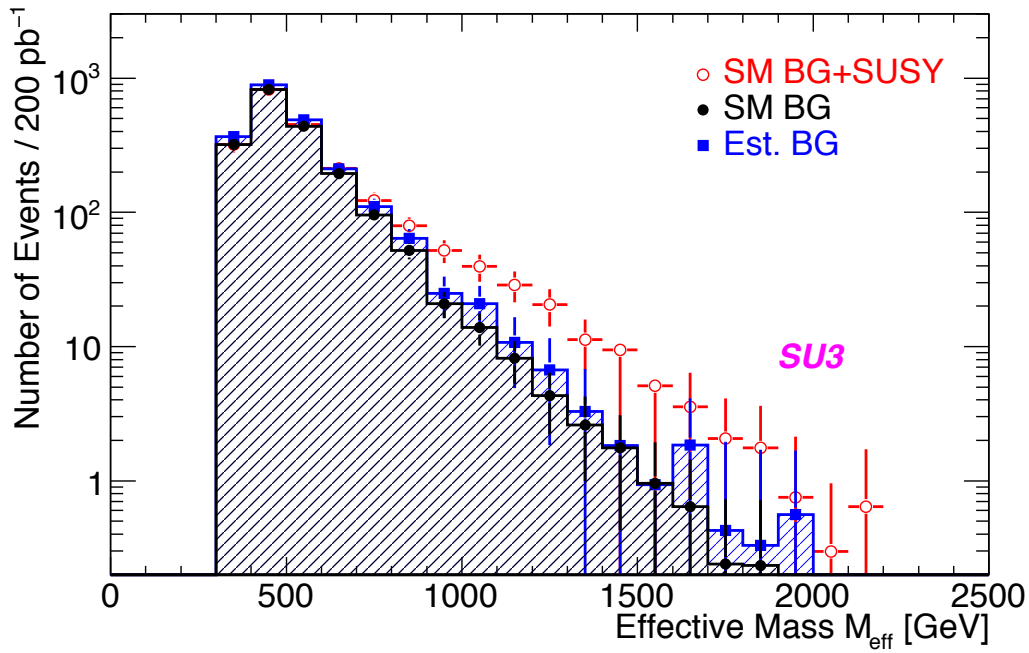
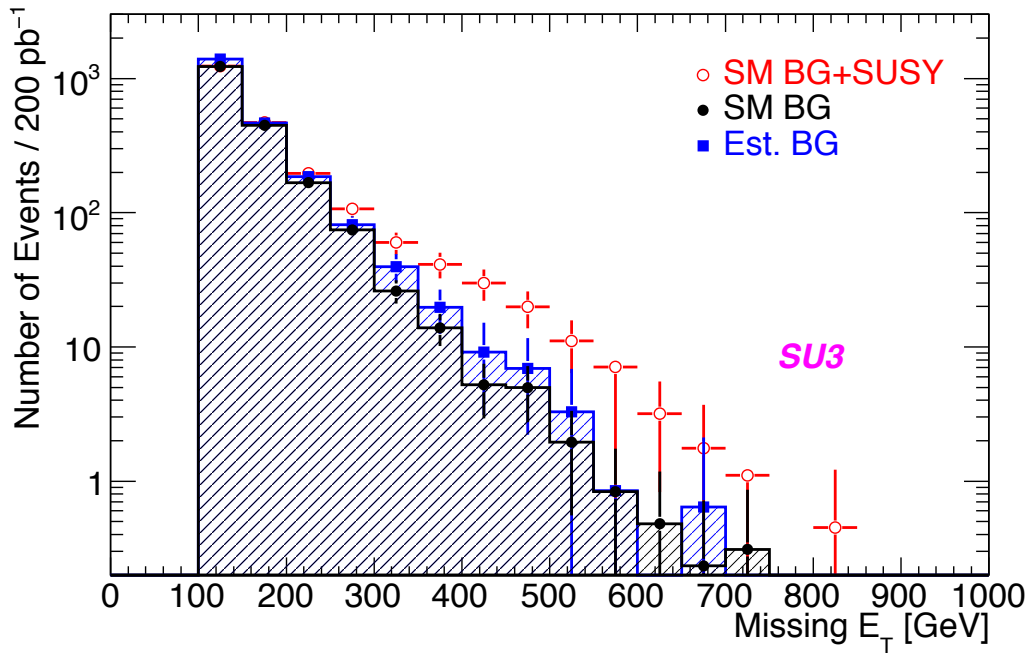


Figure 12.13: E_T^{miss} and effective mass distribution of SU3 signals and Standard Model background for the integrated luminosity of 200 pb⁻¹.

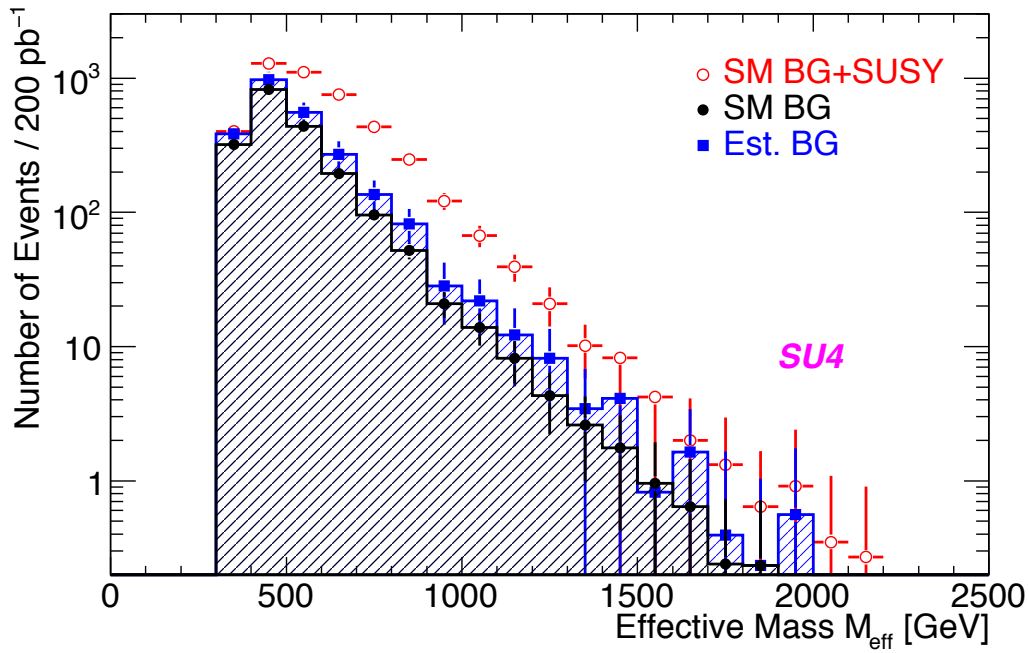
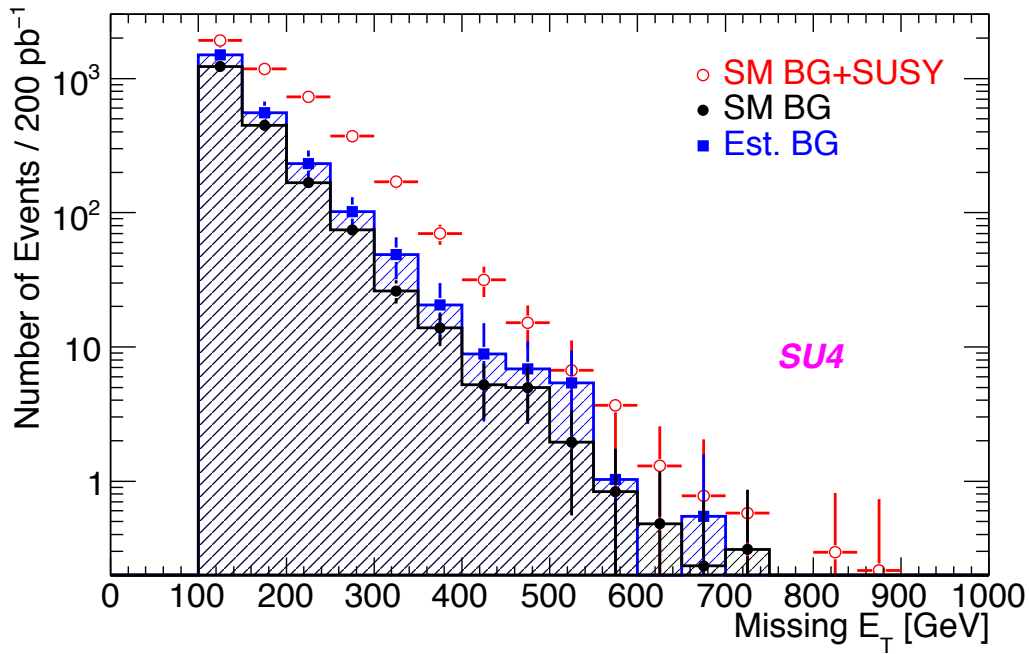


Figure 12.14: E_T^{miss} and effective mass distribution of SU4 signals and Standard Model background for the integrated luminosity of 200 pb^{-1} .

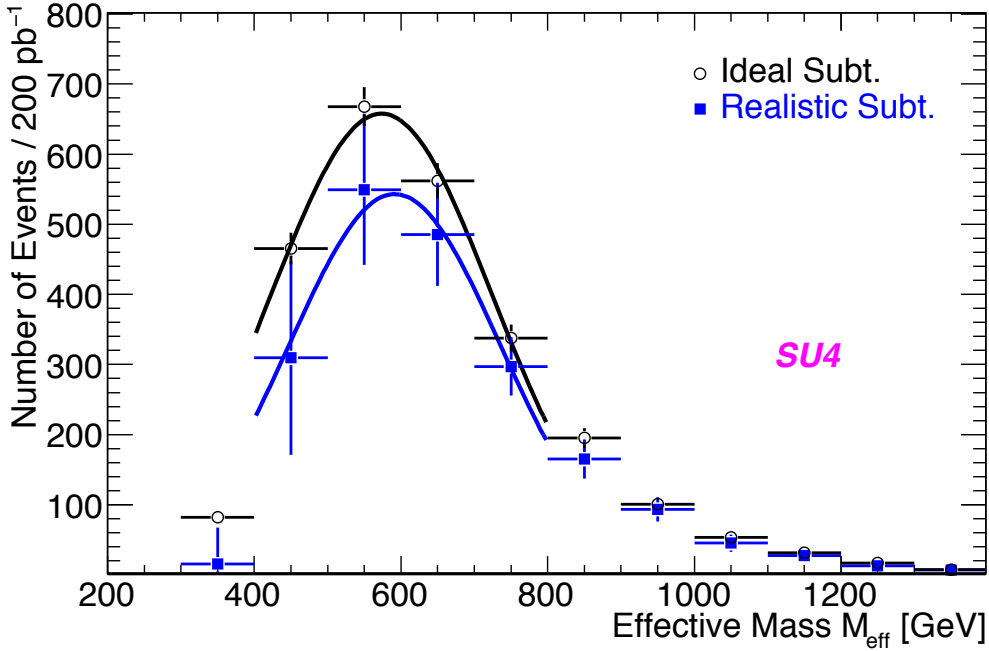


Figure 12.15: Effective mass distribution of SU4 signals for the integrated luminosity of 200 pb^{-1} .

When calculating the significance for each mSUGRA benchmark points, the number of events were counted after the no-lepton search mode event selection, and an additional threshold on the E_T^{miss} or effective mass. Figure 12.16 and 12.17 show the significance for various threshold on E_T^{miss} or effective mass. We adopted the threshold with the maximum significance for each benchmark points. The signal significance of benchmark mSUGRA points are shown in Table 12.20 for ideal conditions (only statistical errors considered), relatively realistic condition with systematic errors considered but ideal subtraction of the background (so this may show a realistic limit of the discovery potential with the standard event selection), and finally the one from the data-driven methods. The numbers in the parentheses show the significance with the K-factor of 1.3 considered for the SUSY processes. Note that K-factors are always considered for the Standard Model processes in this section, except for the QCD multi-jet events. The discovery reach is reduced under realist conditions, but some of the SUSY signals can still be reached or manifest themselves in a prominent way with the integrated luminosity of 200 pb^{-1} .

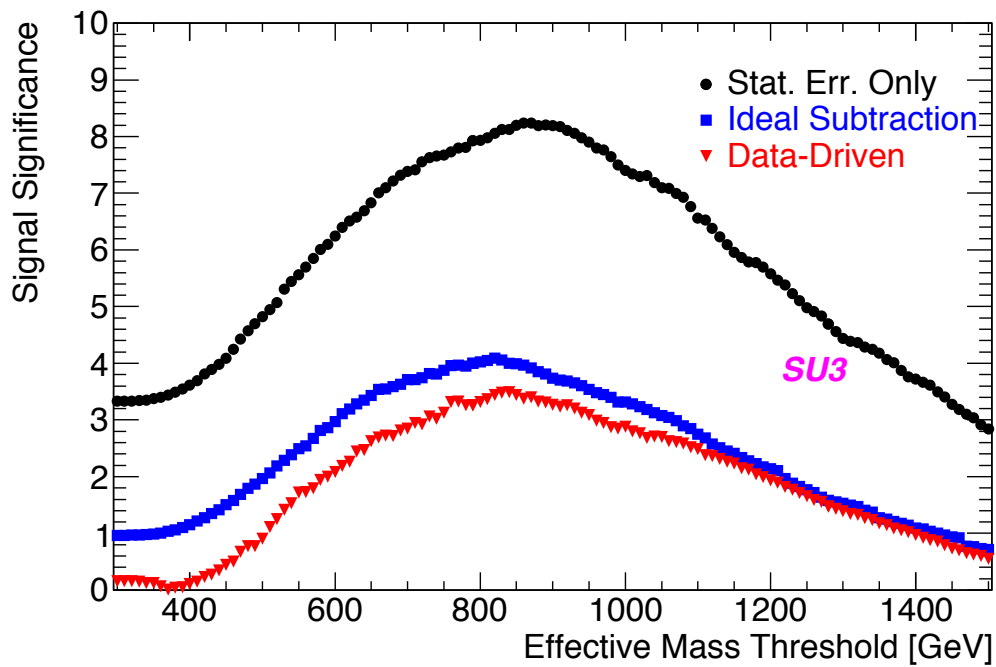
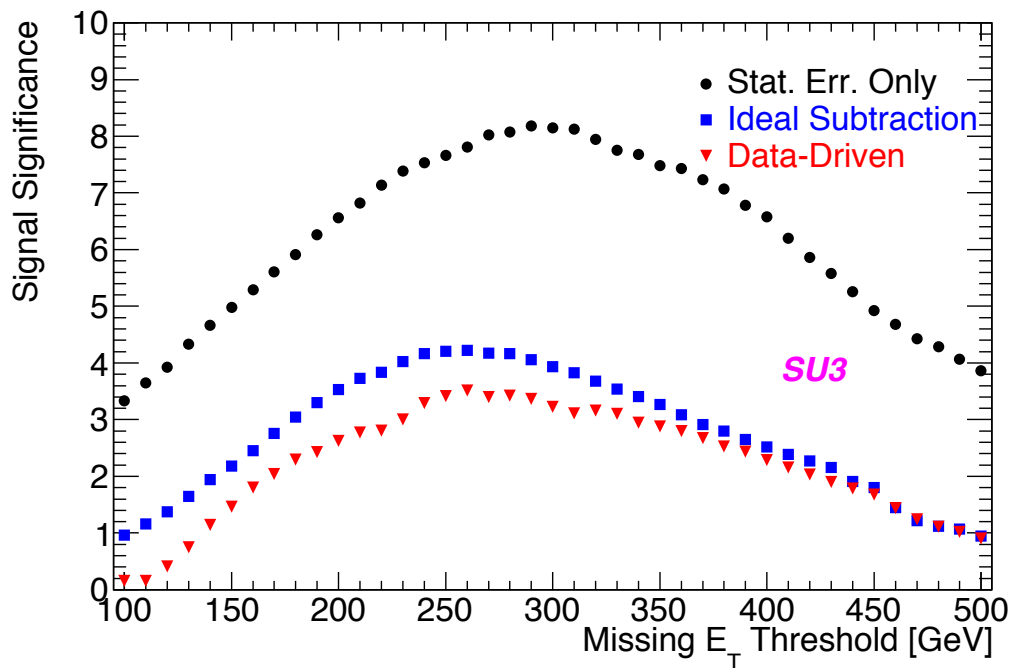


Figure 12.16: Significance of the SUSY signal SU3 scanned over various E_T^{miss} and M_{eff} thresholds for the integrated luminosity of 200 pb^{-1} .

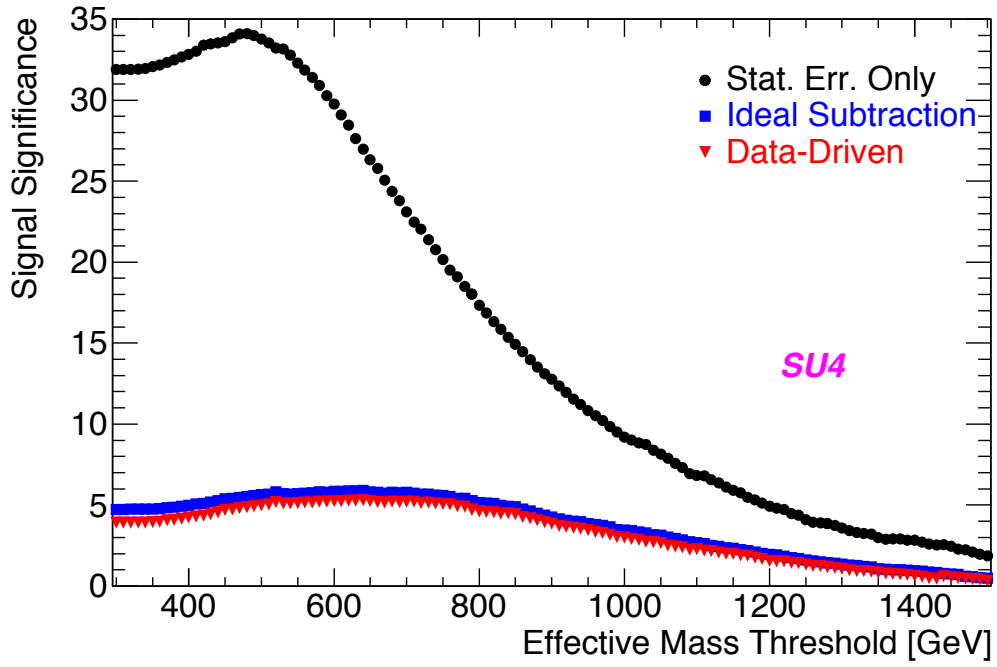
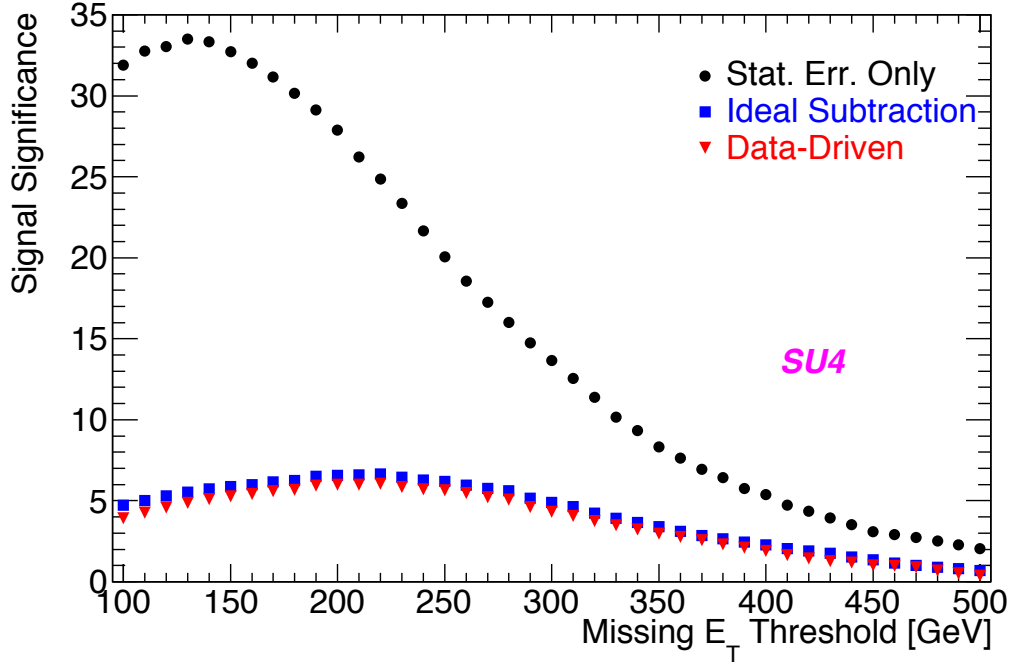


Figure 12.17: Significance of the SUSY signal SU4 scanned over various E_T^{miss} and M_{eff} thresholds for the integrated luminosity of 200 pb^{-1} .

Table 12.20: Significance of mSUGRA benchmark signals for integrated luminosity of 200 pb⁻¹. Numbers in the parentheses are after considering the K-factor of SUSY processes.

| Cut | SU1 | SU3 | SU4 | SU6 | SU8 |
|---------------------------------|-----------|------------|-----------|-----------|-----------|
| Statistical Error Only | 4.4 (5.4) | 8.2 (10.1) | 34.1 (—) | 3.2 (3.9) | 4.2 (5.2) |
| Sys.Err. & Ideal BG Subtraction | 2.4 (2.8) | 4.2 (4.8) | 6.6 (6.8) | 1.8 (2.1) | 2.4 (2.9) |
| Sys.Err. & Data-Driven BG Sub. | 1.7 (2.0) | 3.5 (4.1) | 6.0 (6.2) | 1.3 (1.6) | 1.9 (2.3) |

Chapter 13

Conclusions

The Large Hadron Collider (LHC) is the first collider to probe the physics at the TeV-energy scale. Undiscovered weakly-interacting particles from Supersymmetric or extra dimensional models are good candidates of the dark matter in the Universe, and they may be copiously produced in the LHC collisions.

In this thesis, we considered model-independent searches for physics beyond the Standard Model by event topologies with jets and missing transverse energy (E_T^{miss}). Since jets and E_T^{miss} mostly depend on the calorimeter performance, the first half of this thesis was devoted to the studies of the ATLAS Tile and Liquid Argon calorimeters with the real commissioning data. The latter half of this thesis described the search strategies for the Large Extra Dimensions with monojet signature and R-parity conserving Supersymmetry with “multi-jet + E_T^{miss} ” signature under realistic conditions of early data analysis.

The commissioning of the ATLAS Tile and Liquid Argon Calorimeters were performed with the cosmic data recorded from October 2007 to the Fall of 2008.

The electronic noise was measured in-situ with the random stream data for the first time, in 2008. Liquid Argon calorimeters showed consistency with the expectation, whereas the TileCal showed η -dependent noise and non-Gaussian feature which were not expected and were not treated in the previous reconstruction algorithms. The strategy to cope with such noise feature was developed in order to achieve good energy and E_T^{miss} resolution, and meet the expected performance.

With cosmic ray data, the energy deposits in the calorimeters were investigated. High energy events were observed even after removing the effects from the identified hot channels. TeV-energy deposits in the calorimeters were observed at the rate of a few events per hour. Cosmic Monte Carlo simulation was used to investigate the cause of such high energy events. The energy distribution was well described by the cosmic Monte Carlo simulation, and the origin of the high energy events was confirmed as mostly coming from the bremsstrahlung of the cosmic muons.

The effects of cosmic muons on physics measurements were investigated. High energy deposits in the calorimeters from non-collision sources often originate fake “jets” and E_T^{miss} , and will become background to almost all physics measurements using calorime-

ter information. The strategies to remove or reject such background were proposed by introducing so called the “cleaning cuts” by discriminant variables such as the jet EM fraction, the number of associated tracks to jets, and number of clusters in jets. For pure cosmic events, those variables reject more than 90 % of the cosmic background, still keeping high efficiency (more than 90 %) for real collision signals.

The strategies were further validated with the “event-overlay” technique. It was confirmed that the proposed cleaning techniques were valid even under the condition when the cosmic particles overlap the collision event such as the minimum bias or the QCD dijet events.

Finally, strategies to perform model-independent searches with jets and E_T^{miss} were considered using Monte Carlo simulations.

Strategies with monojet signatures were considered. The expected rate of such non-collision backgrounds was investigated for the collision data taking conditions, and their contributions in various event topologies were estimated. In monojet topology, a signal from the Large Extra Dimension model was used as a benchmark. Without any cleaning cuts, cosmic background is far greater than any other background or signals, but with the use of cleaning cuts, its contribution becomes under control. The effect of cosmic ray overlapping large cross section events such as minimum bias or QCD dijet events is not significant in dijet or multi-jet event topology, but air shower events can still contribute as a background. However, even those events can be rejected by the proposed cleaning cuts.

Searches with multi-jet plus E_T^{miss} signatures were considered for R-parity conserving SUSY models. Data-driven methods to estimate the Standard Model background were proposed and their performance and uncertainty were investigated. We found that signal significance is much degraded in realistic conditions, but even under such cases, some regions of SUSY parameters can be reached by the use of data-driven methods with the integrated luminosity of 200 pb^{-1} .

Appendix A

Contributions in ATLAS Publications and Presentations

All the items are shown from the latest to the oldest except for A.3.4 (from the oldest to the latest for each research topic).

A.1 Publications

A.1.1 Articles

1. ATLAS Collaboration, “*Readiness of the ATLAS Liquid Argon Calorimeter for LHC Collisions*,” submitted to EPJC.
2. ATLAS Collaboration, “*The ATLAS Experiment at the CERN Large Hadron Collider*”, JINST 3 S08003, 2008
3. ATLAS Collaboration, “*Expected Performance of the ATLAS Experiment Detector, Trigger and Physics*,” CERN-OPEN-2008-020, 2008, arXiv:0901.0512
(important contributions in “Jets and Missing Transverse Energy” and “Supersymmetry” chapters)

A.1.2 ATLAS Note

1. H. Okawa et al., “*Calorimeter Commissioning With Cosmic Rays: Cells, Clusters, Jets and Missing E_T* ,” ATLAS Note, ATL-COM-CAL-2008-007, 2008

A.1.3 Proceedings

1. H. Okawa on behalf of the ATLAS Tile Calorimeter Group, “*Commissioning of the ATLAS Tile Calorimeter with Cosmic Ray & Single Beam Data*”, IEEE Nuclear Science Symposium Conference Record, p.3394, 2008

2. H. Okawa et al., “*Calorimeter Commissioning of the ATLAS Detector with Cosmic Ray Data*,” Proceedings of Physical Society of Japan (JPS) Meeting, Vol. 63, 1-1, p.30 (2008) (in Japanese)
3. H. Okawa et al., “*Studies of Validation Method of Missing E_T using Real Data with the ATLAS Detector*,” Proceedings of Physical Society of Japan (JPS) Meeting, Vol. 62, 2-1, p.28 (2007) (in Japanese)
4. H. Okawa et al., “*Estimation of Background to Supersymmetric Events at the ATLAS Experiment*,” Proceedings of Physical Society of Japan (JPS) Meeting, Vol. 62, 1-1, p.21 (2007) (in Japanese)
5. H. Okawa, “*Supersymmetric Particle Search with the ATLAS Detector at the LHC*”, Abstract Collection of 2nd COE RA Young Researcher Exchange Symposium, the University of Tokyo, 21 Century COE QUESTS, p.6, 2007 (in Japanese)

A.2 Public Plots

1. Noise plots in the Approved Tile Calorimeter Plots webpage.
<https://twiki.cern.ch/twiki/bin/view/Atlas/ApprovedPlotsTile>
2. Jet/Etmiss plots from the cosmic ray runs. All the plots in
<https://twiki.cern.ch/twiki/bin/view/Atlas/ApprovedCosmicPlotsJetEtMiss>

A.3 Presentations

A.3.1 International Conference Presentations

1. H. Okawa on behalf of the ATLAS Collaboration, “*Determination of background from W/Z and top. What do we need to find SUSY*” LHC and Dark Matter Workshop, Ann Arbor, USA, Jan. 6-10, 2009
2. H. Okawa on behalf of the ATLAS Collaboration, “*Commissioning of the ATLAS Tile Calorimeter with Cosmic Ray & Single Beam Data*”, IEEE Nuclear Science Symposium, October 24, 2008 the International Congress Center Dresden, Dresden, Germany

A.3.2 ATLAS Workshop Presentations

1. H. Okawa, “*Jets & Missing E_T Quality Studies with Cosmic Ray & Single Beam Data*,” ATLAS Performance and Physics Workshop - Jet/Missing E_T Performance Session, CERN, Switzerland, Nov. 5, 2008
2. H. Okawa et al., “*Jets & Missing E_T in Cosmic Ray and Single Beam Data*,” ATLAS Performance and Physics Workshop - Supersymmetry Working Group Session, CERN, Switzerland, Oct. 3, 2008

3. H. Okawa et al., “*Jets & Missing E_T Studies with Cosmic Ray & Single Beam Data*,” ATLAS Jet/EtMiss Reconstruction Performance Workshop, CERN, Switzerland, Sep. 26, 2008
4. H. Okawa, “*Calorimeter Commissioning with Cosmic Rays Cells, Cluster, Jets & Missing E_T ,*” ATLAS Performance and Physics Workshop - Jet/Missing E_T Performance Session, CERN, Switzerland, Aug. 26, 2008
5. H. Okawa, “*Topocluster Performance Studies in M5 Runs*”, ATLAS Hadronic Calibration Workshop, March 15, 2008 Double Tree Hotel, Tucson, USA
6. H. Okawa et al., “*Missing E_T in Early Data*”, ATLAS Hadronic Calibration Workshop, March 15, 2008 Double Tree Hotel, Tucson, USA
7. H. Okawa (presented by the convenors), “*Calorimeter Noise Measurement & Topocluster Performance*,” ATLAS Hadronic Calibration Workshop, June 24, 2009 Lisbon, Portugal
8. H. Okawa (presented by the convenors), “*Commissioning of Jet/ E_T^{miss} with Cosmic Data & Their Clean-up*,” ATLAS Hadronic Calibration Workshop, June 26, 2009 Lisbon, Portugal

A.3.3 National Meetings and Symposiums

1. H. Okawa et al., “*Calorimeter Commissioning of the ATLAS Detector with Cosmic Ray Data*,” Physical Society of Japan (JPS) Meeting, Kinki University, Osaka, Japan, Mar. 26, 2008
2. H. Okawa et al., “*Studies of Validation Method of Missing E_T using Real Data with the ATLAS Detector*,” Physical Society of Japan (JPS) Meeting, Hokkaido University, Sapporo, Japan, Sep. 24, 2007
3. H. Okawa et al., “*Estimation of Background to Supersymmetric Events at the ATLAS Experiment*,” Physical Society of Japan (JPS) Meeting, Tokyo Metropolitan University, Hachioji, Japan, Mar. 27, 2007.
4. H. Okawa, “*Supersymmetric Particle Search with the ATLAS Detector at the LHC*”, 2nd COE RA Young Researcher Exchange Symposium, the University of Tokyo, Tokyo, Japan, Nov. 6, 2006 (both oral and poster presentations)

A.3.4 ATLAS Internal Presentations

Standard Model Background Studies for Supersymmetric Particle Search

1. H. Okawa et al., “ *$Z \rightarrow \nu\nu$ BG Estimations using Real Data*”, ATLAS Trigger and Physics Week SUSY Working Group Meeting, May 31, 2006

2. H. Okawa et al., “ $Z \rightarrow \nu\nu$ BG Estimations with Data (Full Simulation Studies)”, ATLAS SUSY Working Group Meeting, July 20, 2006
3. H. Okawa et al., “Uncertainties of the Current Estimations of $Z \rightarrow \nu\nu$ BG”, ATLAS SUSY Working Group Meeting, September 13, 2006
4. H. Okawa et al., “No Lepton Mode BG Estimations with Data”, ATLAS Week SUSY Working Group Meeting, October 4, 2006
5. H. Okawa et al., “ $Z \rightarrow ll$ Systematic Errors”, ATLAS SUSY Working Group Phone Meeting, October 25, 2006
6. H. Okawa et al., “BG Estimation in No Lepton Mode & Dilepton Mode”, ATLAS Trigger and Physics Week SUSY Working Group Meeting, November 1, 2006
7. H. Okawa et al., “Estimation of Z/W BG in No Lepton Mode”, ATLAS SUSY Working Group Meeting, January 17, 2007
8. H. Okawa et al., “Summary of Comparison on Dilepton Mode”, ATLAS SUSY Working Group CSC 1 & 2 Meeting, March 7, 2007
9. H. Okawa et al., “MC Method for No Lepton Mode BG & Summary on Dilepton Mode Studies”, ATLAS Trigger and Physics Week, March 21, 2007

Missing E_T Studies with Minimum Bias and W Events

10. H. Okawa et al., “Missing E_T Commissioning using W Events (Template Method)”, ATLAS JetEtMiss Working Group Phone Conference, July 25, 2007
11. H. Okawa et al., “Etmisc CSC note meeting”, ATLAS JetEtMiss Working Group Etmisc CSC Note Meeting, August 29, 2007
12. H. Okawa et al., “Missing E_T Commissioning using the Minimum Bias”, ATLAS Minimum Bias Working Group Meeting, September 10, 2007
13. H. Okawa et al., “Missing E_T Performance Studies using W Template Method”, ATLAS Trigger and Physics Week - JetEtMiss Working Group Meeting, November 7, 2007
14. H. Okawa et al., “Missing E_T Performance Studies using W (Template Method)”, ATLAS JetEtMiss Working Group Phone Conference, December 12, 2007

Calorimeter Commissioning with Cosmic and Single Beam Data

15. H. Okawa, “Topocluster Performance Studies in M5 Run”, ATLAS Tilecal Performance Meeting, Jan. 21, 2008

16. H. Okawa, “*Topocluster Performance Studies in the Barrel with M5 Runs*”, ATLAS LAr Detector + Cosmic Analysis Meeting, Jan. 24, 2008
17. H. Okawa, “*Topocluster Performance Studies in M5 Runs*”, ATLAS Tile Week - Data Preparation, Feb. 6, 2008
18. H. Okawa, “*PMT, Cell Energy Distributions and Topocluster Performance in M5 Runs*”, ATLAS Tilecal Performance Meeting, Mar. 10, 2008
19. H. Okawa (presented by A. Gibson), “*Topocluster Performance Studies with M5 runs*”, ATLAS LAr Detector + Cosmic Analysis Meeting, Mar. 13, 2008
20. H. Okawa, “*PMT Energy Distributions & Noise in M5 runs*”, ATLAS Tilecal Performance Meeting, Apr. 14, 2008
21. H. Okawa, “*Topocluster performance studies with cosmic runs*”, ATLAS LAr Week, Apr. 16, 2008
22. H. Okawa, “*Bad channel search and mysteries of Topoclusters at M7 runs*”, ATLAS Tilecal Performance Meeting, Jun. 9, 2008
23. H. Okawa, “*Topoclusters at M7 Runs*”, ATLAS LAr Weekly Meeting, Jun. 17, 2008
24. H. Okawa, “*Topoclusters at M7 Runs*”, ATLAS LAr Weekly Meeting, Jun. 24, 2008
25. H. Okawa, “*Calorimeter Commissioning with Cosmic Ray Data & towards the First Collision*”, Minimum Bias Meeting, Aug. 4, 2008
26. H. Okawa, “*Preview of TileCal Talks*”, ATLAS Tilecal Performance Meeting, Oct. 13, 2008
27. H. Okawa, “*TileCal noise in recent cosmic runs*”, TileCal Calibration Performance and Tools Meeting, Jan. 12, 2009
28. H. Okawa, “*Electronics Noise*”, TileCal Calibration Performance and Tools Meeting, Feb. 6, 2009
29. H. Okawa, “*Topoclusters and effects of non-Gaussian noise*”, TileCal Data Quality, Performance and Processing Meeting, Mar. 16, 2009
30. H. Okawa, “*Noise Stability of TileCal in Fall’08 Reprocessed Data*”, TileCal Calibration Performance and Tools Meeting, July 27, 2009
31. H. Okawa, “*LAr Pedestal & Noise Stability in Fall’08 Reprocessed Data*”, LAr Weekly Meeting, Oct. 13, 2009

Investigations of Rejecting non-Collision BG in Jets and Missing E_T

32. H. Okawa, “*Jet Performance Studies with M5 data,*” Jet/EtMiss Phone Conference, Apr. 30, 2008
33. H. Okawa, “*Jets from Calorimeter Noise, Bad Channels and Cosmics,*” Jet/EtMiss Phone Conference, Jun. 25, 2008
34. H. Okawa, “*Noise and Jet studies with M7 data,*” TileCal Week, Jul. 3, 2008
35. H. Okawa, “*Calorimeter Commissioning, Fake Jets & Etmiss Studies with Cosmic Ray Data,*” SUSY Working Group Meeting, Sep. 11, 2008
36. H. Okawa, “*Jets and Missing E_T from cosmic and single beam data,*” ATLAS Week, Jet/Etmiss performance meeting, Dec. 2, 2008
37. H. Okawa, “*Jets and Missing E_T in Cosmic and Single Beam Data,*” TileCal Week Performance Session, Dec. 9, 2008
38. H. Okawa, “*Cosmic Ray Analysis: Technical Note,*” Jet/EtMiss Data Preparation Task Force Meeting, Jan. 20, 2009
39. H. Okawa, “*Jet & MET studies with Event Overlay,*” Jet/EtMiss Data Preparation Task Force Meeting, Feb. 18, 2009
40. H. Okawa, “*Jet/Etmiss studies on cosmics data,*” ATLAS Week Combined Performance Session, Feb. 19, 2009
41. H. Okawa, “*Preliminary Results from High Energetic Cosmic Rays in the ATLAS Calorimeter,*” Clustered Physics/Performance Meetings - Plenary analysis session, Mar. 26, 2009
42. H. Okawa, “*Simulation for jet/etmiss studies,*” Cosmic simulation production meeting, Apr. 1, 2009
43. H. Okawa, “*Track & Jet Association in Cosmic Events,*” Inner Detector Software And Performance Weekly Meeting, Apr. 24, 2009
44. H. Okawa, “*Investigations on Track & Jet Association for BG Rejection,*” Clustered Physics/Performance Meetings - Jet/EtMiss Data Preparation Task Force Session, Apr. 27, 2009
45. H. Okawa, “*Background from cosmics in monojet & multi-jet+MET search,*” Clustered Physics/Performance Meetings - SUSY Working Group Meeting, Apr. 29, 2009

Monojet Signature from Large Extra Dimensions

46. H. Okawa, “*Sherpa MC for ADD KK-Graviton & Cosmic BG in Monojet Search,*” TeV-scale Gravity Meeting, Aug. 14, 2009

Appendix B

Optimal Filtering Method

The Optimal Filtering Coefficients (OFC's) are derived as follows [76][80].

First of all, we define the shape of the signal as a function of time $S(t)$, which can be expressed as

$$S(t) = Ag(t). \quad (\text{B.1})$$

Here, A is the amplitude and $g(t)$ is the normalized shape form function. Since the signal is digitized, the ADC-value in each sampling can be described as

$$S_i = Ag(t_i - \tau) + n_i, \quad (\text{B.2})$$

where i corresponds to the “ i ”-th sampling, τ is the phase difference between the digitizer output, and n_i is the noise fluctuation from the average pedestal. Assuming that the phase shift τ is small, (B.2) can be rewritten by Taylor's expansion,

$$S_i \simeq Ag(t_i) - A\tau g'(t_i) + n_i. \quad (\text{B.3})$$

Now, we define two variables u, v ,

$$u = \sum_{i=1}^{N_{\text{sample}}} a_i S_i, \quad (\text{B.4})$$

$$v = \sum_{i=1}^{N_{\text{sample}}} b_i S_i. \quad (\text{B.5})$$

Here, a_i, b_i are free parameters at this point, which will be later be used as OFC's. Then, we require the mean values of u, v to equal,

$$\langle u \rangle = A, \quad (\text{B.6})$$

$$\langle v \rangle = A\tau. \quad (\text{B.7})$$

From (B.3)-(B.7), and assuming that the average of noise fluctuation $\langle n_i \rangle$ is zero (which

is true for Gaussian noise),

$$\begin{aligned}
A &= A \sum_{i=1}^{N_{\text{sample}}} a_i g_i - A\tau \sum_{i=1}^{N_{\text{sample}}} a_i g'_i + \sum_{i=1}^{N_{\text{sample}}} a_i \langle n_i \rangle \\
&= A \sum_{i=1}^{N_{\text{sample}}} a_i g_i - A\tau \sum_{i=1}^{N_{\text{sample}}} a_i g'_i, \tag{B.8}
\end{aligned}$$

$$\begin{aligned}
A\tau &= A \sum_{i=1}^{N_{\text{sample}}} b_i g_i - A\tau \sum_{i=1}^{N_{\text{sample}}} b_i g'_i + \sum_{i=1}^{N_{\text{sample}}} b_i \langle n_i \rangle \\
&= A \sum_{i=1}^{N_{\text{sample}}} b_i g_i - A\tau \sum_{i=1}^{N_{\text{sample}}} b_i g'_i, \tag{B.9}
\end{aligned}$$

where $g(t_i)$ was written as g_i for simplicity. From (B.8) and (B.9), we require the parameters a_i and b_i to satisfy,

$$\sum_{i=1}^{N_{\text{sample}}} a_i g_i = 1, \quad \sum_{i=1}^{N_{\text{sample}}} b_i g_i = 0, \quad \sum_{i=1}^{N_{\text{sample}}} a_i g'_i = 0, \quad \sum_{i=1}^{N_{\text{sample}}} b_i g'_i = -1. \tag{B.10}$$

These set of equations are not enough to determine the OFC parameters (four equations for $2N_{\text{sample}}$ parameters).

On top of the equations above, we require that the set of a_i and b_i minimize the variances of u and v ,

$$\begin{aligned}
\text{Var}(u) &= \text{Var} \left(A \sum_{i=1}^{N_{\text{sample}}} a_i g_i - A\tau \sum_{i=1}^{N_{\text{sample}}} a_i g'_i + \sum_{i=1}^{N_{\text{sample}}} a_i n_i \right) \\
&= \text{Var} \left(\sum_{i=1}^{N_{\text{sample}}} a_i n_i \right), \tag{B.11}
\end{aligned}$$

$$\begin{aligned}
\text{Var}(v) &= \text{Var} \left(A \sum_{i=1}^{N_{\text{sample}}} b_i g_i - A\tau \sum_{i=1}^{N_{\text{sample}}} b_i g'_i + \sum_{i=1}^{N_{\text{sample}}} b_i n_i \right) \\
&= \text{Var} \left(\sum_{i=1}^{N_{\text{sample}}} b_i n_i \right), \tag{B.12}
\end{aligned}$$

and the equations are simplified as above due to the fact that a_i, b_i, g_i, g'_i are constant.

The equations can be further rewritten as,

$$\begin{aligned}
\text{Var}(u) &= \sum_{i=1}^{N_{\text{sample}}} a_i^2 \text{Var}(n_i) + \frac{2}{m} \sum_{i=1}^{N_{\text{sample}}} \sum_{j=i+1}^{N_{\text{sample}}} a_i a_j \sum_{m=1}^m (n_i - \langle n_i \rangle)(n_j - \langle n_j \rangle) \\
&= \frac{1}{m} \sum_{i,j=1}^{N_{\text{sample}}} a_i a_j \sum_{m=1}^m (n_i - \langle n_i \rangle)(n_j - \langle n_j \rangle) \\
&= \frac{1}{m} \sum_{i,j=1}^{N_{\text{sample}}} a_i a_j \sum_{m=1}^m (n_i n_j) \quad (\because \langle n_i \rangle = 0) \\
&= \sum_{i,j=1}^{N_{\text{sample}}} a_i a_j \langle n_i n_j \rangle, \tag{B.13}
\end{aligned}$$

$$\text{Var}(v) = \sum_{i,j=1}^{N_{\text{sample}}} b_i b_j \langle n_i n_j \rangle. \tag{B.14}$$

In order to determine a_i, b_i that satisfy (B.10) and minimize (B.13) and (B.14), we use the method of Lagrange multipliers,

$$\begin{aligned}
F_u(a_1, \dots, a_{N_{\text{sample}}}, \lambda, \kappa) \\
&= \sum_{i,j=1}^{N_{\text{sample}}} a_i a_j \langle n_i n_j \rangle - \lambda \left(\sum_{i=1}^{N_{\text{sample}}} a_i g_i - 1 \right) - \kappa \left(\sum_{i=1}^{N_{\text{sample}}} a_i g'_i \right), \tag{B.15}
\end{aligned}$$

$$\begin{aligned}
F_v(b_1, \dots, b_{N_{\text{sample}}}, \mu, \rho) \\
&= \sum_{i,j=1}^{N_{\text{sample}}} b_i b_j \langle n_i n_j \rangle - \mu \left(\sum_{i=1}^{N_{\text{sample}}} b_i g_i \right) - \rho \left(\sum_{i=1}^{N_{\text{sample}}} b_i g'_i + 1 \right). \tag{B.16}
\end{aligned}$$

Here, $\lambda, \kappa, \mu, \rho$ are the Lagrange multipliers. To derive the equations to determine the parameters, we require the partial derivatives of F_u and F_v to equal zero,

$$\begin{aligned}
\frac{\partial F_u}{\partial a_i} &= 2 \sum_{j=1}^{N_{\text{sample}}} a_j \langle n_i n_j \rangle - \lambda g_i - \kappa g'_i \\
&= \sum_{j=1}^{N_{\text{sample}}} a_j R_{ij} - \lambda g_i - \kappa g'_i = 0 \quad (\because R_{ij} \equiv 2 \langle n_i n_j \rangle) \tag{B.17}
\end{aligned}$$

$$\frac{\partial F_v}{\partial b_i} = \sum_{j=1}^{N_{\text{sample}}} b_j R_{ij} - \mu g_i - \rho g'_i = 0. \tag{B.18}$$

Thus, we obtain $N_{\text{sample}}+2$ equations, for $a_i (i = 1, \dots, N_{\text{sample}})$ and two Lagrange multi-

pliers,

$$\begin{pmatrix} R_{11} & \cdots & R_{1,N_{\text{sample}}} & g_1 & g'_1 \\ \vdots & \ddots & \vdots & \vdots & \vdots \\ R_{N_{\text{sample}},1} & \cdots & R_{N_{\text{sample}},N_{\text{sample}}} & g_{N_{\text{sample}}} & g'_{N_{\text{sample}}} \\ g_1 & \cdots & g_{N_{\text{sample}}} & 0 & 0 \\ g'_1 & \cdots & g'_{N_{\text{sample}}} & 0 & 0 \end{pmatrix} \begin{pmatrix} a_1 \\ \vdots \\ a_{N_{\text{sample}}} \\ \lambda \\ \kappa \end{pmatrix} = \begin{pmatrix} 0 \\ \vdots \\ 0 \\ 1 \\ 0 \end{pmatrix} \quad (\text{B.19})$$

which can be solved to have unique solutions. In the same way, b_i can be derived,

$$\begin{pmatrix} R_{11} & \cdots & R_{1,N_{\text{sample}}} & g_1 & g'_1 \\ \vdots & \ddots & \vdots & \vdots & \vdots \\ R_{N_{\text{sample}},1} & \cdots & R_{N_{\text{sample}},N_{\text{sample}}} & g_{N_{\text{sample}}} & g'_{N_{\text{sample}}} \\ g_1 & \cdots & g_{N_{\text{sample}}} & 0 & 0 \\ g'_1 & \cdots & g'_{N_{\text{sample}}} & 0 & 0 \end{pmatrix} \begin{pmatrix} b_1 \\ \vdots \\ b_{N_{\text{sample}}} \\ \mu \\ \rho \end{pmatrix} = \begin{pmatrix} 0 \\ \vdots \\ 0 \\ 0 \\ -1 \end{pmatrix}. \quad (\text{B.20})$$

As described above, all the components in the matrix (noise correlations, function and its derivative of pulse shape) are determined beforehand in dedicated calibration runs, and allow to determine the Optimal Filtering Coefficients.

Appendix C

Missing E_T Algorithm in ATLAS

Calorimeter Term in E_T^{miss}

The x and y components of the calorimeter term are calculated from the vector sum of energy in each cell.

$$E_{x,y}^{\text{miss,Calo}} = - \sum_{\text{cell}} E_{x,y}^{\text{cell}} \quad (\text{C.1})$$

$$E_x^{\text{cell}} = E^{\text{cell}} \sin \theta \cos \phi \quad (\text{C.2})$$

$$E_y^{\text{cell}} = E^{\text{cell}} \sin \theta \sin \phi \quad (\text{C.3})$$

The angular directions of cells are defined from the central position of the cell. Eight categories exist in the ATLAS framework for the calorimeter term. Four of them are at the EM-scale, and the others are calibrated to the hadronic scale with H1-style or the Local Hadronic Calibration scheme [23]. Random stream data offers a useful training ground to validate the calorimeter term of the E_T^{miss} , and will be mentioned in the next section.

Muon Term in E_T^{miss}

The muon term exploits the information of muon tracks up to the pseudorapidity (η) of 2.7.

$$E_{x,y}^{\text{miss, muon}} = - \sum_{\text{muon}} E_{x,y}^{\text{muon}} \quad (\text{C.4})$$

When $|\eta| < 2.5$, muon tracks with good quality and matching between the Muon Spectrometer and the inner detector are considered. In the region of $2.5 < |\eta| < 2.7$, the muon tracks are solely reconstructed by the Muon Spectrometer, because the region is outside the fiducial volume of the Inner Detector.

Cryostat Term in E_T^{miss}

Cryostat is located between the LAr barrel EM calorimeter and the Tile barrel calorimeter. Its thickness is about half an interaction length. The cryostat term in E_T^{miss} recovers the energy lost in the cryostat by using the correlation of energy between the last layer

of the EM calorimeter and the first layer of the hadronic calorimeter. A similar strategy is used in the end-cap region. The x and y components of E_T^{miss} is defined as follows.

$$E_{x,y}^{\text{miss,Cryo}} = - \sum_{\text{jet}} E_{\text{jet}, x,y}^{\text{Cryo}} \quad (\text{C.5})$$

$$E_{\text{jet}, x,y}^{\text{Cryo}} = w^{\text{Cryo}} \sqrt{E_{\text{jet}, x,y}^{\text{EM3}} \times E_{\text{jet}, x,y}^{\text{Had1}}} \quad (\text{C.6})$$

The cryostat term is calculated from all the reconstructed jets in the event. In (C.6), w^{Cryo} is a calibration weight, $E_{\text{jet}}^{\text{EM3}}$ is the energy of the jet in the third layer of the EM calorimeter, and $E_{\text{jet}}^{\text{Had1}}$ is the energy of the jet in the first layer of the hadronic calorimeter. Two categories exist with regards to the type of jets used. Cone4H1TowerJets are reconstructed with the ATLAS-Cone algorithm with the cone size of 0.4, and the combined towers are used as inputs. Cone4H1TopoJets are the same as Cone4H1TowerJets except that the Topoclusters are used as inputs instead of the towers.

Refined Calibration of E_T^{miss}

Physics analyses will use E_T^{miss} variables with so called the “refined calibration.” The refinement of the calibration of calorimeter cells is done when those cells are associated to high p_T objects. Calorimeter cells are associated with reconstructed high p_T objects in the following order: electrons, photons, muons, hadronically decaying τ leptons, b-jets and light flavor jets. Refined calibration of each object is applied and replace the initial calibration constant of the cells.

Table C.1: E_T^{miss} quantities in ATLAS

| Component | Category | Definition |
|-----------|---------------------|---|
| Calo | MET_Base | E_T^{miss} from all calorimeter cells above 2σ from the noise. Energy is at the EM scale. |
| Calo | MET_Base0 | E_T^{miss} from all calorimeter cells without any threshold. Energy is at the EM scale. |
| Calo | MET_Topo | E_T^{miss} from all calorimeter cells belonging to the Topoclusters. Energy is at the EM scale. |
| Calo | MET_TopoObj | E_T^{miss} from the Topoclusters. Energy is at the EM scale. |
| Calo | MET_Calib | E_T^{miss} from all calorimeter cells above 2σ from the noise. Energy is calibrated with the H1-style. |
| Calo | MET_CorrTopo | E_T^{miss} from all calorimeter cells belonging to the Topoclusters. Energy is calibrated with the H1-style. |
| Calo | MET_LocHadTopo | E_T^{miss} from all calorimeter cells belonging to the Topoclusters. Energy is calibrated with the Local Hadronic Calibration style. |
| Calo | MET_LocHadTopoObj | E_T^{miss} from the Topoclusters. Energy is calibrated with the Local Hadronic Calibration style. |
| Muon | MET_Muon | E_T^{miss} from all the STACO-algorithm muons. Muon Spectrometer tracks used. |
| Muon | MET_MuonBoy_Track | E_T^{miss} from all the isolated STACO muons and muons in gaps. ID and Muon Spectrometer combined tracks used. |
| Muon | MET_MuonBoy_Spectro | E_T^{miss} from all the non-isolated STACO muons Muon Spectrometer tracks used. |
| Muon | MET_MuonBoy | MET_MuonBoy_Track + MET_MuonBoy_Spectro |
| Cryostat | MET_Cryo | Cryostat term calculated from Cone4H1TopoJets |
| Cryostat | MET_CryoCone | Cryostat term calculated from Cone4H1TowerJets |
| Refined | MET_RefEle | E_T from calorimeter cells inside electrons |
| Refined | MET_RefGamma | E_T from calorimeter cells inside photons |
| Refined | MET_RefTau | E_T from calorimeter cells inside taus |
| Refined | MET_RefJet | E_T from calorimeter cells inside jets |
| Refined | MET_RefMuon | E_T from calorimeter cells belonging to non-isolated muons |
| Refined | MET_RefMuon_Track | E_T from calorimeter cells belonging to isolated muons. |
| Refined | MET_CellOut | E_T from calorimeter cells in Topoclusters not belonging to any reconstructed objects |
| All | MET_Final | MET_CorrTopo + MET_Muon + MET_Cryo |
| All | MET_RefFinal | E_T^{miss} for physics analyses. Sum of all Ref categories + MET_MuonBoy + MET_Cryo |

Appendix D

Functions in KK-Graviton Processes

Functions used in Section 11.1.1 are explicitly described [142].

$$F_1(x, y) = \frac{1}{x(y-x-1)} [-4x(1+x)(1+2x+2x^2) + y(1+6x+18x^2+16x^3) - 6y^2x(1+2x) + y^3(1+4x)] , \quad (\text{D.1})$$

$$F_2(x, y) = -(y-x-1)F_1\left(\frac{x}{y-x-1}, \frac{y}{y-x-1}\right) \\ = \frac{1}{x(y-x-1)} [-4x(1+x^2) + y(1+x)(1+8x+x^2) - 3y^2(1+4x+x^2) + 4y^3(1+x) - 2y^4] , \quad (\text{D.2})$$

$$F_3(x, y) = \frac{1}{x(y-x-1)} [1+2x+3x^2+2x^3+x^4 - 2y(1+x^3) + 3y^2(1+x^2) - 2y^3(1+x) + y^4] . \quad (\text{D.3})$$

Appendix E

Monte Carlo Simulation Samples Used

E.1 Samples for Monojet Studies

Table E.1: Cross section and profile of Standard Model samples.

| MC Sample | Generator | xsec [nb] | Generation Cut |
|---|---------------|-----------|--|
| $Z(\rightarrow \nu\bar{\nu}) + \text{jets}$ | Pythia | 3.48 | parton $p_T > 10$ GeV |
| $Z(\rightarrow e^+e^-) + \text{jets}$ | Pythia | 0.610 | $M_{e^+e^-} > 60$ GeV, parton $p_T > 10$ GeV |
| $Z(\rightarrow \mu^+\mu^-) + \text{jets}$ | Pythia | 0.610 | $M_{\mu^+\mu^-} > 60$ GeV, parton $p_T > 10$ GeV |
| $Z(\rightarrow \tau^+\tau^-) + \text{jets}$ | Pythia | 0.604 | $M_{\tau^+\tau^-} > 60$ GeV, parton $p_T > 10$ GeV |
| $W(\rightarrow \tau\nu_\tau) + \text{jets}$ | Pythia | 5.97 | parton $p_T > 10$ GeV |
| $W(\rightarrow \mu\nu_\mu) + \text{jets}$ | Pythia | 5.97 | parton $p_T > 10$ GeV |
| $W(\rightarrow e\nu_e) + \text{jets}$ | Pythia | 5.97 | parton $p_T > 10$ GeV |
| $t\bar{t}$ | MC@NLO | 0.203 | not all hadronic decay |
| Single Top (t-chan) | AcerMC+Herwig | 0.0411 | |
| Single Top (Wt) | AcerMC+Herwig | 0.0144 | |
| QCD dijet (J1) | Pythia | 8.59e5 | $17 \text{ GeV} < \text{1st parton } p_T < 35 \text{ GeV}$ |
| QCD dijet (J2) | Pythia | 5.62e4 | $35 \text{ GeV} < p_T < 70 \text{ GeV}$ |
| QCD dijet (J3) | Pythia | 3241.6 | $70 \text{ GeV} < p_T < 140 \text{ GeV}$ |
| QCD dijet (J4) | Pythia | 150.9 | $140 \text{ GeV} < p_T < 280 \text{ GeV}$ |
| QCD dijet (J5) | Pythia | 5.18 | $280 \text{ GeV} < p_T < 560 \text{ GeV}$ |
| QCD dijet (J6) | Pythia | 0.112 | $560 \text{ GeV} < p_T < 1120 \text{ GeV}$ |
| QCD dijet (J7) | Pythia | 1.07e-3 | $1120 \text{ GeV} < p_T < 2280 \text{ GeV}$ |
| QCD dijet (J8) | Pythia | 1.11e-6 | $p_T > 2280 \text{ GeV}$ |

E.2 Samples for Multi-jet Studies

Table E.2: Cross section and profile of Monte Carlo samples for Z events.

| MC Sample | Generator | xsec [pb] | Generation Cut |
|---|--------------|-----------|---------------------------|
| $Z(\rightarrow \nu\bar{\nu}) + 0$ parton | ALPGEN+JIMMY | 52.54 | 1 jet with $p_T > 30$ GeV |
| $Z(\rightarrow \nu\bar{\nu}) + 1$ parton | ALPGEN+JIMMY | 587.57 | 1 jet with $p_T > 30$ GeV |
| $Z(\rightarrow \nu\bar{\nu}) + 2$ partons | ALPGEN+JIMMY | 326.74 | 1 jet with $p_T > 30$ GeV |
| $Z(\rightarrow \nu\bar{\nu}) + 3$ partons | ALPGEN+JIMMY | 112.53 | 1 jet with $p_T > 30$ GeV |
| $Z(\rightarrow \nu\bar{\nu}) + 4$ partons | ALPGEN+JIMMY | 32.98 | 1 jet with $p_T > 30$ GeV |
| $Z(\rightarrow \nu\bar{\nu}) + 5$ partons | ALPGEN+JIMMY | 9.50 | 1 jet with $p_T > 30$ GeV |
| $Z(\rightarrow e^+e^-) + 0$ parton | ALPGEN+JIMMY | 898.18 | No filter |
| $Z(\rightarrow e^+e^-) + 1$ parton | ALPGEN+JIMMY | 206.57 | No filter |
| $Z(\rightarrow e^+e^-) + 2$ partons | ALPGEN+JIMMY | 72.50 | No filter |
| $Z(\rightarrow e^+e^-) + 3$ partons | ALPGEN+JIMMY | 21.08 | No filter |
| $Z(\rightarrow e^+e^-) + 4$ partons | ALPGEN+JIMMY | 6.00 | No filter |
| $Z(\rightarrow e^+e^-) + 5$ partons | ALPGEN+JIMMY | 1.73 | No filter |
| $Z(\rightarrow \mu^+\mu^-) + 0$ parton | ALPGEN+JIMMY | 900.21 | No filter |
| $Z(\rightarrow \mu^+\mu^-) + 1$ parton | ALPGEN+JIMMY | 205.21 | No filter |
| $Z(\rightarrow \mu^+\mu^-) + 2$ partons | ALPGEN+JIMMY | 69.35 | No filter |
| $Z(\rightarrow \mu^+\mu^-) + 3$ partons | ALPGEN+JIMMY | 21.63 | No filter |
| $Z(\rightarrow \mu^+\mu^-) + 4$ partons | ALPGEN+JIMMY | 6.08 | No filter |
| $Z(\rightarrow \mu^+\mu^-) + 5$ partons | ALPGEN+JIMMY | 1.70 | No filter |
| $Z(\rightarrow \tau^+\tau^-) + 0$ parton | ALPGEN+JIMMY | 902.71 | No filter |
| $Z(\rightarrow \tau^+\tau^-) + 1$ parton | ALPGEN+JIMMY | 209.26 | No filter |
| $Z(\rightarrow \tau^+\tau^-) + 2$ partons | ALPGEN+JIMMY | 70.16 | No filter |
| $Z(\rightarrow \tau^+\tau^-) + 3$ partons | ALPGEN+JIMMY | 21.07 | No filter |
| $Z(\rightarrow \tau^+\tau^-) + 4$ partons | ALPGEN+JIMMY | 6.04 | No filter |
| $Z(\rightarrow \tau^+\tau^-) + 5$ partons | ALPGEN+JIMMY | 1.71 | No filter |

Table E.3: Cross section and profile of Monte Carlo samples for Z events.

| MC Sample | Generator | xsec [pb] | Generation Cut |
|--|--------------|-----------|----------------|
| $W(\rightarrow e\nu_e)+ 0$ parton | ALPGEN+JIMMY | 10184.7 | No filter |
| $W(\rightarrow e\nu_e)+ 1$ parton | ALPGEN+JIMMY | 2112.4 | No filter |
| $W(\rightarrow e\nu_e)+ 2$ partons | ALPGEN+JIMMY | 676.0 | No filter |
| $W(\rightarrow e\nu_e)+ 3$ partons | ALPGEN+JIMMY | 203.3 | No filter |
| $W(\rightarrow e\nu_e)+ 4$ partons | ALPGEN+JIMMY | 56.1 | No filter |
| $W(\rightarrow e\nu_e)+ 5$ partons | ALPGEN+JIMMY | 16.6 | No filter |
| $W(\rightarrow \mu\nu_\mu)+ 0$ parton | ALPGEN+JIMMY | 10125.7 | No filter |
| $W(\rightarrow \mu\nu_\mu)+ 1$ parton | ALPGEN+JIMMY | 2155.5 | No filter |
| $W(\rightarrow \mu\nu_\mu)+ 2$ partons | ALPGEN+JIMMY | 682.3 | No filter |
| $W(\rightarrow \mu\nu_\mu)+ 3$ partons | ALPGEN+JIMMY | 202.0 | No filter |
| $W(\rightarrow \mu\nu_\mu)+ 4$ partons | ALPGEN+JIMMY | 55.5 | No filter |
| $W(\rightarrow \mu\nu_\mu)+ 5$ partons | ALPGEN+JIMMY | 16.3 | No filter |
| $W(\rightarrow \tau\nu_\tau)+ 0$ parton | ALPGEN+JIMMY | 10178.3 | No filter |
| $W(\rightarrow \tau\nu_\tau)+ 1$ parton | ALPGEN+JIMMY | 2106.9 | No filter |
| $W(\rightarrow \tau\nu_\tau)+ 2$ partons | ALPGEN+JIMMY | 672.8 | No filter |
| $W(\rightarrow \tau\nu_\tau)+ 3$ partons | ALPGEN+JIMMY | 202.7 | No filter |
| $W(\rightarrow \tau\nu_\tau)+ 4$ partons | ALPGEN+JIMMY | 55.3 | No filter |
| $W(\rightarrow \tau\nu_\tau)+ 5$ partons | ALPGEN+JIMMY | 17.0 | No filter |

Table E.4: Cross section and profile of Monte Carlo samples for Top and QCD events.

| MC Sample | Generator | xsec [pb] | Generation Cut |
|----------------|-----------|-----------------------|--|
| $t\bar{t}$ | MC@NLO | 0.203 | not all hadronic decay |
| QCD dijet (J1) | Pythia | 8.59×10^8 | $17 \text{ GeV} < \text{leading parton } p_T < 35 \text{ GeV}$ |
| QCD dijet (J2) | Pythia | 5.62×10^7 | $35 \text{ GeV} < p_T < 70 \text{ GeV}$ |
| QCD dijet (J3) | Pythia | 3.24×10^6 | $70 \text{ GeV} < p_T < 140 \text{ GeV}$ |
| QCD dijet (J4) | Pythia | 1.51×10^5 | $140 \text{ GeV} < p_T < 280 \text{ GeV}$ |
| QCD dijet (J5) | Pythia | 5.18×10^3 | $280 \text{ GeV} < p_T < 560 \text{ GeV}$ |
| QCD dijet (J6) | Pythia | 112 | $560 \text{ GeV} < p_T < 1120 \text{ GeV}$ |
| QCD dijet (J7) | Pythia | 1.07 | $1120 \text{ GeV} < p_T < 2280 \text{ GeV}$ |
| QCD dijet (J8) | Pythia | 1.11×10^{-3} | $p_T > 2280 \text{ GeV}$ |

Appendix F

Monte Carlo-based Estimation of $Z(\rightarrow \nu\bar{\nu})$ BG for SUSY Searches

A data-driven method to estimate the $Z(\rightarrow \nu\bar{\nu})$ background in no-lepton search mode for SUSY was mentioned in Section 12.5.1.

Here, a Monte Carlo-based estimation method for $Z(\rightarrow \nu\bar{\nu})$ background is briefly mentioned [A.3.4.6] [A.3.4.7] [A.3.4.9]. The method fully relies on the shape of distributions from a $Z(\rightarrow \nu\bar{\nu})$ Monte Carlo simulation, in order to cope with the limited statistics of $Z(\rightarrow l^+l^-)$ +jets data, which leads to the main limitation of precision of the data-driven estimation method. However, in the Monte Carlo-based method, the major concern is the uncertainty of the normalization, especially when we consider multi-jet signatures. In the Monte Carlo-based estimation, the normalization should be derived from data.

The normalization factor will be extracted with the use of $Z(\rightarrow l^+l^-)$ +jets events, so the $Z(\rightarrow l^+l^-)$ +jets events also play important roles in the Monte Carlo-based method. The diagrammatical overview of this estimation scheme is shown in Figure F.1. The normalization factor extracted from $Z(\rightarrow l^+l^-)$ +jets are also applied to $Z(\rightarrow \nu\bar{\nu})$ +jets Monte Carlo samples, and the samples are used for the estimation.

The advantage of this method is that the statistical uncertainty only contributes to the uncertainty of the normalization. On the other hand, the major challenges for this method would be the validation of the Monte Carlo simulation with data and the understanding of detector performance (e.g. jet energy scale and resolution, E_T^{miss} scale and resolution).

Here, an example is shown for the case center-of-mass energy 14 TeV and 1 fb^{-1} integrated luminosity. Pseudo-data was produced with different Alpgen parameters. Here, the selection cut is slightly different to the case of $\sqrt{s}=10 \text{ TeV}$,

- No isolated electrons and muons
- At least four jets with $p_T > 50 \text{ GeV}$ and $|\eta| < 5.0$, and at least one of them with $p_T > 100 \text{ GeV}$
- Transverse sphericity > 0.2
- $E_T^{\text{miss}} > 100 \text{ GeV}$ and $E_T^{\text{miss}} / M_{eff} > 0.2$

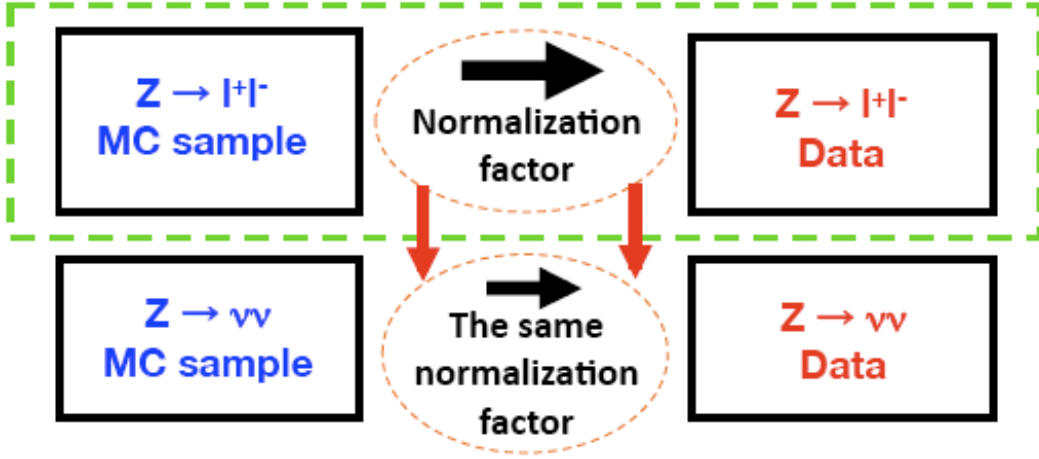


Figure F.1: Overview of quasi-data-driven estimation scheme for $Z(\rightarrow \nu\bar{\nu})$ background. The normalization factor is determined by comparing Monte Carlo and data with $Z(\rightarrow l^+l^-)$ events. The same normalization factor is applied to the $Z(\rightarrow \nu\bar{\nu})$ distributions to reproduce the data from Monte Carlo.

In order to have fully enough statistics of Monte Carlo samples, fast simulation should be used with appropriate corrections applied to recover the detector effects. Here, fast simulation samples with corrections applied to taken into account the lepton efficiency, jet reconstruction efficiency, jet energy scale, and E_T^{miss} scale were used.

The normalization factor can be determined within about 20 % (Figure F.2), and this uncertainty is the dominant source of the overall uncertainty of the estimation, since enough statistics is provided from the Monte Carlo. This factor is applied to the original Monte Carlo distributions. Figure F.3 shows the distributions of E_T^{miss} , effective mass, and the leading jet p_T for $Z(\rightarrow \nu\bar{\nu})$ background. The estimation is consistent with the pseudo-data within the statistical uncertainty.

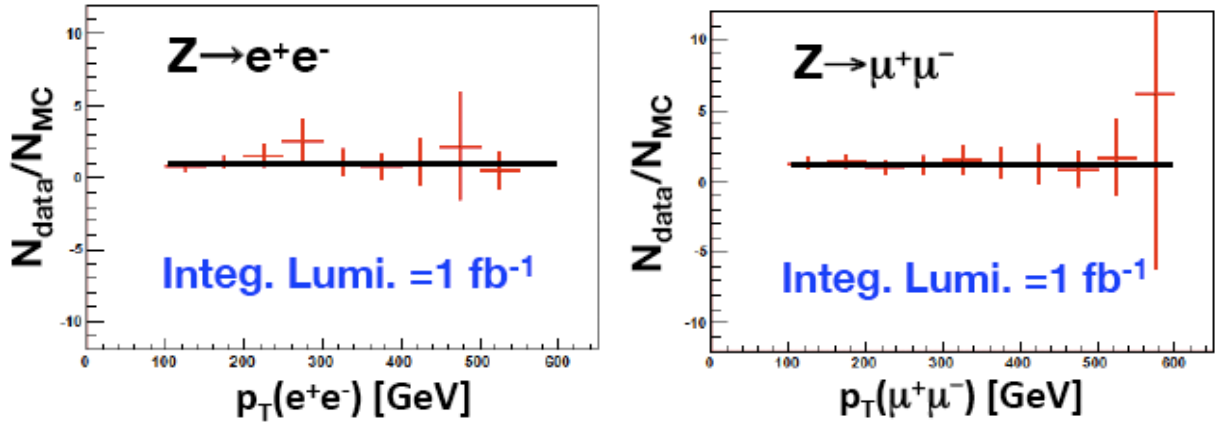


Figure F.2: Normalization factor determined by comparing Monte Carlo and pseudo-data.

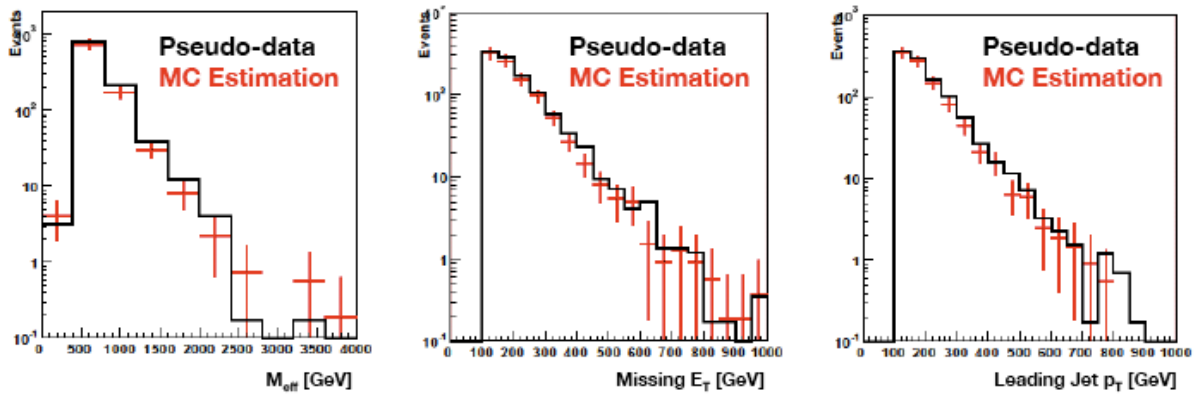


Figure F.3: Estimation of $Z(\rightarrow \nu\bar{\nu})$ background using quasi-data-driven method. Effective mass (left), E_T^{miss} (center), and leading jet p_T (right) distributions are shown.

Bibliography

- [1] H. Yukawa, “*On the Interaction of Elementary Particles. I.*,” Proc. Phys.-Math. Soc. Jpn. **17**, 48 (1935).
- [2] S. Neddermeyer and C. Anderson, “*Note on the Nature of Cosmic Ray Particles*,” Phys. Rev. **51**, 884 (1937).
- [3] J. Street and E. Stevenson, “*New evidence of the Existence of a Particle of Mass Intermediate between the Proton and Electron*,” Phys. Rev. **52**, 1002 (1937).
- [4] Y. Nambu, “*From Yukawa’s Pion to Spontaneous Symmetry Breaking*,” J. Phys. Soc. Jpn. **76**, 111002-1 (2007).
- [5] S. Tomonaga, “*On a Relativistically Invariant Formulation of the Quantum Theory of Wave Fields*,” Prog. Theor. Phys. **1** 27 (1946); Z. Koba, T. Tati, S. Tomonaga, “*On a Relativistically Invariant Formulation of the Quantum Theory of Wave Fields. II.*,” Prog. Theor. Phys. **2**, 101 (1947); Z. Koba, T. Tati, S. Tomonaga, “*On a Relativistically Invariant Formulation of the Quantum Theory of Wave Fields. III.*,” Prog. Theor. Phys. **2**, 198 (1947).
- [6] J. Schwinger, “*On Quantum-Electrodynamics and the Magnetic Moment of the Electron*,” Phys. Rev. **73**, 416 (1948); J. Schwinger, “*Quantum Electrodynamics. I. A Covariant Formulation*,” Phys. Rev. **74**, 1439 (1948).
- [7] R. Feynman, “*Relativistic Cut-Off for Quantum Electrodynamics*,” Phys. Rev. **74**, 1430 (1948).
- [8] M. Gell-Mann, “*A schematic model of baryons and mesons*,” Phys. Lett. **8**, 214 (1964); G. Zweig, “*An SU3 model for strong interaction symmetry and its breaking ; Part I*,” CERN preprint CERN-TH-401 (1964).
- [9] Y. Nambu, M.-Y. Han, “*Three-Triplet Model with Double SU(3) Symmetry*,” Phys. Rev. **139**, B1006 (1965).
- [10] E. Bloom et al., “*High-Energy Inelastic e-p Scattering at 6° and 10°*,” Phys. Rev. Lett. **23**, 930 (1969); M. Breidenbach et al., “*Observed Behavior of Highly Inelastic Electron-Proton Scattering*,” Phys. Rev. Lett. **23**, 935 (1969).
- [11] T. Eichten et al., “*Measurement of the neutrino-nucleon and antineutrino-nucleon total cross sections*,” Phys. Lett. **46B**, 274 (1973).

- [12] J. D. Bjorken, “*Asymptotic Sum Rules at Infinite Momentum*,” Phys. Rev. **179**, 1547 (1969); R. P. Feynman, “*Very High-Energy Collisions of Hadrons*,” Phys. Rev. Lett. **23**, 1415 (1969).
- [13] R. Brandelik et al., “*Evidence for planar events in e^+e^- annihilation at high energies*,” Phys. Lett. **86B**, 243 (1979); D. P. Barber et al., “*Discovery of Three-Jet Events and a Test of Quantum Chromodynamics at PETRA*,” Phys. Rev. Lett. **43**, 830 (1979); Ch. Berger et al., “*Evidence for gluon bremsstrahlung in e^+e^- annihilations at high energies*,” Phys. Lett. **86B**, 418 (1979); W. Bartel et al., “*Observation of planar three-jet events in e^+e^- annihilation and evidence for gluon bremsstrahlung*,” Phys. Lett. **91B**, 142 (1980).
- [14] C. N. Yang, R. L. Mills, “*Conservation of Isotopic Spin and Isotopic Gauge Invariance*,” Phys. Rev. **96**, 191 (1954).
- [15] D. J. Gross, F. Wilczek, “*Ultraviolet Behavior of Non-Abelian Gauge Theories*,” Phys. Rev. Lett. **30**, 1343 (1973); H. D. Polizer, “*Reliable Perturbative Results for Strong Interactions?*,” Phys. Rev. Lett. **30**, 1346 (1973).
- [16] T. Lee, C. N. Yang, “*Question of Parity Conservation in Weak Interactions*,” Phys. Rev. **104**, 254 (1956); C. S. Wu et al., “*Experimental Test of Parity Conservation in Beta Decay*,” Phys. Rev. **105**, 1413 (1957); R. Garwin et al., “*Observations of the Failure of Conservation of Parity and Charge Conjugation in Meson Decays: the Magnetic Moment of the Free Muon*,” Phys. Rev. **105**, 1415 (1957); J. I. Friedman, V. L. Telegdi, “*Nuclear Emulsion Evidence for Parity Nonconservation in the Decay Chain $\pi^+-\mu^+-e^+$* ,” Phys. Rev. **105**, 1681 (1957).
- [17] E. Sudarshan and R. Marshak, “*Chirality Invariance and the Universal Fermi Interaction*,” Phys. Rev. **109**, 1860 (1958); R. Feynman and M. Gell-Mann, “*Theory of the Fermi Interaction*,” Phys. Rev. **109**, 193 (1958).
- [18] S. Weinberg, Phys. Rev. Lett. **19**, 1264 (1967); A. Salam, “*Elementary Particle Physics*,” N. Svartholm ed. (Nobel Symposium No. 8, Almqvist & Wiksell, Stockholm, 1968), p. 367.
- [19] P. Higgs, “*Broken symmetries, massless particles and gauge fields*,” Phys. Lett. **12**, 132 (1964); “*Broken Symmetries and the Masses of Gauge Bosons*,” Phys. Rev. Lett. **13**, 508 (1964); “*Spontaneous Symmetry Breakdown without Massless Bosons*,” Phys. Rev. **145**, 1156 (1966).
- [20] F. Englert, R. Brout, “*Broken Symmetry and the Mass of Gauge Vector Mesons*,” Phys. Rev. Lett. **13**, 321 (1964).
- [21] G. 't Hooft, M. Veltman, “*Regularization and renormalization of gauge fields*,” Nucl. Phys. B **44**, 189 (1972); “*Combinatorics of gauge fields*,” Nucl. Phys. B **50** 318 (1972).
- [22] A. Djouadi, “*The anatomy of electroweak symmetry breaking Tome I: The Higgs boson in the Standard Model*,” Phys. Rep. **457** 1 (2008).

- [23] The ATLAS Collaboration, “*Expected Performance of the ATLAS Experiment, Detector, Trigger and Physics*,” CERN-OPEN-2008-020 (2008).
- [24] K. Jacobs, “*Higgs bosons at the LHC*,” Eur. Phys. J. C **59**, 463 (2009).
- [25] The TEVNPH Working Group for the CDF and D0 Collaborations, “*Combined CDF and D0 Upper Limits on Standard Model Higgs-Boson Production with 2.1-5.4 fb⁻¹ of Data*,” arXiv:0911.3930 [hep-ex] (2009).
- [26] S. Martin, “*A Supersymmetry Primer*,” arXiv:hep-ph/9709356 (1997).
- [27] N. Arkani-Hamed, S. Dimopoulos, G. Dvali, “*The hierarchy problem and new dimensions at a millimeter*,” Phys. Lett. B, **429**, 263 (1998).
- [28] L. Randall, R. Sundrum, “*Large Mass Hierarchy from a Small Extra Dimension*,” Phys. Rev. Lett. **83**, 3370 (1999).
- [29] D. J. Kapner et al., “*Tests of the Gravitational Inverse-Square Law below the Dark-Energy Length Scale*,” Phys. Rev. Lett. **98** 021101 (2007).
- [30] E. G. Adelberger et al., “*Tests of the Gravitational Inverse-Square Law*,” Annu. Rev. Nucl. Part. Sci. **53** 77 (2003).
- [31] G. Abbiendi et al. (OPAL Collaboration), “*Photonic Events with Missing Energy in e⁺e⁻ Collisions at $\sqrt{s} = 189$ GeV*,” Eur. Phys. J. C **18** 253 (2000).
- [32] A. Heister et al. (ALEPH Collaboration), “*Single- and Multi-Photon Production in e⁺e⁻ Collisions at \sqrt{s} up to 209 GeV*,” Eur. Phys. J. C **28** 1 (2003).
- [33] P. Achard et al. (L3 Collaboration), “*Single- and Multi-Photon Events with Missing Energy in e⁺e⁻ Collisions at LEP*,” Phys. Lett. B **587**, 16 (2004).
- [34] J. Abdallah et al. (DELPHI Collaboration), “*Photon Events with Missing Energy in e⁺e⁻ Collisions at $\sqrt{s} = 130$ to 209 GeV*,” Eur. Phys. J. C **38**, 395 (2005).
- [35] V. M. Abazov et al., “*Search for Large Extra Dimensions in the Monojet + E_T^{miss} Channel with the D0 Detector*,” Phys. Rev. Lett. **90** 251802 (2003).
- [36] D. Acosta et al., “*Search for Kaluza-Klein Graviton Emission in p \bar{p} Collisions at $\sqrt{s}=1.8$ TeV Using the Missing Energy Signature*,” Phys. Rev. Lett. **92** 121802 (2004).
- [37] A. Abulencia et al., “*Search for Large Extra Dimensions in the Production of Jets and Missing Transverse Energy in p \bar{p} Collisions at $\sqrt{s} = 1.96$ TeV*,” Phys. Rev. Lett. **97** 171802 (2006).
- [38] V. M. Abazov et al., “*Search for Large Extra Dimensions via Single Photon plus Missing Energy Final States at $\sqrt{s} = 1.96$ TeV*,” Phys. Rev. Lett. **101** 011601 (2008).

- [39] T. Aaltonen et al., “*Search for large extra dimensions in final states containing one photon or jet and large missing transverse energy produced in $p\bar{p}$ Collisions at $\sqrt{s} = 1.96$ TeV,*” Phys. Rev. Lett. **101**, 181602 (2008).
- [40] S. Dimopoulos and G. Landsberg, “*Black Holes at the Large Hadron Collider,*” Phys. Rev. Lett. **87** 161602-1 (2001).
- [41] P. Meade and L. Randall, “*Black holes and quantum gravity at the LHC,*” JHEP **05** 003 (2008).
- [42] P. Lefevre, T. Petterson (editors), “*The Large Hadron Collider, Conceptual Design,*” CERN/AC/95-05 (1995).
- [43] M. Benedikt et al. (editorial board), “*The LHC Design Report Vol.1,*” CERN-2004-003-v1 (2004); “*The LHC Design Report Vol.2,*” CERN-2004-003-v2 (2004); “*The LHC Design Report Vol.3,*” CERN-2004-003-v3 (2004).
- [44] L. Evans, P. Bryant (editors), “*LHC Machine,*” JINST 3 S08001 (2008).
- [45] ATLAS Collaboration, “*The ATLAS Experiment at the CERN Large Hadron Collider,*” JINST 3 S08003 (2008).
- [46] CMS Collaboration, “*The CMS Experiment at the CERN LHC,*” JINST 3 S08004 (2008).
- [47] The LHCb Collaboration, “*The LHCb Detector at the LHC,*” JINST 3 S08005 (2008).
- [48] ALICE Collaboration, “*The ALICE experiment at the CERN LHC,*” JINST 3 S08002 (2008).
- [49] The TOTEM Collaboration, “*The TOTEM Experiment at the CERN Large Hadron Collider,*” JINST 3 S08007 (2008).
- [50] The LHCf Collaboration, “*The LHCf detector at the CERN Large Hadron Collider,*” JINST 3 S08006 (2008).
- [51] ATLAS Collaboration, “*ATLAS Technical Proposal,*” CERN-LHCC-94-43 (1994).
- [52] ATLAS Collaboration, “*ATLAS Detector and Physics Performance, Technical Design Report, Volume 1*” (1999).
- [53] ATLAS Collaboration, “*ATLAS Detector and Physics Performance, Technical Design Report, Volume 2*” (1999).
- [54] ATLAS Inner Detector Community, “*Inner Detector Technical Design Report, Volume I,*” CERN/LHCC/97-16 (1997).
- [55] ATLAS Inner Detector Community, “*Inner Detector Technical Design Report, Volume II,*” CERN/LHCC/97-17 (1997).

- [56] V. Cindro et al., “*The ATLAS Beam Conditions Monitor*,” JINST 3 P02004 (2008).
- [57] ATLAS Pixel Detector Community, “*Pixel Detector Technical Design Report*”, CERN/LHCC/98-13 (1998).
- [58] ATLAS Collaboration, “*Calorimeter Performance Technical Design Report*,” CERN/LHCC/96-40 (1996).
- [59] ATLAS LARG Unit, “*Liquid Argon Calorimeter Technical Design Report*”, CERN/LHCC/96-41 (1996).
- [60] B. Aubert et al., “*Liquid Argon Calorimetry with LHC-Performance Specifications*,” CERN/DRDC/90-31 (1990).
- [61] ATLAS/Tile Calorimeter Collaboration, “*Tile Calorimeter Technical Design Report*”, CERN/LHCC/96-42 (1996).
- [62] M. Bosman et al., “*Developments for a scintillator tile sampling hadron calorimeter with “longitudinal” tile configuration*”, CERN/DRDC/93-3 (1993).
- [63] A. Artamonov et al., “*The ATLAS Forward Calorimeters*,” JINST 3 P02010 (2008).
- [64] ATLAS Muon Collaboration, “*ATLAS Muon Spectrometer Technical Design Report*”, CERN/LHCC/97-22 (1997).
- [65] ATLAS Collaboration, “*ATLAS Forward Detectors for Measurement of Elastic Scattering and Luminosity*,” CERN/LHCC/2008-004 (2008).
- [66] D. Acosta et al., “*The CDF Cherenkov luminosity monitor*,” Nucl. Instrum. Meth. A **461**, 540 (2001).
- [67] U. Amaldi et al. (CERN-Rome Collaboration), “*The real part of the forward proton proton scattering amplitude measured at the CERN intersecting storage rings*,” Phys. Lett. B **66**, 390 (1977).
- [68] ATLAS Level-1 Trigger Group, “*Level-1 Trigger Technical Design Report*,” CERN/LHCC/98-14 (1998).
- [69] ATLAS Collaboration, “*ATLAS DAQ, EF, LVL2 and DCS Technical Progress Report*,” CERN/LHCC/98-16 (1998).
- [70] ATLAS HLT/DAQ/DCS Group, “*ATLAS High-Level Trigger, Data Acquisition and Controls*,” CERN/LHCC/2003-022 (2003).
- [71] <https://twiki.cern.ch/twiki/bin/view/Atlas/L31TriggerMenu>
- [72] C. Fabjan, F. Gianotti, “*Calorimetry for particle physics*,” Rev. Mod. Phys. **75**, 1243 (2003).

- [73] R. Wigmans, *“Calorimetry, Energy Measurement in Particle Physics,”* Oxford University Press (2000).
- [74] Particle Data Group, *“Review of Particle Physics,”* Phys. Lett. B **667**, 1 (2008).
- [75] M. Delmastro, *“Electronic calibration of the ATLAS LAr calorimeters,”* LAr Electronic Calibration Tutorial, 5 May, 2008.
- [76] W. E. Cleland, E. G. Stern, *“Signal processing considerations for liquid ionization calorimeters in a high rate environment,”* Nucl. Instrum. Meth. A **338**, 467 (1994).
- [77] M. Aleksa et al., *“2004 ATLAS Combined Testbeam: Computation and Validation of the Electronic Calibration Constants for the Electromagnetic Calorimeter,”* ATLAS Note, ATL-LAR-PUB-2008-003 (2008).
- [78] D. Banfi et al., *“Cell response equalization of the ATLAS electromagnetic calorimeter without the direct knowledge of the ionization signals,”* JINST **1** P08001 (2006).
- [79] R. Teuscher, *“Energy and time reconstruction for CIS and Physics,”* TileCal Analysis Meeting, Oct. 7, 2002.
- [80] E. Fullana et al., *“Optimal Filtering in the ATLAS Hadronic Tile Calorimeter,”* ATL-TILECAL-2005-001 (2005); E. Fullana, *“Energy reconstruction algorithms for the ATLAS Hadronic Tile Calorimeter and their effect on extra dimensions signatures,”* PhD thesis, IFIC, University of Valencia (2007).
- [81] M. Vincter, *“Energy reconstruction in the calorimeter,”* ATLAS Hadronic Calibration Workshop, Lisbon, Portugal, 23-27 June, 2009.
- [82] G. Schlager, *“The Energy Response of the ATLAS Calorimeter System,”* PhD Thesis, Technische Universitaet Wien, CERN-THESIS-2006-002 (2006).
- [83] I. Abt et al., *“The tracking, calorimeter and muon detectors of the H1 experiment at HERA,”* Nucl. Instr. and Meth. A **386** 348 (1997).
- [84] B. Salvachua et al., *“Comparison of MC based Jet Energy Scales applied after H1 calibration,”* ATLAS Note, ATL-PHYS-INT-2009-050 (2009).
- [85] P. Loch, *“Suggestions for General Energy Reconstruction Scheme for the ATLAS Calorimeters,”* ATLAS Note, CAL-NO-91 (1997).
- [86] T. Barillari et al., *“Local Hadronic Calibration,”* ATLAS Note, ATL-LARG-PUB-2009-001 (2009).
- [87] R. Teuscher, *“Commissioning with Physics data at ATLAS,”* ICHEP2005, Proceedings, ATL-COM-SLIDE-2006-001 (2005).
- [88] R. Teuscher, *“Commissioning: The Road to Physics,”* ATLAS Plenary Week, February, 2006.
<http://indico.cern.ch/conferenceDisplay.py?confId=a056827>

- [89] A. Wright, “*First ‘data’ from LHC*”, Nature Physics, doi:10.1038/nphys005 (2005).
- [90] CERN Press Release “*LHC to restart in 2009*,” December 5, 2008.
<http://press.web.cern.ch/press/PressReleases/Releases2008/PR17.08E.html>
- [91] <https://twiki.cern.ch/twiki/bin/view/Atlas/TrtTrigger>
- [92] Courtesy from S. Menke.
- [93] F. Spano, “*Preliminary noise analysis in CTB, TileCal Analysis & Combined Test Beam*,” 14 February 2005.
<http://indico.cern.ch/getFile.py/access?contribId=s1t2&resId=1&materialId=0&confId=a05600>
- [94] F. Spano, “*Simulation of the full noise pattern in Tile Calorimeter Front End electronics: a phenomenological approach to coherent noise effects*,” ATLAS Note, ATL-COM-TILECAL-2008-009 (2008).
- [95] P. Adragna et al., “*Testbeam Studies of Production Modules of the ATLAS Tile Calorimeter*,” ATLAS Note, ATL-TILECAL-PUB-2009-002 (2009).
- [96] H. Okawa et al., “*Calorimeter Commissioning With Cosmic Rays: Cells, Clusters, Jets and Missing E_T* ,” ATLAS Note, ATL-COM-CAL-2008-007 (2008).
- [97] G. Blanchot et al., “*Electromagnetic Compatibility of a Low Voltage Power Supply for the ATLAS Tile Calorimeter Front-End Electronics*,” 12th Workshop on Electronics for LHC and Future Experiments, Valencia, Spain, Sep. 25-29, 2006.
- [98] R. Stanek, “*Tile Progress Report*,” ATLAS TileCal Meeting, Feb. 13, 2006.
- [99] K. J. Anderson et al., “*Design of the front-end analog electronics for the ATLAS tile calorimeter*,” Nucl. Inst. and Meth. A 551, 469 (2008).
- [100] K. J. Anderson et al., “*Performance and Calibration of the TileCal Fast Readout Using the Charge Injection System*,” ATLAS Note, ATL-TILECAL-INT-2008-002; ATL-COM-TILECAL-2008-003 (2008).
- [101] V. Radeka, “*Electronics for Calorimeter - An Overview of Requirements*,” Proceedings of the First Workshop on Electronics for LHC Experiments, CERN/LHCC/95-56, 235 (1995).
- [102] H. Spieler, “*Front-End Electronics Systems for Particle Detection and Imaging*,” IEEE NSS-MIC Short Course Program, Dresden, Germany, Oct. 19, 2008.
- [103] F. Hubaut et al., “*Testing calorimetric Missing Transverse Energy and jet reconstruction with random and cosmic data*,” ATLAS Note, ATL-PHYS-INT-2009-045 (2009).
- [104] M. C. N. Fiolhais, A. Onofre, “*Minimizing the TileCal correlated noise effect: a simple approach*,” ATLAS Note, ATL-COM-TILECAL-2009-019 (2009).

- [105] S. Yamamoto, “*TileCal Coherent Noise*,” ATLAS TileCal Data Quality, Performance and Processing Meeting, Oct. 12, 2009.
- [106] ATLAS Public Results.
<https://twiki.cern.ch/twiki/bin/view/Atlas/AtlasResults>
- [107] ATLAS Collaboration, “*Readiness of the ATLAS Liquid Argon Calorimeter for LHC Collisions*,” ATLAS Note, ATLAS-LAR-2009-01-001 (2009).
- [108] G. Choudalakis, “*Correction for dead calo cell based on neighbors*,” ATLAS Calorimeter Performance Meeting, 25 Feb., 2009.
<http://indico.cern.ch/contributionDisplay.py?contribId=0&confId=47494>
- [109] G. Choudalakis et al., “*Use of Tracks to Reconstruct Jets in Damaged Calorimeter Regions*,” ATLAS Note, ATL-PHYS-INT-2009-017 (2009).
- [110] <https://twiki.cern.ch/twiki/bin/view/Atlas/LArP3CommissioningUnhappyChannels>
- [111] W. Lampl et al., “*Calorimeter Clustering Algorithms: Description and Performance*,” ATLAS Note, ATL-LARG-PUB-2008-002 (2008).
- [112] <https://twiki.cern.ch/twiki/bin/view/Atlas/TopologicalClustering>
- [113] L. Ma et al., “*Results of 2004 Beam Tests with Topological Clustering Algorithm: Energy Dependence in the EMEC, HEC, and FCAL*,” ATLAS Note, ATL-COM-LARG-2008-007 (2008).
- [114] B. Guo, Topo clusters in Endcap, Endcap Commissioning analysis meeting, November 1, 2007.
<http://indico.cern.ch/getFile.py/access?subContId=0&contribId=1&resId=1&materialId=slides&confId=20575>
- [115] A. Dar, “*Atmospheric Neutrinos, Astrophysical Neutrons, and Proton-Decay Experiments*,” Phys. Rev. Lett. **51**, 227 (1983).
- [116] M. Boonekamp et al., “*Cosmic Ray, Beam Halo and Beam-Gas Rate Studies for ATLAS Commissioning*,” ATLAS Note, ATL-GEN-2004-001 (2004).
- [117] A. Achterberg, “*Cosmic Ray Physics, sources of energetic particles in the universe*,” Lecture notes, University of Utrecht (1997).
- [118] A. van Mil, “*Cosmic-Ray Muons in the L3 Detector*,” PhD thesis, Universiteit Nijmegen (2000).
- [119] R. Teuscher et al., “*Fake Missing Transverse Energy from ATLAS Calorimeter Cosmic Ray Data*,” ATLAS Note, ATL-INT-CAL-2008-001, ATL-COM-CAL-2008-002 (2008).

- [120] P. Mermod et al., “*Effects of ATLAS Tile calorimeter failures on jets and missing transverse energy measurements,*” ATLAS Note, ATL-COM-TILECAL-2008-010 (2008).
- [121] T. Bain, A Study of Jet and Missing Transverse Energy Reconstruction and Data Cleaning Techniques on ATLAS Calorimeter Cosmic Ray Data, Masters Report, University of Toronto, August 21, 2008.
- [122] B. Meirose, R. Teuscher, “*Time of Flight Analysis Using Cosmic Ray Muons in the ATLAS Tile Calorimeter,*” ATLAS Note, ATL-TILECAL-PUB-2008-004 (2008).
- [123] L. Fiorini et al., “*Time Calibration of TileCal Modules with Cosmic Muons,*” ATLAS Note, ATL-TILECAL-PUB-2008-002 (2008).
- [124] C. Clément et al., “*Time Calibration of the ATLAS Hadronic Tile Calorimeter using the Laser System,*” ATLAS Note, ATL-COM-TILECAL-2008-018 (2008).
- [125] M. Volpi et al., “*Time inter-calibration of hadronic calorimeter of ATLAS with first beam data,*” ATLAS Note, ATL-COM-TILECAL-2009-008 (2009).
- [126] J. G. Saraiva et al., “*Synchronization of the ATLAS Tile calorimeter with cosmic muon data,*” ATLAS Note, ATL-COM-TILECAL-2009-024 (2009).
- [127] J. Maneria et al., ATLAS Tile Calorimeter Timing Working Group.
- [128] T. Guillemin et al., “*Time Alignment of the ATLAS Liquid Argon Calorimeters,*” ATLAS Note, ATL-COM-LARG-2009-001 (2009).
- [129] The ATLAS Collaboration, “*Prospects for Supersymmetry and Universal Extra Dimensions discovery based on inclusive searches at a 10 TeV center-of-mass energy with the ATLAS detector,*” ATLAS Note, ATL-PHYS-PUB-2009-084 (2009).
- [130] H. Okawa, “*Determination of background from W/Z and top. What do we need to find SUSY*” LHC and Dark Matter Workshop, Ann Arbor, USA, Jan. 6-10, 2009.
- [131] S. Hillier, A. Watson, D. Damazio, private communication.
- [132] T. Kono, private communication.
- [133] M. Ibe et al., “*Possible signals of wino LSP at the Large Hadron Collider,*” Phys. Lett. B **644** 355 (2007).
- [134] N. Arkani-Hamed, S. Dimopoulos, “*Supersymmetric unification without low energy supersymmetry and signatures for fine-tuning at the LHC,*” JHEP06 073 (2005).
- [135] G. F. Giudice and A. Romanino, “*Split supersymmetry,*” Nucl. Phys. B **699** 65 (2004).
- [136] J. Hewett et al., “*Signatures of long-lived gluinos in split supersymmetry,*” JHEP09 070 (2004).

- [137] L. Vacavant and I. Hinchliffe, “*Signals of models with large extra dimensions in ATLAS*,” J. Phys. G: Nucl. Part. Phys **27** 1839 (2001).
- [138] G. Azuelos et al., “*Phenomenological constraints on extra-dimensional scalars*,” J. Phys. G: Nucl. Part. Phys **31** 1 (2005).
- [139] T. Gleisberg et al., “*Event Generation with SHERPA 1.1*,” JHEP **02** 007 (2009).
- [140] F. Krauss et al., “*AMEGIC++ 1.0 A Matrix Element Generator In C++*,” JHEP **02** 044 (2002).
- [141] T. Gleisberg et al., “*Helicity formalism for spin-2 particles*,” JHEP **09** 001 (2003).
- [142] G. Giudice et al., “*Quantum gravity and extra dimensions at high-energy colliders*,” Nucl. Phys. B **544** 3 (1999).
- [143] T. Han et al., “*Kaluza-Klein states from large extra dimensions*,” Phys. Rev. D **59** 105006 (1999).
- [144] Isajet website: <http://www.hep.fsu.edu/~isajet/>
- [145] F. Caravaglios et al., “*A new approach to multijet calculations in hadron collisions*,” Nucl. Phys. B **539** 215 (1999); M. L. Mangano et al., “*Multijet matrix elements and shower evolution in hadronic collisions: $W B Bbar + N$ jets as a case study*,” Nucl. Phys. B **632** 343 (2002); M. L. Mangano et al., “*ALPGEN, a generator for hard multiparton processes in hadronic collisions*,” JHEP 0307:001 (2003).
- [146] ATLAS Collaboration, “*Data-driven Determination of $t\bar{t}$ Background to Supersymmetry Searches in ATLAS*,” ATLAS Note, ATL-PHYS-PUB-2009-083 (2009).
- [147] M. Hurwitz, “*Understanding the jet energy scale using photon-jet balance*,” ATLAS Note, ATL-PHYS-INT-2009-014 (2009).
- [148] S. Chekanov, “*Understanding the jet energy scale using P_T balance for direct photon production with associated jet*,” ATLAS Note, ATL-COM-PHYS-2009-042 (2009).
- [149] D. Mateos, et al., “*A Simple p_T - and η -Dependent Monte Carlo-Based Jet Calibration*,” ATLAS Note, ATL-COM-PHYS-2009-076 (2009).
- [150] G. Choudalakis, et al., “*In Situ Jet Energy Scale Calibration Using Direct γ +jet Balance*,” ATLAS Note, ATL-COM-PHYS-2009-644 (2009).
- [151] R. Piegaia, et al., “*Measurement of the Jet Energy Resolution in ATLAS using Data-Driven Techniques*,” ATLAS Note, ATL-COM-PHYS-2009-408 (2009).